Performance Assessment and Enhancement of Precision Controlled Structures During Conceptual Design

Homero L. Gutierrez and David W. Miller

February 1999   SERC#1–99

Abstract

Future optical space systems such as interferometers and filled-aperture telescopes will extend the resolution and sensitivity offered by their on-orbit and ground-based predecessors. These systems face the challenge of achieving nanometer and milli-arcsecond precision control of stellar light passing through the optical train of a lightweight, flexible structure subjected to various disturbances. It is advantageous to assess the performance of initial concepts of these precision systems early in the design stage to aid in the requirements flowdown and resource allocation process. A complete end-to-end performance assessment methodology is developed which incorporates disturbance, sensitivity, and uncertainty analysis tools within a common state-space framework. The disturbance analysis is conducted using either a time-domain, frequency-domain, or Lyapunov approach to obtain nominal predictions of performance metric root-mean-square (RMS) values. Calculating power spectral density and cumulative RMS functions of the performance metrics allows critical system modes and frequencies to be identified, and in some instances, contributions from each of the disturbances can be determined. A Lagrange multiplier method is used to derive a governing equation for the sensitivities of the performance metrics with respect to model parameters. For a system whose structural dynamic equations are represented in modal form, the sensitivities can be calculated exactly and efficiently with respect to modal frequencies, masses, and damping ratios. The most critical modal parameters are carried into a parametric uncertainty analysis that seeks to identify the worst-case performance RMS values. A constrained optimization technique is described which searches for the worst-case performance over all allowable parameter values. When required, a performance enhancement approach is used to apply controlled structures technologies such as input/output isolation to achieve large performance changes. Structural modifications based on insight provided by a physical parameter sensitivity analysis are then employed to "fine tune" the performance to keep the worst-case values within the requirements. Analytical physical parameter sensitivities are experimentally validated on a truss structure and used to implement stiffness and mass perturbations that reduce the tip displacement of a flexible appendage. The overall framework is applied to an integrated model of the Space Interferometry Mission to demonstrate its practical use on a large order system.

Acknowledgments

Contents

9

List of Figures

15

List of Tables

Nomenclature

Abbreviations

ACS	attitude control system
CMG	control moment gyro
CST	controlled structures technologies
DOF	degree of freedom
EVP	eigenvalue problem
FEM	finite-element model; finite-element method
FSM	fast steering mirror
IMOS	Integrated Modeling of Optical Systems
JPL	Jet Propulsion Laboratory
NGST	Next Generation Space Telescope
ODL	optical delay line
OPD	optical path difference
PDF	probability density function
PSD	power spectral density
RBE	rigid body element
RMS	root mean square
RWA	reaction wheel assembly
SIM	Space Interferometry Mission
SQP	Sequential Quadratic Programming
WFT	wavefront tilt

Symbols

A	cross-sectional area
A_c	compensator dynamics matrix
A_d	disturbance filter dynamics matrix
A_{zd}	augmented disturbance/plant/control dynamics matrix
B_c	compensator input matrix
B_d	disturbance filter input matrix
B_u	plant control input matrix
B_w	plant disturbance input matrix
B_{zd}	augmented disturbance/plant/control input matrix
C	physical damping matrix
C_c	compensator output matrix
C_d	disturbance filter output matrix
C_{zd}	augmented disturbance/plant/control performance matrix
C_{zx}	plant performance output matrix
D_c	compensator feedthrough matrix

D_d	disturbance filter feedthrough matrix
D_{zd}	augmented disturbance/plant/control feedthrough matrix
E	Young's modulus
G	shear modulus; transfer function matrix
I	cross-sectional bending moment of inertia
J	cross-sectional torsional constant; performance cost
K	stiffness matrix
$\mathcal{K}$	dynamic stiffness matrix $(= -\omega^2 M + K)$
L	Lagrange multiplier matrix; element length
M	mass matrix
$\mathcal{M}$	modal mass matrix
R	transformation from all DOF's to nset DOF's; performance weighting matrix
T	coordinate transformation matrix
W_c, W_o	controllability and observability gramians
d	unity-intensity white noise
p	generic parameter
q	augmented disturbance/plant/control state vector
w	disturbance variable
x	FEM physical DOF's
y	sensor measurement
z	performance variable
Δ	uncertainty block; change in quantity
Γ	modal damping matrix
Ω	modal frequency matrix
Φ	mode shape matrix
Σ	gramian matrix (squared Hankel singular values)
Σ_q	state covariance matrix
α	CELAS scale factor
β	Euler angle for RWA orientation; CONM scale factor
β_u	plant control influence matrix
β_w	plant disturbance influence matrix
γ	Euler angle for RWA orientation
η	FEM modal coordinate vector
ϕ	mode shape vector; phase angle
ψ	particular solution used in eigenvector derivatives
ρ	mass density
σ	standard deviation (= RMS if zero-mean); Hankel singular value
σ^2	variance (= mean-square if zero-mean)
θ	Euler angle for RWA orientation
ζ	modal damping ratio

Subscripts and Superscripts

$(\cdot)^*$	Lagrangian
$(\cdot)^H$	Hermitian (complex-conjugate transpose)
$(\cdot)^T$	transpose
$(\cdot)_{i,j}, (\cdot)_{ij}$	(i,j) entry of a matrix
$(\cdot)_i$	ith entry of a vector

Chapter 1

Introduction

1.1 Background

Two space observatories that will be in operation during the first decade of the 21$^{\text{st}}$ century are the Space Interferometry Mission (SIM) and the Next Generation Space Telescope (NGST). To achieve improvements in angular resolution and sensitivity, they will be pushing the state-of-the-art beyond the level currently used by similar ground-based and space-based systems. The ability of these instruments to satisfy ambitious performance requirements will depend heavily on their structural dynamic behavior [53]. They must achieve precision control and stabilization of the science light using optical elements attached to a lightweight, flexible structure subjected to on-board and external disturbances. They will need to use a combination of optical control and vibration suppression techniques to mitigate the effects of the disturbance-induced response of the structure on the optical performance metrics [51].

The conceptual design phase is a crucial time during which various system architectures are analyzed and enabling technologies are identified. The allocation of design requirements and resources during these early stages of a program is based on preliminary analyses using simplified models that try to capture the behavior of interest [15]. These models are generally suitable for judging relative merits between competing designs in a trade study; however, the validity of their use in making absolute performance assessments is not as clear. It is important that correct decisions be made during the conceptual design process so that costly redesigns at later stages are avoided. A way to account for model deficiencies (*e.g.*, uncertainties) when making performance predictions is therefore beneficial. Furthermore,

Performance
Enhancement

redesign
options

$\delta z / \delta p$

Sensitivity
Analysis

$G_d(\omega)\,;\,A_d,B_d,C_d,D_d$

$G_{zw}(\omega)\,;\,A_{zw},B_{zw},C_{zw},D_{zw}$

z_{req}

d
unit-intensity
white noise

Disturbance
Model

w

Plant Model
(open or
closed-loop)

z
performance
prediction

$+$ $-$

design
margin

performance
assessment

Δ_d

Δ

disturbance
uncertainty

plant
uncertainty
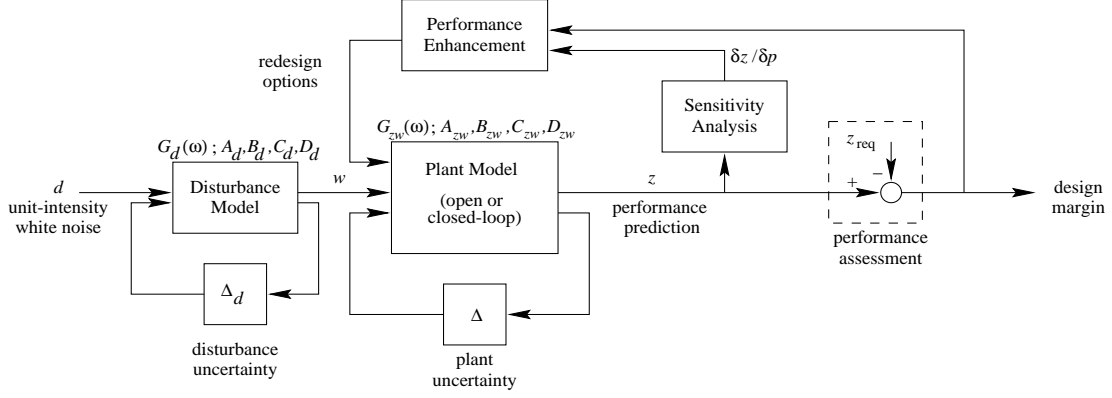
Figure 1.1: Performance assessment and enhancement framework.

it is desirable to have quantitative analysis tools that can be applied to the typical high-performance, controlled optical systems that will be continually developed over the years to come.

In response to these needs, a complete end-to-end methodology is developed which incorporates disturbance, sensitivity, and uncertainty analyses within a common state-space framework. A block diagram of the approach is presented in Figure 1.1, and the goal of the approach is to take a conceptual design, systematically identify the important characteristics of the design, and suggest improvements to the design. A preliminary "point design" is assumed to exist, and the plant model can represent a closed-loop system. Performance outputs z are identified based on system outputs that must meet specified requirements. In a traditional disturbance analysis, disturbances w are propagated through the system model to obtain predictions of the resulting performance. An assessment can then be made by comparing z against the requirements z_{req}. If it is found that all requirements are met, confidence in the ability of the design to meet mission objectives is increased.

Uncertainties in the plant and disturbance models are represented by local Δ blocks. There might be uncertainties in the modal frequencies, for example, or a disturbance filter driven by white noise might have errors in its frequency content or magnitude. It is not suggested that all sources of uncertainty can be modeled by these feedback loops, but they are shown this way for conceptual purposes. An uncertainty analysis can place upper bounds on z, and the bounds can be compared to z_{req}. Not only should a disturbance analysis provide performance estimates of the nominal design, but an uncertainty analysis

should place the equivalent of "error bars" around z_{nominal}. The uncertainty analysis is essentially a disturbance analysis that accounts for uncertainties.

Unsatisfactory results lead to a system improvement phase during which modifications to the design are considered. The objective is to suggest modifications (*e.g.*, applying controlled structures technologies) that lead to acceptable design margins. A sensitivity analysis can be used to identify the critical parameters to which the performance is most sensitive, and these parameters can be targeted for redesign. The improvement phase ends when a comfortable design margin exists, or when it is discovered that z_{req} can only be satisfied if the uncertainty levels are reduced. A rigorous testing program which serves to improve knowledge of the parameters should then be planned.

1.2 Research Objectives and Approach

The primary objectives of the research are summarized below.

- Develop a consistent and general methodology for assessing the performance of systems in which the structural dynamic and control aspects must be considered.

- Implement the methodology as a series of compatible analysis tools that are applied to a nominal system model driven by disturbance models. The tools should consist of

  - a disturbance analysis tool for predicting performance outputs,

  - a sensitivity analysis tool for predicting changes in performance outputs due to changes in model parameters, and

  - an uncertainty analysis tool for estimating variations in the predicted performance outputs due to uncertainties in model parameters.

- Identify computation and time-saving measures that permit the analysis tools to be applied to large-order systems.

- Suggest an approach for performance enhancement that utilizes the analysis results to identify design options with improved performance.

- Validate the analysis tools on various mathematical systems and on an experimental testbed.

- Apply the overall methodology to an existing integrated model of the Space Interferometry Mission.

The approach that is taken to develop the end-to-end methodology is as follows. The governing equations are derived and then implemented in MATLAB code. The code is applied to problems of different levels of complexity, beginning with simple, low-order models that provide an understanding of the basic issues as well as help to validate the equations. Then, the technique is applied to more complex models to investigate issues that might not be readily apparent on the simple models. All of the analysis methods are designed to be applied to the large-order, sophisticated models of systems that motivate this research. An underlying theme is the development of model reduction and other approximation strategies that permit results to be obtained in realistic time without significant loss of accuracy. The product of this work is not only a conceptual methodology, but also a software toolbox that has been tested and which is ready for application to real-world systems.

1.3 Literature Review

The research does build upon previous work in the different areas that are encompassed by the assessment and enhancement framework. Creating the nominal plant and disturbance models occurs during an **integrated modeling** process. A software package called IMOS (Integrated Modeling of Optical Systems) [46] was developed at the Jet Propulsion Laboratory (JPL) to facilitate the generation of initial models of optical instruments. IMOS offers the ability to significantly reduce the time required to take a concept of a system, build an integrated model, and conduct analyses and trade studies. The need for such a capability was described by Laskin and San Martin during a traditional design and analysis exercise on the Focus Mission Interferometer [53].

Modeling precision optical systems requires fundamental knowledge of several distinct disciplines. Structural dynamics is one field, and a popular textbook by Craig [13] offers a good introduction. Since most structural dynamic models are based on the finite-element method, the books by Bathe [5] and Cook [12] should be consulted. Another important aspect of structural modeling is damping, and it is critical that realistic levels of damping be used in the integrated models. In particular, the damping of structures at the small vibration levels that are expected on precision spaceborne optical systems is an area that

has recently been investigated. The research by Ting and Crawley [84] and Ingham [39] was motivated by the lack of experimental data at these low vibration levels.

The reliance of these systems on closed-loop control requires that actuators, sensors, and compensators be included in the integrated model. Introductory textbooks such as those by Van de Vegte [85] and Ogata [71] are useful for a review of classical control design techniques, while that of Zhou *et al.* [88] emphasizes modern control theory approaches. Since most control systems are implemented on digital computers, the standard references by Åström [1] and Franklin and Powell [22] are recommended.

Optical modeling is another area that is essential, and Redding and Breckenridge [78] describe the mathematics behind linear ray trace theory. The main product of the optical modeling process is a sensitivity matrix that relates perturbations in optical quantities such as pathlength and beam walk to motion of the optical elements. A software program called MACOS (Modeling and Analysis for Controlled Optical Systems) [45] creates the sensitivity matrix based on a prescription of optical elements in the system. The optical sensitivity matrix can be readily incorporated with a state-space representation of the structure and control system.

Although disturbance modeling is often overlooked, its importance cannot be understated. All potential disturbance sources that can hinder the performance of a high precision optical system need to be identified. Eyerman and Shea [20] provide a very complete overview of spacecraft disturbances. Two specific disturbances that are anticipated to cause problems for these systems are reaction wheel disturbances and thermal snap. Disturbance characterization efforts related to both have been conducted in recent years. Bialke [6] offers a good explanation of the sources of reaction wheel disturbances. The reaction wheels of the Hubble Space Telescope, in particular, have been extensively analyzed [17], and Melody [60] uses data from tests on a single wheel to derive a stochastic disturbance model. This model serves as the basis for the development of a more general reaction wheel assembly (RWA) disturbance model in Chapter 2. The relatively unknown effects of thermal snap prompted experimental and modeling efforts in this area. Modeling thermal snap phenomena was the subject of research by Kim [49]. The IPEX (Interferometry Program Experiment) sequence of flight experiments was designed to quantify some of the thermal snap and associated microdynamics issues. IPEX-1 (STS-80, Dec. 1996) identified the microdynamic characteristics of the Astro-Spas, a reusable spacecraft scientific platform, using a suite of

accelerometers [54]. IPEX-2 (STS-85, Aug. 1997) studied the representative dynamics of a deployable, pre-loaded truss that was cantilevered from the Astro-Spas. Data suggests the presence of thermal snap-like events that occur during orbital sun-shade transitions; however, SIM-derived structural stability criteria are satisfied [55]. Efforts were also made to use ground test data to quantify the magnitude of various disturbance sources on the Astro-Spas (*e.g.*, rate gyros, tape recorders, thrusters) [30]. Tests such as these should be performed prior to launch of high performance optical systems.

Also of great use when creating large-order integrated models are methods for model reduction. Creating a balanced state-space realization [65] can not only improve the numerical conditioning properties of a model, but it also serves as a technique for identifying states that can be eliminated from the model due to low observability and controllability [88]. For the case of systems dominated by lightly-damped modes, the method proposed by Gregory [27] is an efficient approach for ranking the importance of these modes.

The integrated modeling process is demonstrated by Melody and Neat [63] on JPL's Micro-Precision Interferometer testbed and is experimentally validated based on the comparison of predicted and measured closed-loop transfer functions. It is also demonstrated by Shaklan *et al.* [79] on a SIM precursor design.

The theory behind conducting a stochastic **disturbance analysis** is well-developed. Random vibration textbooks such as those by Crandall [14] and Wirsching [86] characterize the response of systems driven by stochastic inputs in the time-domain (using autocorrelation functions) and equivalently in the frequency-domain (using power spectral density functions). The concept of a linear shaping or "pre-whitening" filter whose input is white noise and whose output is "colored" noise with desired magnitude and spectral content is covered by Brown and Hwang [8]. For the case of state-space systems driven by white noise, the output steady-state covariance matrix is known to be the solution of a Lyapunov equation [2]. These techniques are used extensively for performance assessment throughout this thesis. Sample disturbance analysis results for space optical systems have been presented for SIM [29],[32], an open-loop model of NGST [18], another proposed space interferometer called POINTS [62], and a proposed Space Shuttle interferometry experiment called SITE [15].

A **sensitivity analysis** provides useful information related to how dependent certain quantities of a model are with respect to parameters of the model. Most sensitivities are

computed using a finite-difference approach; however, in certain instances, the sensitivities can be calculated exactly. A goal of the sensitivity analysis framework in Chapter 4 is to derive analytical expressions whenever possible and to avoid the inexact and often inefficient finite-difference technique. A Lagrange multiplier approach is used by Jacques [40] to obtain analytical sensitivities of a system's outputs with respect to various parameters, and this same methodology is employed in Chapter 4. The calculation of sensitivities with respect to physical parameters requires mode shape and frequency derivatives, which fall under the category of eigenvalue and eigenvector derivatives. (A good survey of various methods is provided by Murthy and Haftka [66].) When the parameters are element mass and stiffness properties of a finite-element model, these derivatives can be computed exactly using methods developed by Fox and Kapoor [21] and Nelson [68]. Practical implementation of these methods is done by Kenny [48], and this work is extended for use in Chapter 4. The physical parameter sensitivity analysis framework derived in Chapter 4 for state-space systems is similar to the approach used by Hou and Koganti [36] in the context of integrated controls-structure design.

Past work relevant to the **uncertainty analysis** portion of the performance and enhancement framework includes the robust control design approach of Yang [87] and How [37]. They derive estimates for bounds on a system's $\mathcal{H}_2$ performance that are used in the process of obtaining controllers that have stability and performance robustness to uncertain modal frequencies. An approximate method for predicting worst-case performance RMS values due to parametric uncertainties is that used by Bryson and Mills [9]. An exhaustive search of "corners" of the uncertain parameter space is conducted to identify the combination of parameter bounds that results in the largest RMS value. From a structural dynamics standpoint, the work by Hasselsman *et al.* [33], [34] provides different approaches for estimating uncertainty in transfer function magnitude and phase due to uncertainties in modal parameters. One particular method is the first-order approach that relates the covariance matrix of output quantities in terms of the covariance matrix of uncertain parameters and the sensitivity matrix of the outputs with respect to the parameters. More general treatment of model error and uncertainty from a control aspect is provided by Skelton [80] and Zhou *et al.* [88]. Also applicable to the types of systems under consideration is the work by Campbell and Crawley [10]. Modal parameter uncertainty models developed from 1-g tests are used to identify uncertainties in FEM mass and stiffness properties. These

uncertainties are propagated into modal parameter uncertainty models for the system in a different environment (*e.g.*, 0-*g*) or configuration.

Work in **performance enhancement** includes integrated control/structure optimization. The objective is to develop structure and control designs simultaneously such that the overall system design has improved properties compared to a system design obtained through a traditional, sequential approach. This allows the same performance to be achieved with less control effort or less structural mass, for example. The combined optimization can be a challenging task, especially if the design parameters include stiffness/mass distribution, structural connectivity/topology, actuator/sensor placement and type, and control design parameters. Many of these options need to be fixed ahead of time to make the problem formulation tractable for realistic systems. Solutions are dependent on the type of cost functional specified and the solution technique employed. Jacques uses a typical section approach to gain insight into the control/structure optimization problem [40]. The method developed by Milman *et al.* [64] does not seek the global optimal design, but rather generates a series of Pareto-optimal designs that can help identify the characteristics of better system designs. Masters and Crawley use Genetic Algorithms to identify member cross-sectional properties and actuator/sensor locations that minimize an optical performance metric of an interferometer concept [57]. The approach was experimentally validated on a closed-loop, truss-like testbed [58], and this marks one of the few experimental investigations into integrated control/structure optimization. Another example is the work done at NASA Langley Research Center by Maghami *et al.* [56]. The pointing performance of a large, laboratory testbed was successfully maintained while control effort was decreased. Design parameters were controller gains and cross-sectional properties of groups of truss elements. Topological redesign was performed by Keane on an open-loop, truss structure to minimize the response in a truss member due to an external disturbance [47].

Performance enhancement on systems with uncertain parameters is treated by Parkinson *et al.* [76] and Pritchard *et al.* [77]. The method by Parkinson *et al.* finds an optimal design that satisfies specified constraints even when certain parameters are uncertain. It is a two-step procedure whereby the nominal optimum design is determined first, then a second optimization problem is solved whose constraints are modified by the uncertainties. The effects of uncertainties are calculated based on a first-order approximation. Pritchard *et al.* use a nested procedure in which an inner loop is a standard constrained optimization

problem and an outer loop searches for the optimum design whose performance is least sensitive to specified parameters. Both methods are applied to and demonstrated on simple, static structural problems.

Finally, Crawley *et al.* present a methodology for the conceptual design of controlled structural systems [15]. It applies a controlled structures technology (CST) framework in a consistent level of modeling detail. The goal is to identify the critical disturbance-to-performance transmission paths and to determine the amount of CST options that are required to achieve performance requirements.

1.4 Thesis Overview

Figure 1.2 is designed to provide a sense of the chronological order of the analyses. It also serves as a thesis roadmap to help put the chapter sequence in context. Before any of the performance assessment tools can be applied, a nominal model of the proposed system is needed. For spaceborne systems such as SIM and NGST, an integrated modeling process unifies structural dynamic, control, optics, and disturbance models. An overview of each of these disciplines is offered in Chapter 2, and the SIM integrated model is used as a representative example. Once the model is created, the disturbance analysis is conducted. Chapter 3 describes time-domain, frequency-domain, and Lyapunov analyses that can be used to estimate the nominal root-mean-square (RMS) values of the performance metrics. The chapter also demonstrates how to identify the critical structural modes and disturbances from a frequency-domain analysis. A sensitivity analysis with respect to the modal parameters of the critical modes is then performed, and details are provided in Chapter 4. After the important modal parameters are identified, an uncertainty analysis predicts the worst-case RMS values when the modal parameters are not known exactly but are bounded. Chapter 5 develops a technique that solves a constrained optimization problem in order to find the combination of uncertainties that maximizes the RMS values. When the results are unsatisfactory, the performance enhancement phase is entered. Useful redesign options can be identified by physical parameter sensitivities, and the basic theory is discussed in Chapter 4. The parameters that affect the critical modes are selected for the sensitivity analysis, and this process is also included in Chapter 4. Chapter 7 summarizes various options to try during performance improvement efforts, and it includes an example application to the

integrated modeling (a)

nominal model

disturbance analysis (b)

z_{nom}, critical modes

modal parameter
sensitivity analysis (c)

important modal
parameters

modal parameter to
physical parameter mapping (d)

important physical
parameters

uncertainty analysis
(modal domain) (e)

physical parameter
sensitivity analysis (f)

$z_{nom} + \Delta z$

sensitivities

performance assessment

design margin

performance enhancement process (g)

improved
design (h)

comments

(a) integrates disturbance,
structural, control,
and optical models
[Chap. 2]

(b) 3 types (time-domain,
freq.-domain, Lyap.)
[Chap. 3]

(c) requires state-space
formulation
[Chap. 4]

(d) strain energy plots useful
[Chap. 4]

(e) uses constrained optimization
routine to identify
worst-case parameters
[Chap. 5]

(f) requires mode shape and
frequency derivatives
[Chap. 4,6]

(g) applies CST methodology
[Chap. 7]

(h) if performance
unsatisfactory

Figure 1.2: Analysis procedure.

SIM model. The results of an experimental validation exercise are found in Chapter 6.

Chapter 2

Integrated Modeling

This chapter discusses the integrated modeling approach as motivated by high precision opto-mechanical space systems. Although the contributions in this thesis are primarily related to the development and application of analysis tools, it will be seen that some of the underlying assumptions are based heavily on the type of model being analyzed as well as the type of inputs and outputs. In particular, the specific disciplines that are considered in the modeling process are structural dynamics, controls, and optics. The inputs are stochastic on-board disturbances, and the outputs are optical performance metrics expressed in a root-mean-square (RMS) sense. The first section will explore these different areas of integrated modeling a bit further. Section 2.2 will then describe the integrated model of the Space Interferometry Mission that was developed at the Jet Propulsion Laboratory. This model is frequently used in the other chapters to demonstrate the analysis tools on a realistic system, and a better understanding of the model will help to put the results in perspective. One contribution that is made in the modeling area is the creation of a multiple reaction wheel disturbance model based on an existing model for a single wheel, and the details are provided in Section 2.2.5.

2.1   Integrated Modeling Description

2.1.1   Motivation

As the next generation of space telescopes push the limits of achievable performance, initial end-to-end system modeling will play a greater role in evaluating potential concepts. The

modeling and subsequent analyses will help to identify key trades and to assess the effectiveness of various technologies. These high performance systems will rely on a number of subsystems from different disciplines to help meet requirements. In response to this, models will need to incorporate the disciplines in a unified approach.

For the purposes of this thesis, the term integrated modeling will refer to the process of creating an overall input-output model of a system using modeling tools from a number of distinct disciplines. The correct disciplines can be determined by first identifying what the requirements are that must be satisfied. Then, aspects of the system should be isolated which are needed to accurately predict the quantities on which the requirements are placed. This can be accomplished based on previous modeling experience on similar systems, or it might be an iterative process whereby more disciplines are added as they are deemed important for greater predictive accuracy.

To illustrate this, consider the disciplines required for a model of a spaceborne observatory such as an interferometer, which is the motivation for the work in this thesis. Interferometers typically have tight precision requirements on the phase, pointing, and overlap differences of stellar light beams that are interfered together to produce the desired fringe pattern [11]. Any deviation will lead to a reduction in fringe visibility, and dynamic effects in particular result in so-called "fringe blur." A desired fringe visibility value can be translated into requirements on errors such as pathlength difference. To be able to estimate optical outputs, the integrated model must contain an optical model based on prescriptions of the elements along the optical train. The elements such as mirrors and detectors are attached to a supporting structure, so a structural model is needed. Since dynamic effects are important, a structural dynamic model rather than just a static structural model is required. This is especially true since the interferometer is on a flexible space structure rather than a fairly rigid, ground-based support structure. The flexibility implies that the optical requirements can probably not be met by relying solely on the passive rigidity of the structure, so active optical control must be employed to control the light path. Thus, a control system model should be incorporated as well. Finally, the spacecraft is not perfectly "quiet," and there are sources of disturbances that affect the interferometer's ability to meet the optical requirements. These disturbances should also be characterized and modeled.

Thus, the following disciplines have been identified as important in the integrated modeling process of precision controlled optical systems.

- structural modeling

- control modeling

- performance (*e.g.*, optical) modeling

- disturbance modeling

Each one will now be described in more depth.

2.1.2 Structural modeling

There are several tools available for modeling of structural systems, and they generally are well developed. The most accepted standard is the finite-element method (FEM), and this will be the assumed method of choice. This, of course, is case specific, and there can be instances where the actual system being modeled can be better represented by a different technique. For instance, an interferometer which has large slewing masses on a flexible structure will require multi-body modeling techniques as well as standard FEM-based structural dynamic models.

In the finite-element method, an important consideration is the level of fidelity and discretization that is required. Early generation models of conceptual designs are more useful if they can capture the essential physics of the system with a minimal amount of complexity. This will help during the analysis phase when several types of analysis or trade studies are required and computational effort can become an issue. The amount of fidelity is usually dictated by the frequency range of importance, but this might not be identified until after an initial model has been created and analyzed. Thus, some iteration is possible before an appropriate amount of fidelity is reached. If the frequencies of interest are high, then the fidelity might need to be increased; however, this leads to a larger order model, and the predictive capability of an FEM might become an issue at these higher frequencies.

As an example of model fidelity, consider a long truss-like boom that is a component of a structure. If only the first bending mode is particularly important in the performance output of interest, then the truss can be modeled as a homogeneous beam comprised of enough beam elements to yield a good estimate of the fundamental mode. This might require only five elements as opposed to a number such as 100 (one for each strut in the truss) which would be needed for a detailed model.

The fidelity and discretization issues not only affect the number of elements to use in the model, but also what types of elements to use. For instance, plate-like components might be part of the initial design, but frequency considerations could allow the components to be treated as rigid bodies. Struts that are part of a truss could be modeled by rod elements rather than Bernoulli-Euler beam elements.

Another aspect of structural modeling that is often not provided by an FEM approach deals with structural damping. Unless there are discrete dampers present in a design, the damping is typically specified in terms of modal damping ratios of specific modes. The values are usually conservative (*i.e.*, light damping in the range $\zeta = 0.1\% - 0.5\%$), but efforts should be made to choose damping ratios that are realistic rather than overly conservative or overly ambitious. Specifying damping in this manner does require a structural model in modal coordinates, and this raises the issue of how many modes should be kept in the model.

Thermal modeling can also be placed under the generic heading of structural modeling. If thermal effects are anticipated to cause thermal deformations of optical elements (such as mirrors), and these deformations can contribute as much wavefront error as the dynamic model, then a thermal model should be incorporated into the overall integrated model.

To be accommodated within the analysis framework proposed in this thesis, the final result of structural modeling should be an input-output (*i.e.*, state-space) system of the form shown in Figure 2.1. Section 4.3.1 will provide further detail on how to create this model based on standard structural dynamic equations expressed in modal coordinates.

$$F \longrightarrow \boxed{\begin{array}{c} \text{Structural} \\ \text{model} \end{array}} \longrightarrow x$$
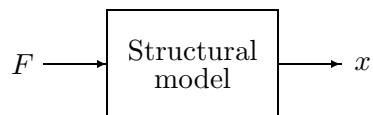
Figure 2.1: Open-loop system provided by structural modeling.

The vector F represents a generic force vector applied at all physical degrees of freedom. A goal of disturbance and control modeling is to identify the degrees of freedom at which the disturbances and control inputs actually enter. Note that this implies the structural modeling process should keep in mind where control inputs act and where potential disturbance sources enter. If the proper degrees of freedom are not exposed in the model, then modifications will have to be made to accommodate these inputs. This can lead to

significant analysis delays if it is not done early in the model generation stage.

The vector x in Figure 2.1 represents all the physical degrees of freedom in the model. A goal of performance and control modeling is to produce estimates of the performance metrics and sensor outputs in terms of these quantities. Although not shown in Figure 2.1, other outputs can be the velocity $\dot{x}$ and acceleration $\ddot{x}$ if they are required.

Only some issues have been mentioned related to structural modeling, and in no way is this brief discussion meant to address all of the requirements of the structural modeling process. In fact, some systems might require a coupled-field formulation (*e.g.*, structural-acoustic coupling [25]), so the structural model block in Figure 2.1 would actually be replaced by a coupled-field model.

2.1.3   Control modeling

When a system relies on closed-loop control to improve its performance, it is the closed-loop system that must be used during performance assessment. One option is to use simple frequency-domain filters that approximate the effects of closed-loop control without actually closing a loop in the model. This approach is used by Jandura when doing isolator trade studies on a SIM model [42]. Another option that is more common is to model the controller explicitly. This requires that a model of the control system be incorporated with the structural model. In the most simplest form, the control model can consist of the three additional components shown in Figure 2.2. A matrix C_{yx} maps the structural states into the ideal sensor measurements y. A controller then takes these measurements and computes a desired control input u applied by the actuators. The matrix β_u then maps the control inputs into forces and/or moments at the appropriate degrees of freedom in the structural model. Note that the feedback used is shown as positive in Figure 2.2 since it is assumed that the controller model incorporates any negative signs due to feedback. As an example, consider a Linear-Quadratic-Gaussian (LQG) compensator. The control input u might be defined as $u = -G\hat{x}$, where G is the Linear Quadratic Regulator (LQR) feedback gain and $\hat{x}$ is the state estimate produced by a Kalman filter [88]. In this case, think of the quantity $\beta_u u$ as being the actual physical forces and/or moments applied to the structure.

This simple representation of the control system in Figure 2.2 is often adequate during a conceptual design phase to examine the benefits and top-level issues of control. The controller can be represented by a continuous-time state-space filter even though the actual
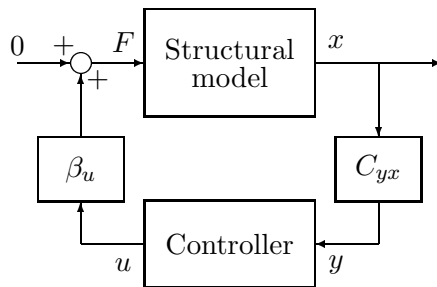
Figure 2.2: Additions made by control modeling.

control system will be implemented in discrete form in a computer. The linear, state-space assumption made in the subsequent chapters is not too restrictive since many control approaches can lead to a control model in this form. What should be kept in mind, though, is that a realistic controller should be used when evaluating the performance of the overall system. For instance, a controller design that achieves good performance at the cost of minimal phase margin would probably lead to instability when implemented in digital form at realistic sampling rates. The original performance predictions would therefore be misleading. As another example, consider a model-based compensator that utilizes precise knowledge of the modal frequencies to achieve many dB of performance improvement. The robustness to errors in the model would more than likely be very poor, and the performance predictions would again be unrealistic.

There are a number of other issues related to control modeling that should be considered in terms of potential importance to fair and accurate system assessment. Figure 2.2 makes the assumption that the sensors provide perfect measurements and that the actuators provide the exact control inputs. This ignores the fact that actual sensors and actuators have internal dynamics and limited range and resolution, and these might lead to performance limitations. The controller design should take these into account either explicitly (such as with appended dynamics to the model) or implicitly (by using realistic gains and bandwidths).

Some issues pertaining to digital control implementation include time delay, quantization, signal processing, and computational precision. A model of time delay can easily be added in the form of a Padé approximation to the control model in order to keep the control design "honest." For the case of high performance systems that push the limits of the

current state of the art, issues such as these might need to be accounted for at some level early in the conceptual design. For other systems, however, these effects can typically be added at later stages when the design and the models are more mature.

A last item associated with real control systems involves sensor and actuator noise, which can also place limitations on performance. These are better classified and modeled as disturbances, so they will be mentioned again in the disturbance modeling section.

2.1.4   Performance modeling

Although at first glance it might appear to be the easiest of the modeling tasks to do, modeling the performance of a system can be quite challenging. This is especially true for the complicated, high performance systems being considered in this thesis. The aim of performance modeling is to provide the relation between states in the model and metrics on which requirements are placed. This is shown in Figure 2.3 as the matrix C_{zx}, which expresses the performances z as a linear combination of the states x.
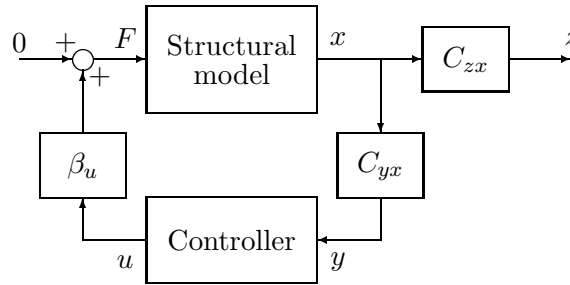
Figure 2.3: Addition made by performance modeling.

The success of a system is usually defined in terms of its ability to achieve certain goals. For a space interferometer, a goal might be to achieve a desired level of accuracy when measuring the angular separation between stars of a specified stellar magnitude. A high-level requirement such as this is often not directly associated with the performance outputs in z. What is normally done in practice is to flow down the high-level requirements into requirements on quantities that can be directly predicted by the integrated model. For instance, the requirements flowdown approach can levy a 1 nm requirement on optical path difference (OPD) for the interferometer case.

The most difficult and often least rigorous part of performance modeling is this flowdown

process. An error budget tree is usually created, and requirements on subsystems are normally allocated in an *ad hoc* fashion. If design decisions and resource allocation are based on an unrealistic requirement, then the final system design might be quite inefficient. Efforts should be made to iterate on the requirements based on preliminary analyses so that a more reasonable allocation is achieved.

Once requirements are placed in terms of quantities that the integrated model can address, then the next step is to determine how to obtain the quantities from the model. This can be straightforward if the requirements are on physical displacements, velocities, or accelerations of points on the structure. For the case of optical systems, the requirements will be on optical quantities, and these are inherently dependent on motion of the optical elements. An additional optical modeling process is needed that provides an estimate of the effect of this motion.

The analysis framework to be discussed in the following chapters assumes that the transformation from structural displacements to performance quantities is linear. It can simply be a C_{zx} matrix as shown in Figure 2.3, or it can be represented by a linear dynamic system if frequency weighting is used. The use of a linear performance model might not be valid in some situations, and this is an issue that must be addressed further when encountered.

If there are multiple performance outputs (*i.e.*, z is a vector), then whenever possible, a weighting matrix should be applied to z and an appropriate norm should be calculated to produce a scalar performance cost. For instance, weightings can be incorporated in a matrix R, and the weighted performance outputs can be denoted by $\overline{z}$.

$$\overline{z} = Rz \tag{2.1}$$

A scalar cost J can then be defined as a norm of $\overline{z}$

$$J = ||\overline{z}|| \tag{2.2}$$

and the weighting matrix R can be absorbed into the C_{zx} matrix.

For the types of systems of interest, the performance requirements will generally be specified in terms of RMS values, which is a 2-norm (*i.e.*, an $\mathcal{H}_2$ measure).

2.1.5 Disturbance modeling

The last major task of the integrated modeling process is to characterize the disturbances w. A key step in creating a disturbance model is specifying the locations on the system at which the physical disturbances act, and this is captured by β_w in Figure 2.4. As mentioned previously, sensor and process noise can corrupt y and u as well, but these disturbances are not explicitly shown. The remaining discussion regarding disturbance modeling will emphasize ways to identify and characterize the disturbances w.
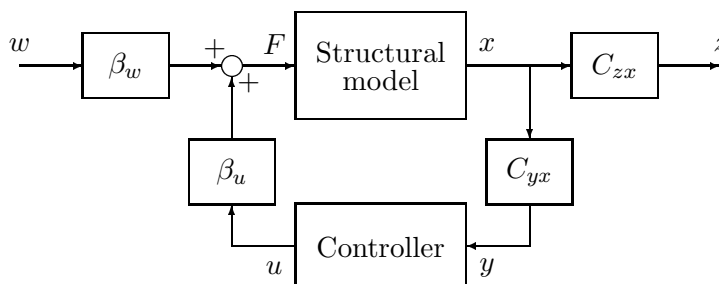
Figure 2.4: Addition made by disturbance modeling.

When assessing the impact of disturbances on high-performance systems, it is critical that the disturbance models be fairly representative of the actual disturbances. An extremely accurate plant model can still produce erroneous results when improperly modeled disturbances are applied to it. If design trades and decisions are based on the results of disturbance analyses that use mismodeled disturbances, then the performance of the actual system in operation might be quite different from that which was predicted. As a result, the disturbance characterization process should be given as high a priority as the integrated modeling process. This is especially true for high performance systems in which even low disturbance levels can cause the response to exceed requirements.

The types of disturbances that can affect a system are numerous, and spacecraft in particular face a myriad of them [20]. Table 2.1 lists some potential disturbances, and they are classified depending on whether the disturbance source is the space environment (external) or a component of the spacecraft (internal). The frequency range column indicates the approximate frequencies at which the disturbances acts.

Disturbances can be quantified by their frequency content, magnitude level, and the

Table 2.1: Listing of some spacecraft disturbances.

Disturbance	Frequency	Description
External		
gravity gradient torque	low	nonuniform gravitational field acting on distributed body
atmospheric torque	low	center of pressure $\neq$ center of mass
magnetic torque	low	net spacecraft magnetic dipole not aligned with external magnetic flux
solar pressure torque	low	center of pressure $\neq$ center of mass
solar thermal flux	low	can cause thermal deformation (static response) and thermal snap (high freq. response) during transients (*e.g.*, sun-shade transition)
Internal		
RWA/CMG	mid/high	series of harmonic disturbances (due to imbalances, bearings, motor ripple and cogging, *etc.*) that are functions of wheel speed
thrusters	low/mid/high	on/off cycling causes impulse-like or step-like disturbances (due to propellant expulsion and/or valve operation)
fluid slosh	low/mid	excitation of propellant or coolant slosh modes in storage tanks causes motion of spacecraft
fluid flow	low/mid/high	propellant or coolant flow and valve operation
servomechanisms	low/mid/high	drive motor disturbances (*e.g.*, friction, cogging, ripple in antenna/solar array gimbals, ODL trolley)
tape recorders	low/mid/high	motion of mechanisms during operation
rate gyros	mid/high	one or more harmonic disturbances due to imbalances in spinning elements
thermal control	low/mid	mechanisms in cryocooler pumps, louvers
sensor noise	low/mid/high	bandwidth/resolution limitations, A/D quantization, electrical noise, *etc.*
actuator noise	low/mid/high	bandwidth/resolution limitations, D/A quantization, electrical noise, *etc.*

location and direction at which they enter the structure. The frequency content determines which modes of the structure can be excited and what the bandwidth of a control system should be. The magnitude level determines how much energy enters the structure. The location and direction information determine to what extent the modes in the frequency range can be excited. This is the disturbability notion from modern control theory, or the modal force notion from structural dynamics. Both can be expressed in terms of the quantity $\Phi^T \beta_w$, where Φ is the modal matrix and β_w is the disturbance influence matrix which maps the disturbances w to the physical DOF's. If ϕ_i is the ith mode in the matrix Φ, then $\phi_i^T \beta_w = 0$ implies that the ith mode is not disturbable by w since the modal force is zero. This arises, for example, when a point force is acting at a location which is a node (zero displacement) for a particular mode of the structure.

Disturbances are also characterized by whether they are stochastic (*i.e.*, random) or deterministic in nature. A deterministic signal is one which can be predicted exactly during the time interval of importance. For example, the harmonic signal $w(t) = 2\sin 5.2t$ is known exactly for any desired time t. Stochastic processes can be deterministic in form, yet can have some random element. The signal $w(t) = 2\sin(5.2t + \phi)$, where ϕ is a random phase angle between 0 and 2π, is an example. Stochastic processes can also be completely nondeterministic in form, such as is the case with most sources of sensor noise.

The deterministic *vs.* stochastic classification can be illustrated with some of the disturbances listed in Table 2.1. Servomechanisms, for instance, can lead to deterministic disturbances. A desired motion of an antenna will require a certain torque, and the reaction torque can be thought of as a disturbance. The drive motors used in servomechanisms can also introduce a stochastic component due to electromechanical noise. Solar pressure torque can be calculated deterministically based on parameters such as the distance from the spacecraft to the Sun, and the absorptivity and reflectance coefficients [50].

Most of the external spacecraft disturbances can lead to internal disturbances. These external disturbances are usually in the form of torques, and ACS actuators (reaction wheels, CMG's, or thrusters) that counteract these in order to maintain pointing requirements can produce other unwanted forces and moments, generally at higher frequencies. Another example is when a sudden change in solar thermal flux leads to on-board thermal snap events due to a spontaneous release of stored strain energy. In these situations, a decision needs to be made regarding whether to ignore the external disturbances or to model them

explicitly, along with the system's response to them. For instance, a gravity gradient torque can be explicitly modeled as an exogenous disturbance, and ACS control loops that are in the spacecraft model can send the appropriate command signals to the reaction wheels. A reaction wheel model which contains as its output the resulting desired torque might also include the disturbance forces and torques that arise.

It might be difficult to create an overall model that is driven by external disturbance estimates and which produces the corresponding internal disturbances. If the external disturbances are ignored, then one option is to assume typical time histories of the internal disturbances based on experience. For example, a thruster firing profile can be created that is typical during station-keeping mode. For the reaction wheel assembly case, typical wheel speed profiles can be assumed, and the resulting wheel-speed-dependent disturbance time histories $w(t)$ can be generated. A potential problem with this approach is that if the sample disturbance time history is not really representative of what can arise during the course of a mission, then multiple analyses need to be conducted that use a series of these sample time histories. If the disturbances are stochastic in nature, then this process can be avoided by using random process theory. "Expected" levels of response can then be predicted by conducting a single analysis; however, a drawback is that worst-case conditions or transient effects might not be identified.

Since disturbances will be modeled primarily as stochastic throughout this thesis, a brief review of the pertinent theory of random processes will now be presented. Certain stochastic processes can be characterized by their so-called correlation and spectral density functions, which in general can be matrices. The correlation function of the random process $w(t)$ is defined as

$$R_{ww}(t_1, t_2) = E\left[w(t_1)w^T(t_2)\right] \qquad (2.3)$$

where $E[\cdot]$ is the expectation operator. If $w(t)$ is stationary (*i.e.*, the statistics of w do not change in time), then R_{ww} is a function of a single time-lag variable τ.

$$R_{ww}(\tau) = E\left[w(t)w^T(t + \tau)\right] \qquad (2.4)$$

The covariance matrix Σ_w will be defined (for zero-mean processes) as the value of the

correlation matrix at $\tau = 0$.

$$
\Sigma_w = R_{ww}(0) \;=\; \begin{bmatrix}
\overline{w_1^2} & \overline{w_1 w_2} & \cdots & \overline{w_1 w_n} \\
\overline{w_2 w_1} & \overline{w_2^2} & \cdots & \overline{w_2 w_n} \\
\vdots & \vdots & \ddots & \vdots \\
\overline{w_n w_1} & \overline{w_n w_2} & \cdots & \overline{w_n^2}
\end{bmatrix}
$$

$$
= \begin{bmatrix}
\sigma_{w1}^2 & \sigma_{w_1 w_2} & \cdots & \sigma_{w_1 w_n} \\
\sigma_{w_2 w_1} & \sigma_{w2}^2 & \cdots & \sigma_{w_2 w_n} \\
\vdots & \vdots & \ddots & \vdots \\
\sigma_{w_n w_1} & \sigma_{w_n w_2} & \cdots & \sigma_{wn}^2
\end{bmatrix} \tag{2.5}
$$

where n is the total number of elements in the vector w, and the notation $\overline{(\cdot)}$ is analogous to the expectation operator. To see why this simplification can be made for zero-mean processes, consider a typical term $\sigma_{w_i w_j}$ in the covariance matrix.

$$
\begin{aligned}
\sigma_{w_i w_j} &= \overline{(w_i - \overline{w}_i)(w_j - \overline{w}_j)} \\
&= \overline{w_i w_j} - \overline{w}_i \overline{w}_j - \overline{w}_i \overline{w}_j + \overline{w}_i \, \overline{w}_j \\
&= \overline{w_i w_j} - \underbrace{\overline{w}_i}_{=0} \underbrace{\overline{w}_j}_{=0} \\
&= \overline{w_i w_j} \tag{2.6}
\end{aligned}
$$

The mean-square values of the elements of w are simply the diagonal entries in the covariance matrix.

$$
(\Sigma_w)_{i,i} = E\left[w_i^2(t)\right] \equiv \overline{w_i^2} \tag{2.7}
$$

where $w_i(t)$ is the ith element in w. If w is zero-mean, then the mean-square values and the variances are identical. *For simplicity, all stochastic processes will be considered to have zero mean. This assumption will be valid throughout this thesis.*

$$
\sigma_{w_i}^2 = E\left[w_i^2(t)\right] - \underbrace{(E\left[w_i\right])^2}_{=0} = \overline{w_i^2} \tag{2.8}
$$

Taking the Fourier transform of Eq. 2.4 produces the spectral density function $S_{ww}(\omega)$ [8].

$$
\begin{aligned}
S_{ww}(\omega) &= \mathcal{F}\left[R_{ww}(\tau)\right] \\
&\equiv \int_{-\infty}^{+\infty} R_{ww}(\tau) e^{-j\omega\tau} \, d\tau \tag{2.9}
\end{aligned}
$$

43

Notice that the factor $\frac{1}{2\pi}$ is *not* included in this definition of the Fourier transform. Other definitions (*e.g.*, [86]) do place this factor in the Fourier transform formula. Either definition will produce the same results in the end as long as the definition is used consistently.

The inverse Fourier transform of $S_{ww}(\omega)$ recovers the correlation function.

$$
\begin{aligned}
R_{ww}(\tau) &= \mathcal{F}^{-1}\left[S_{ww}(\omega)\right] \\
&\equiv \frac{1}{2\pi}\int_{-\infty}^{+\infty} S_{ww}(\omega)e^{+j\omega\tau}\,d\omega
\end{aligned}
\tag{2.10}
$$

Evaluating Eq. 2.10 at $\tau = 0$ will produce the covariance matrix of w.

$$
\Sigma_w = \frac{1}{2\pi}\int_{-\infty}^{+\infty} S_{ww}(\omega)\,d\omega
\tag{2.11}
$$

Eq. 2.11 suggests an alternative approach to calculating the mean-square values of w if the spectral density functions are available, namely

$$
\sigma_{w_i}^2 = [\Sigma_w]_{i,i} = \frac{1}{2\pi}\int_{-\infty}^{+\infty} [S_{ww}(\omega)]_{i,i}\,d\omega
\tag{2.12}
$$

As a matter of terminology, the diagonal elements of the spectral density function matrix are usually referred to as power spectral densities (PSD's). Eq. 2.12 states that the variance is equal to the area beneath the PSD scaled by a factor of $\frac{1}{2\pi}$. In engineering practice, a PSD is typically plotted versus a frequency axis with units in Hz. Making the transformation $\omega = 2\pi f$ in Eq. 2.12 yields

$$
\sigma_{w_i}^2 = \int_{-\infty}^{+\infty} [S_{ww}(f)]_{i,i}\,df
\tag{2.13}
$$

This is a powerful result that will be utilized quite often when frequency-domain disturbance analyses are performed.

2.1.6   Numerical conditioning

An often overlooked aspect of integrated modeling deals with numerical conditioning. Large-order models, in particular, can suffer from poor numerical conditioning if they are created without measures that address this issue. Analysis results can be inaccurate if they are based on a model with a bad numerical representation.

Since integrated models are assumed to be in state-space form, a balancing transformation can be used to convert the system into a balanced realization. (This will be described in more detail in Section 5.3.1.) It is well known that different state representations of a system can still produce the same input-output relationship. Some representations can

be better numerically conditioned than others, as measured by the condition number of the state dynamics matrix A. A balanced realization typically yields a system that has an improved numerical behavior.

One example of a situation that can lead to poor numerical conditioning is when a compensator is designed using classical loop-shaping techniques. The compensator is normally in transfer function form and then converted to state space form via a canonical representation [23]. If the compensator has more than a few states, then the coefficients in the denominator of the transfer function can be fairly large. For instance, a canonical representation of the fourth-order transfer function

$$
\begin{aligned}
\frac{u(s)}{y(s)} = G(s) &= \frac{1}{(s+4)(s+10)(s+40)(s+100)} \\
&= \frac{1}{s^4 + 154s^3 + 6000s^2 + 61600s + 160000}
\end{aligned}
\tag{2.14}
$$

is given by

$$
\dot{x} = \begin{bmatrix} -154 & -6000 & -61600 & -160000 \\ 1 & 0 & 0 & 0 \\ 0 & 1 & 0 & 0 \\ 0 & 0 & 1 & 0 \end{bmatrix} x + \begin{bmatrix} 1 \\ 0 \\ 0 \\ 0 \end{bmatrix} y
$$

$$
u = \begin{bmatrix} 0 & 0 & 0 & 1 \end{bmatrix} x
\tag{2.15}
$$

The condition number of the A matrix is 1.84×10^5. The condition number of a matrix is defined as the ratio of the largest singular value to the smallest singular value. Nearly-singular matrices are characterized by a large condition number. The technique described by Moore in [65] can be used to obtain a balanced realization of the state-space equations in Eq. 2.15. The "balanced" system of equations is then given by

$$
\dot{\tilde{x}} = \begin{bmatrix} -1.445 & 4.131 & 1.613 & 0.4202 \\ -4.131 & -9.246 & -9.766 & -2.356 \\ 1.613 & 9.766 & -37.41 & -19.7 \\ -0.4202 & -2.356 & 19.7 & -105.9 \end{bmatrix} \tilde{x} + \begin{bmatrix} -0.003341 \\ -0.003807 \\ 0.001888 \\ -0.0004856 \end{bmatrix} y
$$

$$
u = \begin{bmatrix} -0.003341 & 0.003807 & 0.001888 & 0.0004856 \end{bmatrix} \tilde{x}
\tag{2.16}
$$

This time the condition number of the A matrix is 38.9, and this represents a significant improvement in the numerical conditioning of the model. Thus, one recommendation that

45

can be made is that compensator state-space representations should be balanced if they are obtained from transfer function form.

Examining Eq. 2.16 further leads to another recommendation. From a numerical precision or model reduction standpoint, it is often advantageous if the transfer functions from the inputs to the outputs have numerical values of similar order of magnitude. To achieve this, the units of the inputs and outputs should be scaled. For instance, if one of the outputs of an interferometer model is OPD, the natural unit of the output might be μm or nm rather than the typical unit of meters. This allows the entries in the C_{zx} matrix to be changed by factors of 10^6 or 10^9, thereby addressing numerical precision limitations.

Transforming a system into a balanced realization can also help in model reduction, as will be seen in Section 5.3.1. A balanced realization is useful in identifying unobservable or uncontrollable states which can be removed from the model. Obtaining a minimal-order model from an initial non-minimal order model is another useful step in improving the numerical conditioning of a system.

Thus, numerical conditioning of integrated models should be considered in as much detail as the actual modeling process. A few recommendations have been provided that make an effort to avoid some potential pitfalls related to this issue, especially when dealing with large-order systems.

2.2   Space Interferometry Mission Overview

The Space Interferometry Mission (SIM) will be one of the first-generation of missions that are being planned as part of NASA's Origins Program [81]. The Origins Program seeks to answer some fundamental questions related to the birth and early evolution of galaxies, stars, and planets [74]. Another objective is the search for potential life-sustaining planets outside of our solar system. SIM is just one of a series of missions shown in Figure 2.5 that will collectively attempt to provide answers to these questions.

This section will begin with the specific objectives of SIM and will provide an overview of its operation. Then the integrated model of SIM that was developed at JPL will be described in detail. The section will conclude with a rigorous development of a disturbance model of a general reaction wheel assembly.
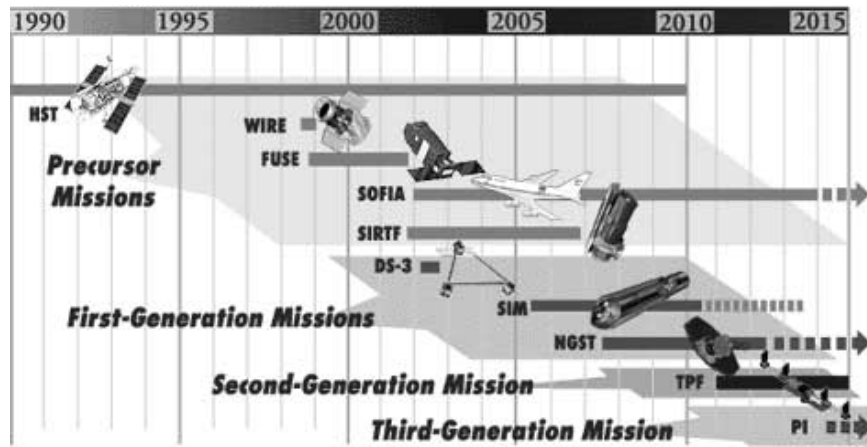
Figure 2.5: Timeline of Origins Program missions [43].
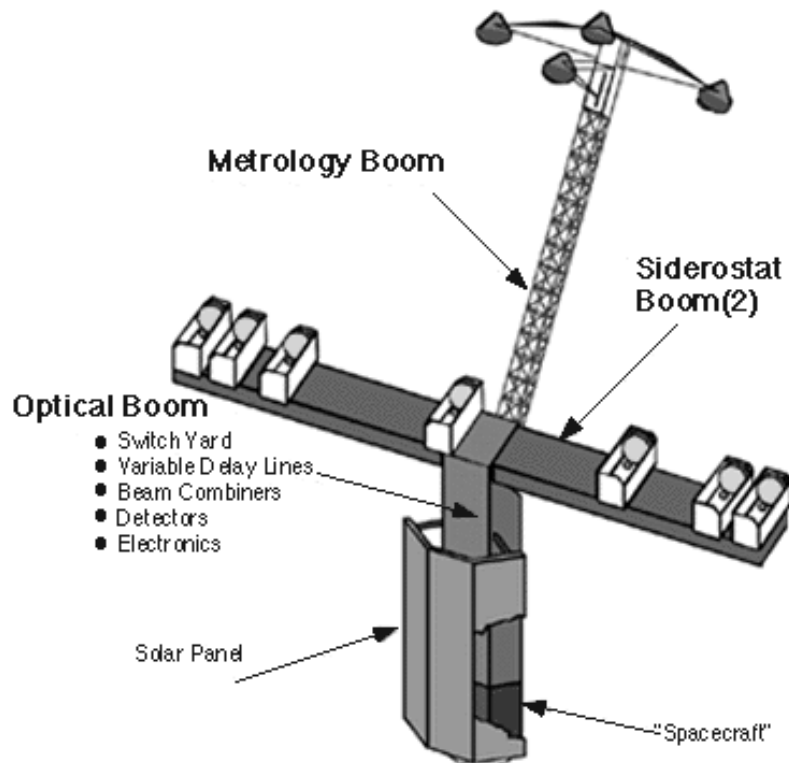
Figure 2.6: SIM Classic concept [44].

2.2.1 Modes of operation

SIM is an optical interferometer that can operate in one of several modes during scientific observations. It consists of a series of seven discrete, separated apertures used to collect the incoming starlight, and these are clearly visible in Figure 2.6. The concept shown in Figure 2.6 will be referred to as SIM Classic, and it will be the concept on which many of the analysis tools developed in this thesis will be demonstrated. Subsequent trade studies at JPL have produced alternative architectures; however, these will not be described, and their analysis will be left for future work.

One of the benefits of interferometry for space-based applications is that it can achieve significant improvements in angular resolution without facing the same cost, mass, and technical issues that could cause larger aperture telescopes to be infeasible with current funding, launch vehicles, and technology. The basic premise behind interferometry is to coherently interfere light from a pair of distributed apertures to produce interference fringes. Scientific information can then be derived from the resulting fringe. Phase information is related to the position of the fringe, and amplitude information is related to the visibility of the fringe. Figure 2.7 includes some of the important elements required by a SIM-like interferometer. The two collecting apertures, which are commonly called siderostats, are used to point at a target of interest by means of a 2-axis gimbal. The light is redirected into the instrument and follows a path through the optical train until arriving at a beam combiner. Also shown in the figure is the path traveled by an internal metrology beam, which is used to measure internal pathlength changes due to motion of the optical elements.

A layered control approach is used while the interferometer is in operation so that pointing and pathlength requirements can be met [53]. Pointing control is distributed among the spacecraft attitude control system (ACS), siderostat pointing mechanisms, and fast steering mirrors (FSM's). The ACS provides large angle, low bandwidth control, the siderostats provide coarse angle, medium bandwidth control, and the FSM's provide high resolution, high bandwidth control. Photos of a commerically available gimbal-mounted mirror and fast steering mirror are shown in Figure 2.8. The pathlength control is distributed in a similar fashion; however, it is accomplished within the same unit, which is known as an optical delay line (ODL). Large path delay (up to approximately 1 meter) is introduced by using a belt-drive mechanism to translate the ODL along a trolley. This is performed at

External path delay

= Bcos θ

common stellar wavefront

siderostat
#1

θ

Baseline   **B**

siderostat
#2

fringe detector

ODL introduces
internal path
delay

—— stellar light

······ internal metrology
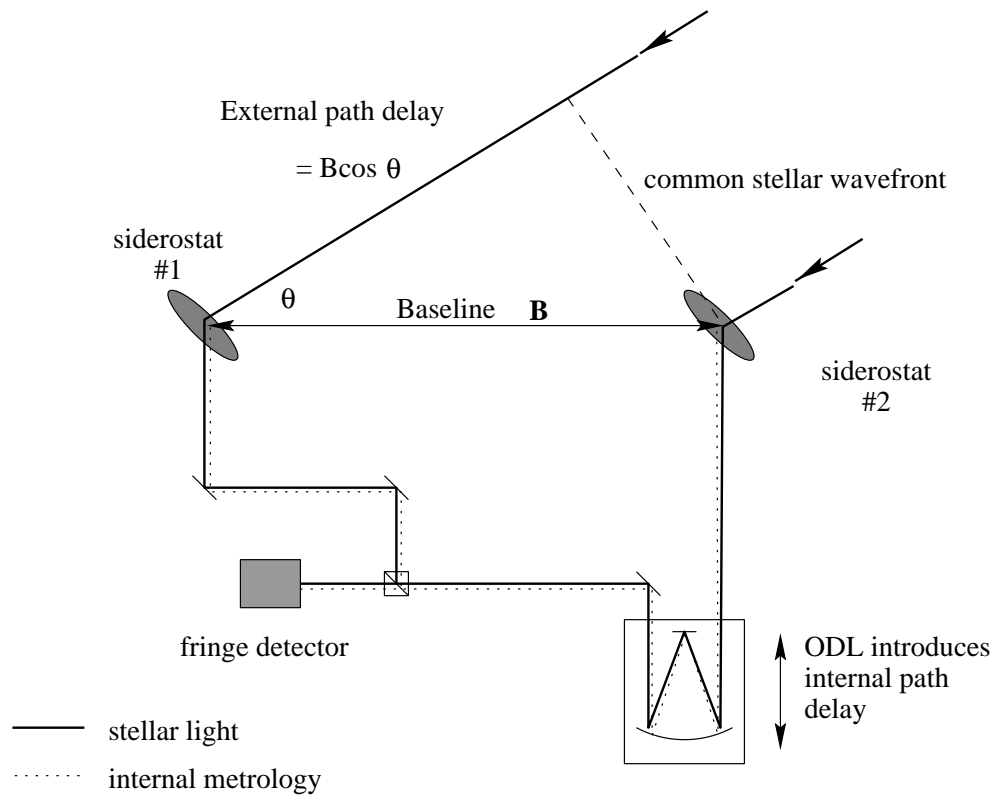
Figure 2.7: Schematic of the basic elements of an interferometer.
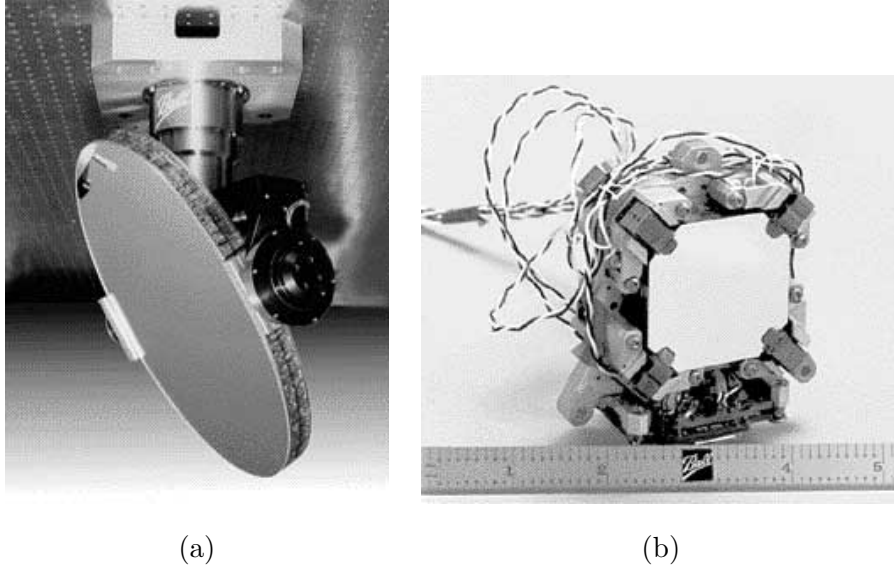
Figure 2.8: (a) Flat mirror attached to a gimbal [4]. (b) Fast-steering mirror [3].

low bandwidth. Medium bandwidth, coarse control is provided by a voice coil, while high bandwidth, fine control is provided by a piezoelectric (PZT) actuator [53]. This staged control approach is necessary to achieve the high resolution, large stroke requirements for interferometry.

SIM's three primary modes of operation are astrometry, rotation synthesis imaging, and nulling. Astrometry involves measuring the angular separation between stellar objects, and SIM's wide-angle astrometry goal is $4\,\mu$arcsec [75]. An important quantity needed when performing astrometry is the angle θ between the baseline vector $\boldsymbol{B}$ and the star line of sight, as indicated in Figure 2.7. An external metrology system located at the end of the metrology boom is used to accurately measure the baseline $\boldsymbol{B}$. The ODL is used to adjust the internal path delay in one arm of the interferometer and cancel the external path delay in the other arm due to off-axis viewing. The external path delay divided by the magnitude of $\boldsymbol{B}$ provides an estimate of the cosine of the angle θ. During an observation of a faint science target (up to 20th magnitude), two pairs of siderostats form the guide interferometers and point at bright reference stars to help maintain the desired attitude of the spacecraft [75]. A third pair of siderostats, using information from the guide interferometers, is then slewed to the science target star, and the process of fringe acquisition and tracking begins. The two outermost siderostats will typically be used to form the science baseline since astrometric accuracy varies linearly with the length of the baseline [75].

During the imaging mode, SIM rotates about the line of sight to the object and takes $u - v$ measurements by alternating between pairs of siderostats to create baselines of different lengths and orientations. As in the astrometry mode, two guide interferometers track bright stars as the third interferometer makes the necessary measurements on the target. At each orientation, amplitude and phase information is obtained from the fringe position and visibility, and *a posteriori* data processing synthesizes the actual image from the measurements in the $u - v$ plane [75]. Since the maximum baseline is 10 meters, an angular resolution is achieved that is several times better than that of the Hubble Space Telescope.

The nulling mode is used during imaging when light from a very bright star would otherwise hide any neighboring planets. In this case, the science light is sent to a nulling beam combiner, which introduces a 180° phase shift to light in one arm of the interferometer. This phase shift is designed to null the light arriving exactly down the line of sight by a factor of $\frac{1}{10000}$ [75]. This provides a means of direct planet detection, which is in contrast to indirect techniques which infer the existence of an orbiting planet based on a parent star's "wobble," for example.

Each of these operational modes has a unique set of requirements that must be met for successful operation. As motivated earlier, such a complicated system requires an integrated modeling approach for performance assessment. The structural, optical, and control models will now be discussed in depth.

2.2.2 Finite-element model

The SIM finite-element model was created at JPL using the Integrated Modeling of Optical Systems (IMOS) software package [46]. IMOS is a set of MATLAB functions that offer the capability for structural dynamic, optical, control, and thermal modeling. An attractive feature of IMOS is that it can be used to create complete end-to-end models within one computational environment. This facilitates trade studies and other analyses of early generation system concepts.

Figure 2.9(a) shows the stick representation of the finite-element model of SIM. Node locations are represented by circles, and elements are represented by line segments. Figure 2.9(b) shows the ray trace of stellar light passing through one arm of a guide interferometer. The siderostat booms and the metrology boom are modeled by Bernoulli-Euler beam elements. Each of the two siderostat booms is considered to be a box beam and is
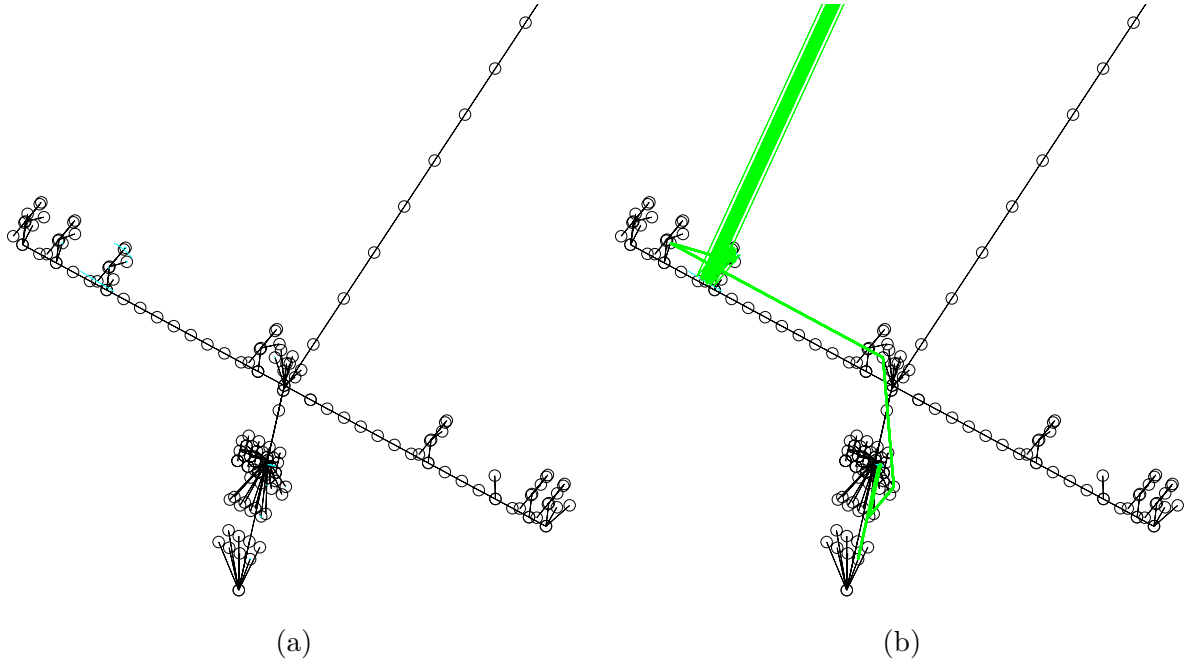
Figure 2.9: (a) SIM finite-element model. (b) Ray trace through $+x$ arm of guide #1 interferometer.

discretized using 15 nodes. Rigid elements attach the 7 siderostat center-of-mass nodes to neighboring nodes on the siderostat boom. Rigid elements also attach various mirrors to the support structure. The metrology boom is represented simply as a thin walled cylinder and is discretized using 10 nodes. The beam launchers at the end of the metrology boom are accounted for by a lumped, rigid-body mass [42].

The optics boom is treated as a rectangular rigid body with a total mass of $1200\,\mathrm{kg}$. Attached to it via rigid elements are 8 beam combiner nodes, 8 upper switchyard mirror nodes, 8 lower switchyard mirror nodes, 8 fold mirror nodes, and 8 ODL center-of-mass nodes.

Attached to one of the nodes along the optics boom is a coincident node at which the reaction wheel assembly (RWA) is located. The two nodes are joined by an ideal hexapod isolator model that represents a Stewart platform configuration of six struts [82]. When the struts are perfectly pinned at their ends and are modeled by six identical axial springs with stiffness k, the resulting stiffness matrix can be shown to be diagonal and in terms of the

strut length L, as given in Eq. 2.17 [82].

$$
K_{\text{iso}} = k
\begin{bmatrix}
2 & 0 & 0 & 0 & 0 & 0 \\
0 & 2 & 0 & 0 & 0 & 0 \\
0 & 0 & 2 & 0 & 0 & 0 \\
0 & 0 & 0 & \frac{1}{2}L^2 & 0 & 0 \\
0 & 0 & 0 & 0 & \frac{1}{2}L^2 & 0 \\
0 & 0 & 0 & 0 & 0 & 2L^2
\end{bmatrix}
\tag{2.17}
$$

For the special case of an axisymmetric payload attached to one side of the hexapod, the mass matrix of the hexapod/payload configuration can be shown to be in terms of the payload mass m, mass moments of inertia I_{xx}, I_{yy}, and I_{zz} about the hexapod geometric center, and the vertical distance Δz of the payload center of mass from the hexapod geometric center [82].

$$
M_{\text{iso}} = m
\begin{bmatrix}
1 & 0 & 0 & 0 & \Delta z & 0 \\
0 & 1 & 0 & -\Delta z & 0 & 0 \\
0 & 0 & 1 & 0 & 0 & 0 \\
0 & -\Delta z & 0 & I_{xx}/m & 0 & 0 \\
\Delta z & 0 & 0 & 0 & I_{yy}/m & 0 \\
0 & 0 & 0 & 0 & 0 & I_{zz}/m
\end{bmatrix}
\tag{2.18}
$$

The "bounce" mode of the hexapod assembly occurs at a frequency of $\sqrt{\frac{2k}{m}}$, and it is this value with which the isolator "corner" frequency will be associated.

Other locations of compliance within the finite-element model include one-dimensional spring elements representing the ODL voice coils, ODL piezoelectric stacks, ODL cage axial stiffness, and fast steering mirrors. The spring constants were chosen to yield local modes of these components at 3.5 Hz, 5 kHz, 900 Hz, and 7 kHz, respectively, based on representative masses assigned to each component. The seven siderostat bays are represented by 6×6 stiffness and mass matrices obtained from more detailed siderostat bay modeling. This allows relative motion between the siderostat bays (with their associated optical elements) and the siderostat boom on which they are placed.

The total number of degrees of freedom (DOF's) is 1296, which is a result of 6 active DOF's at all 212 nodes in the FEM. Since quite a number of rigid elements are used, constraint equations lead to only 352 independent DOF's. Thus, the size of K and M used

in the modal analysis is 352×352. The mode shapes can then be expanded back to all 1296 DOF's for modal animation or incorporation into an input-output model.

2.2.3   Optical model

The SIM optical model is characterized by an optical prescription for the various elements in the interferometer. This involves specifying the location, orientation, and type of each element. One set of optical prescriptions is used to define the path of the incoming starlight as it enters a siderostat bay, travels down the optical train, and finally reaches the beam combiner location. Another set is used to define the path traveled by the internal metrology laser beam. The internal metrology beam begins at the beam combiner location, travels "upstream" until it reaches the center of the siderostat mirror (at which point it is assumed to strike a retroreflector), and then it retraces its path back to the beam combiner. Both of these types of prescriptions are defined for each arm of all three interferometers.

Figure 2.10(a) and Figure 2.10(b) show two views of a stellar ray trace through an interferometer arm. The elevation angle of the light is $55°$, and the azimuth angle is $0°$. Figure 2.10(c) and Figure 2.10(d) are two close-up views of a siderostat bay. Although actually a continuous surface, the stellar wavefront is represented by a bundle of 13 parallel rays which are distributed across a circular area $33\,\mathrm{cm}$ in diameter. The light is redirected to a parabolic primary mirror of a beam compressor, and then to a parabolic secondary mirror. The beam compression ratio is 11, and the light exits the compressor as a smaller diameter, collimated beam. It then strikes the fast steering mirror, which is a flat, circular mirror. From there it proceeds to two consecutive fold mirrors which are used to redirect the light toward the switchyard area.

After reflecting off a switchyard flat mirror, the light hits a lower switchyard mirror, and then is redirected by another fold mirror into the delay line. This can be seen in a side view of the ODL model in Figure 2.11. The first mirror that is encountered after the fold mirror is the parabolic primary mirror of the ODL. The light reflects toward a small, flat secondary mirror which is attached to a PZT stack. Upon striking this mirror, the light is sent back to the primary mirror and then emerges from the ODL on its way to the beam combiner.

The next step in the optical modeling process is to estimate the effects of motion of the optical elements on various metrics [78]. The MACOS (Modeling and Analysis of Controlled
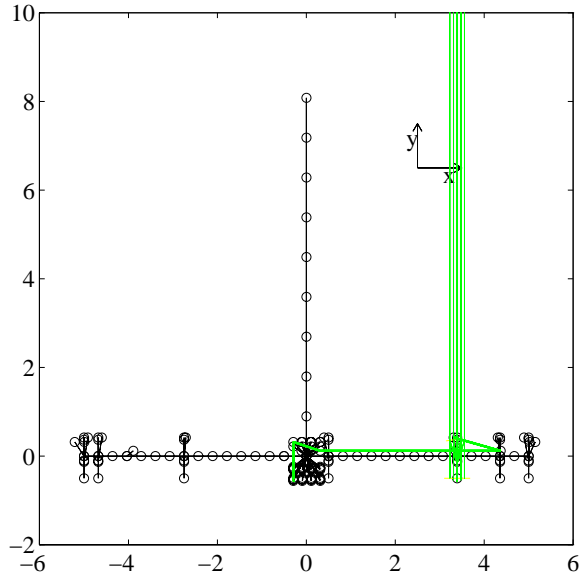
(a)
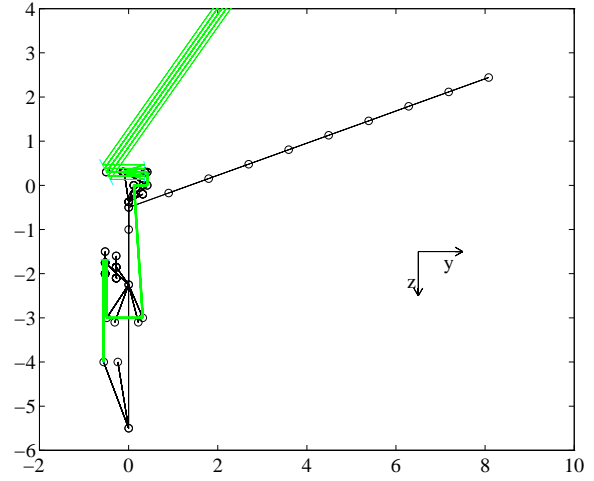
(b)
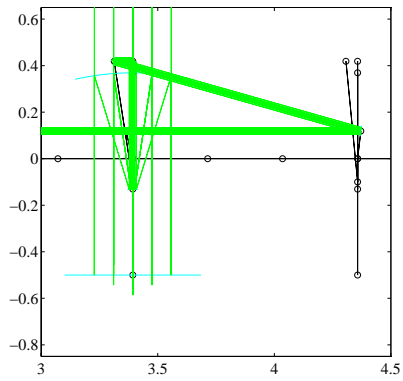
(c)
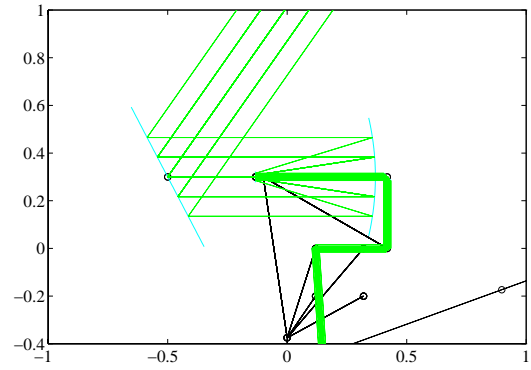
(d)

Figure 2.10: (a) Bottom view of ray trace. (b) Side view of ray trace. (c) Bottom view of ray trace through siderostat bay. (d) Side view of ray trace through siderostat bay.
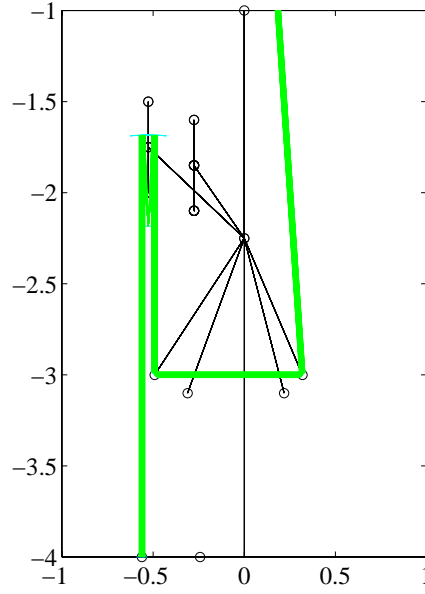
Figure 2.11: Side view of ray trace through ODL assembly.

Optical Systems) program is used to create a linear model in the form of an optical "C" matrix, which maps element motion into metrics such as pathlength, tilt, and spot motion [45]. The outputs are for *each* of the rays in the light bundle, and the metrics for the bundle as a whole are obtained by averaging over the rays. The main product of optical modeling is this sensitivity matrix, and it allows optical control loops to be closed and optical-related performance predictions to be made.

2.2.4 Optical control

The block diagrams in Figure 2.12 show two types of control loops that are implemented in the SIM integrated IMOS model. Figure 2.12(a) represents the pathlength control architecture, which consists of three compensators: K_{vc} (ODL voice coil), K_{pzt} (ODL piezo), and K_{ft} (fringe tracker). The outer loop is closed during fringe tracking mode once the white-light fringe has been acquired. (Note: The fringe acquisition process is not explicitly modeled, but the outer loop can be broken to examine the OPD levels due to disturbances.) It is assumed that the ODL trolley has been locked in place once the fringe is acquired; therefore, ODL trolley control is not shown. A CCD detector in the beam combiner measures the interference fringe position, which is related to the actual total OPD. In the block
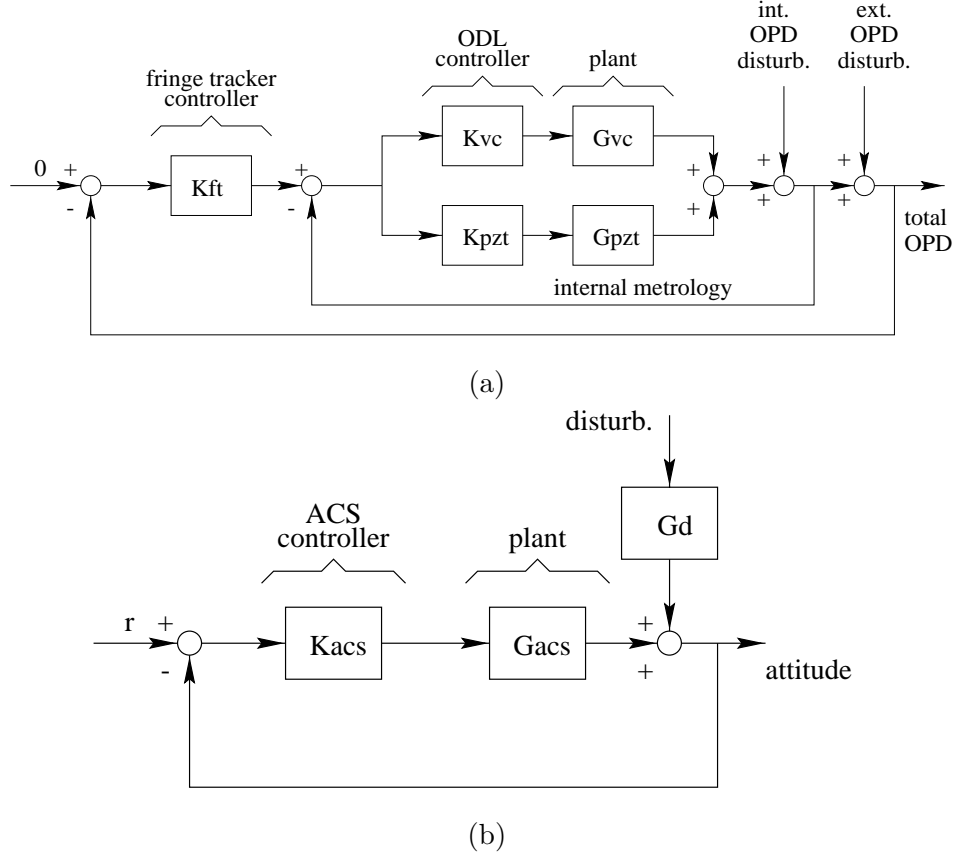
Figure 2.12: (a) Block diagram of ODL and fringe tracker controllers. (b) Block diagram of ACS controller.

diagram, this measurement is assumed to be ideal, and practical considerations such as fringe tracker noise and sampled-data effects (due to finite integration time on the detector) are not shown. The desired total OPD value is indicated to be zero, which is the criterion for equal pathlength in two arms of an interferometer. The measured variation from zero is then provided to the fringe tracker compensator, which sends a desired command to the optical delay line. Subtracted from this command is the measured internal OPD from the internal metrology laser system, and the difference represents the net change in OPD that the ODL must introduce.

The ODL control design places the voice coil and piezo loops in parallel, and as mentioned previously, the two actuators are designed to operate at different bandwidths and stroke ranges. The compensators were obtained using classical loop-shaping methods, and their transfer function magnitudes are shown in Figure 2.13(a). The control design achieves a realistic loop gain ($< 150\,\mathrm{dB}$) and bandwidth ($300\,\mathrm{Hz}$) which are comparable to those

Table 2.2: Dependence of CCD integration time and fringe tracker bandwidth on stellar magnitude [38].

Stellar Magnitude	Integration time (milli-seconds)	Approximate fringe tracker bandwidth (Hz)
5.6	1	100
8.1	10	10
10.6	100	1

achieved on ground testbeds [73],[72],[67]. As in most of the ground-based ODL's, the ODL in the SIM model contains a second PZT stack which is back-to-back with the PZT that holds the secondary mirror. The second PZT is driven by the same signal which is sent to the other PZT, thereby minimizing the reaction forces imparted on the structure. The same control design is used in each of the three interferometers due to similar structural dynamics, as seen by the voice coil coil and piezo actuators. As a result, K_{vc} and K_{pzt} are 3×3 diagonal transfer function matrices with identical entries along the diagonal.

The loop-shaped design of the fringe tracker compensator is shown in Figure 2.13(b). The difference between the compensators for the guide interferometers and the compensator for the science interferometer is meant to account for the fact that the science interferometer will typically be observing a faint star. The fringe detector CCD camera has to integrate for a significantly longer time to collect enough photons for a good signal; consequently, this limits the bandwidth of the fringe tracker compensator. Table 2.2 provides an estimate of how integration time and fringe tracker bandwidth depend on the brightness of the star being observed. When the science star is faint enough, the outer fringe tracking loop cannot be closed, and feedforward techniques must be implemented. (For example, the science interferometer's ODL can be commanded by the same signals sent to the guide interferometer ODL's. Also, accelerometers placed on the siderostats can provide estimates of external OPD errors, and these can be fed forward to the science interferometer as well.) The nominal fringe tracker control designs use a 100 Hz bandwidth on the guide interferometers and a 1 Hz bandwidth on the science interferometer.

Figure 2.14 plots the singular values of the sensitivity transfer function matrices for both the internal metrology ODL loops and the fringe tracker loops for all three interferometers.
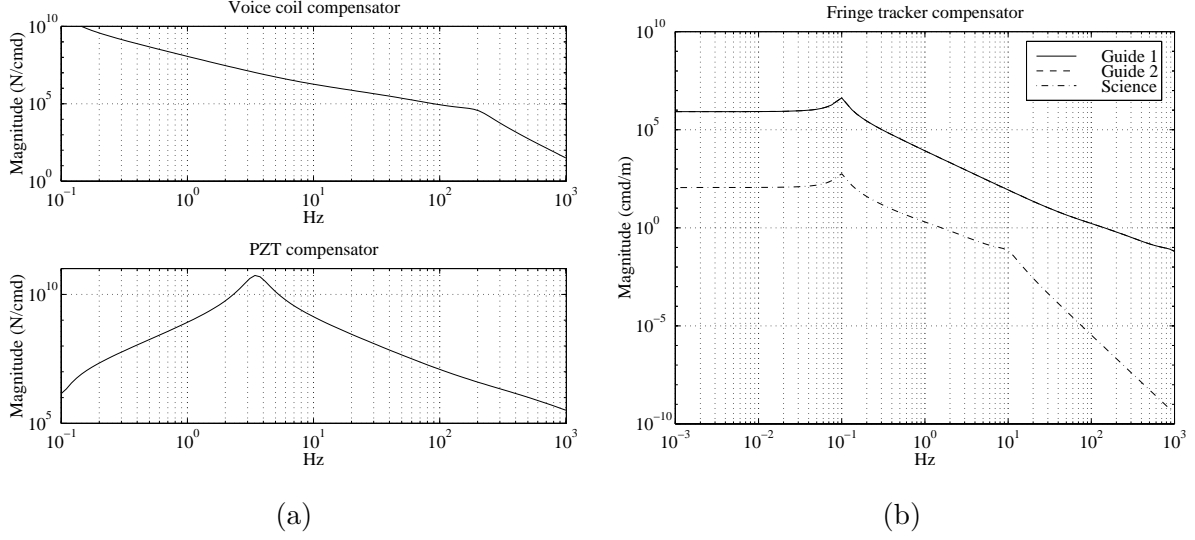
Figure 2.13: (a) Transfer function magnitudes of voice coil controller K_{vc} (top) and PZT controller K_{pzt} (bottom). (b) Transfer function magnitudes of fringe tracker controller.

The sensitivity transfer function matrix for a system with loop gain GK is defined as $(I + GK)^{-1}$, and large peaks in the maximum singular value of this function indicate frequencies at which the system is sensitive to perturbations [28]. The sensitivity transfer function is also good at indicating the frequency range over which the control is effective in minimizing the effects of disturbances. Figure 2.14(a) shows that the ODL loops can reject internal pathlength disturbances up to about 200 Hz. The fringe tracker sensitivity in Figure 2.14(b) shows that the two guide interferometers (represented by the two smallest singular values) have good disturbance rejection properties up to about 60 Hz, while the science interferometer (associated with the largest singular value) is limited to about 7 Hz due to its lower bandwidth. The sensitivity transfer function does not provide an indication of the stability of a system, so a Nyquist or a Nichols plot must be provided as well [28]; however, all controllers discussed in this section produce a stable system, and these plots will be omitted.

A last control loop found within the integrated SIM model is the attitude control system. The ACS loop shown in Figure 2.12(b) is in the form of a standard regulator, and the control model simply assumes that the ACS compensator K_{acs} outputs desired moments M_x, M_y, M_z based on a measure of the difference between the desired attitude and the actual attitude. The compensator is in the form of a proportional-derivative (PD) controller with a
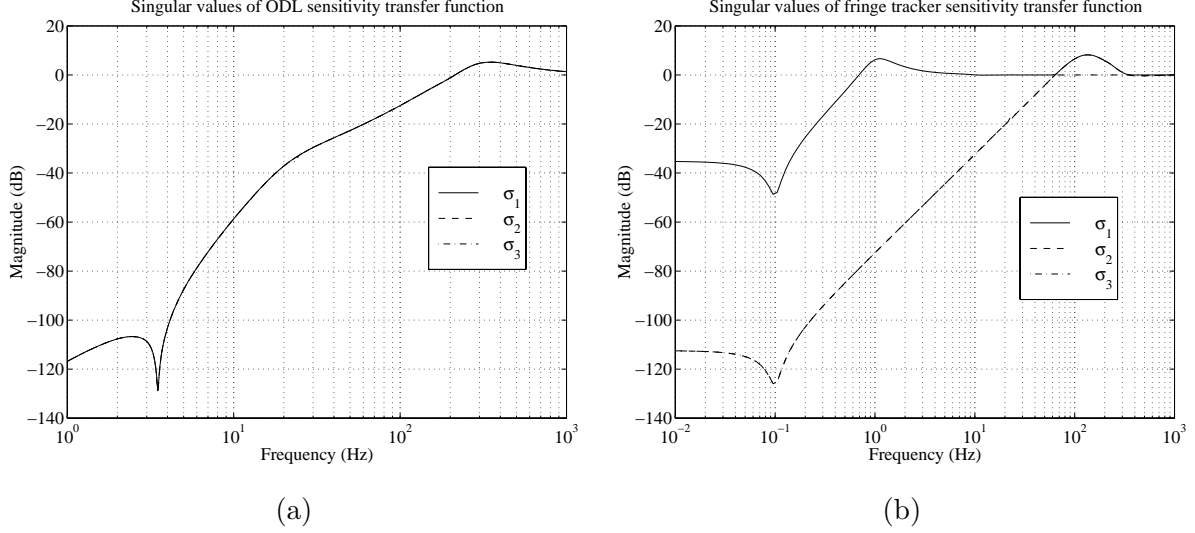
Figure 2.14: (a) Singular values of ODL sensitivity transfer function matrix. (b) Singular values of fringe tracker sensitivity transfer function matrix (with internal metrology loop closed).

highly-damped 2nd order lag filter to introduce a -20dB/decade roll-off at high frequencies. The diagonal elements of the 3×3 compensator transfer function matrix are plotted in Figure 2.15(a), and the slight difference in magnitude is due to non-identical spacecraft mass moments of inertia about the principal axes. The corresponding singular value plot of the sensitivity transfer function is shown in Figure 2.15(b), and it is evident that the ACS loop has a bandwidth of approximately $0.1\,\text{Hz}$.

In the current SIM Classic model, no loops are closed between wavefront tilt measurements and the fast-steering mirrors. If performance assessment does reveal that wavefront tilt metrics exceed requirements, then these loops can be closed using compensators that are of the same form as those used in ground-based experimental testbeds [70].

2.2.5 Reaction wheel assembly stochastic disturbance model

Now that the SIM integrated model has been described, the remaining task is to quantify anticipated disturbances. One source of unwanted forces and moments on SIM and other space-based observatories is the reaction wheel assembly (RWA). Reaction wheels can impart disturbances at mid to high frequencies. The high frequencies can be beyond the bandwidth of the optical control, thereby necessitating the use of some form of isolation. Accurate reaction wheel disturbance models can lead to an increased level of confidence in
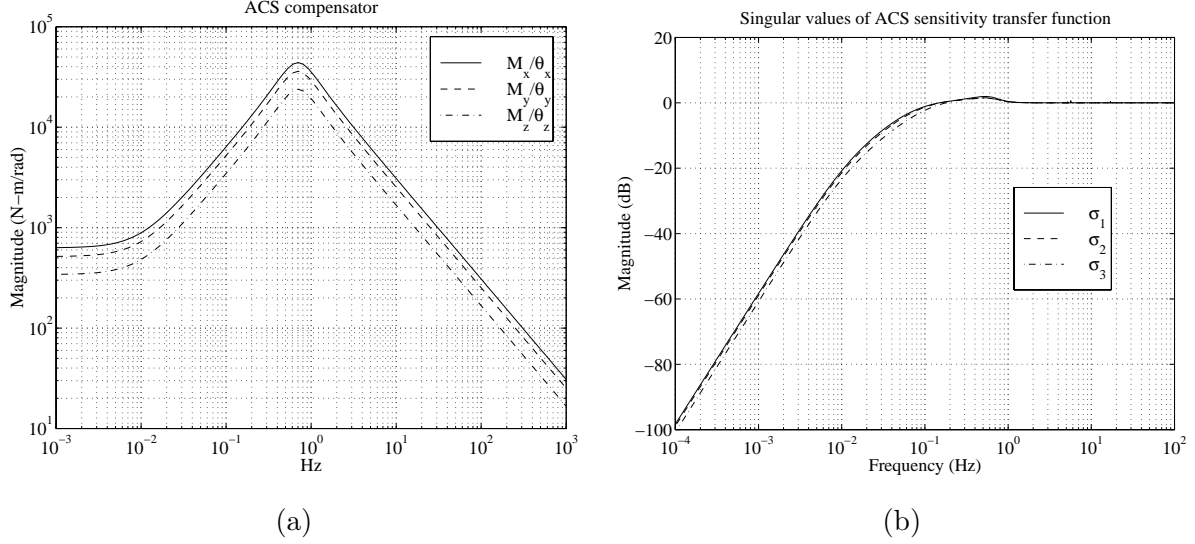
Figure 2.15: (a) ACS compensator. (b) Singular values of ACS sensitivity transfer function matrix.

the amount of isolation needed, as determined by subsequent analyses.

Reaction wheels pose an interesting modeling challenge because of the nature of disturbances that arise from them. The disturbance forces and moments are typically modeled as a series of harmonic components whose amplitudes are proportional to the square of the wheel speed. The constants of proportionality as well as the frequencies of the harmonics are usually derived from experimental data. An example of this can be found in Reference [17].

This section presents a methodology by which disturbances of this type, and due to several reaction wheels, can be combined to produce estimates of disturbances acting in the spacecraft frame. The reaction wheel speeds are treated as random variables in order to enable the computation of the "expected" level of disturbances. This leads to a frequency-domain model that can then be propagated through the spacecraft model to obtain estimates of the performance metrics.

2.2.5.1 Motivation

Because of the need to exert torque about several axes, a reaction wheel assembly normally will contain multiple wheels whose spin axes are at different orientations. In addition, redundancy increases the number beyond that necessary for control about a given set of axes. The ability to precisely predict the speed of each wheel (and hence the resulting disturbances) during the course of an observation is difficult. Although the attitude control

logic that is used to issue commands to each wheel is known *a priori*, what is not known to the the same level of certainty is the external torque disturbance which the wheels are counteracting. Also, the initial wheel speeds at the start of an observation might be impossible to predict. It is for these reasons that conducting a time simulation might not be desirable. While initial conditions on wheel speeds can be assumed and external-torque time histories can be estimated, the resulting simulation is valid only for that particular case. What is more useful is a sense of how the performance metrics of interest (*e.g.*, optical path difference) are affected by disturbances arising from all possible combinations of wheel speed variations. Running countless time simulations to try numerous combinations is prohibitive due to the computational expense.

A possible alternative is to estimate what the disturbances are "on average." These disturbances can then be used in a first-cut performance assessment. If performance requirements are easily met even when appropriate bounds (*e.g.*, 3σ) are placed on the outputs, then the first-cut analysis might be all that is needed. If, however, the results of the analysis are unclear as to whether the requirements can be satisfied, then a more refined approach is necessary.

The "on-average" disturbance approach motivates the treatment of wheel speed as a random variable. Making this assumption enables the mathematics of stochastic processes to be applied in a systematic manner. Stochastic process theory is attractive because it permits a random process to be described in the frequency domain by a power spectral density (PSD) function. This can then be used in a frequency-domain disturbance analysis, which can be less computationally intensive that a time-domain simulation. Another advantage to the "on-average" approach is that external torque models and initial wheel speeds are not required.

The following analysis is somewhat analogous to the derivation by Melody in [60]. Melody treats the wheel speed as a random variable and proceeds to derive expressions for the PSD's of axial force, radial force, and radial torque for a single wheel. The objective of the current work is to follow a similar approach, but to consider the general case of multiple wheels at specified orientations with respect to the spacecraft axes.

2.2.5.2   Disturbance Model and Nomenclature

We begin by defining a reaction wheel disturbance model consisting of a series of harmonic components of the form

$$m_{ijk}(t) = C_{jk} f_i^2 \sin(2\pi h_{jk} f_i t + \phi_{ijk}) \tag{2.19}$$

where

$$
\begin{array}{rcl}
m & = & \text{disturbance force } (j = 1, 2, 3) \text{ or torque } (j = 4, 5, 6) \\[4pt]
i & = & \text{wheel number } (1, 2, \ldots, N); \ N = \text{total number of wheels} \\[4pt]
j & = & \text{disturbance number } (1, 2, \ldots, 6); \ (\text{see Eq. 2.21}) \\[4pt]
k & = & \text{harmonic number } (1, 2, \ldots, n_j); \ n_j = \text{number of} \\[2pt]
  &   & \text{harmonics for } j\text{th disturbance number} \\[4pt]
C_{jk} & = & \text{amplitude coefficient for } k\text{th harmonic of } j\text{th} \\[2pt]
  &   & \text{disturbance; assumed the same for all wheels} \\[4pt]
f_i & = & \text{wheel speed of } i\text{th wheel (in Hz)} \\[4pt]
h_{jk} & = & \text{ratio of frequency of } k\text{th harmonic of } j\text{th disturbance} \\[2pt]
  &   & \text{to frequency of wheel rotation; assumed the same for all wheels} \\[4pt]
\phi_{ijk} & = & \text{phase angle of } k\text{th harmonic of } j\text{th disturbance of } i\text{th wheel}
\end{array}
$$

Both f_i and ϕ_{ijk} are assumed to be independent random variables. By independent we mean that the joint probability density function (PDF) can be written as the product of the individual PDF's. If we use the notation $f_X(x)$ to denote the PDF of the random variable X, then independence implies $f_{H_{jk}\Phi_{ijk}}(h_{jk}, \phi_{ijk}) = f_{H_{jk}}(h_{jk}) f_{\Phi_{ijk}}(\phi_{ijk})$.

The total disturbance of type j for the ith wheel is simply the sum over the harmonics.

$$m_{ij}(t) = \sum_{k=1}^{n_j} m_{ijk}(t) \tag{2.20}$$

Let us now define the disturbances in the local coordinate frame of a wheel. The pre-
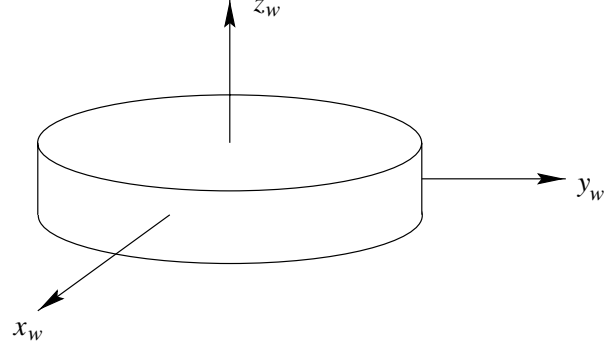
Figure 2.16: Local wheel frame (z axis along spin axis, x axis and y axis in plane of wheel).

superscript w signifies that the disturbances are expressed in the wheel frame.

$$
{}^{w}\mathbf{m}_i(t) = {}^{w}\left\{\begin{array}{c} m_1(t) \\ m_2(t) \\ m_3(t) \\ m_4(t) \\ m_5(t) \\ m_6(t) \end{array}\right\}_i = {}^{w}\left\{\begin{array}{c} F_x(t) \\ F_y(t) \\ F_z(t) \\ M_x(t) \\ M_y(t) \\ M_z(t) \end{array}\right\}_i \tag{2.21}
$$

The local wheel axes are shown in Figure 2.16. These axes remain fixed in space and do not rotate as the wheel spins. F_x and F_y are the radial forces, F_z is the axial force, M_x and M_y are the torques about orthogonal radial axes, and M_z is the torque about the wheel's spin axis. One simplification that can be made (and which is supported by experimental data) is that M_z is approximately zero. For instance, the causes that contribute to M_z (torque ripple and motor cogging) were found to be negligible for the Hubble Space Telescope reaction wheels [60]. Recall however that the torque required for attitude control is provided by M_z. This torque will not be included in the disturbance model since it is assumed that it will be accounted for in the ACS loop of the closed-loop spacecraft model.

The radial disturbances are assumed to rotate in the plane of the wheel at the frequencies of the harmonics. Hence, the disturbance forces in, and the moments about, the y axis are 90° out of phase with the disturbance forces in, and moments about, the x axis. This suggests that the following relationship holds:

$$
\phi_{ijk} = \phi_{i(j-1)k} + \frac{\pi}{2}, \quad j = 2, 5 \tag{2.22}
$$

2.2.5.3 Transformation of Disturbances

The transformation of the disturbances from the local wheel frame to the global spacecraft frame requires a rotation matrix. The orientation of the wheel frame relative to the spacecraft frame can be specified by a set of Euler angles. Define the so-called XYZ Euler angles as follows. Begin by having the local wheel axes aligned with the spacecraft axes[1]. Each of the three Euler angles specifies rotation about an intermediate axis. In particular, let

$$\beta \;=\; \text{angle of rotation about original } z \text{ axis}$$
$$\theta \;=\; \text{angle of rotation about new } y \text{ axis after previous rotation}$$
$$\gamma \;=\; \text{angle of rotation about new } x \text{ axis after previous rotation}$$

These rotations are shown in Figure 2.17.
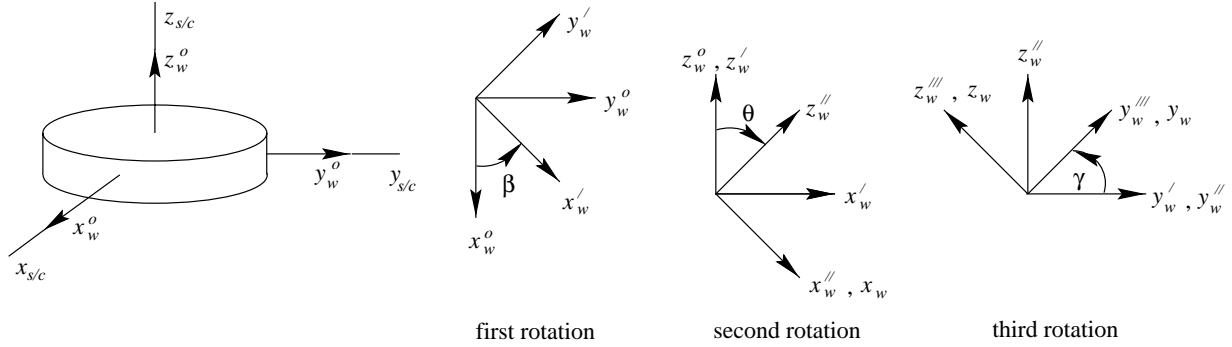
Figure 2.17: XYZ Euler angles (x_w, y_w, and z_w are axes of actual wheel frame).

Let

$^{s/c}\mathbf{p}$ be a vector in the spacecraft axes

$^{w}\mathbf{p}$ be a vector in the wheel axes

R_i be the 3×3 rotation matrix from the ith wheel frame to the spacecraft frame.

Then $^{s/c}\mathbf{p} = R_i{}^{w}\mathbf{p}$, and it can be shown that R_i is of the form

$$
R_i =
\begin{bmatrix}
\mathrm{c}\beta_i\mathrm{c}\theta_i & \mathrm{c}\beta_i\mathrm{s}\theta_i\mathrm{s}\gamma_i - \mathrm{s}\beta_i\mathrm{c}\gamma_i & \mathrm{c}\beta_i\mathrm{s}\theta_i\mathrm{c}\gamma_i + \mathrm{s}\beta_i\mathrm{s}\gamma_i \\[4pt]
\mathrm{s}\beta_i\mathrm{c}\theta_i & \mathrm{s}\beta_i\mathrm{s}\theta_i\mathrm{s}\gamma_i + \mathrm{c}\beta_i\mathrm{c}\gamma_i & \mathrm{s}\beta_i\mathrm{s}\theta_i\mathrm{c}\gamma_i - \mathrm{c}\beta_i\mathrm{s}\gamma_i \\[4pt]
-\mathrm{s}\theta_i & \mathrm{c}\theta_i\mathrm{s}\gamma_i & \mathrm{c}\theta_i\mathrm{c}\gamma_i
\end{bmatrix}
\tag{2.23}
$$

---

[1]Note: The "spacecraft" axes might not be the same as the global axes (*e.g.*, the coordinate frame used to build the finite-element model). In this thesis, the spacecraft axes will refer to the coordinate frame whose origin is at the location at which the disturbance forces and moments are desired. In most cases, this frame will be parallel to but displaced from the global frame.

65

where "c" is an abbreviation for "cos" and "s" is an abbreviation for "sin".

The axes now need to be displaced to account for the fact that all the wheels are not at the same location. A simplifying assumption is that the spin axis (z axis) of all the wheels intersect at a point, which happens to coincide with the origin of the spacecraft axes. Let the distance from this point to each of the wheel frame origins be d. Then the vector from the spacecraft frame origin to the origin of the ith wheel frame is given by

$$
{}^{s/c}\mathbf{r}_i = R_i{}^{w}\mathbf{r}_i = R_i \begin{bmatrix} 0 \\ 0 \\ d \end{bmatrix}
\tag{2.24}
$$

and is shown graphically in Figure 2.18.
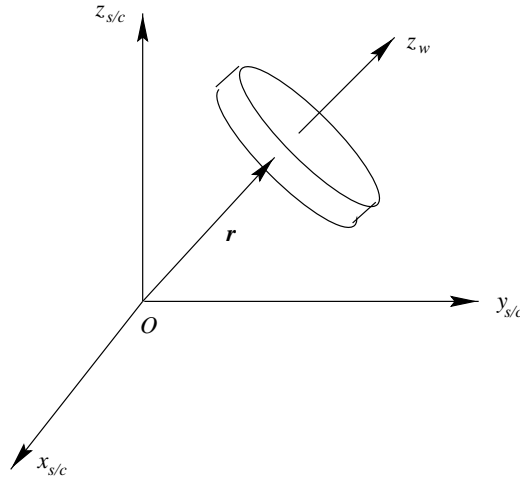
Figure 2.18: Position vector $\mathbf{r}$, which locates the wheel frame origin in the spacecraft frame.

The moment about O (in the spacecraft frame) due to the forces F_x, F_y, F_z in the wheel frame is given by the cross product

$$
{}^{s/c}\mathbf{r}_i \times \left(R_i \left\{ \begin{matrix} F_x \\ F_y \\ F_z \end{matrix} \right\}_i^{w} \right)
$$

We can now express in the spacecraft frame the disturbance forces and moments due to a single wheel. The disturbances can be written in terms of the rotation matrix R_i, the moment arms $\mathbf{r}_i$, and local disturbances ${}^{w}\mathbf{m}_i$. As a means of simplification, the cross

66

product $\mathbf{r} \times (\ )$ can be written as a matrix multiplication as follows

$$\mathbf{r}_i \times \mathbf{a} = \underbrace{\begin{bmatrix} 0 & -r_3 & r_2 \\ r_3 & 0 & -r_1 \\ -r_2 & r_1 & 0 \end{bmatrix}_i}_{\equiv \mathcal{R}_i} \mathbf{a} \tag{2.25}$$

The disturbance vector in the spacecraft frame is therefore

$$^{s/c}\mathbf{m}_i(t) = \begin{bmatrix} R_i & 0_{3\times 3} \\ \mathbf{r}_i \times (R_i & R_i \end{bmatrix} {}^{w}\mathbf{m}_i(t) = \underbrace{\begin{bmatrix} R_i & 0_{3\times 3} \\ \mathcal{R}_i R_i & R_i \end{bmatrix}}_{\text{call this } T_i} {}^{w}\mathbf{m}_i(t) = T_i {}^{w}\mathbf{m}_i(t) \tag{2.26}$$

The individual wheel disturbances can then be summed to obtain the overall disturbance acting in the spacecraft frame.

$$^{s/c}\mathbf{m}(t) = \sum_{i=1}^{N} {}^{s/c}\mathbf{m}_i(t) = {}^{s/c}\begin{Bmatrix} m_1(t) \\ m_2(t) \\ m_3(t) \\ m_4(t) \\ m_5(t) \\ m_6(t) \end{Bmatrix} = {}^{s/c}\begin{Bmatrix} F_x(t) \\ F_y(t) \\ F_z(t) \\ M_x(t) \\ M_y(t) \\ M_z(t) \end{Bmatrix} \tag{2.27}$$

2.2.5.4   Calculation of the Spectral Density Matrix

The objective now is to derive the spectral density matrix of $^{s/c}\mathbf{m}(t)$. The first step is to determine the correlation matrix, $R_{s/c\mathbf{m}}(t_1, t_2)$. Let $E[(\cdot)]$ signify the expectation operator.

$$R_{s/c\mathbf{m}}(t_1, t_2) = E\left[{}^{s/c}\mathbf{m}(t_1) {}^{s/c}\mathbf{m}^T(t_2) \right] \tag{2.28}$$

$$= E\left[\left(\sum_{p=1}^{N} {}^{s/c}\mathbf{m}_p(t_1) \right) \left(\sum_{q=1}^{N} {}^{s/c}\mathbf{m}_q^T(t_2) \right) \right] \tag{2.29}$$

Now substitute the transformation $^{s/c}\mathbf{m}_i(t) = T_i {}^{w}\mathbf{m}_i(t)$ (which was defined in Eq. 2.26).

$$R_{s/c\mathbf{m}}(t_1, t_2) = E\left[\left(\sum_{p=1}^{N} T_p {}^{w}\mathbf{m}_p(t_1) \right) \left(\sum_{q=1}^{N} {}^{w}\mathbf{m}_q^T(t_2) T_q^T \right) \right] \tag{2.30}$$

$$= E\left[\sum_{p=1}^{N} \sum_{q=1}^{N} T_p {}^{w}\mathbf{m}_p(t_1) {}^{w}\mathbf{m}_q^T(t_2) T_q^T \right]$$

67

Neither T_p nor T_q is a function of a random variable, so the expectation operator can be brought inside the summation.

$$R_{s/c\mathbf{m}}(t_1, t_2) = \sum_{p=1}^{N}\sum_{q=1}^{N} T_p \underbrace{E\left[{}^w\mathbf{m}_p(t_1){}^w\mathbf{m}_q^T(t_2)\right]}_{=R_{w\mathbf{m}_p{}^w\mathbf{m}_q}(t_1,t_2)} T_q^T \tag{2.31}$$

$$= \sum_{p=1}^{N}\sum_{q=1}^{N} T_p \begin{bmatrix} & \vdots & \\ \cdots & R_{w m_{pr}{}^w m_{qs}}(t_1, t_2) & \cdots \\ & \vdots & \end{bmatrix} T_q^T$$

Thus, the correlation matrix of ${}^{s/c}\mathbf{m}$ can be written in terms of the transformation matrices T_p and T_q and the cross-correlation matrix of ${}^w\mathbf{m}_p$ and ${}^w\mathbf{m}_q$, where p and q loop over the number of wheels.

As shown in Eq. 2.31, scalar cross-correlation terms like $R_{w m_{pr}{}^w m_{qs}}(t_1, t_2)$ appear. Expanding this term using Eq. 2.19 and Eq. 2.20,

$$R_{w m_{pr}{}^w m_{qs}}(t_1, t_2)$$

$$= E\left[m_{pr}(t_1)m_{qs}(t_2)\right] \tag{2.32}$$

$$= E\left[\left\{\sum_{k=1}^{n_r} C_{rk} f_p^2 \sin(2\pi h_{rk} f_p t_1 + \phi_{prk})\right\}\left\{\sum_{l=1}^{n_s} C_{sl} f_q^2 \sin(2\pi h_{sl} f_q t_2 + \phi_{qsl})\right\}\right]$$

$$= E\left[\sum_{k=1}^{n_r}\sum_{l=1}^{n_s} C_{rk} C_{sl} f_p^2 f_q^2 \sin(2\pi h_{rk} f_p t_1 + \phi_{prk})\sin(2\pi h_{sl} f_q t_2 + \phi_{qsl})\right]$$

Making use of the trigonometric identity $\sin A \sin B = \frac{1}{2}\left[\cos(A-B) - \cos(A+B)\right]$ leads to

$$R_{w m_{pr}{}^w m_{qs}}(t_1, t_2) = E\left[\sum_{k=1}^{n_r}\sum_{l=1}^{n_s} \frac{C_{rk} C_{sl} f_p^2 f_q^2}{2}\left\{\cos\left(2\pi(h_{rk} f_p t_1 - h_{sl} f_q t_2) + \phi_{prk} - \phi_{qsl}\right)\right.\right. \tag{2.33}$$

$$\left.\left. - \cos\left(2\pi(h_{rk} f_p t_1 + h_{sl} f_q t_2) + \phi_{prk} + \phi_{qsl}\right)\right\}\right]$$

The random variables are f_p, f_q, ϕ_{prk}, and ϕ_{qsl}. We make the following assumptions:

- ϕ's are independent (except when Eq. 2.22 is in effect)

- ϕ's are uniform random variables over the interval $[0, 2\pi]$

- f's are independent, and the probability density function of the pth wheel is expressed as $f_{FP}(f_p)$

We now consider several cases.

Case 1

$p = q$ and $r = s$ (*i.e.*, same wheel and same disturbance number)

This case is identical to that considered by Melody in [60]. The result is equivalent to

$$R_{w_{m_{pr}} w_{m_{pr}}}(t_1, t_2) = \sum_{k=1}^{n_r} \frac{C_{rk}^2}{2} E\left[f_p^4 \cos\left(2\pi h_{rk} f_p (t_1 - t_2)\right)\right] \tag{2.34}$$

Letting $t_1 - t_2 = \tau$ leads to the following stationary autocorrelation function.

$$R_{w_{m_{pr}} w_{m_{pr}}}(\tau) = \sum_{k=1}^{n_r} \frac{C_{rk}^2}{2} E\left[f_p^4 \cos\left(2\pi h_{rk} f_p \tau\right)\right] \tag{2.35}$$

Case 2

$p = q$ and $(r, s) \in [(1, 2), (2, 1), (4, 5), (5, 4)]$ (*i.e.*, same wheel, and disturbances are of the same type and $90°$ out of phase)

Appendix B derives the result

$$R_{w_{m_{pr}} w_{m_{ps}}}(\tau) = \mp \sum_{k=1}^{n_r} \frac{C_{rk}^2}{2} E\left[f_p^4 \sin\left(2\pi h_{rk} f_p \tau\right)\right], \quad \begin{cases} - & , \quad r > s \\ + & , \quad r < s \end{cases} \tag{2.36}$$

Case 3

$p = q$ and $(r, s) \notin [(1, 2), (2, 1), (4, 5), (5, 4)]$ and $r \neq s$ (*i.e.*, remaining combinations of r and s for the same wheel)

Using the definition of the expectation operator to rewrite Eq. 2.33 produces

$$R_{w_{m_{pr}} w_{m_{ps}}}(t_1, t_2) = \sum_{k=1}^{n_r} \sum_{l=1}^{n_s} \int_{-\infty}^{+\infty} \int_0^{2\pi} \int_0^{2\pi} \frac{C_{rk} C_{sl} f_p^4}{2} \{\cos\left[2\pi f_p (h_{rk} t_1 - h_{sl} t_2) + \phi_{prk} - \phi_{psl}\right]$$

$$\tag{2.37}$$

$$- \cos\left[2\pi f_p (h_{rk} t_1 + h_{sl} t_2) + \phi_{prk} + \phi_{psl}\right]\} \frac{1}{2\pi} \frac{1}{2\pi} f_{F_P}(f_p) d\phi_{prk} d\phi_{psl} df_p = 0$$

The entire expression is equal to zero because ϕ_{prk} and ϕ_{psl} are uniformly distributed over $[0, 2\pi]$ and are independent. To see this, consider the following simplified case.

$$\int_0^{2\pi} \cos(\phi + A) d\phi = 0 \tag{2.38}$$

Integrating a cosine function over one period will always produce zero. So for every cosine term that contains a ϕ_{prk} or ϕ_{psl}, the integral from 0 to 2π with respect to ϕ_{prk} or ϕ_{psl} will vanish.

Case 4

$p \neq q$ (*i.e.*, different wheels and any combination of disturbances)

Allowing different wheel speeds still produces the same result.

$$R_{w_{m_{pr}}w_{m_{qs}}}(t_1, t_2) = \sum_{k=1}^{n_r} \sum_{l=1}^{n_s} \int_{-\infty}^{+\infty} \int_0^{2\pi} \int_0^{2\pi} \frac{C_{rk}C_{sl}f_p^2 f_q^2}{2} \{\cos\left(2\pi(h_{rk}f_p t_1 - h_{sl}f_q t_2) + \phi_{prk} - \phi_{qsl}\right)$$
(2.39)
$$- \cos\left(2\pi(h_{rk}f_p t_1 + f_q h_{sl}t_2) + \phi_{prk} + \phi_{qsl}\right)\} \frac{1}{2\pi}\frac{1}{2\pi}f_{FP}(f_p)f_{FQ}(f_q)d\phi_{prk}d\phi_{qsl}df_q df_p = 0$$

since ϕ_{prk} and ϕ_{qsl} are uniformly distributed over $[0, 2\pi]$ and are independent.

At this point, all the various correlation functions have been computed. The next step is to derive the spectral density functions. Taking the Fourier transform of Eq. 2.31 (which can be done since all the nonzero correlation functions have been shown to be functions of a single time-lag variable τ) results in

$$S_{s/c\mathbf{m}}(\omega) = \sum_{p=1}^{N} \sum_{q=1}^{N} T_p \begin{bmatrix} & \vdots & \\ \cdots & S_{w_{m_{pr}}w_{m_{qs}}}(\omega) & \cdots \\ & \vdots & \end{bmatrix} T_q^T$$
(2.40)

where $S_{s/c\mathbf{m}}(\omega)$ signifies the spectral density matrix of the reaction wheel disturbances in the spacecraft frame.

The spectral density functions corresponding to each of the four cases can now be determined.

Case 1

$p = q$ and $r = s$

As before, this case was considered by Melody in [60]. The resulting PSD is given by

$$S_{w_{m_{pr}}w_{m_{pr}}}(\omega) = \sum_{k=1}^{n_r} \frac{\pi C_{rk}^2 \omega^4}{2(2\pi h_{rk})^5} \left[f_{FP}\left(\frac{\omega}{2\pi h_{rk}}\right) + f_{FP}\left(\frac{-\omega}{2\pi h_{rk}}\right) \right]$$
(2.41)

Case 2

$p = q$ and $(r, s) \in [(1, 2), (2, 1), (4, 5), (5, 4)]$

Appendix B derives the following result.

$$S_{w_{m_{pr}}w_{m_{ps}}}(\omega) = \pm \sum_{k=1}^{n_r} \frac{j\pi C_{rk}^2 \omega^4}{2(2\pi h_{rk})^5} \left[f_{F_P}\left(\frac{\omega}{2\pi h_{rk}}\right) + f_{F_P}\left(\frac{-\omega}{2\pi h_{rk}}\right) \right], \quad \begin{cases} + & , \quad r > s \\ - & , \quad r < s \\ j & = \sqrt{-1} \end{cases}$$
$$(2.42)$$

Note that this only differs from the result of the $p = q$ and $r = s$ case by a factor of $\pm j$.

Case 3 and Case 4

These cases lead to the result $S_{w_{m_{pr}}w_{m_{qs}}}(\omega) = 0$ since the corresponding correlation functions are zero.

The double sum in Eq. 2.40 can be replaced by a single sum since all the terms in which $p \neq q$ drop out.

$$S_{s/c\mathbf{m}}(\omega) = \sum_{p=1}^{N} T_p \begin{bmatrix} & & \vdots & & \\ \cdots & & S_{w_{m_{pr}}w_{m_{ps}}}(\omega) & & \cdots \\ & & \vdots & & \end{bmatrix} T_p^T = \sum_{p=1}^{N} T_p S_{w\mathbf{m}_p}(\omega) T_p^T \qquad (2.43)$$

If we make the further assumption that all the wheels have the same wheel speed probability density function, namely $f_{F_1}(f_1) = f_{F_2}(f_2) = \cdots = f_{F_N}(f_N)$, as well as the same amplitude coefficients and harmonics, then we obtain

$$S_{s/c\mathbf{m}}(\omega) = \sum_{p=1}^{N} T_p \begin{bmatrix} & & \vdots & & \\ \cdots & & S_{w_{m_{pr}}w_{m_{ps}}}(\omega) & & \cdots \\ & & \vdots & & \end{bmatrix} T_p^T \qquad (2.44)$$

$$= \sum_{p=1}^{N} T_p \begin{bmatrix} S_{m_1}(\omega) & S_{m_1 m_2}(\omega) & & & & \\ S_{m_2 m_1}(\omega) & S_{m_2}(\omega) & & & & \\ & & S_{m_3}(\omega) & & & \\ & & & S_{m_4}(\omega) & S_{m_4 m_5}(\omega) & \\ & & & S_{m_5 m_4}(\omega) & S_{m_5}(\omega) & \\ & & & & & S_{m_6}(\omega) \end{bmatrix} T_p^T$$

and elements not shown are equal to zero. For simplicity we use the notation $S_{m_j}(\omega)$ to represent the PSD of the jth disturbance of a single wheel in local wheel coordinates.

$S_{m_j m_k}(\omega)$ represents the cross-spectral density function of the jth and kth disturbances of the wheel. For example, $S_{m_3}(\omega)$ is the PSD of the axial force disturbance, while $S_{m_4 m_5}(\omega)$ is the cross-spectral density function of the radial moment in the x direction and the radial moment in the y direction.

Eq. 2.44 is the final result that is desired. It gives the 6×6 spectral density matrix of the disturbances acting in spacecraft axes due to the contributions of all individual wheel disturbances. It requires information on the number of wheels (N), the orientation of the wheels (T_p), and the spectral density matrix of the local disturbances of a single wheel ($S_w \mathbf{m}_p$).

2.2.5.5 Implementation

Eq. 2.44 has been implemented in MATLAB, and sample results are presented here to illustrate its use. As an example, consider four Hubble reaction wheels oriented such that their spin axes are $63°$ from the spacecraft z axis. Assume that they are spaced symmetrically about the z axis. Let the maximum wheel speed be $3000\,\mathrm{RPM}$ and the minimum wheel speed be $0\,\mathrm{RPM}$. Also, assume that all wheel speeds are equally likely. In other words, let each wheel speed be a random variable with uniform probability density function in the range $[0, 3000]\,\mathrm{RPM}$. Consider that the center of each wheel is $0.25\,\mathrm{m}$ from the point at which the overall disturbance forces and torques are desired. We anticipate that the disturbance spectral density functions computed in this situation will represent the "on average" spectral content of the disturbances during observation modes. As the wheels counteract external torques during an observation, they can achieve any allowable wheel speed. The wheel speeds can probably be considered as random variables. On the other hand, this might not represent the anticipated spectral content during a slew. In that case, the wheel speeds follow some predetermined speed profile.

Figure 2.19 shows the PSD's of the three disturbances modeled by Melody in [60] for a Hubble reaction wheel. The radial force PSD is equivalent to $S_{m_1}(\omega)$ and $S_{m_2}(\omega)$ in Eq. 2.44. The axial force PSD is equivalent to $S_{m_3}(\omega)$, and the radial torque PSD is equivalent to $S_{m_4}(\omega)$ and $S_{m_5}(\omega)$. The cross-spectral density functions are not shown, but those arising from Case 2 are equal in magnitude to those plotted. (Recall that Eq. 2.42 indicates only a factor of $\pm j$ difference.)

Applying Eq. 2.44 produces the series of PSD's found in Figure 2.20. These represent
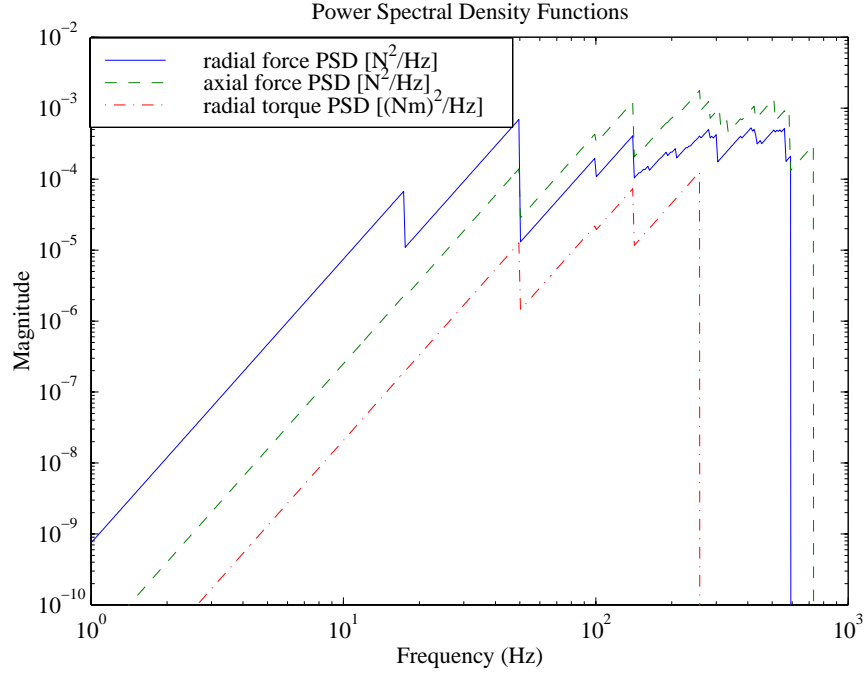
Figure 2.19: Power spectral density functions of disturbances from a Hubble-class reaction wheel with uniform probability density function in the interval $[0, 3000]$ RPM. Based on the disturbance model from Melody [60].

the diagonal elements of $S_{s/c_\mathbf{m}}(\omega)$. Due to the symmetry of the problem, the F_x and F_y PSD's overlap, as do the M_x and M_y PSD's.

The off-diagonal elements (*i.e.*, cross-spectral density functions) are not all zero, as indicated in Figure 2.21. A representative subset of these functions is plotted. Since cross-spectral density functions are typically complex-valued, both the magnitude and phase are shown. Note that the phase corresponding to the larger magnitude functions is $\pm 90°$, which indicates a factor of $\pm j$. The phase corresponding to the smaller magnitude functions is corrupted by numerical noise.

2.2.5.6   Comments

Because the wheel speeds and phase angles of the harmonics are treated as independent random variables, the disturbance spectral densities can be thought of as the "expected" levels. What this approach probably does not capture is the worst-case disturbance level. Lifting some of the assumptions on independence might lead to a better approximation of the
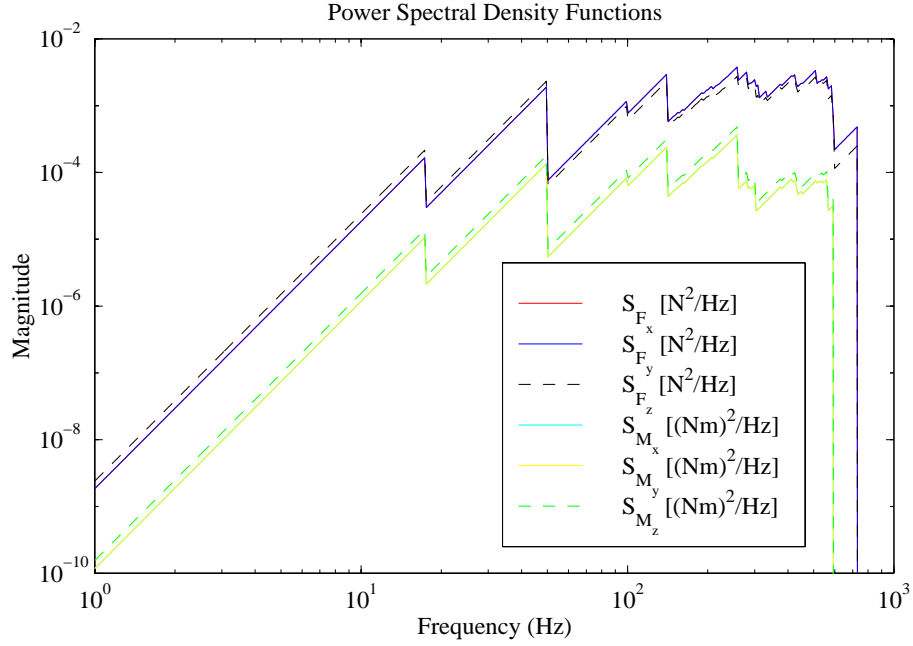
Figure 2.20: Power spectral density functions of disturbances in spacecraft frame. RWA assumed to consist of 4 Hubble-class reaction wheels with one wheel's Euler angles specified by $(\beta, \theta, \gamma) = (0°, 63°, 0°)$. The other wheels are arranged symmetrically about the z axis.
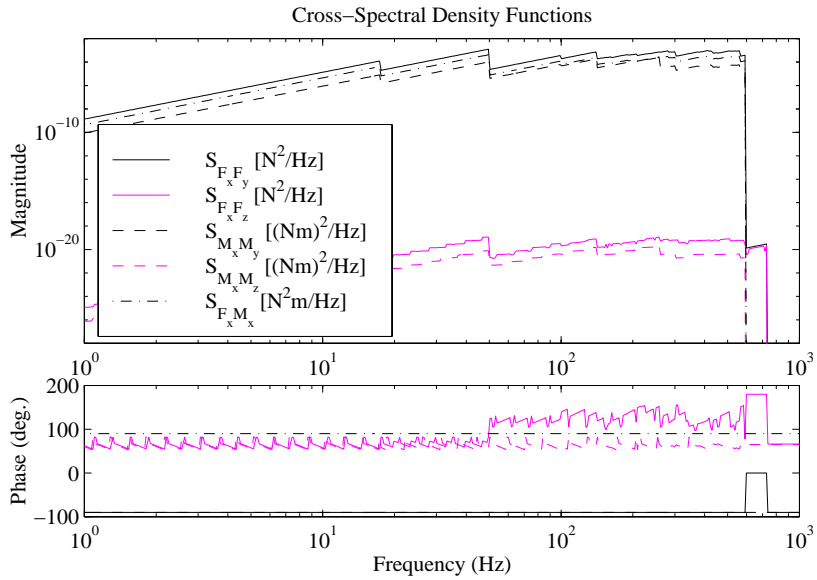
Figure 2.21: Representative cross-spectral density functions of disturbances in spacecraft frame. Based on same number of wheels and orientations as in previous figure.

worst case. For instance, Eq. 2.33 can be used as the starting point, and new assumptions such as that all wheels are at the same speed (*i.e.*, $f_p = f_q = f$) and all disturbances are at the same "clock angle" (*i.e.*, ϕ_{prk}, $\phi_{qsl} \rightarrow \phi_{rk}$, ϕ_{rk}) can be made. Following the same procedure as has been outlined previously will lead to a different expression for the total disturbance spectral density matrix than what is shown in Eq. 2.44. The assumption of equivalent wheel speeds is valid when wheel speeds "cross" as angular momentum is transferred from one wheel to another. Further analysis is required to determine how well the frequency-domain approach can predict the effects of these scenarios.

Another issue not brought up in this section but which is of concern is how resonances of the reaction wheel and/or the test mount affect the PSD's. Reference [17] clearly shows a case where the mount resonance at approximately $100\,\mathrm{Hz}$ is visible in a waterfall plot from a test of a single Hubble reaction wheel. Reference [6] describes some internal wheel modes that can occur below $100\,\mathrm{Hz}$. Figure 2.20 indicates a large amount of energy above $100\,\mathrm{Hz}$. It might be unlikely that this energy will be unattenuated before it propagates into the spacecraft. A possible remedy is to create a physical model which includes the effects of wheel resonances and mount dynamics. If the true disturbance sources can be identified from the test data, then they can be used to drive the physical model which has been coupled to the spacecraft model. This should provide the most accurate results, but it is unclear whether the complexity of this approach will outweigh any improved accuracy.

One last issue deals with how appropriate it is to use reaction wheel disturbance models derived from "blocked-force" tests (*i.e.*, tests conducted when the wheel is mounted to a rigid base). The impedance of the spacecraft at the location of the RWA will be different from that which the wheel sees during the test. Consequently, the actual disturbances entering the spacecraft might not be the same as what is modeled. It is recommended that more work in this area be conducted to see if a truly coupled model is required.

2.3 Summary

This chapter has provided an overview of the integrated modeling process. This process unifies structural, control, performance, and disturbance models into an overall disturbance-to-performance model required for performance assessment. To help illustrate this, the Space Interferometry Mission has been described and has served as an example of a high

performance optical system. The structural, control, and optical models were described in some detail so that the results of analyses in later chapters can be better understood.

In addition, a general methodology has been developed which uses individual reaction wheel stochastic disturbance models to produce the total spectral density function matrix of the disturbances in the spacecraft frame. The spectral density function matrix for the disturbances of a single wheel is first derived in the local wheel frame. This is based on a harmonic disturbance model which treats the wheel speed and phase angles as random variables. This work extends the results presented by Melody in [60] by also deriving the cross-spectral density functions. A coordinate transformation is then applied to express the disturbances in the spacecraft frame, and the contributions from all the wheels are summed. This then facilitates their use in subsequent disturbance analyses.

Chapter 3

Disturbance Analysis Framework

After developing an integrated model of a nominal system design, as described in the previous chapter, the next step is to assess the performance when the model is subjected to anticipated disturbances. Disturbance analyses are usually conducted in order to predict the effect of disturbances on system outputs of interest. The disturbances can be modeled in a number of forms, and as a result, various types of disturbance analyses can be performed. This chapter summarizes three particular types of disturbance analyses and illustrates the use of a MATLAB code that was developed to implement each one.

3.1 Types of Disturbance Analyses

There are at least three ways in which a disturbance analysis can be conducted on the nominal plant model. The approaches include:

- time domain

- frequency domain

- Lyapunov

This section will introduce each one and then demonstrate their use on a simple single degree-of-freedom system. Practical issues related to the accuracy of the results will be discussed. Section 3.3 will show sample results of a frequency-domain analysis on a model of the Space Interferometry Mission (SIM).
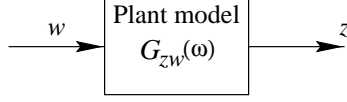
Figure 3.1: Plant disturbance-to-performance filter.

3.1.1 Time-domain analysis

We begin by assuming that we have a linear, time-invariant system described by the state-space system of equations

$$\dot{q}_p = A_{zw}\, q_p(t) + B_{zw}\, w(t)$$
$$z(t) = C_{zw}\, q_p(t) + D_{zw}\, w(t) \tag{3.1}$$

where q_p consists of states of the structural system and possibly states of a compensator if control loops are closed. Equivalently, the system can be described in the frequency-domain by the transfer function

$$G_{zw}(\omega) = C_{zw}(j\omega I - A_{zw})^{-1}B_{zw} + D_{zw} \tag{3.2}$$

The disturbances, w, are inputs to the system, while the performances, z, are outputs of interest. We can show this pictorially in Figure 3.1 with a block diagram.

Measured time histories of the disturbances $w(t)$ often exist due to test data. The disturbances $w(t)$ might also be generated from a time-domain model of the disturbance phenomenon. This can arise in the case when some disturbances are best modeled in the time domain because of their transient nature, such as thruster firings or thermal snap events.

Once the initial condition on the state vector, $q_p(0)$, is specified, numerical integration of Eq. 3.1 can then be performed using standard techniques to obtain estimates of the performance time histories $z(t)$. An introductory survey of several difference-method techniques (*e.g.*, Euler's method, Runge-Kutta, predictor-corrector) can be found in Reference [83]. These methods approximate the continuous-time first-order Eq. 3.1 with a difference equation such as

$$\frac{(q_p)_{n+1} - (q_p)_n}{\Delta t} = A_{zw}\, (q_p)_n + B_{zw} w_n$$
$$z_n = C_{zw}\, (q_p)_n + D_{zw}\, w_n \tag{3.3}$$

where the notation $(\cdot)_n$ indicates the value of the quantity $(\cdot)$ at the nth time step.

Each method can be classified according to its order of accuracy and level of complexity, and there is typically a trade between the accuracy and the complexity of a method. Furthermore, the stability of the error is also an important property of a chosen technique. The upper bound on the integration time step Δt is usually a threshold value Δt_{crit} that is unique to the technique. If $\Delta t > \Delta t_{\text{crit}}$, then the error will grow at each time step rather than be well behaved. On the other extreme, Δt should be small enough such that the highest frequency of interest in the response of the system can be captured with sufficient resolution; however, it can not be made arbitrarily small because this comes at the cost of increased computation time. If long time histories are required to ensure that steady-state conditions are reached, the computational expense can become prohibitively expensive.

Once an estimate of $z(t)$ is obtained, statistics such as root-mean-square (RMS) values can be computed from these analytical time histories. An advantage is that transient effects can be analyzed, which cannot be done for the frequency-domain approach which is described next. Time-domain performance specifications are another reason why a time simulation is conducted. In addition, maximum values or threshold crossings of the response can be determined from the time simulation.

3.1.2   Frequency-domain analysis

As is often the case, a time-domain analysis can be transformed into the frequency domain. One such example is the familiar input-output relation of linear systems. In the time domain, the output can be expressed as a convolution of the input with the impulse-response function of the system. In the frequency domain (*i.e.*, Laplace domain), the output is equal to the input multiplied by the transfer function.

For the disturbance analysis situation of interest here, we can envision that measured or analytical disturbances can be expressed in the frequency domain as power spectral densities (PSD's). The concept of a spectral density function was introduced earlier in Section 2.1.5. Rather than beginning with the PSD's, another possibility is that the disturbances are stochastic in nature and are modeled as the outputs of a linear filter driven by unit-intensity white noise d, as shown in Figure 3.2 [8],[2]. This filter is often referred to as a "shaping" or "pre-whitening" filter. Because of the unit-intensity assumption, the disturbance spectral density matrix of the output of the filter is given by

$$S_{ww}(\omega) = G_d(\omega)G_d^H(\omega) \tag{3.4}$$
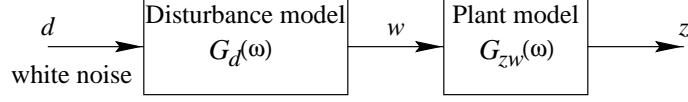
Figure 3.2: Disturbance filter and plant disturbance-to-performance filter.

Thus, $S_{ww}(\omega)$ can be specified directly or can be obtained from a shaping filter model.

In either case, given the disturbance spectral density matrix $S_{ww}(\omega)$ and the transfer function matrix $G_{zw}(\omega)$, the performance spectral density matrix can be computed from the relation (see [86])

$$S_{zz}(\omega) = G_{zw}(\omega)S_{ww}(\omega)G_{zw}^H(\omega) \tag{3.5}$$

This can also be expressed in the more typical frequency units of Hz.

$$S_{zz}(f) = G_{zw}(f)S_{ww}(f)G_{zw}^H(f) \tag{3.6}$$

$S_{ww}(\omega)$ can be a continuous function of frequency, or for the case of disturbances consisting of a series of discrete harmonics, it can contain impulses at the frequencies of the harmonics. In the latter case, $S_{zz}(\omega)$ will also contain a series of impulses.

$S_{zz}(\omega)$ provides information on the frequency content of the performance metrics. As shown previously in Eq. 2.11, integrating the elements of a spectral density function matrix across frequency and scaling by $\frac{1}{2\pi}$ (if the frequency is in rad/s) yields the covariance matrix (for zero-mean processes).

$$
\begin{aligned}
\Sigma_z &= \frac{1}{2\pi}\int_{-\infty}^{+\infty} S_{zz}(\omega)\,d\omega \\
&= \int_{-\infty}^{+\infty} S_{zz}(f)\,df
\end{aligned}
\tag{3.7}
$$

The variance of the ith performance metric is therefore given by

$$
\begin{aligned}
\sigma_{z_i}^2 = [\Sigma_z]_{i,i} &= \frac{1}{2\pi}\int_{-\infty}^{+\infty} [S_{zz}(\omega)]_{i,i}\,d\omega \\
&= \int_{-\infty}^{+\infty} [S_{zz}(f)]_{i,i}\,df \\
&= 2\int_{0}^{+\infty} [S_{zz}(f)]_{i,i}\,df
\end{aligned}
\tag{3.8}
$$

Taking the square root of $\sigma_{z_i}^2$ produces the root-mean-square (RMS) value. This is convenient since in many instances requirements are placed on RMS values of the performance metrics. The quantity $2\,[S_{zz}(f)]_{i,i}$ will be referred to as a one-sided PSD.

80

Although Eq. 3.8 provides an attractive way to determine the mean-square value of the performance, there are some practical issues that can affect the accuracy of the results. The first issue arises when the disturbance spectral density matrix is either measured experimentally or generated analytically and is passed on to the person who will conduct the disturbance analysis. An incorrect assumption might be made regarding the form of the PSD's (*e.g.*, rad/s *vs.* Hz, one-sided *vs.* two-sided). It is therefore extremely important that there are no misunderstandings if such a hand-off occurs.

Two other issues deal with numerical integration. The *df* in Eq. 3.8 is replaced by the frequency resolution Δf. Too large of a Δf can cause important narrowband features (*e.g.*, lightly-damped modes) to be missed. This can result in an incorrect RMS estimate, so it is important that additional frequency points be added around each mode and at the frequency of each mode (where the peak occurs). The appropriate number is directly related to the damping and frequency of each mode since a mode's "bandwidth" is proportional to the quantity $\zeta\omega$. The number to add is also dependent on how strongly each mode appears in the outputs of interest. For example, there is no need to increase the frequency resolution around a mode that is completely unobservable or undisturbable. Rather than stating any rules of thumb, it is recommended that a cumulative RMS plot (which is discussed shortly) be inspected to determine if the frequency resolution is sufficient.

The limits of integration usually span a finite frequency range when a numerical integration scheme such as trapezoidal integration is used. (The frequency limits might also be set by the frequency range of a measured PSD.) This results in Eq. 3.8 being expressed in terms of the minimum and maximum frequencies, $f_{\min}$ and $f_{\max}$.

$$\sigma_{z_i}^2 \approx 2 \int_{-f_{\min}}^{+f_{\max}} [S_{zz}(f)]_{i,i} \ df \tag{3.9}$$

It is important to ensure that the frequency range that contributes most to the RMS value is sufficiently captured within these limits. This also impacts model reduction since important modes within the range should be retained. One way to check this is by computing the cumulative RMS function.

Cumulative RMS and cumulative variance functions

Define a cumulative RMS function $\sigma_{z_i,c}(f_o)$ as

$$\sigma_{z_i,c}(f_o) = \left(2 \int_{-f_{\min}}^{+f_o} [S_{zz}(f)]_{i,i} \, df \right)^{\frac{1}{2}} \tag{3.10}$$

where $f_o \in [\ f_{\min} \ \ \dots \ \ f_{\max}\ ]$. If most of the energy lies within this range, then $\sigma_{z_i,c}(f_{\max})$ should be very close to the true value σ_{z_i}. An indication that the frequency range might not be sufficient is if the cumulative RMS curve has a significant slope (when plotted on a linear vertical scale) near either $f_{\min}$ or $f_{\max}$. This would suggest that frequencies just below or just above the range would contribute a non-negligible amount. Consequently, one clue that the frequency range is sufficient is if it appears as if the cumulative RMS curve is asymptotically approaching a horizontal line near the frequency limits.

It should be pointed out, however, that even if the cumulative RMS has this feature, it still does not ensure a correct overall RMS value. Lightly-damped modes that are well outside the bandwidth can still contribute a significant amount of energy. To avoid this situation, the PSD should roll off at a rate such that an unmodelled mode at higher frequencies would still not be able to contribute significantly to the RMS.

Besides indicating if the frequency range of integration is sufficient, a cumulative RMS curve can also help to identify the frequencies of critical structural modes in the system. The important modes are often those that are lightly damped, and these manifest themselves as sharp "steps" in a cumulative RMS curve. To notice why this is the case, first differentiate the square of Eq. 3.10 with respect to f_o.

$$\begin{aligned}
\frac{d\sigma_{z_i,c}^2(f_o)}{df_o} &= \frac{d}{df_o} \left(2 \int_{-f_{\min}}^{+f_o} [S_{zz}(f)]_{i,i} \, df \right) \\
&= 2S_{zz}(f_o)
\end{aligned} \tag{3.11}$$

The function $\sigma_{z_i,c}^2(f_o)$ is the cumulative variance, and its slope at a particular frequency is simply twice the value of the PSD at that frequency. So if f_o is in the vicinity of a lightly-damped mode, $[S_{zz}(f)]_{i,i}$ will be large, thereby implying that the slope will be steep. $[S_{zz}(f)]_{i,i}$ is also always a positive and real function since it is a PSD; consequently, the cumulative variance is a non-decreasing function.

Another use of the cumulative variance plot is to determine if there are enough frequency points around the critical modes. If the locations of frequency points are indicated on the

plot, then the "density" of points within each step can be examined. A sharp step that is comprised of only a few points is an indication that the frequency resolution is not sufficient. Since the cumulative variance (area) rapidly changes in the vicinity of a mode, a more accurate estimate requires enough points to capture this rate of change.

The cumulative variance can also provide a quick indication of the percent contribution of each of the lightly-damped modes. First define a normalized cumulative variance function that has a maximum value of 1.

$$\tilde{\sigma}^2_{z_i,c}(f_o) \equiv \frac{\sigma^2_{z_i,c}(f_o)}{\sigma^2_{z_i,c}(f_{\max})} \tag{3.12}$$

When a sharp step is present in a plot of $\tilde{\sigma}^2_{z_i,c}(f_o)$ due to a mode, that mode's contribution can be approximated as the "height" of the step. For example, if the step begins at a value of 0.2 and ends at a value of 0.9, then the mode responsible for that step can be thought of as contributing about 70% to the overall variance. This is not as simple to do when there are closely-spaced modes; however, the plot still can indicate the contributions from all modes in a certain frequency range.

Since a cumulative RMS function and the associated cumulative variance function contain useful information, it is recommended that either one of them always be plotted with the corresponding PSD. It is for this reason that most of the PSD plots in this thesis have a cumulative RMS subplot above them.

Disturbance contributions

While the cumulative RMS function indicates critical modes, what is also important is identifying which disturbances excite the critical modes the most. To help with this, disturbance contributions can be calculated.

For the special case when all the disturbances are uncorrelated, the spectral density matrix $S_{ww}(\omega)$ will be a diagonal matrix. Eq. 3.5 can then be simplified to

$$S_{z_k z_k}(\omega) = \sum_{i=1}^{\# \text{ of dist.}} \underbrace{|G_{z_k w_i}(j\omega)|^2 S_{w_i w_i}(\omega)}_{\equiv S_{(z_k z_k)_i}(\omega)} \tag{3.13}$$

where $S_{z_k z_k}(\omega)$ is the PSD of the kth performance metric, $S_{w_i w_i}(\omega)$ is the PSD of the ith disturbance, and $G_{z_k w_i}(j\omega)$ is the transfer function from the ith disturbance to the kth performance. These are all scalar functions of frequency. The notation $S_{(z_k z_k)_i}$ is used to

represent the contribution of the ith disturbance to the kth performance. Eq. 3.13 indicates that the overall performance PSD can be though of as a sum of PSD's due to each of the separate disturbances. At a particular frequency, the percent contribution of the ith disturbance can be calculated to be

$$\% \text{ contribution} = \frac{S_{(z_k z_k)_i}(\omega)}{S_{z_k z_k}(\omega)} \times 100\% \tag{3.14}$$

This value can also be plotted as a function of frequency for each of the performance metrics. Near the frequencies of the critical modes, the plot can help identify which disturbances are exciting the important modes the most. If the disturbances are correlated, then a disturbance contribution approximation can be made which ignores the off-diagonal terms in $S_{ww}(\omega)$.

Summary of frequency-domain analysis steps

Generally, the frequency-domain approach is more efficient than a time-domain analysis. The most computationally-intensive task that is required is evaluating the transfer function matrix. After that, only matrix multiplications and numerical integration (*e.g.*, trapezoidal integration) is necessary. The key computation steps involve:

- Determining the transfer function matrix $G_{zw}(\omega)$ from Eq. 3.2. (If A_{zw} is fairly large, a brute force inversion of $j\omega I - A_{zw}$ would be impractical. A state transformation that produces a diagonal A_{zw} would lead to a more efficient computation.)

- Performing the matrix multiplication in Eq. 3.6 at each frequency.

- Numerically integrating the PSD's (Eq. 3.9).

- Calculating the cumulative RMS and/or variance curves from Eq. 3.10 and Eq. 3.12.

- Calculating the disturbance contributions using Eq. 3.13 and Eq. 3.14 (for uncorrelated disturbances).

3.1.3 Lyapunov analysis

The third type of disturbance analysis can be conducted if the disturbances are modeled as the outputs of a shaping filter, as discussed in Section 3.1.2. Assume that the disturbance
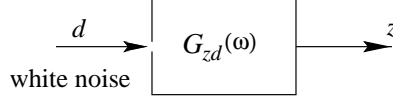
Figure 3.3: White noise-to-performance filter.

filter in Figure 3.2 can be expressed in the state-space form

$$
\begin{aligned}
\dot{q}_d(t) &= A_d\, q_d(t) + B_d\, q_d(t) \\
w(t) &= C_d\, q_d(t)
\end{aligned}
\tag{3.15}
$$

In order to keep the disturbance w from having infinite energy, there should be no feedthrough matrix D_d. (If the disturbance filter does have a D_d term, consult Section 5.3.1.3 for a method to remove D_d by augmenting the model with high frequency poles.) By placing this state-space system in series with the plant state-space equations from Eq. 3.1, an overall system of the form

$$
\begin{aligned}
\dot{q}(t) &= A_{zd}\, q(t) + B_{zd}\, d(t) \\
z(t) &= C_{zd}\, q(t)
\end{aligned}
\tag{3.16}
$$

can be created. Figure 3.3 shows the corresponding block diagram.

If the system is asymptotically stable, then the state covariance matrix Σ_q is obtained from the following steady-state Lyapunov equation

$$
A_{zd}\Sigma_q + \Sigma_q A_{zd}^T + B_{zd}B_{zd}^T = 0
\tag{3.17}
$$

This is a matrix equation in the unknown matrix Σ_q, and solution techniques are available through standard commercial software packages such as MATLAB. It should be emphasized that Σ_q represents the *steady-state* covariance matrix. One can imagine that if the stochastic disturbances w are suddenly applied to the system, there will be a period when transient behavior is dominant and the performance outputs are non-stationary. The dynamics of $\Sigma_q(t)$ are governed by [24]

$$
A_{zd}\Sigma_q(t) + \Sigma_q(t)A_{zd}^T + B_{zd}B_{zd}^T = \dot{\Sigma}_q(t)
\tag{3.18}
$$

and it is assumed that the initial state covariance matrix Σ_{q_o} is specified. When these transients decay away, the outputs can be characterized as stationary random processes with a covariance matrix equal to Σ_q.

The performance covariance matrix is then given by

$$
\begin{aligned}
\Sigma_z &= E\left[zz^T\right] \\
&= E\left[C_{zd}qq^TC_{zd}^T\right] \\
&= C_{zd}E\left[qq^T\right]C_{zd}^T \\
&= C_{zd}\Sigma_qC_{zd}^T
\end{aligned}
\tag{3.19}
$$

The RMS values of the performance metrics are given by the square roots of the diagonal entries in Σ_z, where Σ_z is of the form

$$
\Sigma_z =
\begin{bmatrix}
\sigma_{z_1}^2 & \sigma_{z_1z_2} & \cdots & \sigma_{z_1z_n} \\
\sigma_{z_2z_1} & \sigma_{z_2}^2 & \cdots & \sigma_{z_2z_n} \\
\vdots & \vdots & \ddots & \vdots \\
\sigma_{z_nz_1} & \sigma_{z_nz_2} & \cdots & \sigma_{z_n}^2
\end{bmatrix}
\tag{3.20}
$$

and n is the total number of elements in the performance vector z.

Thus, the Lyapunov method provides a relatively direct way of arriving at the RMS estimates (in the sense of statistical steady state) by solving one matrix equation (Eq. 3.17) and computing a matrix triple product (Eq. 3.19). It theoretically accounts for all frequencies and, therefore, does not suffer from the frequency resolution and frequency range issues of the frequency-domain approach. It provides the *exact* mean-square values of the performance variables. Of course, this is subject to the accuracy of the disturbance and plant models.

In certain instances, the quantity of interest is a weighted sum of other performance outputs. If the z_i in Eq. 3.20 represent these weighted outputs, then the performance cost J (a scalar) can be defined as

$$
J = \text{trace}\left[\Sigma_z\right] = \sigma_{z_1}^2 + \sigma_{z_2}^2 + \cdots + \sigma_{z_n}^2
\tag{3.21}
$$

The percent contribution of the ith weighted output to the overall performance cost is then

$$
\% \text{ contribution} = \frac{\sigma_{z_i}^2}{J} \times 100\%
\tag{3.22}
$$

The Lyapunov approach does suffer from a few drawbacks. It does not provide any direct insight into the frequency content of the outputs. Rather, it yields the overall variances of the states and the outputs. Since the disturbance spectral density matrix $S_{ww}(\omega)$ can

be obtained from Eq. 3.4, a frequency-domain analysis can still be conducted to identify critical modes and disturbances. A time-domain analysis can also be done by creating a representative white-noise disturbance $d(t)$ and performing a time-simulation of the state-space system in Eq. 3.16.

Another potential drawback is that the time to solve the Lyapunov equation can be excessive for large-order systems. In such cases, model reduction should first be performed to bring the number of states to a reasonable level without sacrificing the predictive capability of the model. Some model reduction techniques produce a D term, but this presents a problem from a Lyapunov standpoint because of the infinite energy that passes through from the assumed driving white-noise process. Techniques to model the feedthrough terms with high-frequency poles are therefore required, and one approach is discussed in Section 5.3.1.3.

3.1.4   Comments

The type of disturbance models available and the type of insight desired will dictate which of the three approaches to use, but whenever possible, more than one of these techniques should be periodically implemented to validate the results of the primary analysis. For example, a discrepancy between a Lyapunov analysis and a frequency-domain analysis might indicate that the frequency range or resolution is not sufficient in Eq. 3.9. It should be mentioned that the sensitivity analysis framework and uncertainty analysis framework to be introduced in later chapters both utilize the Lyapunov approach. These powerful tools can be applied when the system is modeled in this manner.

The next section will show the consistency that is achieved in the results when all three approaches are demonstrated on a low-order example problem. It will also provide a sense of the time required to perform each approach.

3.2   Demonstration of Analysis Methods on a Single DOF System

The simple mass-spring system of Figure 3.4 will be used to illustrate the three analysis methods. The disturbance is a force acting on the mass, and this force is the output of a first-order system driven by unit-intensity white noise. The performance is the position of the mass. The mass and stiffness parameters were chosen to yield a natural frequency of
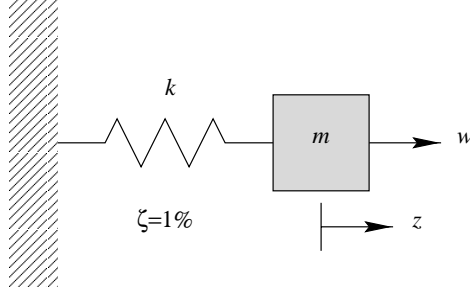
Figure 3.4: Single DOF system.

(a) (b)
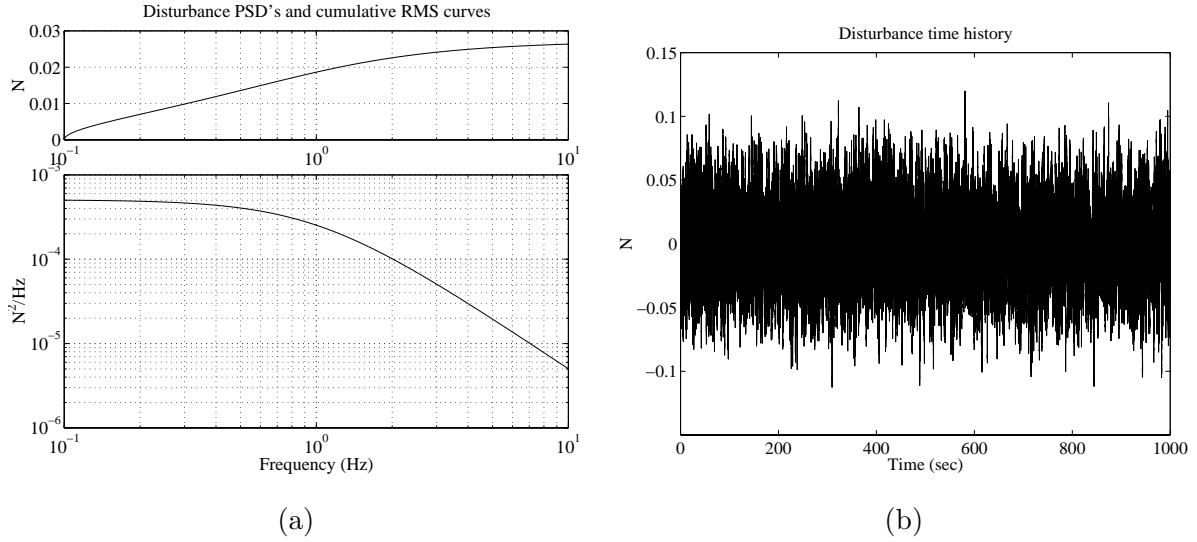
Figure 3.5: (a) Disturbance PSD and cumulative RMS. (b) Disturbance time history.

1 Hz, and the modal damping was specified to be 1%. A function called `dist_analysis.m` has been written in MATLAB to perform each of the techniques.

The PSD of the disturbance is shown in Figure 3.5(a). Notice that the corner frequency is at about 1 Hz and that the slope at high frequencies is −2. This is consistent with the earlier statement that the disturbance filter is first order. The PSD can be thought of as the square of the transfer function (recall Eq. 3.4). So a slope of −1 in the transfer function translates to a slope of −2 in the PSD. Plotted above the disturbance PSD is a cumulative RMS curve. As defined in Section 3.1.2, it represents the RMS contribution as a function of frequency. The disturbance time history in Figure 3.5(b) was generated by letting a pseudo-white noise process drive the disturbance first-order filter.

The disturbance time history was then taken as the input to the spring-mass system.
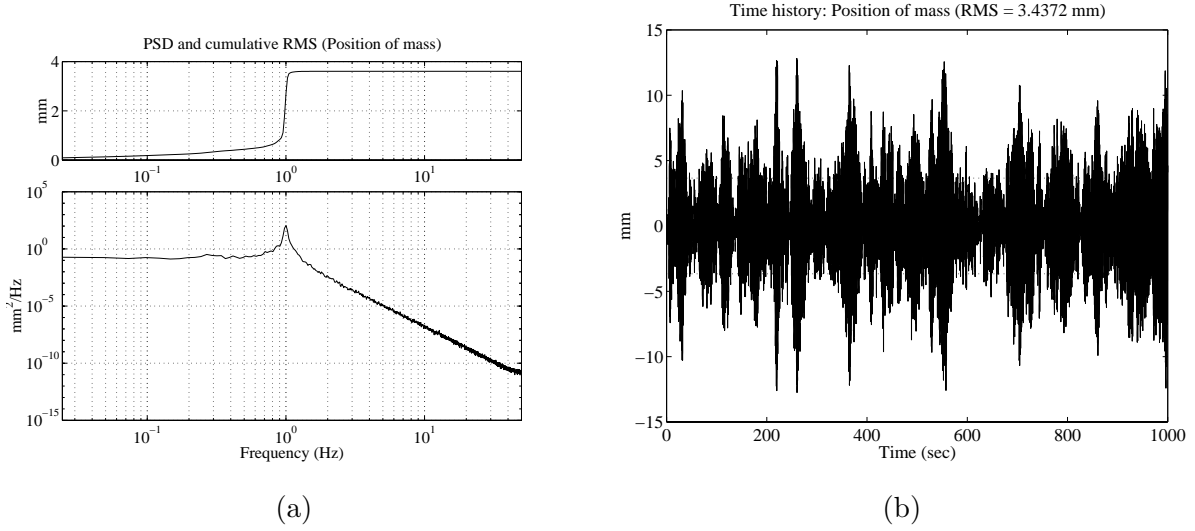
Figure 3.6: (a) Performance PSD and cumulative RMS curve computed from the time history shown in (b).

The analysis code `dist_analysis.m` uses the MATLAB command `lsim` to perform the numerical integration of the state-space equations. (More efficient numerical integration code probably exists, but for the time being, `lsim` is used.) The plot in Figure 3.6(b) shows the response of the mass. The code `dist_analysis.m` provides the option of computing the PSD's from the time simulation results. This permits an evaluation of the frequency-domain properties of the disturbance-induced response. Figure 3.6(a) contains the PSD computed from the sample time history, and the cumulative RMS curve is shown above the PSD. Notice that it asymptotes to a value of about 3.6 mm. If the cumulative RMS curve is still rising at the maximum frequency, this is an indication that the higher frequencies are contributing a significant amount of energy. Consequently, a larger frequency range is required. Notice that the "jump" in the curve occurs at the frequency of the mode.

The pure frequency-domain analysis involved taking the analytical disturbance PSD in Figure 3.5(a) and propagating it through the system transfer function via Eq. 3.5. The resulting performance PSD is shown in Figure 3.7. As expected, it looks very similar to the PSD in Figure 3.6(a), which was computed from the time history.

One issue that needs to be addressed when performing a disturbance analysis is related to the accuracy of the results. Assuming that the disturbance and plant models are correct, errors can still arise due to insufficient frequency resolution, time history length, *etc.* Figure 3.8 contains plots that help to illustrate this point.
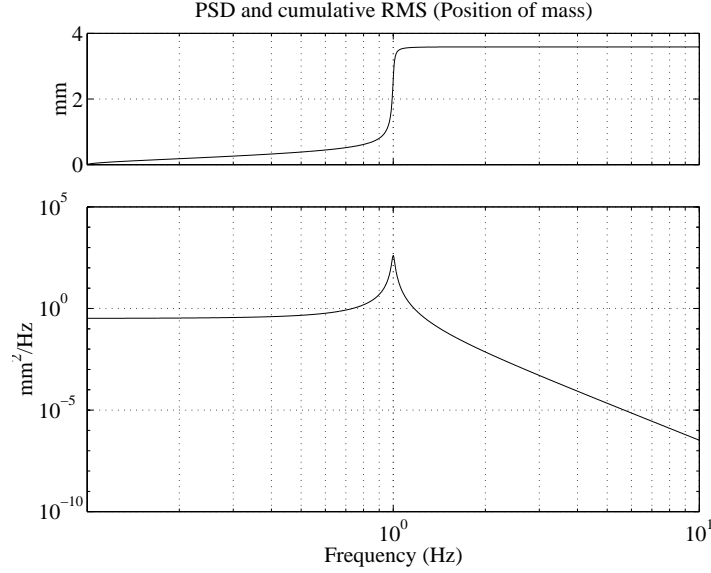
Figure 3.7: Performance PSD (bottom) and cumulative RMS (top) from frequency-domain analysis.

The two plots in Figure 3.8(a) address the frequency resolution issue. The horizontal axes are in terms of the number of original frequency points logarithmically spaced within the desired frequency range. The term "original" is used because `dist_analysis.m` augments the original frequency vector with more points within the bandwidth of each lightly-damped mode, including at the frequency of the mode. This ensures that the resonant peaks are accurately captured. Lack of frequency points can manifest itself as higher apparent damping. The upper plot in Figure 3.8(a) shows how the RMS value computed from the performance PSD appears to asymptote to the exact solution (obtained from the Lyapunov equation) as more frequency points are used. However, this comes at the cost of a slight increase in computation time, as indicated in the lower plot. Choosing the right number of frequency points is therefore quite important. For the case of disturbance PSD's from test data, the frequency resolution might be fixed. If the resolution is found to be insufficient, then efforts should be made to add more points via interpolation.

The plots in Figure 3.8(b) address the issue of the length of the disturbance time history used in a time-domain analysis. A nominal disturbance time history was created which was 5000 s in length and had a time step of 0.01 s (*i.e.*, Nyquist frequency of 50 Hz). A number of different cases were run in which the time simulation was stopped prior to reaching 5000 s. The RMS values computed from performance time histories of different lengths are indicated

90
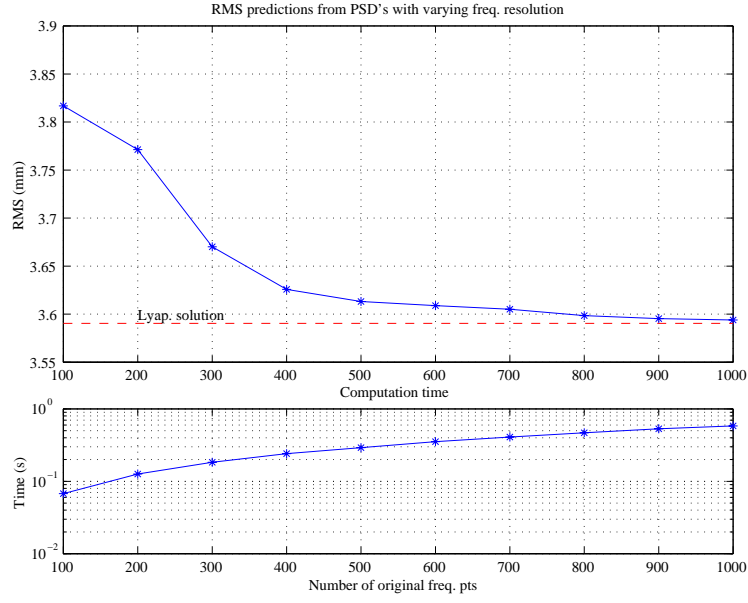
(a)
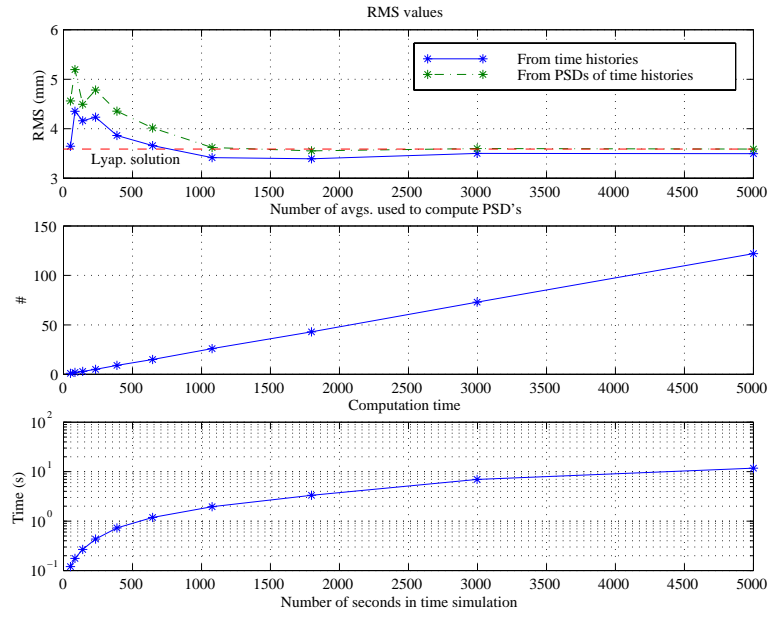
(b)

Figure 3.8: Effects of (a) frequency resolution and (b) truncated time-domain simulation.

in the upper subplot of Figure 3.8(b). The RMS values computed from the time histories' PSD's are also shown on the same subplot. The general trend is that errors on the order of 10% can exist for short time simulations (when compared to the exact Lyapunov solution), while the errors become small for longer time simulations. This suggests that when time simulations are performed and statistical steady-state results are desired, simulations of varying time length should be conducted to provide confidence that transient effects are not dominant. However, if transient results are desired, then this issue does not need to be considered.

The middle subplot of Figure 3.8(b) indicates the number of averages used when computing the PSD's from the time histories. Longer time histories allow more averages to be taken, thereby producing more accurate PSD's. The bottom subplot shows the solution time for each time simulation case. As expected, longer time histories require more computation time. Comparing the two bottom subplots of Figure 3.8(a) and Figure 3.8(b), we notice that to achieve approximately the same error level requires on the order of $2\,\mathrm{s}$ for the time-domain case and on the order of $0.2\,\mathrm{s}$ for the frequency-domain case. This represents a factor of 10 improvement in solution time for the frequency-domain approach. It should be noted that an efficient transfer function computation routine is used (`qbode.m`) for the frequency-domain calculations, while the standard MATLAB time-simulation routine `lsim` is used for the time integration. A more efficient time-simulation code might narrow the gap between the two methods.

The results of this section reveal the consistency achieved with the disturbance analysis code `dist_analysis.m` for the three different approaches. Some issues that need to be kept in mind have been discussed. The next section will demonstrate the frequency-domain method on a more realistic system and show the insights that can be provided by such an approach.

3.3 Frequency-Domain Disturbance Analysis on SIM

The SIM Classic model will now be used to illustrate the benefits of a frequency-domain disturbance analysis. Figure 3.9 shows a stick representation of the finite-element model, along with a ray trace of stellar light passing through two arms of one of the guide interferometers.

Some specific model parameters are:
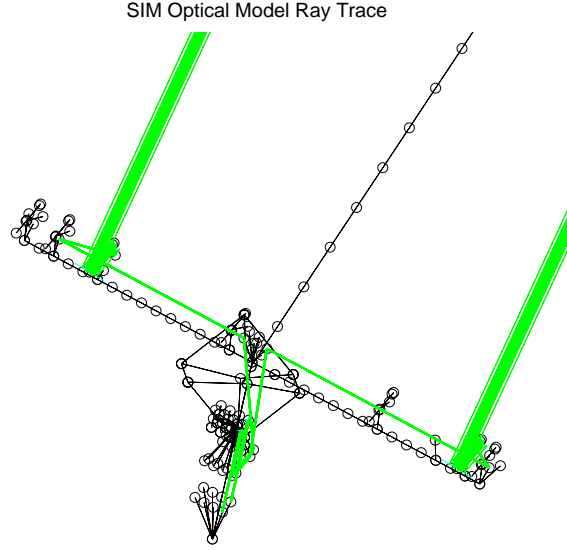
Figure 3.9: Stellar ray trace through guide interferometer #1 of SIM.

- 10 Hz 6-axis isolator (50% damping) at the reaction wheel assembly location

- 0.1% modal damping for structural modes

- 100 Hz bandwidth on fringe tracking control

In the sample results to follow, the performance metrics are:

1. total stellar optical path difference (OPD)

2. differential wavefront tilt (DWFT), x component in detector axes

3. differential wavefront tilt (DWFT), y component in detector axes

4. differential beam shear (DBS), x component in detector axes

5. differential beam shear (DBS), y component in detector axes

The full-order closed-loop SIM model in this case consists of 309 states. To avoid large order models such as this, model reduction should be performed. One approach is to first transform the state-space system to a balanced realization such that the observability and controllability gramians are diagonal and equal [65]. States corresponding to small gramian values (*i.e.*, states which are not very disturbable or observable) are eliminated. As mentioned previously, a D term can arise from this method if the reduced states are

assumed to be infinitely fast. Finite-frequency poles should be augmented to the system to remove the D term if a Lyapunov analysis is to be conducted (see Section 5.3.1.3).

In the general MIMO case, if the inputs and outputs are not normalized properly, specific input-output pairs can have different units. The corresponding transfer functions might differ significantly in magnitude. Model reduction might then eliminate states that are not "important" in the larger magnitude transfer functions, but which can be important in other transfer functions. For example, consider a one-input, two-output, second-order transfer function matrix given by

$$G(s) = \begin{bmatrix} \frac{y_1(s)}{u(s)} \\ \frac{y_2(s)}{u(s)} \end{bmatrix} = \begin{bmatrix} \frac{1}{s^2+2\zeta_1\omega_1 s+w_1^2} + \frac{10^{-4}}{s^2+2\zeta_2\omega_2 s+w_2^2} \\ \frac{10^{-4}}{s^2+2\zeta_1\omega_1 s+w_1^2} - \frac{10^{-2}}{s^2+2\zeta_2\omega_2 s+w_2^2} \end{bmatrix} \tag{3.23}$$

where the specific values of the parameters are $\zeta_1 = 0.1\%$, $\zeta_2 = 0.2\%$, $\omega_1 = 1\,\mathrm{rad/s}$, and $\omega_2 = 100\,\mathrm{rad/s}$. Figure 3.10 demonstrates the model reduction process on this system. The two subplots in the lower left show the nominal transfer function magnitudes. The second transfer function is several orders of magnitude smaller than the first transfer function. The gramian values of the balanced system are shown in the upper left subplot, and based on the sharp drop after the second state, the last two states might be chosen for elimination. This will cause the reduced system to miss the second mode, which is dominant in the second transfer function. If this transfer function is scaled to be the same order as the first, then the balanced system will have gramian values that are similar in magnitude, as is evident in the upper right subplot. This would be an indication that the last two states should not be reduced from the system.

Figure 3.11 shows a representative disturbance-to-performance transfer function from the SIM model before and after model reduction. The model reduction was only performed once. In actuality, the model reduction process should be iterative in nature, and states should be removed until performance predictions begin to deviate by a predetermined amount. (Note: `dist_analysis.m` does not perform model reduction. The state-space system should be reduced prior to being sent to this function.)

The representative disturbance source is that due to the reaction wheel assembly (RWA). Figure 3.12 shows the PSD's of the three force and three moment disturbances (in spacecraft axes) caused by four Hubble-class reaction wheels. The PSD's are derived based on an assumption of random wheel speeds with uniform probability density in the range
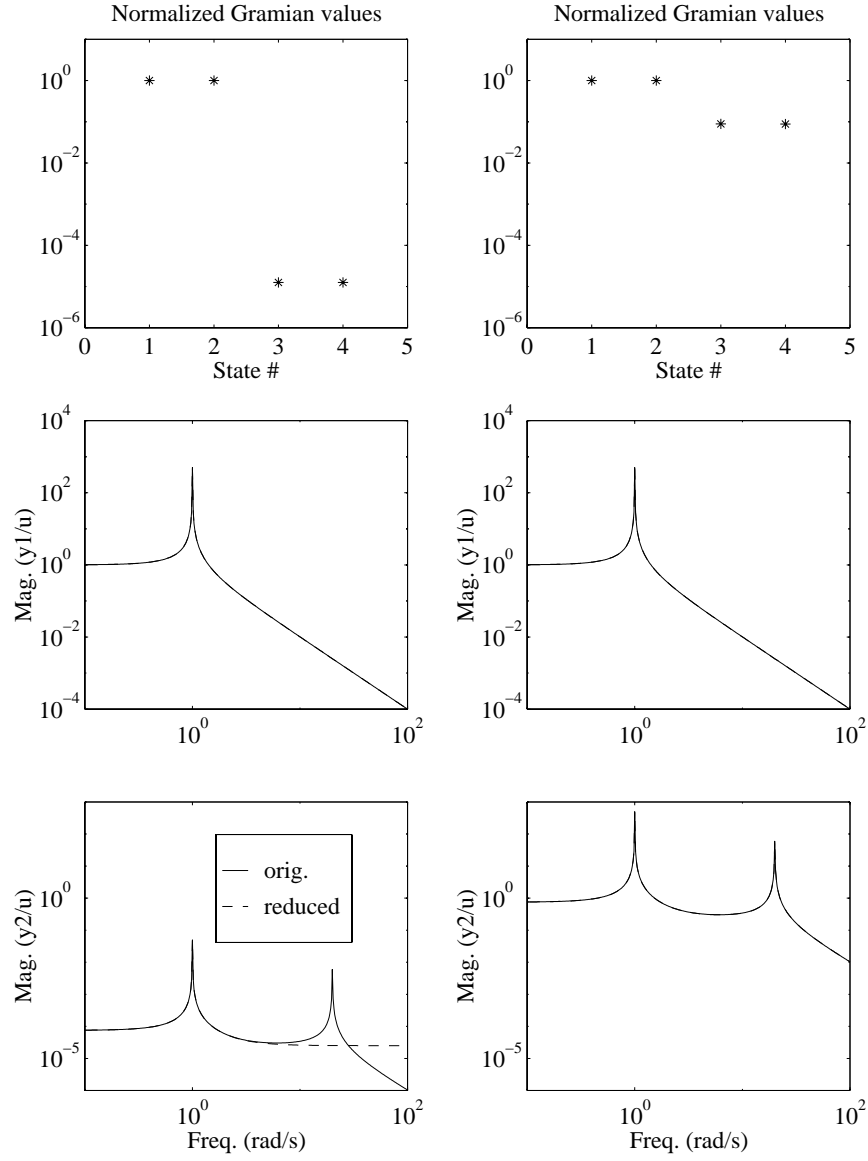
Figure 3.10: Example of balanced model reduction on original system (plots on left) and system with scaled output 2 (plots on right).
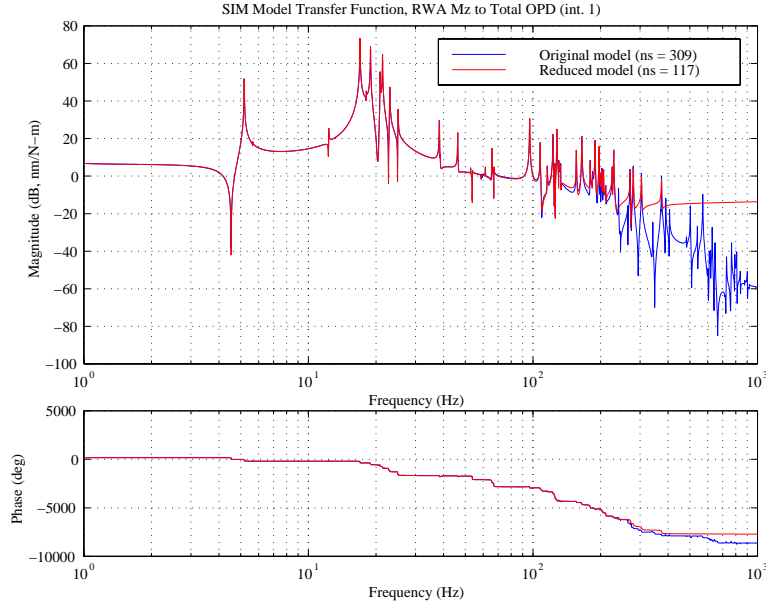
Figure 3.11: Example disturbance-to-performance transfer function before and after model is reduced.

[0,3000] RPM. The wheels are assumed to be symmetrically oriented about the z axis, with their spin axes $63°$ away from the z axis. The larger magnitude curves are force PSD's while the lower magnitude curves are moment PSD's. (See Section 2.2.5 for a derivation of these PSD's.) As shown in Section 2.2.5, some cross-spectral density terms are nonzero and have magnitudes comparable to that of the PSD's. The next section will compare results obtained when these terms are kept (*i.e.*, S_{ww} is fully-populated) and when these terms are neglected (*i.e.*, S_{ww} is diagonal).

Figure 3.13 shows the RMS values of the five performance outputs for cases with different initial frequency resolution. Three curves are shown in each subplot. One corresponds to the RMS values computed from PSD's of the full-order model using a fully-populated cross-spectral density disturbance matrix. Another corresponds to the results from a full-order model with a diagonal cross-spectral density matrix. The third is based on a reduced-order model (117 states) with a diagonal cross-spectral density matrix. The fact that these curves overlap almost exactly in all the subplots is an indication that neglecting the cross-spectral terms is a valid approximation in this case. Another conclusion is that the reduced model retains a sufficient number of states for accurate performance predictions.

Figure 3.14 shows the time required to compute all five performance RMS values as
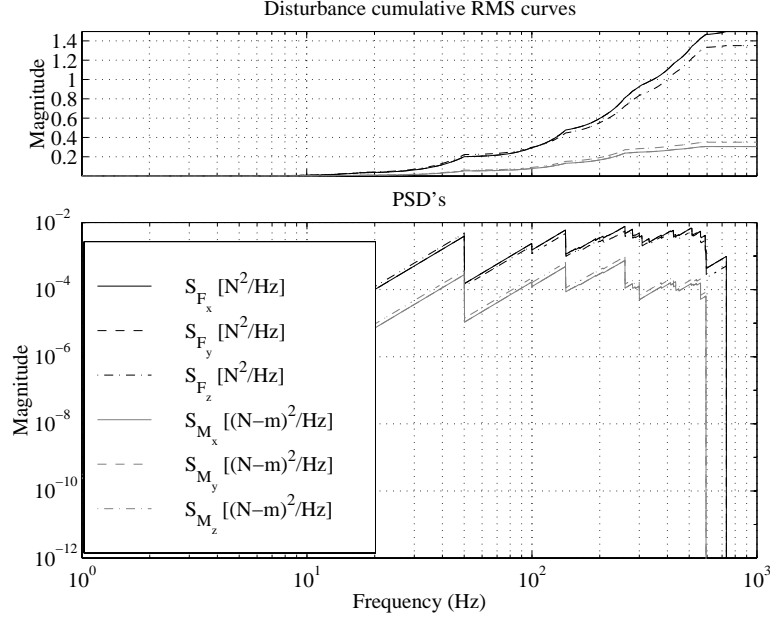
Figure 3.12: Cumulative RMS curves (top) and PSD's (bottom) of RWA distur-
bances.

a function of frequency resolution and model type. It indicates that a slight decrease in computation time can be achieved if the disturbances are uncorrelated (*i.e.*, the disturbance spectral density matrix is diagonal). A significant savings is achieved by using a lower-order model.

For the case of the full-order model driven by uncorrelated disturbances, Eq. 3.5 produces the OPD PSD shown in the middle plot of Figure 3.15. The cumulative RMS plot indicates a total RMS value of approximately 6.4 nm. The lower plot in Figure 3.15 is meant to help visualize which disturbances are contributing most. For uncorrelated disturbances, the overall PSD is the superposition of PSD's due to each disturbance (see Eq. 3.13). At a particular frequency, the relative percent contribution from each disturbance can be calculated. The plot indicates this by using black for 100% contribution and white for 0%. For example, across the frequency range from 16–22 Hz (where the larger steps occur in the cumulative RMS plot), it appears as if the dominant disturbance is M_z.

Figure 3.16 shows an example of a normalized cumulative variance plot. This plot is obtained by first squaring each value of the cumulative RMS curve and then dividing by the largest value (as defined in Eq. 3.12). Each frequency point is denoted with a +, and the fact that there are approximately 15 frequency points around the dominant mode at 16.97 Hz
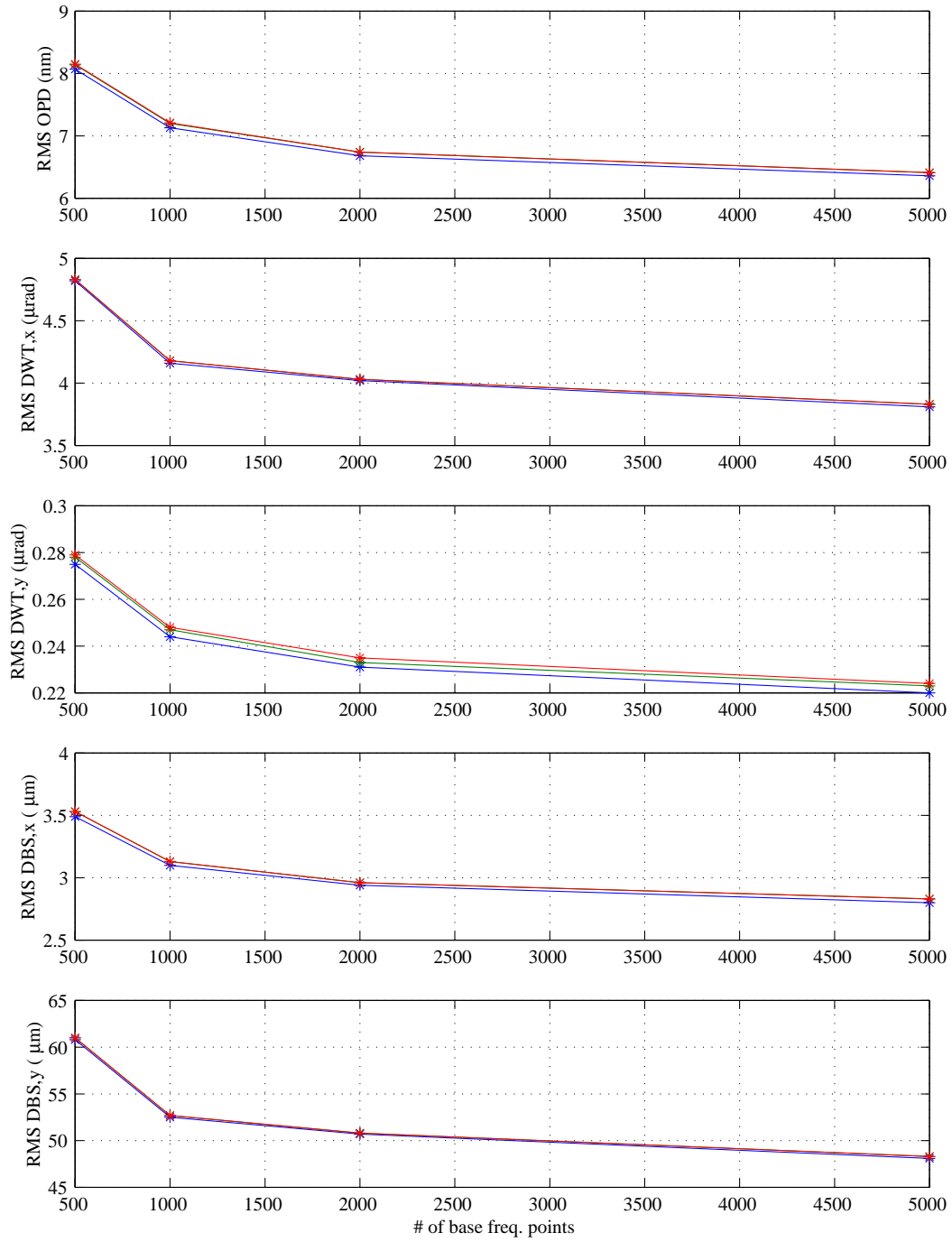
Figure 3.13: RMS estimates of the five performance metrics as a function of frequency resolution, model order, and disturbance correlation.
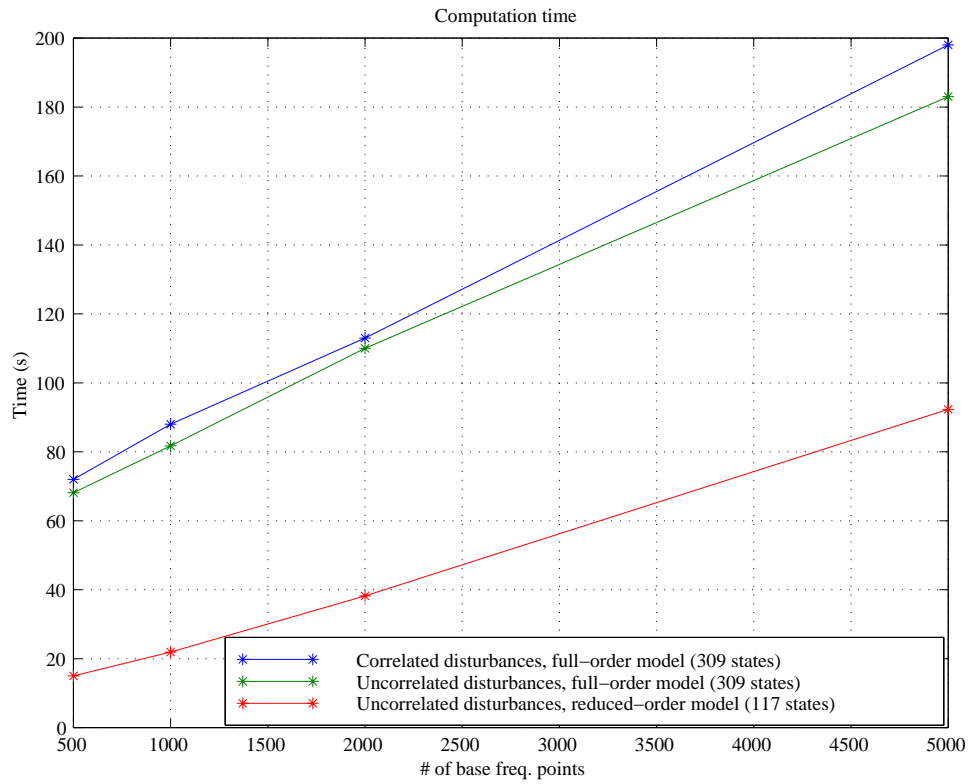
Figure 3.14: Computation times corresponding to the runs in Figure 3.13.
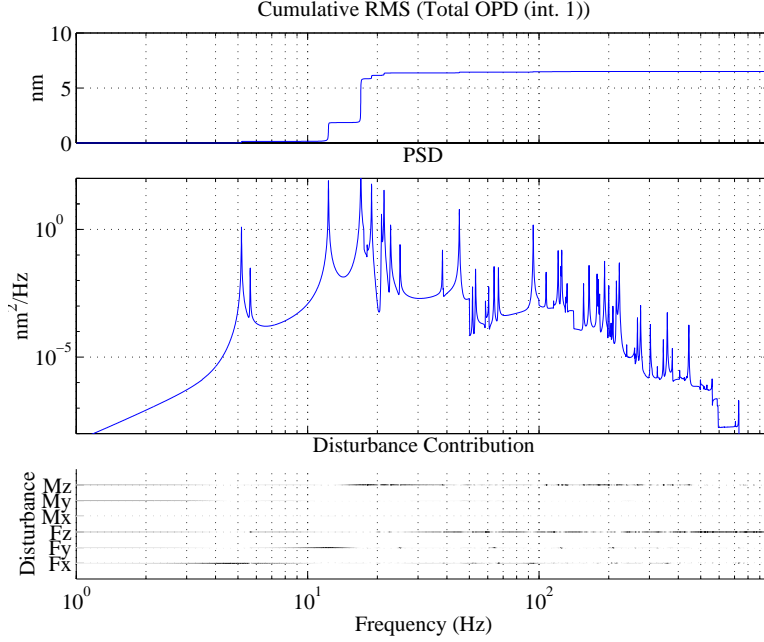
Figure 3.15: Cumulative RMS (top), PSD (middle), and disturbance contribution (bottom) for total OPD.

is an indication that the resolution is adequate. The gaps in points near the beginning and end of the corresponding step suggest that better accuracy might be achieved if additional frequency values are added at these locations. The function `dist_analysis.m` includes the option of allowing the user to interactively choose important frequencies by selecting frequencies where the largest "steps" occur.

The critical frequencies and disturbances can be summarized in bar chart form, and an example is presented in Figure 3.17. The plot lists several frequencies that were identified from the cumulative variance plot and indicates the percent contribution to the overall variance by the structural modes at those frequencies. Furthermore, each bar is subdivided in proportion to the percent contribution to the PSD by each disturbance. As can be seen, M_z is the disturbance that most excites the modes at 16.97 Hz, 18.89 Hz, and 21.38 Hz.

PSD plots and critical frequency bar charts for the remaining four performance metrics are not shown but do indicate that the mode at 16.97 Hz is the problem mode in all cases, and it is excited most by M_z. If it is determined that some or all of the performance metrics do not satisfy requirements, then information such as this can help suggest performance-improving redesigns.

To summarize, frequency-domain disturbance analyses can provide vital information
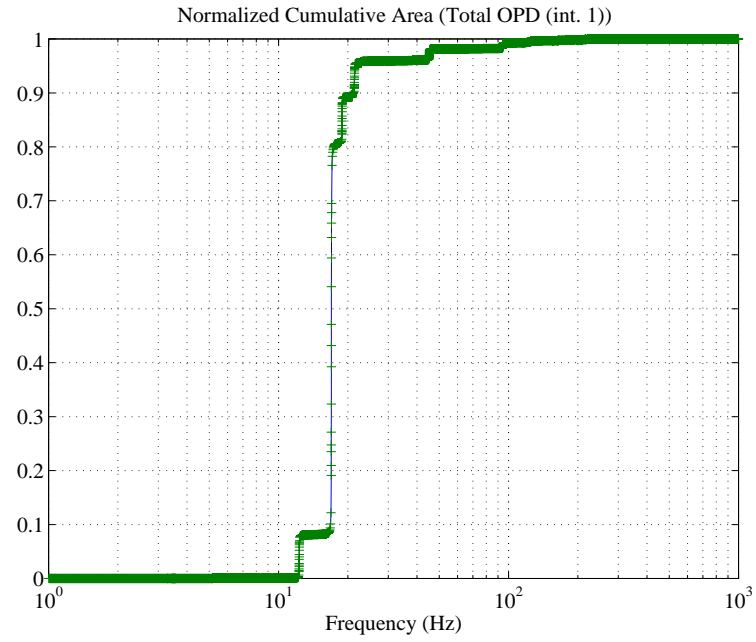
Figure 3.16: Cumulative variance plot used to identify critical frequencies.
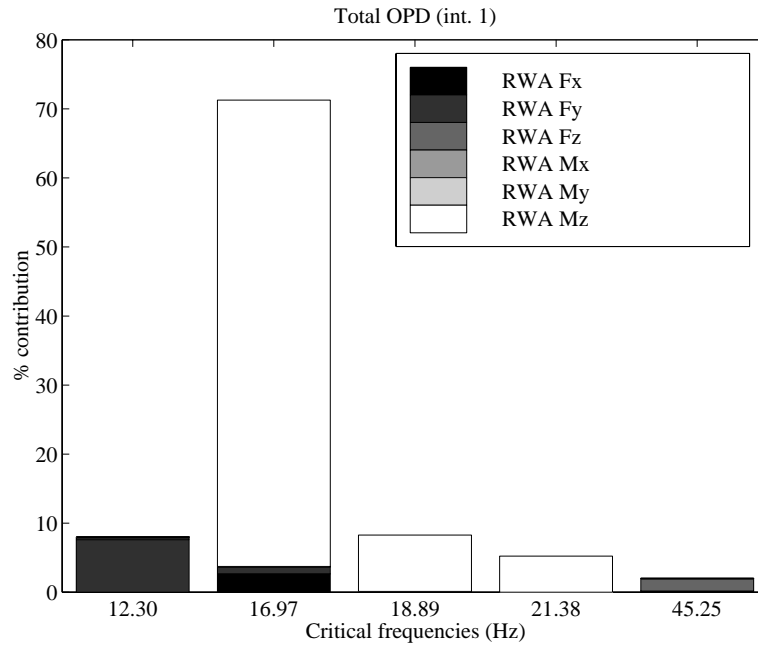
Figure 3.17: Bar chart showing percent contribution of each mode to overall performance variance. Disturbance contribution to PSD at each frequency is indicated by the relative partition of each bar.

concerning important frequency ranges and dominant disturbances, as was seen in this example for SIM. The next step is to perform a sensitivity analysis on parameters affecting the critical modes.

3.4   Summary

The development within the MATLAB framework of the function `dist_analysis.m` permits three types of disturbance analyses to be performed on a state-space model of a system. Depending on the form of the disturbance model, either time-domain, frequency-domain, or Lyapunov analyses can be conducted. Practical considerations regarding frequency resolution and time simulation lengths have been investigated using a simple one DOF system driven by band-limited white noise. The one DOF system was also used to help validate the code by comparing results obtained from the three different types of disturbance analyses. The SIM example analysis demonstrated the useful information that can be provided by a frequency-domain analysis. Neglecting the off-diagonal terms of a disturbance cross-spectral density matrix was shown to be a good approximation. This enabled disturbance contribution plots to be created and then to be used to identify important disturbances. Results showed that the M_z RWA disturbance excited three of the critical modes the most. The next chapter will introduce a method for computing the sensitivities of the performance RMS values with respect to modal parameters of the critical modes and physical parameters of the finite-element model.

Chapter 4

Sensitivity Analysis Framework

Determining the sensitivity of certain outputs (*e.g.*, performance metrics) of a system with respect to model parameters can provide useful information. For example, when correlating a model to test data, sensitivities can indicate which parameters should be tweaked and in which direction. Another use of sensitivities is to predict how performance predictions can vary if specific parameters contain some degree of uncertainty. Also, when it is found that a system does not satisfy specified performance requirements, sensitivity information can identify which components in the system are important. The most crucial parameters might be the focus of future testing programs that seek to accurately identify them, thereby reducing the uncertainty and leading to a more accurate model. Or the parameters might be the focus of redesign efforts that attempt to reduce the sensitivity to uncertainty. Finally, another possible use of a sensitivity analysis is to supply gradient information to any optimization routines are that implemented during the design phase. Because of applications such as these, a sensitivity analysis framework is therefore beneficial, and this chapter describes initial progress made in this area.

The following section describes the mathematical theory for computing sensitivities when the system is written in state-space form. The results are then specialized to the case when the structural equations of motion are expressed in modal form, and natural frequencies, modal damping ratios, and modal masses appear explicitly. Computation of sensitivities is demonstrated on models of different order: a single degree-of-freedom system, a multi-degree-of-freedom system (20 DOF's), and a closed-loop model of SIM Classic. Comparing the results obtained analytically with the results obtained from finite-difference approxi-
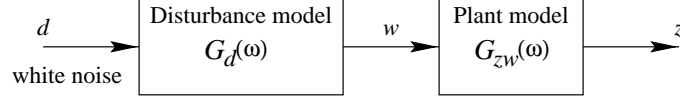
Figure 4.1: Disturbance filter and plant disturbance-to-performance filter.

mations reveals the numerical conditioning problems associated with large-order models. Section 4.5 then discusses the computation of sensitivities with respect to physical parameters of a finite-element model. The technique is applied to a beam example and a model of SIM Classic.

4.1 System State-Space Representation

As before, we assume that the mathematical description of the time-invariant system of interest is in linear state-space form. The overall system block diagram is shown in Figure 4.1, where z is a vector containing the performance metrics, and the physical disturbances w are modeled as the outputs of a filter that shapes unit-intensity, Gaussian white noise d. It is important to emphasize that all of the results presented in this chapter rely on a disturbance model of the form

$$
\begin{aligned}
\dot{q}_d &= A_d\, q_d + B_d\, d \\
w &= C_d\, q_d
\end{aligned}
\tag{4.1}
$$

Since all physical disturbance processes have finite energy, the feedthrough term D_d is assumed to be zero.

In general, there can exist a closed-loop control system consisting of a suite of sensors and actuators. The open-loop dynamics of the plant are given by

$$
\left\{ \begin{array}{c} \dot{q}_p \\ z \\ y \end{array} \right\} =
\left[\begin{array}{ccc} A_p & B_w & B_u \\ C_z & D_{zw} & D_{zu} \\ C_y & D_{yw} & D_{yu} \end{array} \right]
\left\{ \begin{array}{c} q_p \\ w \\ u \end{array} \right\}
\tag{4.2}
$$

Sensor outputs are denoted by y, and control actuator inputs are denoted by u. In the closed-loop case, a compensator commands u based on the measurements y. The general form of a strictly proper, linear, dynamic compensator is

$$
\begin{aligned}
\dot{q}_c &= A_c\, q_c + B_c\, y \\
u &= C_c\, q_c
\end{aligned}
\tag{4.3}
$$

104

The closed-loop dynamics of the plant are then

$$
\left\{ \begin{array}{c} \dot{q}_p \\ \dot{q}_c \end{array} \right\} = \left[\begin{array}{cc} A_p & B_u C_c \\ B_c C_y & A_c + B_c D_{yu} C_c \end{array} \right] \left\{ \begin{array}{c} q_p \\ q_c \end{array} \right\} + \left[\begin{array}{c} B_w \\ B_c D_{yw} \end{array} \right] w
$$

$$
z = \left[\begin{array}{cc} C_z & D_{zu} C_c \end{array} \right] \left\{ \begin{array}{c} q_p \\ q_c \end{array} \right\} + D_{zw} w \tag{4.4}
$$

Placing the plant in series with the disturbance filter produces the following overall state-space form.

$$
\underbrace{\left\{ \begin{array}{c} \dot{q}_d \\ \dot{q}_p \\ \dot{q}_c \end{array} \right\}}_{\dot{q}} = \underbrace{\left[\begin{array}{ccc} A_d & 0 & 0 \\ \left[\begin{array}{c} B_w \\ B_c D_{yw} \end{array} \right] C_d & A_p & B_u C_c \\ & B_c C_y & A_c + B_c D_{yu} C_c \end{array} \right]}_{A_{zd}} \underbrace{\left\{ \begin{array}{c} q_d \\ q_p \\ q_c \end{array} \right\}}_{q} + \underbrace{\left[\begin{array}{c} B_d \\ 0 \\ 0 \end{array} \right]}_{B_{zd}} d
$$

$$
z = \underbrace{\left[\begin{array}{ccc} D_{zw} C_d & C_z & D_{zu} C_c \end{array} \right]}_{C_{zd}} \left\{ \begin{array}{c} q_d \\ q_p \\ q_c \end{array} \right\} \tag{4.5}
$$

which can be written more compactly as

$$
\dot{q} = A_{zd} q + B_{zd} d
$$

$$
z = C_{zd} q \tag{4.6}
$$

As described in Section 3.1.3, a nominal disturbance analysis consists of solving first for the state covariance matrix Σ_q from the Lyapunov equation

$$
A_{zd}\Sigma_q + \Sigma_q A_{zd}^T + B_{zd}B_{zd}^T = 0 \tag{4.7}
$$

and then computing the performance covariance matrix Σ_z from

$$
\Sigma_z = C_{zd}\Sigma_q C_{zd}^T \tag{4.8}
$$

According to Eq. 3.20, the diagonal terms of Σ_z represent the mean-square values $\sigma_{z_i}^2$, and the root-mean-square (RMS) values are simply σ_{z_i}. We continue to assume zero-mean processes; therefore, the term "standard deviation" is used synonymously with "RMS", and the term "variance" is used synonymously with "mean square."

If we are only interested in the variance of the ith performance metric, then we need only to use the ith row of C_{zd} in Eq. 4.8.

$$C_{zd} = \begin{bmatrix} * & * & * \\ \cdots & C_i & \cdots \\ * & * & * \end{bmatrix} \leftarrow i\text{th row} \qquad (4.9)$$

The corresponding variance of this performance metric is given by

$$\sigma_{z_i}^2 = C_i \Sigma_q C_i^T \qquad (4.10)$$

The next section will derive the sensitivity of this quantity with respect to model parameters.

4.2 Governing Sensitivity Equation

Let p be a generic parameter that might or might not appear explicitly in the state-space representation of the system model. The sensitivity (*i.e.*, derivative) that we would like to find is

$$\frac{\partial \sigma_{z_i}}{\partial p} = \text{sensitivity of } i\text{th performance RMS with respect to } p \qquad (4.11)$$

The first step is to find the derivative of the variance $\sigma_{z_i}^2$ with respect to p. We cannot take the derivative of Eq. 4.10 with respect to p directly because Σ_q is the solution to Eq. 4.7; therefore, Σ_q is implicitly dependent on p. To get around this problem, we can treat the Lyapunov equation (Eq. 4.7) as a constraint equation, and augment it to Eq. 4.10 via a symmetric Lagrange multiplier matrix L_i. (A subscript i is used since there will be a different matrix for every performance metric.) The notation $\left(\sigma_{z_i}^2\right)^*$ is used to denote the Lagrangian of $\sigma_{z_i}^2$.

$$\begin{aligned} \left(\sigma_{z_i}^2\right)^* &= \sigma_{z_i}^2 + \text{trace}\left[L_i\left(A_{zd}\Sigma_q + \Sigma_q A_{zd}^T + B_{zd}B_{zd}^T\right)\right] \\ &= C_i\Sigma_q C_i^T + \text{trace}\left[L_i\left(A_{zd}\Sigma_q + \Sigma_q A_{zd}^T + B_{zd}B_{zd}^T\right)\right] \end{aligned} \qquad (4.12)$$

The derivative of the variance $\sigma_{z_i}^2$ with respect to p is equal to the derivative of the Lagrangian function if and only if the derivatives with respect to Σ_q and L_i are equal to zero. (See [40].)

$$\frac{\partial \sigma_{z_i}^2}{\partial p} = \left.\frac{\partial \left(\sigma_{z_i}^2\right)^*}{\partial p}\right|_{\frac{\partial \left(\sigma_{z_i}^2\right)^*}{\partial L_i}=0,\, \frac{\partial \left(\sigma_{z_i}^2\right)^*}{\partial \Sigma_q}=0} \qquad (4.13)$$

The derivative with respect to L_i is

$$\frac{\partial \left(\sigma_{z_i}^2\right)^*}{\partial L_i} = \frac{\partial}{\partial L_i}\text{trace}\left[L_i\left(A_{zd}\Sigma_q + \Sigma_q A_{zd}^T + B_{zd}B_{zd}^T\right)\right] \tag{4.14}$$

$$= \frac{\partial}{\partial L_i}\text{trace}\left[L_i\ A_{zd}\Sigma_q\right] + \frac{\partial}{\partial L_i}\text{trace}\left[L_i\ \Sigma_q A_{zd}^T\right]$$

$$+ \frac{\partial}{\partial L_i}\text{trace}\left[L_i\ B_{zd}B_{zd}^T\right] = 0 \tag{4.15}$$

The following matrix derivative formula from [88] is helpful in simplifying Eq. 4.15 further.

$$\frac{\partial}{\partial X}\text{trace}\left[AXB\right] = \frac{\partial}{\partial X}\text{trace}\left[BAX\right] = \frac{\partial}{\partial X}\text{trace}\left[XBA\right] = A^T B^T \tag{4.16}$$

Applying Eq. 4.16 to Eq. 4.15 and making use of the fact that Σ_q is symmetric leads to

$$\frac{\partial \left(\sigma_{z_i}^2\right)^*}{\partial L_i} = \Sigma_q A_{zd}^T + A_{zd}\Sigma_q + B_{zd}B_{zd}^T = 0 \tag{4.17}$$

This just recovers the Lyapunov constraint equation in Eq. 4.7.

The derivative of Eq. 4.12 with respect to Σ_q is

$$\frac{\partial \left(\sigma_{z_i}^2\right)^*}{\partial \Sigma_q} = \frac{\partial}{\partial \Sigma_q}\text{trace}\left[C_i\Sigma_q C_i^T + L_i\left(A_{zd}\Sigma_q + \Sigma_q A_{zd}^T + B_{zd}B_{zd}^T\right)\right] \tag{4.18}$$

$$= \frac{\partial}{\partial \Sigma_q}\text{trace}\left[C_i\Sigma_q C_i^T\right] + \frac{\partial}{\partial \Sigma_q}\text{trace}\left[L_i\ A_{zd}\Sigma_q\right]$$

$$+ \frac{\partial}{\partial \Sigma_q}\text{trace}\left[L_i\ \Sigma_q A_{zd}^T\right] = 0 \tag{4.19}$$

Applying Eq. 4.16 to Eq. 4.19 and making use of the fact that L_i is symmetric leads to

$$\frac{\partial \left(\sigma_{z_i}^2\right)^*}{\partial \Sigma_q} = C_i^T C_i + L_i A_{zd} + A_{zd}^T L_i = 0 \tag{4.20}$$

As can be seen, this produces another Lyapunov equation that is used to determine L_i.

$$L_i A_{zd} + A_{zd}^T L_i + C_i^T C_i = 0 \tag{4.21}$$

This can be recognized as a dual form of the standard Lyapunov equation given in Eq. 4.7.

Taking the derivative of Eq. 4.12 with respect to p leads to

$$\frac{\partial \sigma_{z_i}^2}{\partial p} = \text{trace}\left[\Sigma_q \frac{\partial (C_i^T C_i)}{\partial p}\right] + \text{trace}\left[L_i\left(\frac{\partial A_{zd}}{\partial p}\Sigma_q + \Sigma_q \frac{\partial A_{zd}^T}{\partial p} + \frac{\partial (B_{zd}B_{zd}^T)}{\partial p}\right)\right] \tag{4.22}$$

Note: The following identity was used in the process of obtaining Eq. 4.22.

$$\text{trace}\left[C_i\Sigma_q C_i^T\right] = \text{trace}\left[\Sigma_q C_i^T C_i\right] \tag{4.23}$$

In performance modeling, the actual performance might be equal to a weighted sum of individual system outputs. For example, let the performance "cost" J be defined as

$$
\begin{aligned}
J &= E\left[z^T z\right] \\
&= \operatorname{trace}\left[E\left[zz^T\right]\right] \\
&= \operatorname{trace}\left[E\left[C_{zd}qq^T C_{zd}^T\right]\right] \\
&= \operatorname{trace}\left[C_{zd}E\left[qq^T\right]C_{zd}^T\right] \\
&= \operatorname{trace}\left[C_{zd}\Sigma_q C_{zd}^T\right]
\end{aligned}
\tag{4.24}
$$

The sensitivity of J can be obtained by following a similar procedure as has just been described. The resulting equation is

$$
\frac{\partial J}{\partial p} = \operatorname{trace}\left[\Sigma_q \frac{\partial(C_{zd}^T C_{zd})}{\partial p}\right] + \operatorname{trace}\left[L\left(\frac{\partial A_{zd}}{\partial p}\Sigma_q + \Sigma_q \frac{\partial A_{zd}^T}{\partial p} + \frac{\partial(B_{zd}B_{zd}^T)}{\partial p}\right)\right]
\tag{4.25}
$$

In this situation, there is only one Lagrange multiplier matrix L, and it is the solution of

$$
LA_{zd} + A_{zd}^T L + C_{zd}^T C_{zd} = 0
\tag{4.26}
$$

As before, Σ_q is the solution of Eq. 4.7.

In summary, Eq. 4.22 is used to obtain the exact sensitivity $\frac{\partial \sigma_{z_i}^2}{\partial p}$. It requires the solution of two Lyapunov equations (one for L_i and one for Σ_q) as well as the computation of the derivatives of the system state-space matrices with respect to the parameter p. The next section will specialize the results to the case when p is a modal parameter that appears explicitly in A_{zd}. Section 4.5 will then take the results one step further by allowing p to be a physical parameter of the finite-element model.

4.3   Modal Parameter Sensitivities

4.3.1   Structural modal form

When dealing with large order structural models, it is convenient to transform to modal coordinates prior to creating the open-loop state-space system in Eq. 4.2. The standard equation of motion of a discretized structural system in physical coordinates is

$$
M\ddot{x} + C\dot{x} + Kx = \beta_u u + \beta_w w
\tag{4.27}
$$

where M is the mass matrix, C is the damping matrix, K is the stiffness matrix, and β_u and β_w map the control inputs u and disturbances w to the physical degrees of freedom. Sensor and performance outputs can also typically be expressed as linear combinations of the physical DOF's.

$$y \;=\; C_{yx}x \tag{4.28}$$

$$z \;=\; C_{zx}x \tag{4.29}$$

where C_{yx} and C_{zx} map the physical DOF's in x to the outputs of interest. Note that no feedthrough of disturbances (including sensor noise) to the sensors or performances is included; however, this can be done explicitly if desired.

The mode shapes and natural frequencies are obtained from the generalized eigenproblem

$$K\tilde{\Phi} = M\tilde{\Phi}\tilde{\Omega}^2 \tag{4.30}$$

where $\tilde{\Phi}$ consists of the mode shapes organized column-wise, and $\tilde{\Omega}^2$ is a diagonal matrix with the squares of the corresponding natural frequencies placed along the diagonal.

$$\tilde{\Omega}^2 = \begin{bmatrix} \ddots & & \\ & \omega_i^2 & \\ & & \ddots \end{bmatrix} \tag{4.31}$$

Usually only a truncated set of mode shapes is used, and the following transformation is made

$$x = \Phi\eta \tag{4.32}$$

where Φ represents a subset of the columns of $\tilde{\Phi}$. After some matrix manipulation, Eq. 4.27 becomes

$$I\ddot{\eta} + 2Z\Omega\dot{\eta} + \Omega^2\eta = \mathcal{M}^{-1}\Phi^T\beta_u u + \mathcal{M}^{-1}\Phi^T\beta_w w \tag{4.33}$$

while Eqs. 4.28 and 4.29 become

$$y \;=\; C_{yx}\Phi\eta \tag{4.34}$$

$$z \;=\; C_{zx}\Phi\eta \tag{4.35}$$

Rewriting in state-space form leads to

$$\underbrace{\begin{Bmatrix} \dot{\eta} \\ \ddot{\eta} \end{Bmatrix}}_{\dot{q}_p} = \underbrace{\begin{bmatrix} 0 & I \\ -\Omega^2 & -2Z\Omega \end{bmatrix}}_{A_p} \underbrace{\begin{Bmatrix} \eta \\ \dot{\eta} \end{Bmatrix}}_{q_p} + \underbrace{\begin{bmatrix} 0 \\ \mathcal{M}^{-1}\Phi^T\beta_u \end{bmatrix}}_{B_u} u + \underbrace{\begin{bmatrix} 0 \\ \mathcal{M}^{-1}\Phi^T\beta_w \end{bmatrix}}_{B_w} w \tag{4.36}$$

$$y = \underbrace{C_{yx}\begin{bmatrix} \Phi & 0 \end{bmatrix}}_{C_y}\left\{\begin{array}{c} \eta \\ \dot{\eta} \end{array}\right\} + \underbrace{0}_{D_{yu}}u + \underbrace{0}_{D_{yw}}w \tag{4.37}$$

$$z = \underbrace{C_{zx}\begin{bmatrix} \Phi & 0 \end{bmatrix}}_{C_z}\left\{\begin{array}{c} \eta \\ \dot{\eta} \end{array}\right\} + \underbrace{0}_{D_{zu}}u + \underbrace{0}_{D_{zw}}w \tag{4.38}$$

All of the D terms are zeros because of the assumptions that have been made. Proportional damping is specified, which implies that Z is a diagonal matrix whose ith diagonal element is the modal damping ratio ζ_i of the ith mode in Φ.

$$Z = \begin{bmatrix} \ddots & & \\ & \zeta_i & \\ & & \ddots \end{bmatrix} \tag{4.39}$$

The diagonal matrix Ω contains the natural frequencies of the kept modes. The diagonal matrix $\mathcal{M}$ is the modal mass matrix and is computed from $\Phi^T M \Phi$.

$$\mathcal{M} = \begin{bmatrix} \ddots & & \\ & m_i & \\ & & \ddots \end{bmatrix} \tag{4.40}$$

The mode shapes can be mass-normalized such that $\mathcal{M}$ is nominally the identity matrix. Substituting Eq. 4.36 and Eq. 4.37 into the state-space model in Eq. 4.5 results in an A_{zd} matrix of the form

$$A_{zd} = \begin{bmatrix} \begin{bmatrix} A_d \\ \begin{bmatrix} 0 \\ \mathcal{M}^{-1}\Phi^T\beta_w \\ 0 \end{bmatrix} C_d \end{bmatrix} & \begin{bmatrix} 0 \\ \begin{bmatrix} 0 & I \\ -\Omega^2 & -2Z\Omega \end{bmatrix} \\ B_c C_{yx}\begin{bmatrix} \Phi & 0 \end{bmatrix} \end{bmatrix} & \begin{bmatrix} 0 \\ \begin{bmatrix} 0 \\ \mathcal{M}^{-1}\Phi^T\beta_u \end{bmatrix} C_c \\ A_c \end{bmatrix} \end{bmatrix} \tag{4.41}$$

and a C_{zd} matrix of the form

$$C_{zd} = \begin{bmatrix} 0 & C_{zx}\begin{bmatrix} \Phi & 0 \end{bmatrix} & 0 \end{bmatrix} \tag{4.42}$$

For a given mode number i, the associated modal parameters are m_i, ζ_i, and ω_i. All three of these quantities appear explicitly in the A_{zd} matrix given by Eq. 4.41, but do not appear explicitly in C_{zd}. The only modal information in C_{zd} is contained in the mode shape matrix Φ.

4.3.2 Simplification of governing equation

Analyzing Eq. 4.22, we notice that the computation of the sensitivity is straightforward if the parameter p appears in any of the matrices A_{zd}, B_{zd}, and C_i. Consider first the case when p is a modal parameter, namely either the natural frequency ω, damping ratio ζ, or modal mass m of an open-loop mode. These parameters only appear in the A_{zd} matrix, as can be seen in Eq. 4.41. Thus, Eq. 4.22 reduces to

$$\frac{\partial \sigma_{z_i}^2}{\partial p} = \text{trace}\left[L_i \left(\frac{\partial A_{zd}}{\partial p} \Sigma_q + \Sigma_q \frac{\partial A_{zd}^T}{\partial p} \right) \right] \tag{4.43}$$

Eq. 4.43 is used to determine the sensitivity of the variance $\sigma_{z_i}^2$. What is actually desired is the sensitivity of the RMS value σ_{z_i}. This can be derived by applying the following simple rule from calculus.

$$\frac{\partial \left[f^2(x) \right]}{\partial x} = 2f(x)\frac{\partial \left[f(x) \right]}{\partial x} \tag{4.44}$$

$$\Rightarrow \quad \frac{\partial \left[f(x) \right]}{\partial x} = \frac{1}{2f(x)}\frac{\partial \left[f^2(x) \right]}{\partial x} \tag{4.45}$$

Therefore, the sensitivity of a performance RMS value is given by

$$\frac{\partial \sigma_{z_i}}{\partial p} = \frac{1}{2\sigma_{z_i}}\frac{\partial \sigma_{z_i}^2}{\partial p} \tag{4.46}$$

$$= \frac{1}{2\sigma_{z_i}}\text{trace}\left[L_i \left(\frac{\partial A_{zd}}{\partial p} \Sigma_q + \Sigma_q \frac{\partial A_{zd}^T}{\partial p} \right) \right] \tag{4.47}$$

Since only modal parameters are being considered at this point, the parameters p can be defined as

$$p \in \left[\begin{array}{ccc} \omega_j & \zeta_j & m_j \end{array} \right] \tag{4.48}$$

where $j = 1, \ldots, \#$ of modes. Although entries of the mode shape vector ϕ_j are not included, the following derivation can be easily extended to handle these parameters.

The matrix derivatives needed in Eq. 4.47 are $\frac{\partial A_{zd}}{\partial \omega_j}$, $\frac{\partial A_{zd}}{\partial \zeta_j}$, and $\frac{\partial A_{zd}}{\partial m_j}$. These derivatives can be determined by inspection, and they are

$$\frac{\partial A_{zd}}{\partial \omega_j} = \left[\begin{array}{cccc} 0 & 0 & & 0 \\ 0 & \left[\begin{array}{c} 0 \\ \quad \end{array} \right. & 0 & & 0 \\ 0 & \left[\begin{array}{ccc} 0 & & \\ & -2\omega_j & \\ & & 0 \end{array} \right] & \left[\begin{array}{ccc} 0 & & \\ & -2\zeta_j & \\ & & 0 \end{array} \right] & 0 \\ 0 & & 0 & & 0 \end{array} \right] \tag{4.49}$$

$$\frac{\partial A_{zd}}{\partial \zeta_j} = \begin{bmatrix} 0 & 0 & 0 \\ 0 & \begin{bmatrix} 0 & 0 \\ \begin{bmatrix} 0 \\ 0 \\ 0 \end{bmatrix} & \begin{bmatrix} 0 \\ -2\omega_j \\ 0 \end{bmatrix} \end{bmatrix} & 0 \\ 0 & 0 & 0 \end{bmatrix} \qquad (4.50)$$

$$\frac{\partial A_{zd}}{\partial m_j} = \begin{bmatrix} 0 & 0 & 0 \\ \begin{bmatrix} \begin{bmatrix} 0 \\ -\phi_j^T \beta_w \\ 0 \end{bmatrix} \end{bmatrix} C_d & \begin{bmatrix} 0 & 0 \\ 0 & 0 \end{bmatrix} & \begin{bmatrix} 0 \\ -\phi_j^T \beta_u \end{bmatrix} C_c \\ 0 & 0 & 0 \end{bmatrix} \qquad (4.51)$$

The matrix derivatives with respect to ω_j and ζ_j consist entirely of zeros except at the locations where those specified modal parameters appear. For the case of the modal mass sensitivities, the matrix derivatives are only slightly more complicated. In addition, notice that the modal masses are assumed to be nominally equal to one because of the mass-normalization of the mode shapes.

In order to compare sensitivities taken with respect to parameters of different units (as is the case when the parameters are frequency and damping), compute a normalized sensitivity as follows.

$$\frac{p_{\text{nom}}}{(\sigma_{z_i})_{\text{nom}}} \frac{\partial \sigma_{z_i}}{\partial p} = \frac{\frac{\partial \sigma_{z_i}}{(\sigma_{z_i})_{\text{nom}}}}{\frac{\partial p}{p_{\text{nom}}}} \approx \frac{\frac{\Delta \sigma_{z_i}}{(\sigma_{z_i})_{\text{nom}}}}{\frac{\Delta p}{p_{\text{nom}}}} \approx \frac{\% \text{ change in } \sigma_{z_i}}{\% \text{ change in } p} \qquad (4.52)$$

This normalized sensitivity indicates the percent change in the performance RMS for a small percent change in the parameter. For instance, a normalized sensitivity value of -0.75 with respect to the frequency of a particular mode implies that a 1% increase in the frequency will result in a 0.75% *decrease* in the RMS value. Although a 1% parameter change might be large enough such that the constant sensitivity approximation is invalid, comparing normalized sensitivities in this manner still provides a sense of the relative influence of the parameters on the performance metric.

Instead of computing the sensitivity exactly, another approach is to approximate the derivative with a simple finite difference. The parameter p is changed by an amount Δp, and the change $\Delta \sigma_{z_i}$ in the RMS value is computed after the disturbance analysis is performed

Table 4.1: Number of Lyapunov equations needed for exact and approximate sensitivity calculations. n_s is the number of states in A_{zd}.

Method	Comments	# of Lyap. equations
Exact	• 1 order n_s Lyap. equation to obtain nominal Σ_q	
	• 1 order n_s Lyap. equation to obtain L_i for each z_i	$1 + n_z$
Finite difference	• 1 order n_s Lyap. equation to obtain nominal Σ_q	
	• 1 order n_s Lyap. equation to obtain Σ_q for every perturbed parameter	$1 + n_p$

again. The sensitivity is then given by the approximation

$$\frac{\partial \sigma_{z_i}}{\partial p} \approx \frac{\Delta \sigma_{z_i}}{\Delta p} \tag{4.53}$$

Table 4.1 compares the computational expense involved in calculating either the exact or approximate sensitivities of all n_z performance metrics with respect to a total of n_p modal parameters for a system of order n_s. It is assumed that the majority of the expense comes from solving the Lyapunov equation, so it is sufficient to compare the number of Lyapunov equations that need to be solved. For instances when there are more parameters than performance metrics, it appears as if it is more efficient to compute the sensitivities analytically. Otherwise, the finite-difference approach can yield significant time savings, but the results are only approximate, and as will be shown later, the finite-difference method can be numerically ill-conditioned for large-order problems.

4.4 Demonstration of Modal Parameter Sensitivity Analysis

This section shows sample sensitivity analysis results for systems of varying order. A single DOF spring-mass system is considered first. This is followed by a multi-DOF spring-mass system with 20 masses. The section concludes with a demonstration of the analysis on a model of SIM Classic.
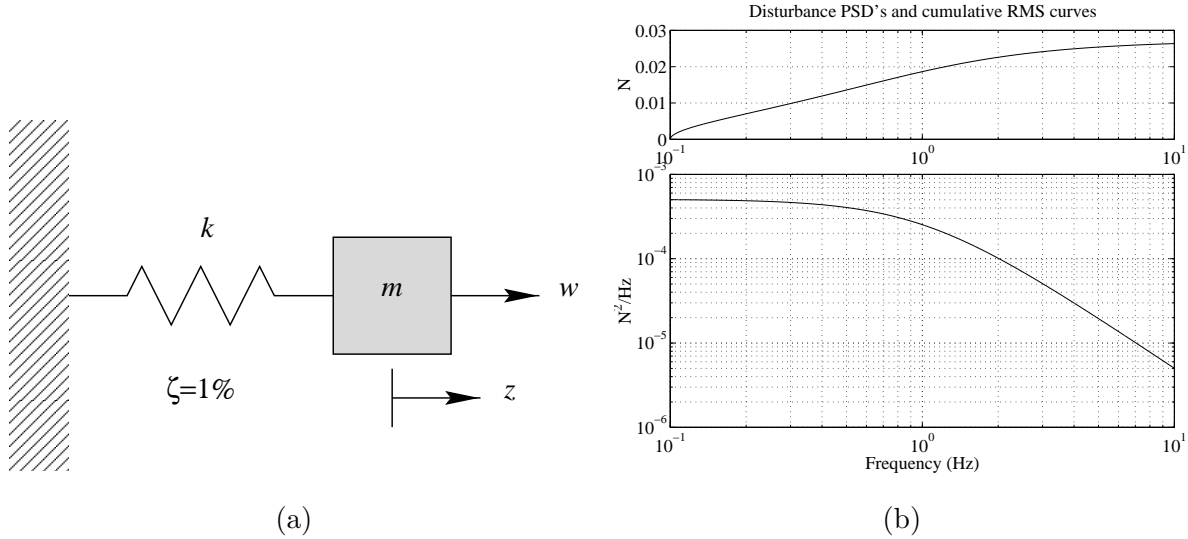
Figure 4.2: (a) Single DOF system. (b) Disturbance PSD (bottom) and cumulative RMS (top).

4.4.1 Single DOF system

The simple mass-spring system of Figure 4.2(a) is identical to the one presented in Section 3.2. The mass and stiffness values were chosen to obtain a natural frequency of 1 Hz, and the modal damping is 1%. Recall that the performance is the position of the mass, and the disturbance force w acts on the mass. This force is the output of a first-order system driven by unit-intensity white noise. The PSD of the disturbance is shown in Figure 4.2(b). Plotted above the disturbance PSD is the cumulative RMS curve.

Placing the disturbance filter in series with the plant leads to a form equivalent to Eq. 4.6. Solving the Lyapunov equation given by Eq. 4.7 yields the state covariance matrix Σ_q, which can then be substituted into Eq. 4.8 to determine the performance covariance matrix Σ_z. Since there is only one performance metric in this case, Σ_z is a scalar and equals the variance σ_z^2. For the specific numerical values in this problem, the RMS turns out to be about 3.6 mm. The normalized sensitivities of this value with respect to the natural frequency, damping ratio, and modal mass can be determined by solving for the Lagrange multiplier matrix from Eq. 4.21 and then applying Eqs. 4.47–4.52.

The results are presented in bar chart form in Figure 4.3. The horizontal axis represents the normalized sensitivity, and the vertical axis represents the open-loop mode with which the modal parameters are associated. The mode is identified by its undamped natural frequency. The values of the black, gray, and white bars are the normalized sensitivities

114
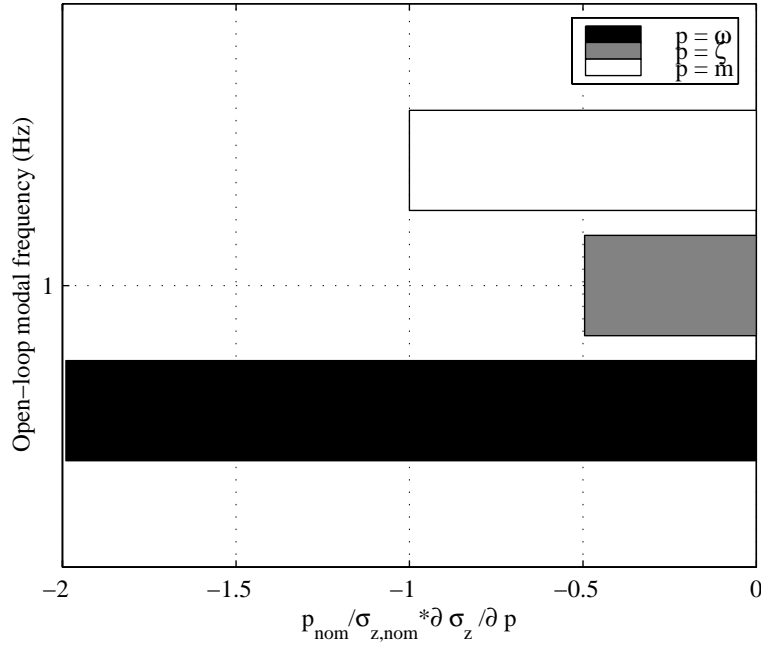
Figure 4.3: Normalized sensitivities of SDOF system performance with respect to modal parameters.

with respect to the natural frequency, damping ratio, and modal mass, respectively. All three sensitivities are negative, which indicates that an increase in any parameter will cause the RMS to decrease. However, the RMS sensitivity to the frequency is about four times larger than the damping sensitivity and about twice as large as the modal mass sensitivity. The bar chart indicates that raising the frequency by 1% will lower the RMS by 2%. Of course in reality, the frequency cannot be changed directly. Rather, only physical properties of the system (*e.g.*, stiffness, mass) can be modified to affect the frequency. Another item of practicality is that even though the sensitivities have been normalized to address the issue of units, they still might not be comparable. For instance, does a 1% change in frequency "equal" a 1% change in damping? If the sensitivities are to be used to identify parameters for redesign, then an additional normalization step should be done that takes into account engineering judgment to "equalize" parameter changes based on the apparent "cost" of varying the parameters. For example, a 10% change in damping might be deemed to require the same amount of resources as a 2% change in the frequency. If the sensitivities are to be used to identify parameters for an uncertainty analysis, then the additional normalization step might incorporate the uncertainty range for each parameter.

Figure 4.4: Magnitudes of the percent errors in the finite-difference approximation to the sensitivities with respect to frequency (left) and damping (right) as a function of parameter perturbation size.

Validation of the analytical sensitivities shown in Figure 4.3 involved computing a finite-difference approximation (Eq. 4.53) by perturbing each parameter and determining the resulting change in the RMS value. The magnitude of the percent error between the finite-difference value and the exact value is shown as a function of perturbation size in Figure 4.4. The errors in the sensitivities with respect to frequency and damping decrease as the perturbation size becomes smaller. This is expected because the $\frac{\Delta \sigma_{z_i}}{\Delta p}$ approximation to the derivative should approach the exact answer in the limit as Δp approaches 0. In reality, numerical precision limitations can arise, and this might explain the "kink" in the curves at a perturbation size of about $10^{-5}\%$.

4.4.2 Multi-DOF system

To demonstrate the method on a slightly more complicated system, the 20 mass/19 spring example problem in Figure 4.5(a) was created. Each mass and spring constant was randomly selected from a specified interval. Modal damping was uniformly assigned a value of 0.1%. There are six disturbance input locations at DOF's 7 through 12. The performance metric is the differential motion of the two end masses (*i.e.*, $z = x_{20} - x_1$). The PSD's of the six disturbances are shown in Figure 4.5(b). They are bandpass in nature, with the peak magnitude occurring at 100 Hz and the low and high frequency asymptotes having values of $+4$ and -4, respectively. Only two curves are visible because the first three disturbance PSD's overlap to form the larger magnitude curve, and the last three overlap to form the

smaller magnitude curve. The disturbance filter that created the PSD's in Figure 4.5(b) was augmented to the spring/mass system's state-space representation. The frequency-domain disturbance analysis discussed in Section 3.1.2 was used to create the plot in Figure 4.5(c), which shows the PSD of the performance metric and its corresponding cumulative RMS curve. The modal parameters associated with the first three modes were selected for the sensitivity analysis because the largest contributions to the RMS are due to these modes. The normalized sensitivities are presented in Figure 4.5(d), and the largest one corresponds to the frequency of the third mode. All the normalized sensitivities are negative, and the first mode is unique in that the sensitivity with respect to modal mass is larger in magnitude than the sensitivity with respect to frequency.

Figure 4.6 shows the comparison between the exact sensitivities and the approximate finite-difference sensitivities. Each row of subplots is associated with a particular mode while each column is associated with either the frequency or damping parameter of the mode. (Modal mass sensitivity errors are not shown, but they exhibit a similar trend.) As the perturbation size becomes smaller, the trend is initially the same as that found for the single DOF case. However, a point is reached when the errors start to climb as Δp decreases. Thus, numerical issues arise sooner for this larger order system. Nevertheless, errors on the order of only 0.1% can be achieved by choosing a $\frac{\Delta p}{p}$ of 0.1% for the finite-difference approximation.

4.4.3   SIM Classic

The model used to demonstrate the sensitivity analysis methodology on a realistically-sized problem is the three-baseline integrated model of SIM developed at JPL and described in Chapter 2. Recall that some model parameters are:

- 10 Hz 6-axis isolator (50% damping) at the reaction wheel assembly location (IM-PORTANT NOTE: The SIM model used in this chapter contains a slightly improved isolator model. This results in a small shift in the frequencies of the open-loop modes. The critical frequencies identified in the frequency-domain disturbance analysis of Section 3.3 do not correspond exactly to the critical frequencies identified in this section.)

- 0.1% modal damping for structural modes

- 100 Hz bandwidth on fringe tracking control
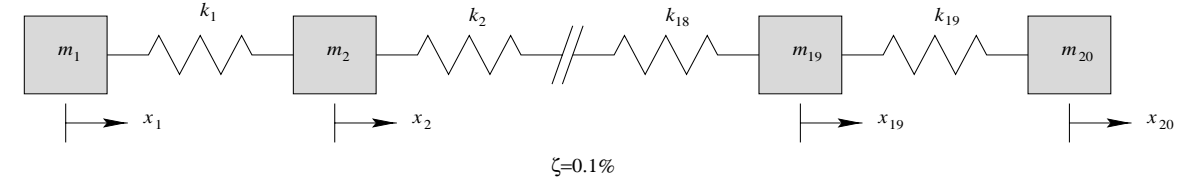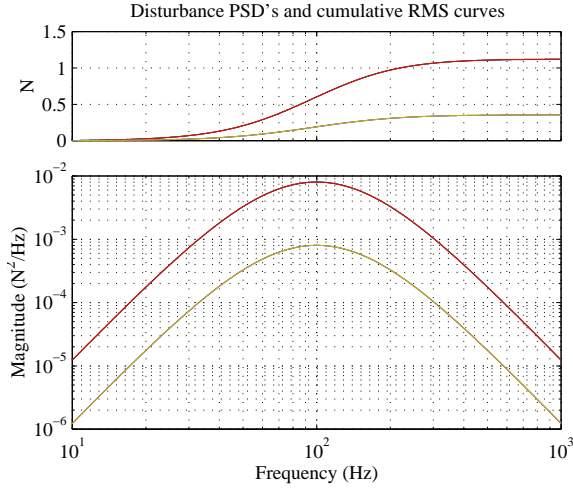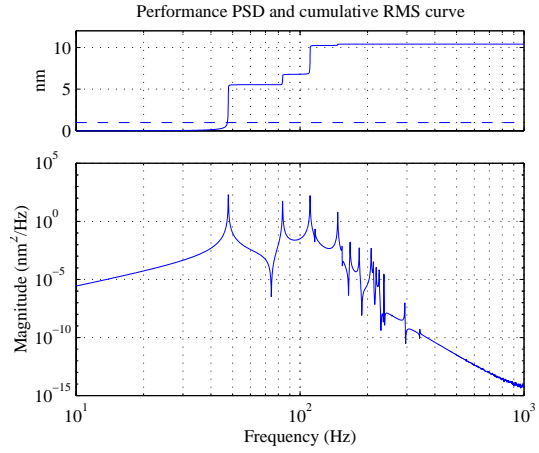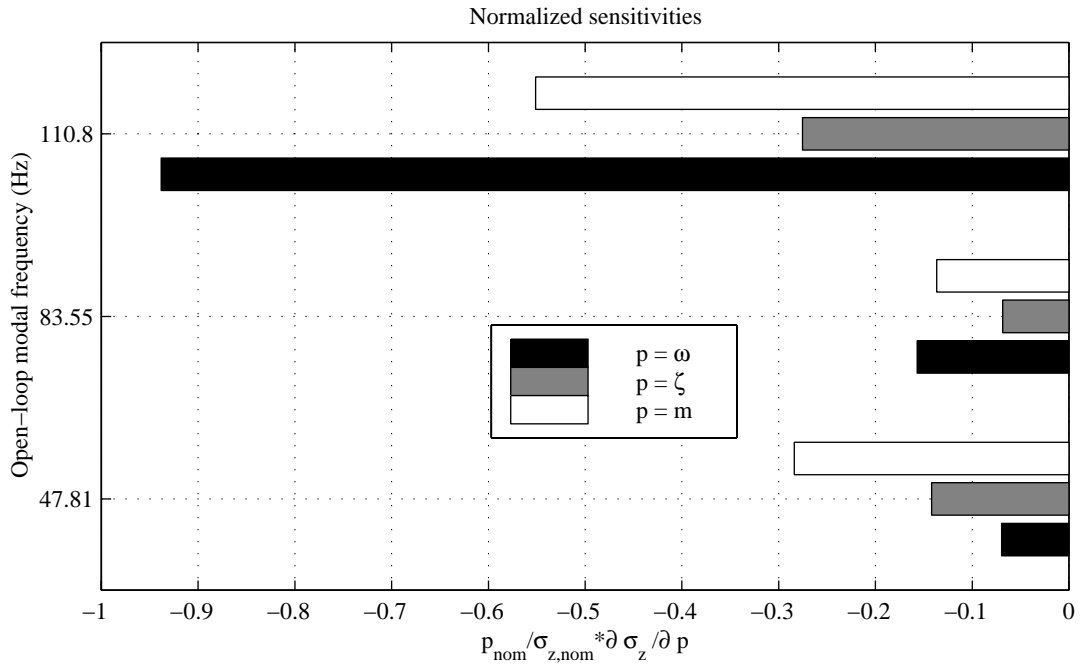
Figure 4.5: (a) 20 DOF spring/mass system. (b) Disturbance PSD's (bottom) and cumulative RMS (top). (c) Performance PSD (bottom) and cumulative RMS (top). (d) Normalized sensitivities of critical modes.
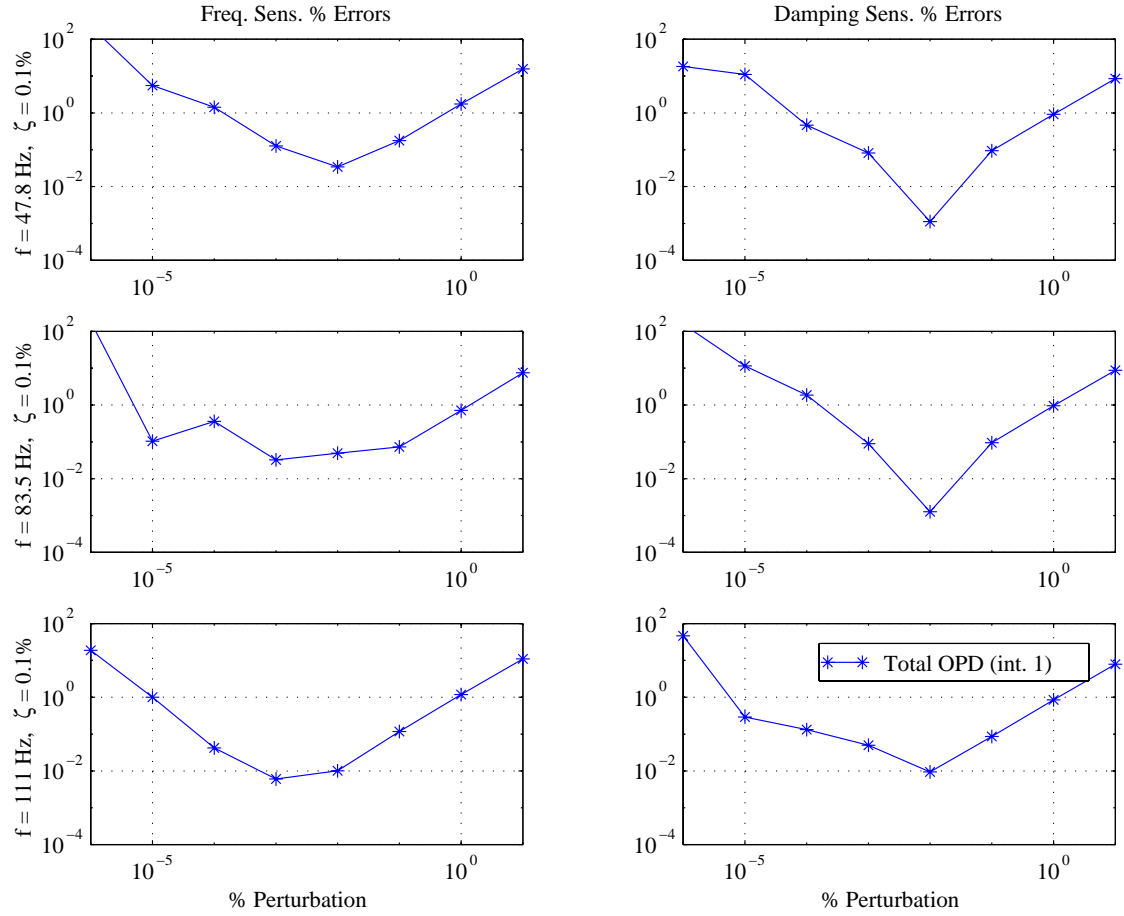
Figure 4.6: Magnitudes of the percent errors in the finite-difference approxima-
tion to the sensitivities with respect to frequency (left) and damping
(right) as a function of parameter perturbation size.

The optical path difference (OPD) of guide interferometer #1 is the performance metric selected for the modal parameter sensitivity analysis.

In order to maintain the explicit modal parameter dependence in A_{zd}, as indicated in Eq. 4.41, the model could not be reduced using a technique such as balanced model reduction [65]. However, since the Lyapunov equation can only be solved for strictly stable systems, the translational rigid-body mode states had to be removed. It was assumed that these modes are unobservable in the optical performance metrics of interest and can be eliminated by a strict truncation. Since SIM constantly undergoes rigid-body translation as it moves through inertial space, this should only cause SIM's siderostats to sample a different portion of the incoming stellar wavefront during an observation. This translation should not affect differential pathlength or wavefront tilt metrics.

The strict truncation of rigid-body mode states led to A_{zd} being of order 307 (= disturbance states + modal states + compensator states). Solving a 307th order Lyapunov equation took on average 110 seconds on a Sun Ultra 1. This is not an unreasonably long computation time, but the restriction on model reduction can pose a problem for higher-order systems. The sensitivity analysis technique that has been described relies on the specific form of A_{zd}. Application to much larger systems will require the technique to be modified so that alternative model reduction approaches can be accommodated.

The reaction wheel assembly (RWA) disturbances are modeled by fourth-order band-pass filters that approximate the analytical PSD's derived in Section 2.2.5. Figure 4.7 plots both the analytical PSD's and the PSD's of the filter. The six disturbances are the three forces and three moments acting at the interface between the RWA and the spacecraft. Note that the PSD's are similar to those used in the multi-DOF case of the previous section.

The sensitivity analysis requires that the disturbances be modeled by shaping filters driven by white noise. The analytical PSD's have a characteristic "sawtooth" shape and can not be represented exactly in state-space form. The "smooth" curves represent a simple, low-order approximation to the more complex PSD's. They are based on a disturbance filter of the form

$$G_d(s) = \frac{As^2}{(s + \omega_o)^4} \tag{4.54}$$

$$G_d(\omega) = \frac{A(j\omega)^2}{(j\omega + \omega_o)^4} \tag{4.55}$$

The approximate disturbance PSD's are therefore of the form

$$
\begin{aligned}
S_{ww}(\omega) &= G_d(\omega)G_d^H(\omega) \\
&= \left[\frac{A(j\omega)^2}{(j\omega + \omega_o)^4} \right] \left[\frac{A(-j\omega)^2}{(-j\omega + \omega_o)^4} \right] \\
&= \frac{A^2\omega^4}{(j\omega + \omega_o)^4(-j\omega + \omega_o)^4}
\end{aligned}
\tag{4.56}
$$

The double zero at $s = 0$ creates the $+4$ slope in the PSD at low frequencies, while the fourth-order pole causes the high frequency slope to be -4. The actual analytical PSD's drop to zero magnitude at the frequency corresponding to the highest harmonic of the maximum wheel speed. A faster roll-off can be achieved in the approximate PSD's by using more poles; however, this comes at the cost of more states in the system. The corner frequency ω_o was arbitrarily chosen to be at the geometric mean of the frequencies of the first and last "drops" in the analytical PSD's. Referring to Figure 4.7, these frequencies are at about $18\,\mathrm{Hz}$ and $720\,\mathrm{Hz}$. This placed the center frequency of the band-pass filter in a location that one might choose by visual inspection. The magnitudes of the filter-based PSD's were chosen such that the overall RMS values matched those of the analytical PSD's. In other words, both the analytical and the approximate PSD's contain the same amount of energy.

It can be seen that the "smooth" filter-based PSD's do not fit the "sawtooth" analytical PSD's extremely well; however, a better result can be achieved with a higher-order shaping filter model. Since the main goal of this section is to demonstrate the sensitivity analysis technique, no further effort was made to obtain a close fit. In practice, further iterations should be made in creating a more accurate disturbance filter model.

Rather than computing sensitivities with respect to parameters of all the modes in the system, a frequency-domain disturbance analysis can be used first to identify which modes are the most critical. The disturbance PSD's are simply those corresponding to the approximate PSD's. They are shown alone in Figure 4.8(a), and the resulting PSD of the OPD is presented in Figure 4.8(b). Also plotted in Figure 4.8(b) is the disturbance contribution plot that indicates which disturbances are dominant across the frequency range. It is based on the approximation that the disturbance cross-spectral density matrix is diagonal. The critical modes from the cumulative variance plot in Figure 4.9(a) are summarized in Figure 4.9(b).
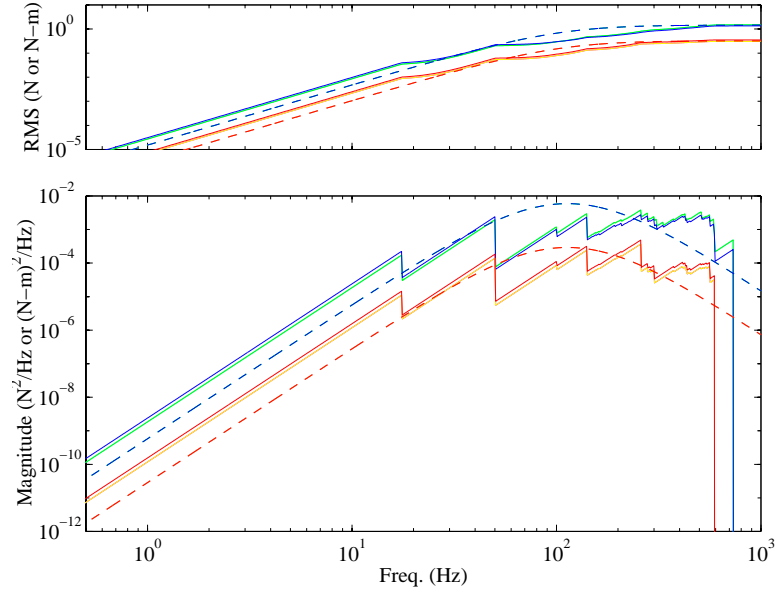
Figure 4.7: Analytical RWA disturbance PSD's and approximate PSD's from low-order filter (bottom). Cumulative RMS curves (top).

(a)   (b)
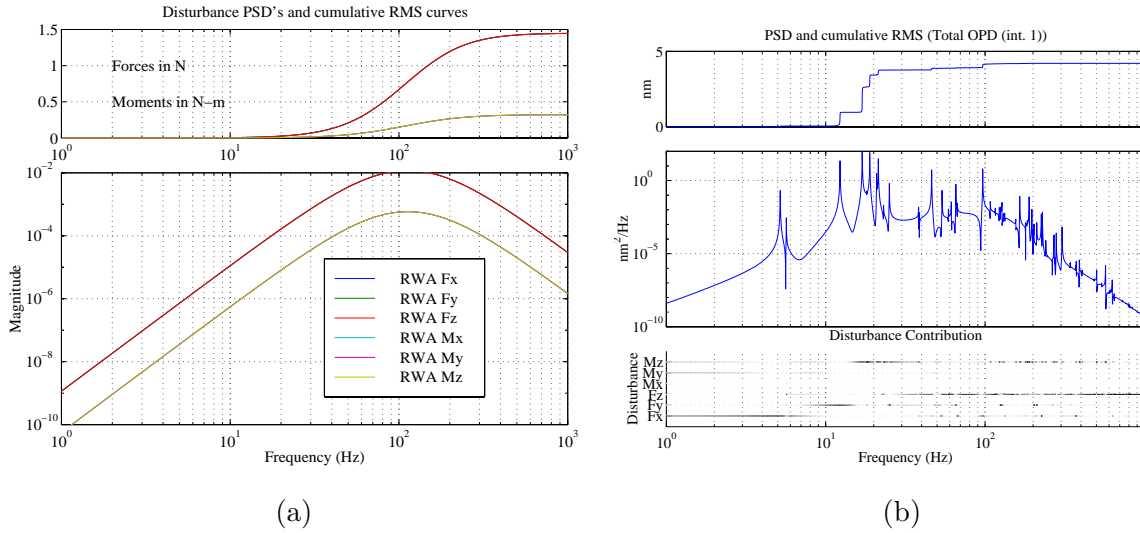
Figure 4.8: (a) Approximate PSD's from low-order filter (bottom), and cumulative RMS curves (top). (b) Performance PSD (middle), cumulative RMS (top), and disturbance contribution (bottom).
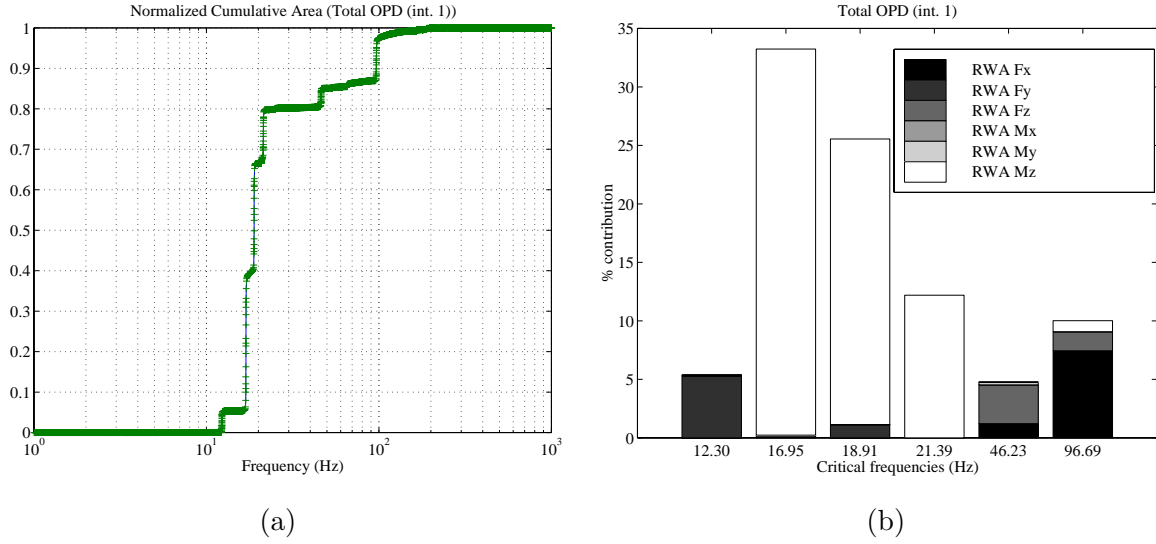
Figure 4.9: (a) Cumulative performance variance. (b) Critical frequencies and disturbances.

The six most critical modes, along with three others, were selected for the sensitivity analysis. Applying Eqs. 4.47–4.52 to this system (after solving Eq. 4.7 and Eq. 4.21) produced the sensitivity results shown in Figure 4.10. The largest sensitivity corresponds to the frequency of the 16.95 Hz mode, and this is consistent with the fact that this mode dominates the response, as indicated in Figure 4.9(b). It is not surprising that there appears to be a correlation between the critical modes in Figure 4.9(b) and the modes with the largest sensitivities in Figure 4.10. This suggests that an alternative means of identifying critical modes is by simply performing a sensitivity analysis with respect to open-loop modal parameters. The three additional non-critical modes carried into the sensitivity analysis have negligible sensitivities, and this further confirms that these modes do not contribute much to the overall RMS value.

It is interesting to note that in this example case, all the sensitivities with respect to frequency are positive. All the sensitivities shown thus far for the SDOF case and the MDOF case were negative, implying that increasing modal frequencies, damping, and mass would improve the performance. This SIM case suggests that increasing the modal frequencies will actually make the OPD performance worse. It is anticipated that as the systems being modeled and analyzed become more complex, non-intuitive results such as this will occur more frequently.
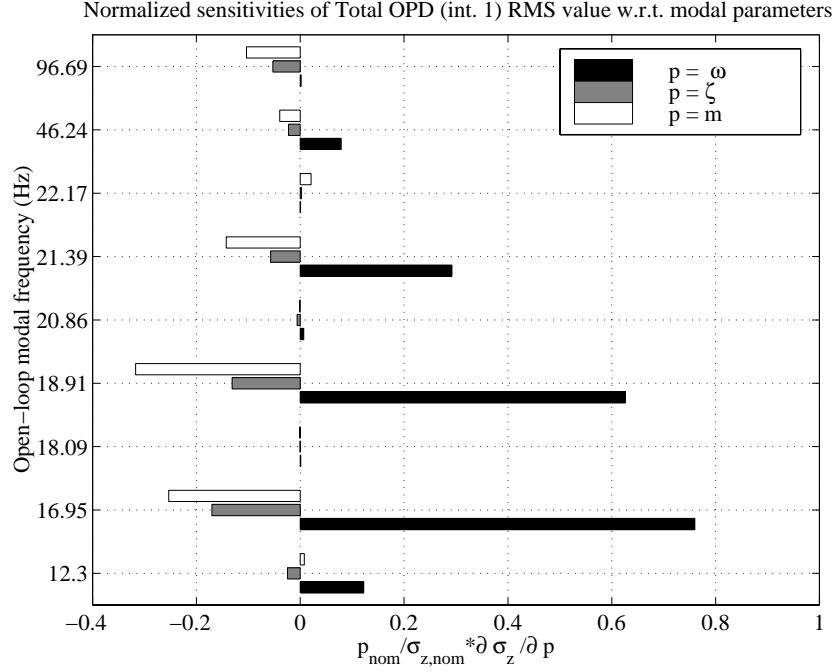
Figure 4.10: Normalized modal parameter sensitivities.

Attempts to validate the analytical sensitivities with finite-difference results did not meet with any success. Figure 4.11 shows the same type of percent error plot as has been shown for the previous two cases. The percent difference between the finite-difference approximations and the analytical results increases drastically as the perturbation size is made smaller. The smallest percent difference is on the order of 10%, and this corresponds to a perturbation size of 10%. For this large-order system, numerical conditioning problems appear to be a major issue. This trend was somewhat evident when going from the one DOF system to the multi-DOF system.

One possible reason for this might be explained as follows. Consider computing the sensitivity with respect to damping by the finite-difference approach. The first step is to solve a 307th order Lyapunov equation to obtain the state covariance matrix. Pre- and post-multiplying by the appropriate C matrix produces the desired mean-square value. The damping ratio for a specified mode is then perturbed by a small amount, and the Lyapunov equation is solved again. So of all the 307^2 entries in the A_{zd} matrix, only one value is changed by a small percent. If the matrix is not well-conditioned, then the solution of the Lyapunov equation might not vary smoothly as the parameter is varied smoothly. This, however, does not explain why the analytical sensitivities do not suffer from poor numerical
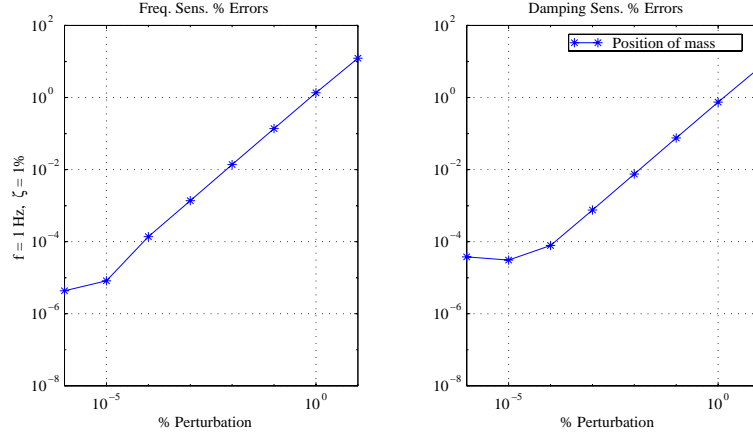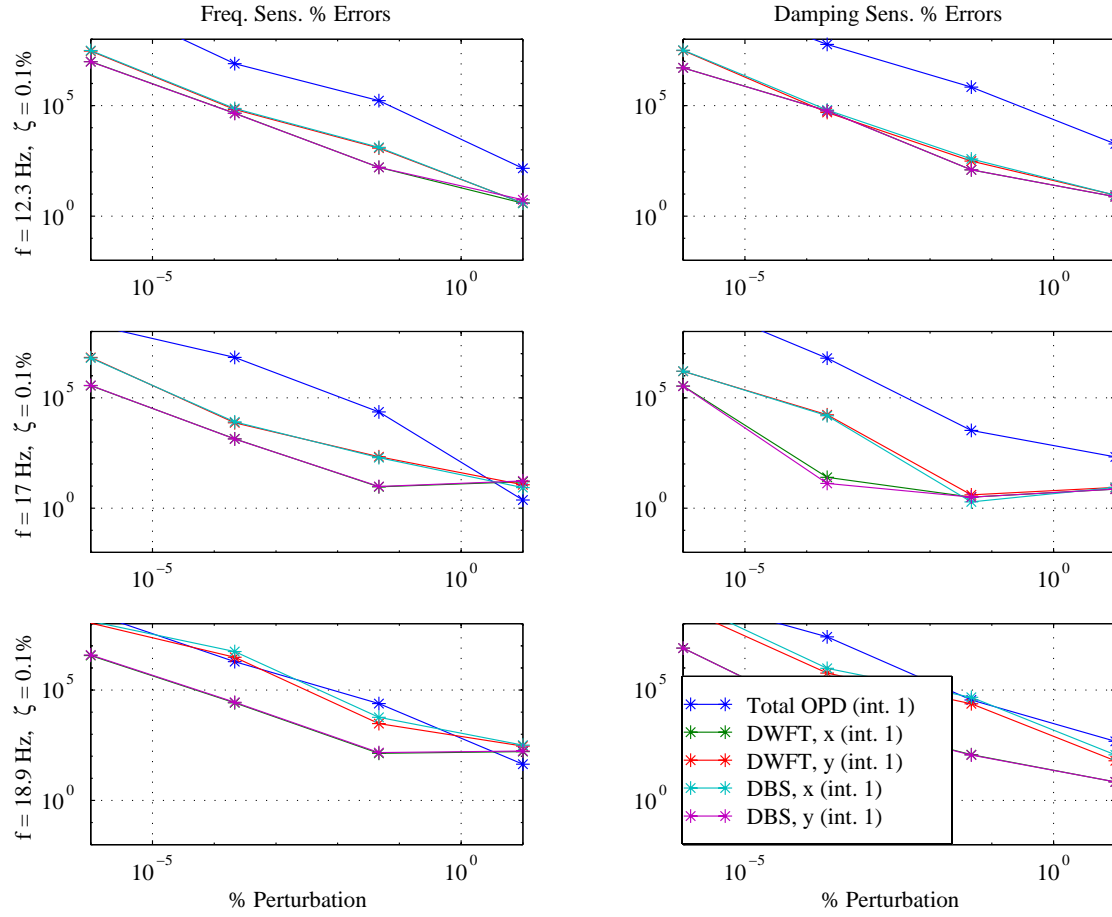
Figure 4.11: Magnitudes of the percent errors in the finite-difference approxima-
tion to the sensitivities with respect to frequency (left) and damping
(right) as a function of perturbation size.

conditioning if it is present. Further investigation into this effect is recommended.

At this point, the results shown in Figure 4.10 cannot be verified, but since the sen-
sitivities are the expected order of magnitude, then some confidence can be placed in the
accuracy of the results. As will be shown in Section 5.4.4, the use of these analytical sensi-
tivities in an example SIM uncertainty analysis yields results that are consistent with those
obtained using another method. This will serve to indirectly validate the sensitivities.

4.5   Physical Parameter Sensitivities

Of particular use in the early design phases of a system is the ability to identify modifications
that can improve the performance of the system. This is especially true when it is discovered

during performance assessment analyses that the nominal design fails to meet specified requirements. Identifying areas for redesign can be made easier if sensitivity information is available. Sensitivities reveal the amount of change in the performance metrics that can be achieved by varying parameters in a model of the system. Parameters with large sensitivities can then be the focus of structural redesigns and/or uncertainty management.

Section 4.3 introduced a method to compute the exact sensitivities with respect to open-loop modal parameters. While these sensitivities do identify which modes are the most important, they do not reveal directly what physical characteristics of the design should be modified to affect the modes and improve the performance. Physical parameter sensitivities are therefore more intuitive, and this fact motivated the efforts to expand the sensitivity analysis to include physical parameters.

The following section presents the mathematics behind computing sensitivities with respect to physical parameters. The model is assumed to be in state-space form, and the general case assumes that disturbance filter and compensator dynamics are also present. As is shown, the derivatives of the finite-element model mode shapes, natural frequencies, and modal masses with respect to the parameters are required. Section 4.5.2 reviews the theory behind eigenvalue and eigenvector derivatives of structural systems with no repeated eigenvalues. The analytical sensitivities are then compared to finite-difference approximations on a simple cantilever beam example. To explore issues faced when dealing with large-order models, an integrated model of SIM Classic is used to demonstrate the technique. Potential simplifications to the sensitivity equations are investigated in order to reduce computational effort.

4.5.1 Derivation of physical parameter sensitivities

In Section 4.1, the overall state-space system was placed into the form

$$
\begin{aligned}
\dot{q} &= A_{zd}\, q + B_{zd}\, d \\
z &= C_{zd}\, q
\end{aligned}
\tag{4.57}
$$

Section 4.3.1 showed that for the case of a structural model in modal coordinates with control loops closed, the state-space matrices are given by

$$A_{zd} = \begin{bmatrix} A_d & 0 & 0 \\ \begin{bmatrix} \begin{bmatrix} 0 \\ \mathcal{M}^{-1}\Phi^T\beta_w \\ 0 \end{bmatrix} \end{bmatrix} C_d & \begin{bmatrix} 0 & I \\ -\Omega^2 & -2Z\Omega \end{bmatrix} & \begin{bmatrix} 0 \\ \mathcal{M}^{-1}\Phi^T\beta_u \end{bmatrix} C_c \\ & B_c C_{yx} \begin{bmatrix} \Phi & 0 \end{bmatrix} & A_c \end{bmatrix} \qquad (4.58)$$

$$B_{zd} = \begin{bmatrix} B_d \\ 0 \\ 0 \end{bmatrix} \qquad (4.59)$$

$$C_{zd} = \begin{bmatrix} 0 & C_{zx} \begin{bmatrix} \Phi & 0 \end{bmatrix} & 0 \end{bmatrix} \qquad (4.60)$$

where

$$
\begin{aligned}
A_d, B_d, C_d &= \text{disturbance filter state-space matrices} \\
A_c, B_c, C_c &= \text{compensator state-space matrices} \\
\Omega, Z, \mathcal{M}, \Phi &= \text{modal frequency, damping, mass, and mode shape matrices} \\
\beta_u, \beta_w &= \text{control and disturbance influence matrices} \\
C_{yx}, C_{zx} &= \text{transformation matrices from FEM physical DOF's} \\
&\qquad \text{to sensor and performance measurements}
\end{aligned}
$$

These matrices are valid when the state vector is ordered as $q^T = \begin{bmatrix} q_d & q_p & q_c \end{bmatrix}^T$, $i.e.$, the disturbance filter states are placed first, followed by the plant modal states and the compensator states. Another assumption is that there is no direct feedthrough of either the disturbances or the control inputs to the performance variables. In other words, $D_{zw} = 0$ and $D_{zu} = 0$, which result in the first and last zeros in the C_{zd} matrix.

For convenience, the sensitivity of the variance of the ith performance metric with respect to the parameter p is repeated here. (It was derived in Section 4.2.)

$$\frac{\partial \sigma_{z_i}^2}{\partial p} = \text{trace} \left[\Sigma_q \frac{\partial (C_i^T C_i)}{\partial p} \right] + \text{trace} \left[L_i \left(\frac{\partial A_{zd}}{\partial p} \Sigma_q + \Sigma_q \frac{\partial A_{zd}^T}{\partial p} + \frac{\partial (B_{zd} B_{zd}^T)}{\partial p} \right) \right] \qquad (4.61)$$

where C_i is the ith row of C_{zd}, and the state covariance matrix Σ_q and the Lagrange multiplier matrix L_i are obtained from the following Lyapunov equations.

$$A_{zd}\Sigma_q + \Sigma_q A_{zd}^T + B_{zd} B_{zd}^T = 0 \qquad (4.62)$$

$$A_{zd}^T L_i + L_i A_{zd} + C_i^T C_i = 0 \tag{4.63}$$

If p is a physical parameter of the finite-element model, then in general it will not appear explicitly in the state-space matrices A_{zd}, B_{zd}, or C_{zd}. However, the mode shapes in Φ, the modal frequencies in Ω , and the modal masses in $\mathcal{M}$ can depend on p. Thus, the parameter dependence can be expressed in functional notation as

$$A_{zd} \rightarrow A_{zd}(\Phi(p), \Omega(p), \mathcal{M}(p)) \tag{4.64}$$

$$C_{zd} \rightarrow C_{zd}(\Phi(p)) \tag{4.65}$$

Notice that the modal damping matrix Z has not been mentioned yet. In most situations, damping is specified in terms of modal damping rather than as a physical damping matrix C. As a result, Z will not be a function of a physical parameter in the model. The damping ratios ζ_i are specified rather than derived. This is the reason why damping parameter dependence will not be carried into the subsequent derivation.

Since B_{zd} is only a function of the disturbance filter B_d matrix, Eq. 4.61 can be simplified to

$$\frac{\partial \sigma_{z_i}^2}{\partial p} = \text{trace}\left[\frac{\partial C_i}{\partial p}\Sigma_q C_i^T + C_i \Sigma_q \frac{\partial C_i^T}{\partial p}\right] + \text{trace}\left[L_i\left(\frac{\partial A_{zd}}{\partial p}\Sigma_q + \Sigma_q \frac{\partial A_{zd}^T}{\partial p}\right)\right] \tag{4.66}$$

The matrix derivatives $\frac{\partial C_i}{\partial p}$, $\frac{\partial A_{zd}}{\partial p}$, and their transposes need to be computed. By invoking the chain rule based on the parameter dependence expressed in Eq. 4.64 and Eq. 4.65, the derivatives can be written as

$$\frac{\partial A_{zd}}{\partial p} = \sum_{j=1}^{N}\left(\underbrace{\frac{\partial A_{zd}}{\partial \omega_j}}_{\dagger}\underbrace{\frac{\partial \omega_j}{\partial p}}_{\ddagger} + \underbrace{\frac{\partial A_{zd}}{\partial m_j}}_{\dagger}\underbrace{\frac{\partial m_j}{\partial p}}_{\ddagger} + \sum_{i=1}^{n}\underbrace{\frac{\partial A_{zd}}{\partial \Phi_{ij}}}_{\dagger}\underbrace{\frac{\partial \Phi_{ij}}{\partial p}}_{\ddagger} \right) \tag{4.67}$$

$$\frac{\partial C_{zd}}{\partial p} = \sum_{j=1}^{N}\sum_{i=1}^{n}\underbrace{\left[\begin{array}{ccc} 0 & \frac{\partial C_z}{\partial \Phi_{ij}} & 0 \end{array}\right]}_{\dagger}\underbrace{\frac{\partial \Phi_{ij}}{\partial p}}_{\ddagger} \tag{4.68}$$

where N is the number of modes in Φ, and n is the number of degrees of freedom. Recall that the matrices Ω and $\mathcal{M}$ in Eq. 4.58 are diagonal.

$$\Omega = \begin{bmatrix} \ddots & & \\ & \omega_j & \\ & & \ddots \end{bmatrix}, \ \mathcal{M} = \begin{bmatrix} \ddots & & \\ & m_j & \\ & & \ddots \end{bmatrix} \ \text{where } j = 1, 2, \ldots, N \tag{4.69}$$

At this point, it is apparent that two types of derivatives are required. The first type involves state-space matrix derivatives with respect to frequencies, mode shapes, and modal masses (*e.g.*, $\frac{\partial A_{zd}}{\partial \omega_j}$, $\frac{\partial A_{zd}}{\partial m_j}$, $\frac{\partial A_{zd}}{\partial \Phi_{ij}}$, and $\frac{\partial C_{zd}}{\partial \Phi_{ij}}$). They are indicated by a † in Eqs. 4.67 and 4.68. The second type involves the mode shape, frequency, and modal mass derivatives, namely $\frac{\partial \Phi_{ij}}{\partial p}$, $\frac{\partial \omega_j}{\partial p}$ and $\frac{\partial m}{\partial p}$. These are indicated by a ‡ in Eqs. 4.67 and 4.68. The first type will be examined next, and Section 4.5.2 will discuss the mode shape, frequency, and modal mass derivatives.

First examine the computation of $\frac{\partial A_{zd}}{\partial \omega_j}$ and $\frac{\partial A_{zd}}{\partial m_j}$. If A_{zd} is of the form shown in Eq. 4.58, then these derivatives are very straightforward to compute. In fact, they were required in Section 4.3.2 for the sensitivities with respect to modal parameters, and the results shown in Eq. 4.49 and Eq. 4.51 are repeated here.

$$\frac{\partial A_{zd}}{\partial \omega_j} = \begin{bmatrix} 0 & 0 & 0 \\ 0 & \begin{bmatrix} \begin{bmatrix} 0 & & \\ & -2\omega_j & \\ & & 0 \end{bmatrix} \end{bmatrix} & \begin{bmatrix} 0 & & \\ & -2\zeta_j & \\ & & 0 \end{bmatrix} & 0 \\ 0 & 0 & 0 \end{bmatrix} \tag{4.70}$$

$$\frac{\partial A_{zd}}{\partial m_j} = \begin{bmatrix} \begin{bmatrix} \begin{bmatrix} 0 \\ -\phi_j^T \beta_w \\ 0 \end{bmatrix} \end{bmatrix} C_d & \begin{bmatrix} 0 & 0 \\ 0 & 0 \end{bmatrix} & \begin{bmatrix} 0 \\ -\phi_j^T \beta_u \\ 0 \end{bmatrix} C_c \end{bmatrix} \tag{4.71}$$

It is important to note that when using numerical software such as MATLAB, sparse matrices can be used to alleviate the storage requirements of a matrix comprised almost entirely of zeros. This also helps to reduce the time required to perform matrix manipulations.

The derivatives with respect to Φ_{ij} can also be obtained by inspection. If we make the standard assumption that the mode shapes are mass normalized such that $\mathcal{M} = I$, then

$$\frac{\partial A_{zd}}{\partial \Phi_{ij}} = \begin{bmatrix} \begin{bmatrix} \begin{bmatrix} 0 \\ (1_{i,j}^{n \times N})^T \beta_w \\ 0 \end{bmatrix} \end{bmatrix} C_d & \begin{bmatrix} 0 & 0 \\ 0 & 0 \end{bmatrix} & \begin{bmatrix} 0 \\ (1_{i,j}^{n \times N})^T \beta_u \\ 0 \end{bmatrix} C_c \\ & B_c C_{yx} \begin{bmatrix} (1_{i,j}^{n \times N}) & 0 \end{bmatrix} & \end{bmatrix} \tag{4.72}$$

$$\frac{\partial C_{zd}}{\partial \Phi_{ij}} = \begin{bmatrix} 0 & C_{zx} \begin{bmatrix} (1_{i,j}^{n \times N}) & 0 \end{bmatrix} & 0 \end{bmatrix} \tag{4.73}$$

where the notation $(1_{i,j}^{n \times N})$ is used to designate an $n \times N$ matrix whose only nonzero entry has a value of 1 at the ith row and jth column.

Although these derivatives are relatively easy to derive, the real expense is apparent when one considers the number of these derivatives that is required, especially for those with respect to the elements of the mode shape matrix. Eq. 4.67 and Eq. 4.68 indicate that $\frac{\partial A_{zd}}{\partial \Phi_{ij}}$ and $\frac{\partial C_{zd}}{\partial \Phi_{ij}}$ must be evaluated a total of $n \times N$ times each. For a realistically sized problem, N might be on the order of 100 while n might be on the order of 1000. This would imply that there are a total of 100,000 matrix derivatives each for $\frac{\partial A_{zd}}{\partial \Phi_{ij}}$ and $\frac{\partial C_{zd}}{\partial \Phi_{ij}}$. For each one, there is also an associated matrix multiplication. This can quickly increase the time required to compute the matrix derivatives. A later section will discuss approximations and other techniques that can speed up the computations.

4.5.2 Mode shape and natural frequency derivatives

As mentioned previously, the other type of derivative found in Eq. 4.67 and Eq. 4.68 deals with mode shape, frequency, and modal mass derivatives with respect to physical parameters. These fall within the general category of eigenvalue and eigenvector sensitivities, which have been the focus of much research over the last several decades. These sensitivities have found widespread use in structural optimization routines and finite-element model updating. The classic reference is by Fox and Kapoor [21], and the approach used by Nelson [68] for eigenvector derivatives will be outlined here. For more references pertaining to general eigenproblem sensitivities, refer to Reference [66]. These references only discuss mode shape and frequency derivatives; therefore, computing modal mass derivatives was a new capability that had to be added.

4.5.2.1 Derivation

The eigenvalue derivative can be determined by first considering the familiar eigenvalue problem for a structural system.

$$\left(-\omega_j^2 M + K\right)\phi_j = 0 \tag{4.74}$$

M is the mass matrix and K is the stiffness matrix, and both are assumed to be symmetric. For the jth mode, ω_j^2 is the associated eigenvalue and ϕ_j is the associated eigenvector. In

more familiar structural dynamic terminology, ω_j is the natural frequency and is a diagonal entry in the modal frequency matrix Ω. The vector ϕ_j is the mode shape and is a column of the modal matrix Φ.

Differentiating both sides of Eq. 4.74 with respect to a structural parameter p and pre-multiplying by ϕ_j^T leads to

$$\underbrace{\phi_j^T \left(-\omega_j^2 M + K\right)}_{=\left[\left(-\omega_j^2 M + K\right)\phi_j\right]^T = 0} \frac{\partial \phi_j}{\partial p} + \phi_j^T \left(-\omega_j^2 \frac{\partial M}{\partial p} + \frac{\partial K}{\partial p}\right) \phi_j - \frac{\partial \omega_j^2}{\partial p} \underbrace{\phi_j^T M \phi_j}_{=1} = 0 \qquad (4.75)$$

and it can be seen that the unity modal mass normalization of the mode shapes has been enforced. Solving for the eigenvalue derivative $\frac{\partial \omega_j^2}{\partial p}$ produces the simple result

$$\frac{\partial \omega_j^2}{\partial p} = \phi_j^T \left(-\omega_j^2 \frac{\partial M}{\partial p} + \frac{\partial K}{\partial p}\right) \phi_j \qquad (4.76)$$

Eq. 4.76 indicates that the derivative of the squared natural frequency of the jth mode is given in terms of the corresponding mode shape and frequency as well as the mass and stiffness derivatives with respect to the parameter p. It does not depend on knowing the values of other modal frequencies and mode shapes.

Unfortunately, computing the mode shape derivative requires substantially more effort. Prior to the pre-multiplication step that produced Eq. 4.75, the following intermediate equation can be obtained.

$$\underbrace{\left(-\omega_j^2 M + K\right)}_{\equiv \mathcal{K}_j} \frac{\partial \phi_j}{\partial p} = \underbrace{\frac{\partial \omega_j^2}{\partial p} M \phi_j - \left(-\omega_j^2 \frac{\partial M}{\partial p} + \frac{\partial K}{\partial p}\right) \phi_j}_{\equiv b_j} \qquad (4.77)$$

Once Eq. 4.76 is evaluated, the right-hand side of Eq. 4.77 is known. Also, the coefficient matrix in front of $\frac{\partial \phi_j}{\partial p}$ is known. Eq. 4.77 is therefore of the form

$$\mathcal{K}_j \frac{\partial \phi_j}{\partial p} = b_j \qquad (4.78)$$

where we will refer to $\mathcal{K}_j$ as the dynamic stiffness matrix associated with the jth mode. Eq. 4.78 is a system of linear equations in terms of the elements of the vector $\frac{\partial \phi_j}{\partial p}$. A direct solution can not be obtained via a procedure such as Gauss-Jordan elimination and back substitution because $\mathcal{K}_j$ is a singular matrix. This is evident because Eq. 4.74 has nonzero solutions for ϕ_j. In particular, $\mathcal{K}_j$ will have a rank of $n-1$ if all the ω_j are unique, i.e., if there are no repeated eigenvalues [35]. If a particular problem does have repeated

131

eigenvalues, then alternative solution techniques are required. However, the remainder of this section will only consider the case of distinct modal frequencies.

The solution procedure begins by assuming that $\frac{\partial \phi_j}{\partial p}$ can be expressed as the sum of a particular solution of Eq. 4.77 and a homogeneous solution. Since the mode shape vector ϕ_j is in the nullspace of $\mathcal{K}_j$, as indicated by Eq. 4.74, the homogeneous solution is ϕ_j multiplied by an undetermined scalar a. Denote the particular solution as ψ_j and write $\frac{\partial \phi_j}{\partial p}$ as

$$\frac{\partial \phi_j}{\partial p} = \psi_j + a\phi_j \tag{4.79}$$

Differentiating the mass normalization relation $\phi_j^T M \phi_j = 1$ with respect to p produces

$$\frac{\partial \phi_j^T}{\partial p} M \phi_j + \phi_j^T \frac{\partial M}{\partial p} \phi_j + \phi_j^T M \frac{\partial \phi_j}{\partial p} = 0 \tag{4.80}$$

Noting that the first term is just the transpose of the third term leads to

$$2\phi_j^T M \frac{\partial \phi_j}{\partial p} + \phi_j^T \frac{\partial M}{\partial p} \phi_j = 0 \tag{4.81}$$

Replacing $\frac{\partial \phi_j}{\partial p}$ by the right-hand side of Eq. 4.79 results in

$$2\phi_j^T M \left(\psi_j + a\phi_j \right) + \phi_j^T \frac{\partial M}{\partial p} \phi_j = 0 \tag{4.82}$$

which can be expanded to give

$$2 \underbrace{\phi_j^T M \psi_j}_{=0} + 2a \underbrace{\phi_j^T M \phi_j}_{=1} + \phi_j^T \frac{\partial M}{\partial p} \phi_j = 0 \tag{4.83}$$

To see why the first term is set to zero, notice that Eq. 4.79 explicitly separates the homogeneous solution $a\phi_j$ from the particular solution ψ_j. Hence, ψ_j does not have a component in the direction of ϕ_j. In fact, ψ_j can be thought of as a linear combination of all of the remaining eigenvectors since the mode shapes are linearly independent. In other words, ψ_j is in the column space of the matrix

$$\begin{bmatrix} \phi_1 & \phi_2 & \cdots & \phi_{j-1} & \phi_{j+1} & \cdots & \phi_m \end{bmatrix} \tag{4.84}$$

All of these modes are mass orthogonal to ϕ_j; therefore, $\phi_j^T M \psi_j = 0$. Solving Eq. 4.83 for a produces

$$a = -\frac{1}{2} \phi_j^T \frac{\partial M}{\partial p} \phi_j \tag{4.85}$$

The technique used by Nelson in Reference [68] to obtain the particular solution ψ_j involves constraining one of the elements of ψ_j to be zero. The element is arbitrarily chosen

to be the degree of freedom associated with the largest component (in magnitude) of the mode shape ϕ_j. Imposing a value of zero allows a row and column of $\mathcal{K}_j$ to be removed, thereby truncating Eq. 4.78 into a non-singular set of linear equations of the form

$$\tilde{\mathcal{K}}_j \tilde{\psi}_j = \tilde{b}_j \qquad (4.86)$$

which can be solved using standard techniques such as Gauss-Jordan elimination (rather than by inverting $\tilde{\mathcal{K}}_j$). The vector ψ_j is then simply $\tilde{\psi}_j$ with a zero inserted at the appropriate location.

Once the mode shape derivatives have been determined, the modal mass derivatives readily follow. The modal mass equation is given by

$$m_j = \phi_j^T M \phi_j \qquad (4.87)$$

Differentiating with respect to p leads to

$$\frac{\partial m_j}{\partial p} = 2\phi_j^T M \frac{\partial \phi_j}{\partial p} + \phi_j^T \frac{\partial M}{\partial p} \phi_j \qquad (4.88)$$

Since $\frac{\partial \phi_j}{\partial p}$ and $\frac{\partial M}{\partial p}$ have already been calculated, the right-hand side is known.

To summarize, the eigenvalue derivative for each mode is computed using Eq. 4.76. The mode shape derivative is computed by first solving for the scaling factor a in Eq. 4.85 to obtain the homogeneous solution $a\phi_j$. The particular solution ψ_j is obtained by solving Eq. 4.86, which is the same as Eq. 4.77, but with one degree of freedom removed. The modal mass derivative is given by Eq. 4.88.

4.5.2.2 Example Beam Element Derivatives

The key to being able to compute eigen-sensitivities with respect to physical parameters is whether it is possible to evaluate the matrix derivatives $\frac{\partial K}{\partial p}$ and $\frac{\partial M}{\partial p}$. Notice that the term $\left(-\omega_j^2 \frac{\partial M}{\partial p} + \frac{\partial K}{\partial p} \right) \phi_j$ appears in both the equation for the eigenvalue derivative (Eq. 4.76) and the right-hand side of the eigenvector derivative equation (Eq. 4.77). K and M are the system stiffness and mass matrices in global coordinates and typically have contributions from many different elements. What is usually done in practice is to first compute derivative matrices at the element level, then transform to global coordinates, and keep a running sum from all the contributing elements [48].

Table 4.2: DOF ordering for a single, two-node Bernoulli-Euler beam element.

#	DOF	Description
1	x_1	Node 1 displacement in x
2	y_1	Node 1 displacement in y
3	z_1	Node 1 displacement in z
4	θ_{x_1}	Node 1 rotation about x
5	θ_{y_1}	Node 1 rotation about y
6	θ_{z_1}	Node 1 rotation about z
7	x_2	Node 2 displacement in x
8	y_2	Node 2 displacement in y
9	z_2	Node 2 displacement in z
10	θ_{x_2}	Node 2 rotation about x
11	θ_{y_2}	Node 2 rotation about y
12	θ_{z_2}	Node 2 rotation about z

Take for example the element stiffness matrix for a two-node, constant cross-section, Bernoulli-Euler beam element with shear deformation and rotary inertia effects ignored. Assume that the local degrees of freedom are ordered as shown in Table 4.2.

The general form of the matrix is (see for example Reference [13])

$$K_{\text{element}} =$$

$$
\begin{bmatrix}
\frac{EA}{L} & & & & & & -\frac{EA}{L} & & & & & \\
 & \frac{12EI_z}{L^3} & & & & \frac{6EI_z}{L^2} & & -\frac{12EI_z}{L^3} & & & & \frac{6EI_z}{L^2} \\
 & & \frac{12EI_y}{L^3} & & -\frac{6EI_y}{L^2} & & & & -\frac{12EI_y}{L^3} & & -\frac{6EI_y}{L^2} & \\
 & & & \frac{GJ}{L} & & & & & & -\frac{GJ}{L} & & \\
 & & -\frac{6EI_y}{L^2} & & \frac{4EI_y}{L} & & & & \frac{6EI_y}{L^2} & & \frac{2EI_y}{L} & \\
 & \frac{6EI_z}{L^2} & & & & \frac{4EI_z}{L} & & -\frac{6EI_z}{L^2} & & & & \frac{2EI_z}{L} \\
-\frac{EA}{L} & & & & & & \frac{EA}{L} & & & & & \\
 & -\frac{12EI_z}{L^3} & & & & -\frac{6EI_z}{L^2} & & \frac{12EI_z}{L^3} & & & & -\frac{6EI_z}{L^2} \\
 & & -\frac{12EI_y}{L^3} & & \frac{6EI_y}{L^2} & & & & \frac{12EI_y}{L^3} & & \frac{6EI_y}{L^2} & \\
 & & & -\frac{GJ}{L} & & & & & & \frac{GJ}{L} & & \\
 & & -\frac{6EI_y}{L^2} & & \frac{2EI_y}{L} & & & & \frac{6EI_y}{L^2} & & \frac{4EI_y}{L} & \\
 & \frac{6EI_z}{L^2} & & & & \frac{2EI_z}{L} & & -\frac{6EI_z}{L^2} & & & & \frac{2EI_z}{L}
\end{bmatrix}
$$

(4.89)

The element mass matrix can either be created using a lumped mass approach or a consistent mass formulation. The form of the element mass matrix used in IMOS (and based on NASTRAN's formulation) is

$$M_{\text{element}} = \frac{\rho A L}{420} \times$$

$$
\left[\begin{array}{cccccccccccc}
\boxed{175} & & & & & & \boxed{35} & & & & & \\
 & 156 & & & 22L & & & 54 & & & & -13L \\
 & & 156 & & & -22L & & & 54 & & 13L & \\
 & & & 105\frac{(I_y+I_z)}{A} & & & & & & & & \\
 & & -22L & & 4L^2 & & & & -13L & & -3L^2 & \\
 & 22L & & & & 4L^2 & & 13L & & & & -3L^2 \\
\boxed{35} & & & & & & \boxed{175} & & & & & \\
 & 54 & & & 13L & & & 156 & & & & -22L \\
 & & 54 & & & -13L & & & 156 & & 22L & \\
 & & & & & & & & & 105\frac{(I_y+I_z)}{A} & & \\
 & & 13L & & & -3L^2 & & & 22L & & 4L^2 & \\
 & -13L & & & -3L^2 & & & -22L & & & & 4L^2
\end{array}\right]
$$

$$(4.90)$$

The entries that are boxed are the result of a NASTRAN technique that averages the lumped mass and consistent mass entries associated with the axial (*i.e.*, extensional) degrees of freedom.

The parameter dependence of K_{element} and M_{element} can be expressed as

$$K_{\text{element}} \to K_{\text{element}}(A, J, I_y, I_z, E, G, L) \tag{4.91}$$

$$M_{\text{element}} \to M_{\text{element}}(\rho, A, I_y, I_z, L) \tag{4.92}$$

where

$$
\begin{aligned}
A &= \text{cross-sectional area} \\
J &= \text{cross-sectional torsional constant} \\
I_y &= \text{cross-sectional bending moment of inertia about the } y \text{ axis} \\
I_z &= \text{cross-sectional bending moment of inertia about the } z \text{ axis} \\
E &= \text{Young's modulus} \\
G &= \text{shear modulus} \\
L &= \text{element length} \\
\rho &= \text{mass density}
\end{aligned}
$$

For simplicity, the element length L will be treated as constant; hence, no sensitivities will be computed with respect to this parameter. The difficulty arises due to the fact that a change in an element's length affects the nodal locations of all elements "downstream" of the element. This implies that the transformation from local to global coordinates for each element is no longer a constant based on the original geometry of the model. The transformation matrix becomes a function of the changes in element lengths, which greatly increases the difficulty of the problem. This is one of the reasons why structural redesigns based on changing the topology of a model are hard to implement using a gradient approach.

Nevertheless, the remaining beam element parameters can be accommodated in the derivative equations previously introduced. Therefore, the physical parameter p satisfies

$$p \in \left[\begin{array}{ccccccc} A & J & I_y & I_z & E & G & \rho \end{array} \right]$$

The matrix derivatives $\frac{\partial K_{\text{element}}}{\partial p}$ and $\frac{\partial M_{\text{element}}}{\partial p}$ can be computed symbolically and stored in an element library for subsequent use.

Having evaluated these derivatives, the next step is to transform to global coordinates via the element transformation matrix T_k, which satisfies

$$\phi_{j,k} = T_k \tilde{\phi}_{j,k} \tag{4.93}$$

where $\tilde{\phi}_{j,k}$ represents the entries of the jth mode shape that correspond to the kth beam element's DOF's in local coordinates. The vector $\phi_{j,k}$ is simply the same vector expressed in global coordinates. It can be shown that

$$\left(-\omega_j^2 \frac{\partial M}{\partial p} + \frac{\partial K}{\partial p} \right) \phi_j = \sum_{k=1}^{\# \text{ of elements}} T_k \left(-\omega_j^2 \frac{\partial M_{\text{element}}}{\partial p} + \frac{\partial K_{\text{element}}}{\partial p} \right) \tilde{\phi}_{j,k} \tag{4.94}$$

The left hand side of the equation is the term that appears in both the eigenvalue and eigenvector derivatives, as mentioned previously. The summation extends over all the elements of interest containing the parameter p. Eq. 4.76 becomes

$$\frac{\partial \omega_j^2}{\partial p} = \sum_{k=1}^{\# \text{ of elements}} \tilde{\phi}_{j,k}^T \left(-\omega_j^2 \frac{\partial M_{\text{element}}}{\partial p} + \frac{\partial K_{\text{element}}}{\partial p} \right) \tilde{\phi}_{j,k} \tag{4.95}$$

while Eq. 4.77 becomes

$$\underbrace{\left(-\omega_j^2 M + K \right)}_{\equiv \mathcal{K}_j} \frac{\partial \phi_j}{\partial p} = \frac{\partial \omega_j^2}{\partial p} M \phi_j - \sum_{k=1}^{\# \text{ of elements}} T_k \left(-\omega_j^2 \frac{\partial M_{\text{element}}}{\partial p} + \frac{\partial K_{\text{element}}}{\partial p} \right) \tilde{\phi}_{j,k} \tag{4.96}$$

4.5.2.3 Example Generalized Spring and Inertia Derivatives

Although element derivative matrices have been shown only for the case of beam elements, the same procedure can be applied to more complicated elements such as plates. In addition, early generation finite-element models typically incorporate generalized spring (*e.g.*, CELAS) and inertia (*e.g.*, CONM) elements. In the most general form, each of these elements can be characterized by a 6×6 matrix. (The following equations are also valid for matrices of other sizes.) Let them be denoted by K_{CELAS} and M_{CONM}, respectively. Introduce scalar factors α and β that are used to capture overall stiffness and mass increases as represented by αK_{CELAS} and βM_{CONM}, where α and β are nominally equal to 1. If $p = \alpha$ or β, then Eq. 4.95 and Eq. 4.96 can be written as

$$\frac{\partial \omega_j^2}{\partial \alpha} = \phi_{j,\text{CELAS}}^T \underbrace{\frac{\partial(\alpha K_{\text{CELAS}})}{\partial \alpha}}_{=K_{\text{CELAS}}} \phi_{j,\text{CELAS}} \tag{4.97}$$

$$\frac{\partial \omega_j^2}{\partial \beta} = -\omega_j^2 \phi_{j,\text{CONM}}^T \underbrace{\frac{\partial(\beta M_{\text{CONM}})}{\partial \beta}}_{=M_{\text{CONM}}} \phi_{j,\text{CONM}} \tag{4.98}$$

$$\mathcal{K}_j \frac{\partial \phi_j}{\partial \alpha} = \frac{\partial \omega_j^2}{\partial \alpha} M \phi_j - \underbrace{\frac{\partial(\alpha K_{\text{CELAS}})}{\partial \alpha}}_{=K_{\text{CELAS}}} \phi_{j,\text{CELAS}} \tag{4.99}$$

$$\mathcal{K}_j \frac{\partial \phi_j}{\partial \beta} = \frac{\partial \omega_j^2}{\partial \beta} M \phi_j + \omega_j^2 \underbrace{\frac{\partial(\beta M_{\text{CONM}})}{\partial \beta}}_{=M_{\text{CONM}}} \phi_{j,\text{CONM}} \tag{4.100}$$

The previous equations assume that K_{CELAS} and M_{CONM} are expressed in the global coordinate frame. $\phi_{j,\text{CELAS}}$ represents the entries in ϕ_j that correspond to the CELAS DOF's, while $\phi_{j,\text{CONM}}$ represents the entries in ϕ_j that correspond to the CONM DOF's.

4.5.3 Implementation

An IMOS-compatible series of MATLAB functions that compute structural eigenvalue and eigenvector derivatives for beam elements was written by S. Kenny (MIT) and are documented in Reference [48]. The main piece of code is called `nelson.m`, and it was used to obtain the results presented in the following sections. Furthermore, the code was also modified to compute modal mass sensitivities (Eq. 4.88), and a new function `nelson_mod.m` was created to calculate sensitivities with respect to the α and β parameters associated with CELAS and CONM elements.

Another modification that was made to `nelson.m` and implemented in `nelson_mod.m` involves accounting for rigid-body elements (RBE's) that result in constraint equations relating certain "master" DOF's (called the nset) and "slave" DOF's (called the mset). RBE's are often found in first-generation conceptual models since much of the detailed design has yet to be done. Certain components of the model are simply treated as behaving like a rigid body.

To see how the constraint relations affect the equations for eigenvalue and eigenvector derivatives, first write the standard undamped, unforced equations of motion for a finite-element model.

$$M\ddot{x} + Kx = 0 \tag{4.101}$$

Assume the mass and stiffness matrices are partitioned according to the nset and mset DOF's.

$$
\begin{aligned}
M &= \begin{bmatrix} M_{nn} & M_{nm} \\ M_{mn} & M_{mm} \end{bmatrix} \\
K &= \begin{bmatrix} K_{nn} & K_{nm} \\ K_{mn} & K_{mm} \end{bmatrix} \\
x &= \begin{Bmatrix} x_n \\ x_m \end{Bmatrix}
\end{aligned}
\tag{4.102}
$$

A constraint matrix T_c relates the nset DOF's to the mset DOF's.

$$x_m = T_c x_n \tag{4.103}$$

The physical DOF's x can therefore be expressed in terms of x_n.

$$x = \underbrace{\begin{Bmatrix} I \\ T_c \end{Bmatrix}}_{\equiv R} x_n \tag{4.104}$$

Reducing out the mset DOF's from Eq. 4.101 results in

$$\underbrace{R^T M R}_{\tilde{M}} \ddot{x}_n + \underbrace{R^T K R}_{\tilde{K}} x_n = 0 \tag{4.105}$$

It is these reduced matrices that are typically used in the generalized eigenproblem to compute the mode shapes and natural frequencies of the system.

$$\tilde{K}\Phi_n = \tilde{M}\Phi_n\Omega \tag{4.106}$$

where Φ_n is the mode shape matrix whose rows correspond to the nset DOF's. The modes can be expanded to all the DOF's via the relation $\Phi = R\Phi_n$.

The eigenvalue derivative equation for this reduced system is in the form of Eq. 4.76 and can be written as

$$\frac{\partial \omega_j^2}{\partial p} = \{\phi_j\}_n^T \left(-\omega_j^2 \frac{\partial \tilde{M}}{\partial p} + \frac{\partial \tilde{K}}{\partial p}\right)\{\phi_j\}_n \tag{4.107}$$

where $\{\phi_j\}_n$ represents the jth mode shape at only the nset DOF's. However, the matrix derivatives $\frac{\partial \tilde{M}}{\partial p}$ and $\frac{\partial \tilde{K}}{\partial p}$ are not known directly because the reduction process in Eq. 4.105 combines the effect of all partitions of the unreduced M and K. It is easier to determine the matrix derivatives $\frac{\partial M}{\partial p}$ and $\frac{\partial K}{\partial p}$ first. Eq. 4.107 can be written in terms of these derivatives as follows.

$$\begin{aligned}
\frac{\partial \omega_j^2}{\partial p} &= \{\phi_j\}_n^T R^T \left(-\omega_j^2 \frac{\partial M}{\partial p} + \frac{\partial K}{\partial p}\right) R\{\phi_j\}_n \tag{4.108} \\
&= \{\phi_j\}_n^T \underbrace{R^T \left(-\omega_j^2 \frac{\partial M}{\partial p} + \frac{\partial K}{\partial p}\right)\phi_j}_{\equiv d_j} \tag{4.109}
\end{aligned}$$

Once the vector d_j is computed, it can be stored and subsequently used in the eigenvector derivative equation (Eq. 4.77), which is repeated here.

$$\underbrace{\left(-\omega_j^2\tilde{M} + \tilde{K}\right)}_{\equiv \tilde{\mathcal{K}}_j}\frac{\partial\{\phi_j\}_n}{\partial p} = \frac{\partial \omega_j^2}{\partial p}\tilde{M}\{\phi_j\}_n - d_j \tag{4.110}$$

After applying Nelson's method to solve for the eigenvector derivative, the vector can then be expressed at all the DOF's by multiplying by R.

$$\frac{\partial \phi_j}{\partial p} = R\frac{\partial\{\phi_j\}_n}{\partial p} \tag{4.111}$$

The modal mass derivative is then obtained using Eq. 4.88.

4.6 Demonstration of Physical Parameter Sensitivity Analysis

4.6.1 Cantilever beam

To validate the equations that have been presented for physical parameter sensitivities, a cantilever beam example was created. The beam depicted in Figure 4.12(a) is assumed to be made from aluminum, with density $2700 \, \text{kg/m}^3$, Young's modulus $70 \, \text{GPa}$, length $0.50 \, \text{m}$, width $1 \, \text{cm}$, and height $1.8 \, \text{cm}$. The primary bending direction is in the horizontal plane (*i.e.*, the plane perpendicular to the page). The disturbance is a tip force oriented at a $45°$ angle in the plane of the cross-section. It is bandlimited white noise with intensity $10^{-4} \, \text{N}^2/\text{Hz}$ across the frequency range of the beam dynamics, as shown in Figure 4.12(b). The performance metric is the tip displacement (in millimeters) along the same direction. The RMS is $0.43 \, \text{mm}$, as indicated in Figure 4.12(c). The beam is modeled with a single Bernoulli-Euler beam element with six DOF's at the tip node. The use of additional finite elements would lead to better estimates of the modal frequencies; however, the purpose of the model is to demonstrate the physical parameter sensitivities. Consequently, a single beam element model was deemed sufficient. The stiffness and mass matrices are of the form given in Eq. 4.89 and Eq. 4.90. Due to the fixed end, the first six rows and columns of K_{element} and M_{element} are deleted.

The modal frequencies and mode shape descriptions are listed in Table 4.3. Only the first four modes are disturbable and observable, which is the reason why just four resonant peaks are visible in the performance PSD plot.

Performing a sensitivity analysis of the tip displacement RMS with respect to modal parameters results in the normalized sensitivities presented in Figure 4.13(a). As is evident, the first mode is the most dominant, followed by the second mode. Perturbing the frequency, modal mass, or damping of the higher modes has no appreciable affect. To confirm the mode shape descriptions in Table 4.3, the strain energy contribution from the four primary types of beam deformation (1 axial, 2 bendings, 1 twist) are displayed in Figure 4.13(b). Due to the form of the element stiffness matrix given in Eq. 4.89, the modes are uncoupled, meaning that there are no extension/twist or bending/twist coupled modes. The first four modes are characterized by bending, the fifth mode is an axial mode, and the sixth mode is a torsion mode.
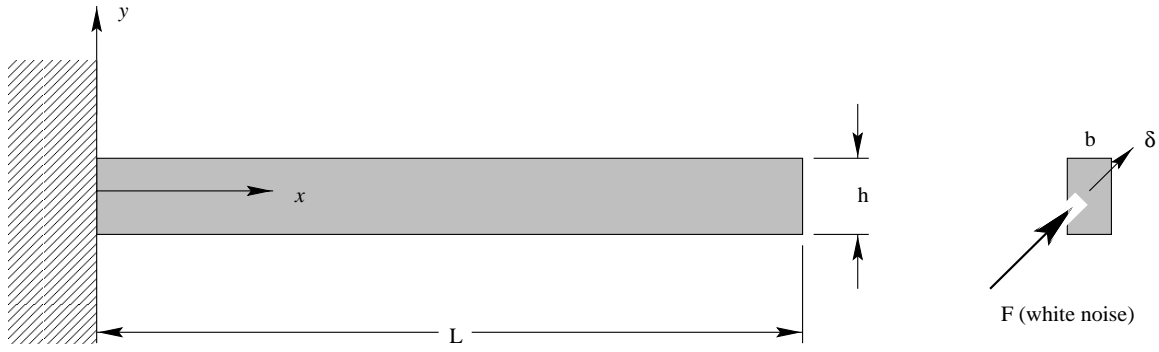
(a)
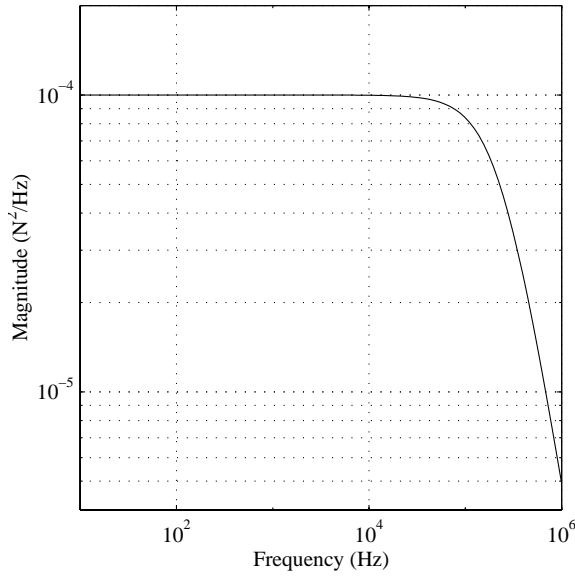
(b)
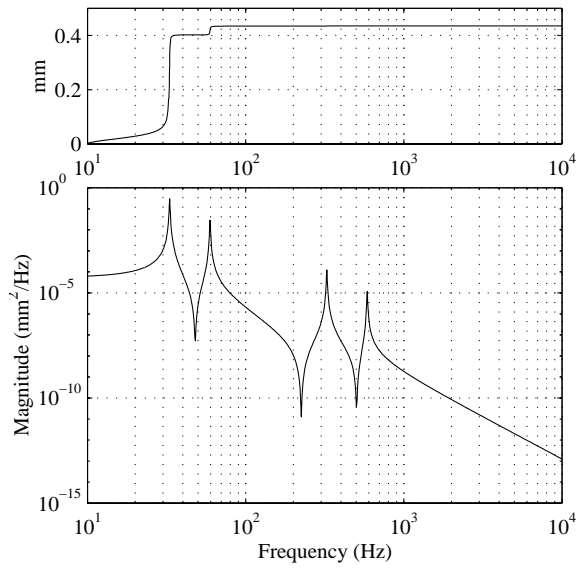
(c)

Figure 4.12: (a) Cantilever beam demonstration case. (b) Tip force disturbance PSD. (c) Tip displacement cumulative RMS (top) and PSD (bottom).

Table 4.3: Cantilever beam frequencies and mode shapes.

Freq. (Hz)	Mode shape description
33.1	horizontal bending
59.5	vertical bending
326	2nd horizontal bending
586	2nd vertical bending
2510	axial
3240	torsion

(a)

(b)
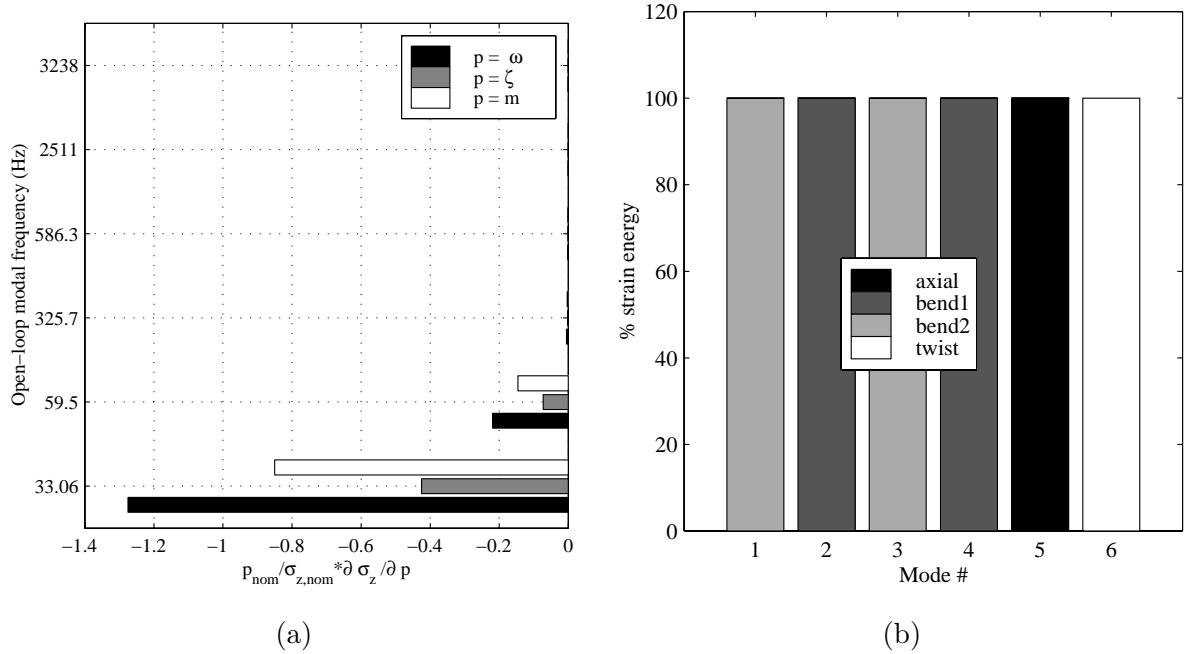
Figure 4.13: (a) Performance RMS normalized sensitivities with respect to modal parameters. (b) Strain energy contributions to each mode from the four types of beam deformation.

Table 4.4: Notation used for the four types of beam deformation. (jth mode, kth beam element)

element DOF's	mode shape components	element stiffness submatrix
axial (1,7)	$\tilde{\phi}_{j,k,\text{axial}}$	$K_{k,\text{axial}}$
bending 1 (2,6,8,12)	$\tilde{\phi}_{j,k,\text{bend1}}$	$K_{k,\text{bend1}}$
bending 2 (3,5,9,11)	$\tilde{\phi}_{j,k,\text{bend2}}$	$K_{k,\text{bend2}}$
twist (4,10)	$\tilde{\phi}_{j,k,\text{twist}}$	$K_{k,\text{twist}}$

The strain energy contributions are determined as follows. First consider the mode shape partitioning shown symbolically below.

$$\phi_j \quad \xrightarrow{1} \quad \phi_{j,k} \quad \xrightarrow{2} \quad \tilde{\phi}_{j,k} \quad \xrightarrow{3} \quad \tilde{\phi}_{j,k,\text{axial}}, \ \tilde{\phi}_{j,k,\text{bend1}}, \ \tilde{\phi}_{j,k,\text{bend2}}, \ \tilde{\phi}_{j,k,\text{twist}}$$

Specifically, for the jth mode shape ϕ_j, the steps are:

1. Extract a vector of size 12×1 that corresponds to the 12 DOF's of the kth beam element.

2. Transform the vector to local element coordinates.

3. Split this vector into four separate vectors, each of which corresponds to the DOF's of one of the deformation types.

In addition, the rows and columns associated with the different sets of DOF's can be extracted from the element stiffness matrix (recall Eq. 4.89) to form smaller stiffness submatrices. The notation is summarized in Table 4.4. The modal strain energies for the different types of motion are simply

$$U_{j,k,\text{axial}} = \frac{1}{2}\tilde{\phi}_{j,k,\text{axial}}^T K_{k,\text{axial}} \tilde{\phi}_{j,k,\text{axial}} \tag{4.112}$$

$$U_{j,k,\text{bend1}} = \frac{1}{2}\tilde{\phi}_{j,k,\text{bend1}}^T K_{k,\text{bend1}} \tilde{\phi}_{j,k,\text{bend1}} \tag{4.113}$$

$$U_{j,k,\text{bend2}} = \frac{1}{2}\tilde{\phi}_{j,k,\text{bend2}}^T K_{k,\text{bend2}} \tilde{\phi}_{j,k,\text{bend2}} \tag{4.114}$$

$$U_{j,k,\text{twist}} = \frac{1}{2}\tilde{\phi}_{j,k,\text{twist}}^T K_{k,\text{twist}} \tilde{\phi}_{j,k,\text{twist}} \tag{4.115}$$

Dividing through by the total modal strain energy

$$U_{j,\text{total}} = \frac{1}{2}\phi_j^T K \phi_j = \frac{1}{2}\omega_j^2 \tag{4.116}$$

143

yields the percent contribution, which is plotted in Figure 4.13(b).

One use of decomposing the element strain energies in this manner is to help identify which physical parameters should be carried into the sensitivity analysis. As will be discussed shortly, the time required to complete the sensitivity analysis is proportional to the number of parameters; therefore, reducing the total number will lead to significant time savings.

Based on the form of the beam element stiffness matrix in Eq. 4.89, the following mapping between physical parameters and affected element modes can be created.

$$
\begin{aligned}
E, A &\longrightarrow \quad \text{axial mode} \\
E, I_z &\longrightarrow \quad \text{bending mode 1} \\
E, I_y &\longrightarrow \quad \text{bending mode 2} \\
G, J &\longrightarrow \quad \text{torsion mode}
\end{aligned}
$$

The parameters to choose can be qualitatively determined by first identifying the critical modes from modal parameter sensitivity results (*e.g.*, Figure 4.13(a)) and/or cumulative RMS plots (*e.g.*, Figure 4.12(c)). Then, strain energy contribution plots (such as Figure 4.13(b)) and/or mode shape animation software can help to isolate what type of motion is associated with each mode. Finally, a mapping from physical parameters to different deformation types is used to select the important parameters. In this simple beam example, this process can be implemented quite easily, and the results are intuitive. However, for more complicated systems the results might be harder to interpret. Applying this methodology to a model of SIM will be the subject of the next section.

Table 4.5 compares the analytical performance RMS sensitivity results with results obtained by a finite difference approach (perturbation size = 0.1%). Also shown are the results when only a subset of all six modes is used. With the exception of E, all other parameters show good correlation between the finite difference and analytical values. The sensitivities with respect to G and J are zero since these parameters only affect the torsion mode, and this mode does not influence the tip displacement. The parameters A and ρ have the same sensitivities because they appear in exactly the same fashion in the element mass matrix. Normally the two would have different sensitivities because A also appears in the stiffness matrix while ρ does not, but because the axial mode (which A affects) does not contribute to the tip displacement RMS, A and ρ in this case exhibit equivalent

sensitivities. They have negative sensitivities, which agrees with the modal mass sensitivities found in Figure 4.13(a). These sensitivities are negative, which implies that increasing the modal mass will decrease the RMS. But an increased modal mass can be achieved by increasing either ρ or A, and the physical parameter sensitivities in Table 4.5 also indicate that increasing these quantities will reduce the RMS.

The largest sensitivities correspond to E and I_y, and this supports the findings in Figure 4.13. Mode 1, which is the dominant mode, is characterized by bending mode type 2. The physical parameter mapping indicates that E and I_y affect this mode, and bending about the y-axis corresponds to the "weak" bending direction.

The columns in Table 4.5 that correspond to the analytical predictions are based on retaining all or only a subset of the modes when evaluating the A_{zd} and C_{zd} matrix derivatives in Eq. 4.67 and Eq. 4.68. These derivatives involve summing over 1 to N, where N is the total number of modes. The column headings that take integer values from 1 to 6 indicate what value of N was used to compute the sensitivity values in the columns of the table. For instance, the column with the heading "4" means that only the first four modes were used in the calculations.

This is the first attempt at investigating time-saving simplifications that can be exploited in models of appreciable size. As shown previously, the first two modes are the dominant contributors to the tip displacement RMS. The analytical approximation that only uses these two modes produces reasonably accurate sensitivities. The maximum error does not exceed 0.4%. Even the approximation that only retains the first mode does a good job of estimating most of the sensitivities. Notice that the sensitivity with respect to I_z goes to zero in this one-mode approximation since I_z has no effect on the primary bending mode.

These results suggest that only the modes in the frequency range where most of the RMS contribution occurs need to be used in Eq. 4.67 and Eq. 4.68 in order to obtain good estimates of the sensitivities. While this appears to hold for this simple example, the next section will explore how valid the assumption is for the more complicated SIM model.

Although not used here, a time-saving measure which does not introduce any approximations is based on looping only over the DOF's in Eq. 4.67 and Eq. 4.68 at which

- disturbances enter (based on β_w),

- control inputs are applied (based on β_u),

Table 4.5: Comparison of tip displacement RMS normalized sensitivities with respect to beam properties.

p	$\frac{p_{\text{nom}}}{\sigma_{z,\text{nom}}}\frac{\Delta\sigma_z}{\Delta p}$ (finite diff.)	$\frac{p_{\text{nom}}}{\sigma_{z,\text{nom}}}\frac{\partial\sigma_z}{\partial p}$ (analytical), # of modes =					
		6	5	4	3	2	1
A	-0.2498	-0.2500	-0.2500	-0.2500	-0.2499	-0.2490	-0.2127
J	1.08×10^{-7}	0	0	0	0	0	0
I_z	-0.1099	-0.1100	-0.1100	-0.1100	-0.1096	-0.1096	0
I_y	-0.6394	-0.6400	-0.6400	-0.6400	-0.6400	-0.6375	-0.6375
E	-0.7493	-0.6739	-0.6739	-0.6739	-0.6738	-0.6713	-0.6375
G	1.08×10^{-7}	0	0	0	0	0	0
ρ	-0.2498	-0.2500	-0.2500	-0.2500	-0.2499	-0.2490	-0.2127
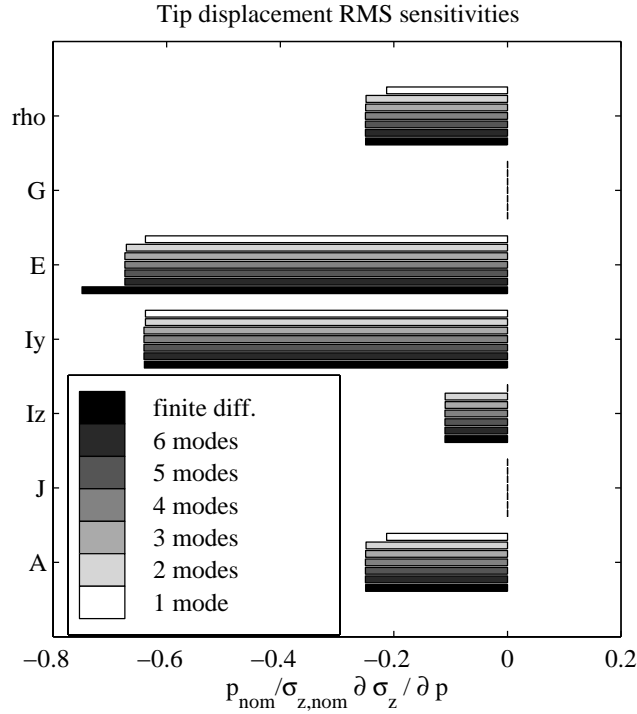
Figure 4.14: Bar chart representation of Table 4.5.

- sensor measurements are made (based on C_{yx}),

- and performance metrics are obtained (based on C_{zx}).

These DOF's are the ones that are important in A_{zd} and C_{zd}. The DOF's that fall into these categories should only be a fraction of the total number of DOF's. The remaining DOF's contribute nothing because $\frac{\partial A_{zd}}{\partial \Phi_{ij}} = 0$ and $\frac{\partial C_{zd}}{\partial \Phi_{ij}} = 0$ for values of i that correspond to these DOF's.

As a simple illustrative example, consider a system which is open loop (hence no β_u or C_{yx}) and which has a single disturbance and collocated performance metric. Assume there are 1000 DOF's, and the disturbance and performance are associated with DOF #100. Then β_w and C_{zx} contain only one nonzero element at the 100th entry.

$$\beta_w^T \;\; = \;\; C_{zx} \;\; = \;\; [0 \;\; \cdots \;\; 0 \;\; 1 \;\; 0 \;\; \cdots \;\;\;\; 0]$$

$$\uparrow \;\; \text{100th element}$$

(4.117)

The terms $\Phi^T \beta_w$ and $C_{zx}\Phi$ which appear in Eqs. 4.58 and 4.60 are given by

$$C_{zx}\Phi = \left(\Phi^T \beta_w\right)^T = \left[\;\; \Phi_{(100,1)} \;\; \cdots \;\; \Phi_{(100,1000)} \;\; \right] = \text{100th row of } \Phi \qquad (4.118)$$

Thus, the second summation in Eq. 4.67 and Eq. 4.68 needs to be evaluated only when $i = 100$. This leads to significant time savings with no loss of accuracy.

4.6.2 SIM Classic

Results of a physical parameter sensitivity analysis on the model of SIM Classic will now be presented. Figure 4.15 summarizes the results of the disturbance analysis and modal parameter sensitivity analysis that have previously been done. Figure 4.15(a) shows the familiar finite-element model and ray trace. Approximate PSD's of RWA disturbance forces and moments are plotted in Figure 4.15(b), and the resulting PSD of the OPD is shown in Figure 4.15(c). The modal parameter sensitivities are presented in Figure 4.15(d)

To help identify which stiffness-related physical parameters should be used in the sensitivity analysis, the percent strain energy stored in various elements was computed. Figure 4.16(a) shows the distribution of strain energy for the 16.95 Hz mode. The left subplot shows the contribution from all the beam elements in the model. Elements 1–14 correspond to the beam elements on the $-x$ siderostat boom, elements 15–28 correspond to those on the $+x$ siderostat boom, and elements 29–37 correspond to those on the metrology boom.

(a)

(b)

(c)

(d)
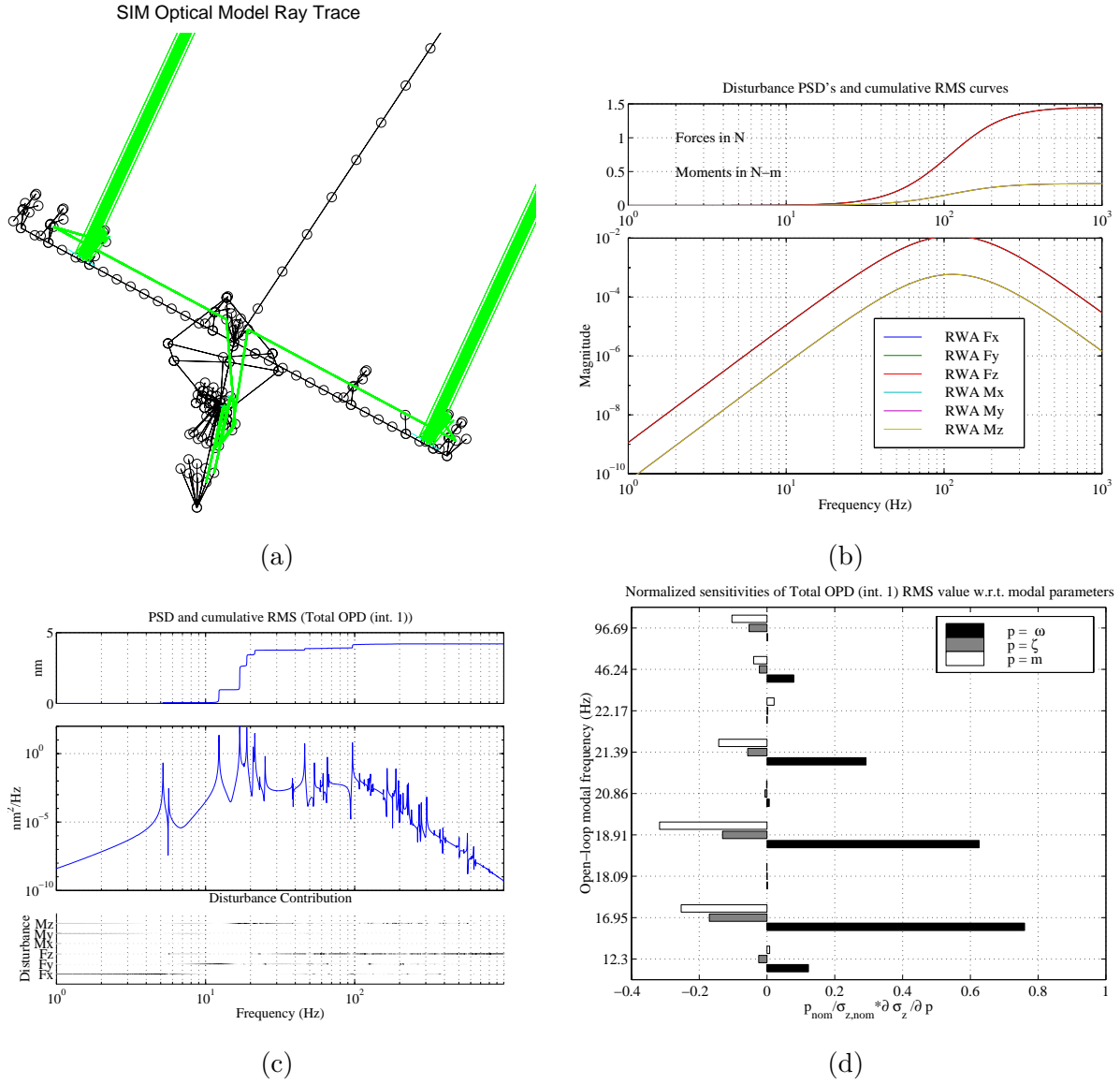
Figure 4.15: (a) Stellar ray trace through guide interferometer #1 of SIM. (b) Approximate PSD's (bottom) and cumulative RMS (top) of reaction wheel disturbances. (c) Performance PSD (bottom) and cumulative RMS (top). (d) Normalized sensitivities of performance RMS with respect to modal parameters of critical modes.
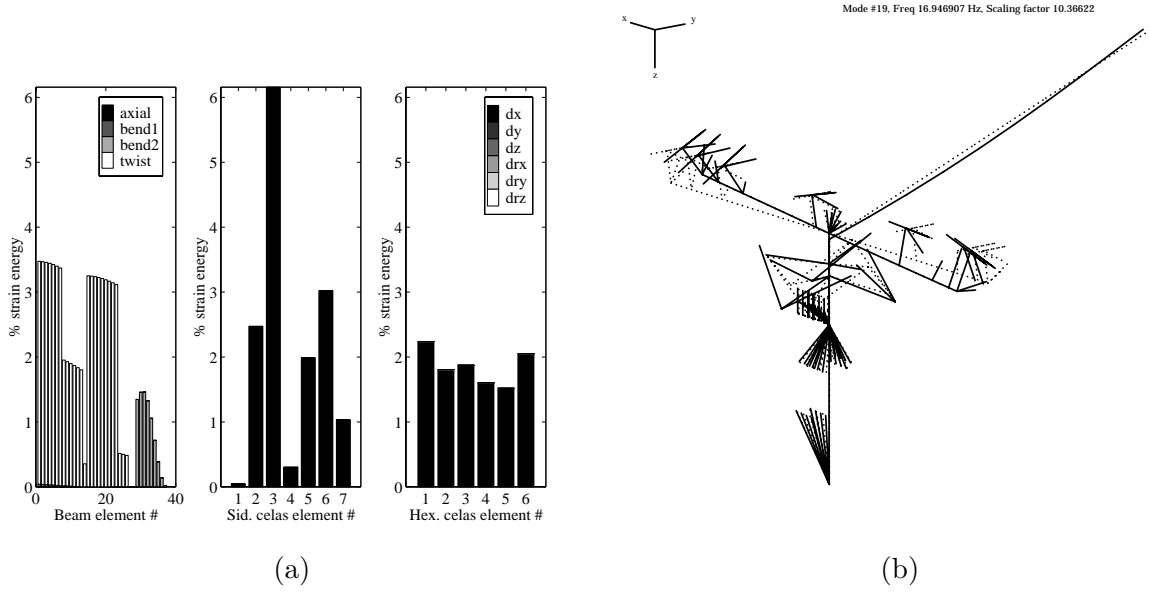
Figure 4.16: (a) Strain energy contributions for the 16.95 Hz mode. (b) Mode shape of the 16.95 Hz mode.

All the beam elements are ordered beginning at the root of each boom. Eqns. 4.112–4.115 were used to calculate the strain energy in the four different types of beam deformation, and the results indicate that all the siderostat boom elements are in torsion while the metrology boom is in bending. Most of the siderostat boom elements contain more than twice the strain energy stored in the metrology boom elements. This suggests that the parameters which should have a large effect on this mode are G and J of the siderostat boom. Recall that G and J will have the same sensitivities because only the product GJ appears in a beam element's stiffness matrix. Examining the mode shape in Figure 4.16(b) reveals that the siderostat booms are indeed undergoing torsion, and the boom tips are 180° out of phase.

The middle subplot in Figure 4.16(a) shows the strain energy fraction stored in each of the siderostat bay generalized spring elements. The SIM model includes these CELAS elements to try to capture local flexibility between a siderostat bay and the supporting siderostat boom. Since these CELAS elements are in the form of a fully-populated 6×6 stiffness matrix, the strain energy could not be decomposed into contributions from deformations such as extension and twist. Instead, the total strain energy in each CELAS element was computed as

$$\frac{1}{2}\phi_{j,\text{CELAS}}^{T}K_{\text{CELAS}}\phi_{j,\text{CELAS}} \tag{4.119}$$

149

The largest strain energy fraction is found in siderostat CELAS element #3. In Figure 4.16(b), this siderostat is the third one from the left, and in Figure 4.15(a), it is the leftmost one through which stellar light is passing. The siderostat bays are numbered starting with the outboard bay on the $+x$ arm, proceeding to the inboard bay on the $+x$ arm, then starting with the outboard siderostat on the $-x$ arm and proceeding to the inboard siderostat on the same arm. Other potential parameters for the sensitivity analysis are the α and β parameters associated with this siderostat bay. As discussed previously, these are scalar factors that multiply the nominal K_{CELAS} and M_{CONM} matrices to capture overall stiffness and mass increases or decreases.

The next largest contributor to the strain energy is siderostat CELAS element #6, and this is the other siderostat that forms the pair for the guide interferometer shown in Figure 4.15(a). The relative motion of the siderostats is difficult to see in the displayed mode shape in Figure 4.16(b), so it is harder to verify the strain energy results based on this picture; however, the use of modal animation software to zoom into areas of the model did confirm the results.

The right subplot of Figure 4.16(a) shows the contributions from another class of strain energy storage elements, namely the hexapod strut elements. These are also modeled with CELAS elements, but instead of being characterized by a full 6×6 stiffness matrix, the end of each strut is joined to a coincident node with a diagonal K_{CELAS} in local strut coordinates. This permits the contributions to be further decomposed into differential motion in each of the six axes. However as expected, the plot shows that the strain energy is dominated by axial (*i.e.*, dx) deformation of the six struts that form the hexapod. The modal animation software (called XVIEW) does not use visible line elements to represent spring elements, and this is the reason why the hexapod appears to be "discontinuous" in Figure 4.16(b).

The two other dominant modes at 18.91 Hz and 21.39 Hz are characterized by local modes of the siderostat bays, as shown in Figure 4.17. Both the mode shapes and the siderostat CELAS strain energy plots clearly indicate which bays have the largest motion. Siderostats 1 and 3 participate the most at 18.91 Hz, while siderostats 5 and 6 participate the most at 21.39 Hz. The motion of the siderostats is comprised mostly of rotation about x with some displacement in y. Recall that siderostats 3 and 6 collect the light for guide interferometer #1; consequently, any motion by them will have a strong effect on the OPD.

The results of the physical parameter sensitivity analysis are presented in Figure 4.18.

Mode #21, Freq 18.907816 Hz, Scaling factor 14.25589

(a)

(b)

Mode #23, Freq 21.39061 Hz, Scaling factor 14.707899

(c)

(d)
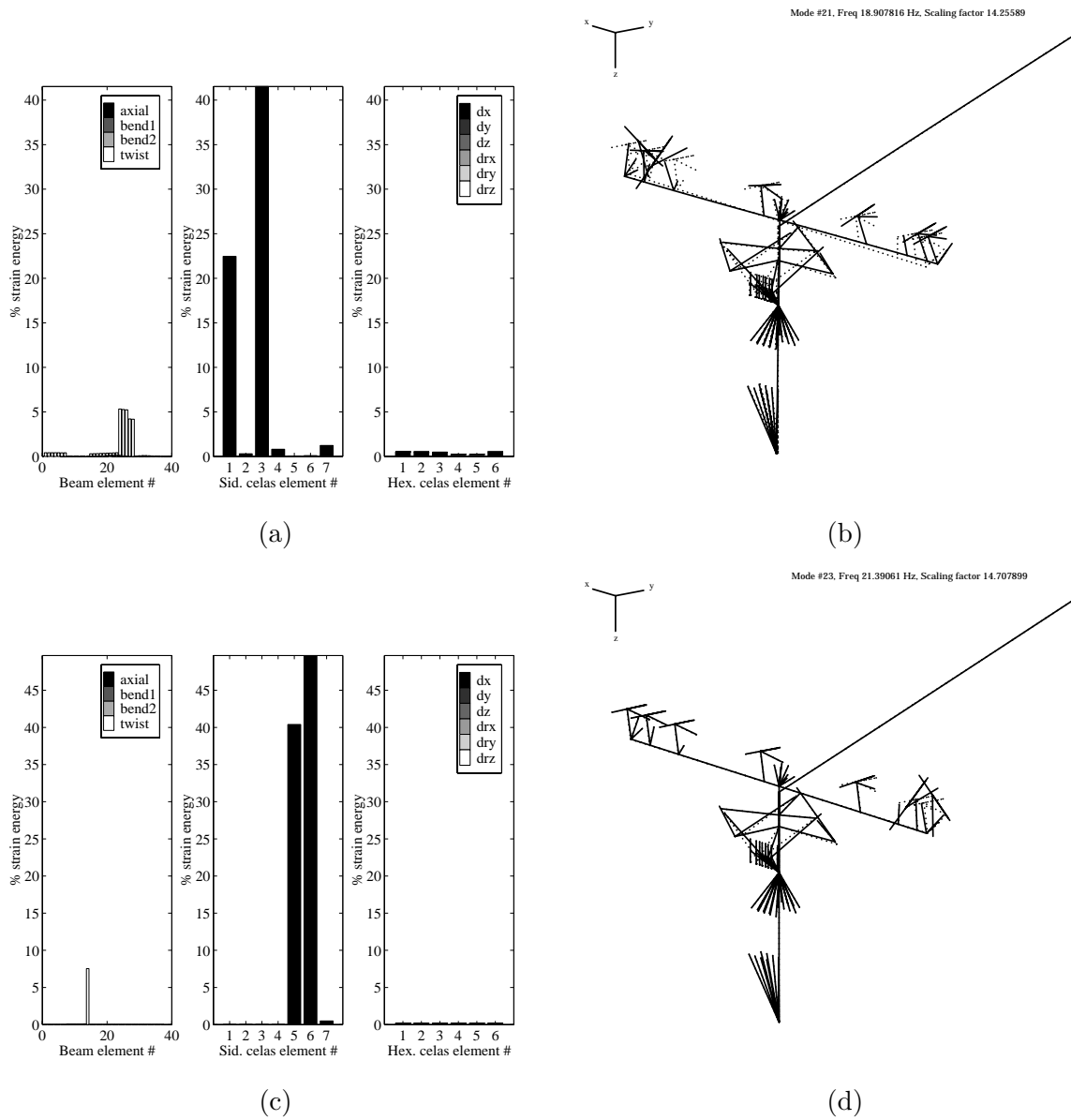
Figure 4.17: (a) Strain energy contributions for the 18.91 Hz mode. (b) Mode shape of the 18.91 Hz mode. (c) Strain energy contributions for the 21.39 Hz mode. (d) Mode shape of the 21.39 Hz mode.

Two different sets of modes were used in the computations, and the plot shows that no appreciable change in the predicted sensitivities occurs when more modes are used. This confirms that the dominant modes are present in both sets of modes. Although the strain energy contributions suggest that only certain parameters should be important, more are included in the figure to check if the intuitive choices are correct. Parameters A through ρ are the material and geometric properties of the siderostat boom. Parameters $a1$ through $a7$ represent the α factors for each of the seven siderostat bay CELAS elements. Parameters $b1$ through $b7$ represent the β factors for each of the seven siderostat bay CONM elements. Note that hexapod stiffness parameters and metrology boom parameters were not included in the analysis.

Figure 4.18 does confirm that G and J are the most important parameters of the siderostat boom. Also, α_3 and β_3 have relatively large sensitivities. Since siderostat bay 3 has large strain energy contribution in two out of the three critical modes, it makes sense that the OPD is very sensitive to α_3. The large sensitivity with respect to β_3 is also intuitive and can be explained as follows. In the local mode at 18.91 Hz, the siderostat bay undergoes large motion relative to the siderostat boom to which it is attached. Changing the mass and inertia properties (which β_3 controls) of the bay should affect this motion. It is interesting that the α_3 and β_3 sensitivities are opposite in sign, but this is not contradictory. A positive sensitivity with respect to β_3 suggests that decreasing the mass and inertia of the bay will improve the performance. This should lead to an increase in the frequency of the local siderostat mode. A negative sensitivity with respect to α_3 suggests that increasing the stiffness of the siderostat mount will also improve the performance, but this should increase the frequency of the local mode as well. These results imply that the local dynamics of the siderostat bays are important. What is surprising is that the sensitivities with respect α_5 and β_5 (the stiffness and mass parameters associated with siderostat 5) are fairly large. This siderostat is not part of guide interferometer #1; however, it does undergo motion in the two critical modes at 16.95 Hz and 21.39 Hz. The sensitivities suggest that the frequency of this mount mode should be lowered, which is opposite of what should be done to siderostat bay 3. The results might be indicating that the local mount modes should be individually "tuned" to improve the performance.

The next largest parameter sensitivities for the siderostat boom correspond to the cross-sectional area A and material density ρ of the siderostat boom beam elements. Since

Normalized Sensitivities of Total OPD (int. 1) RMS value w.r.t to physical parameters
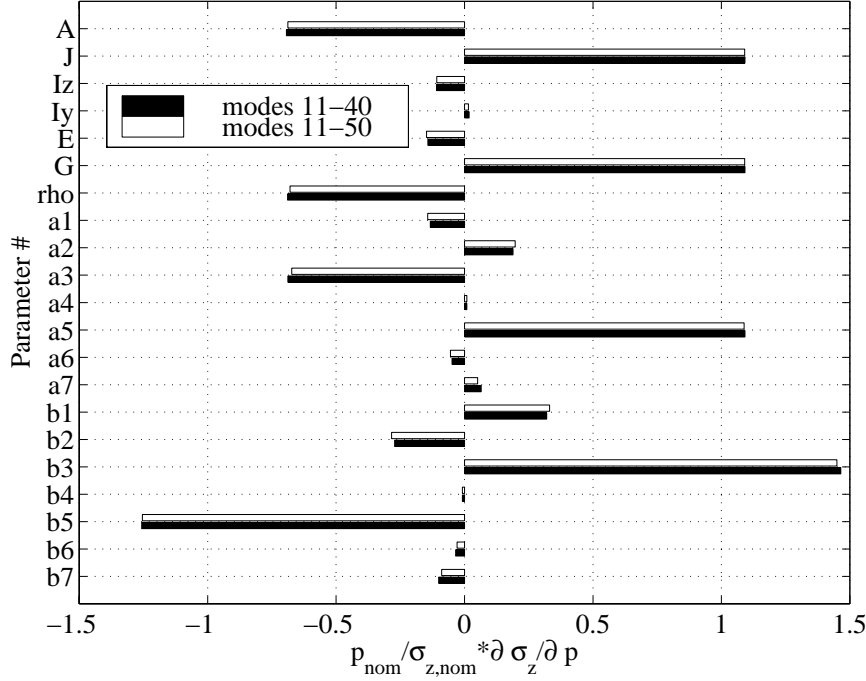
Figure 4.18: SIM physical parameter sensitivities.

extension of the siderostat boom does not contribute to the critical mode at 16.95 Hz, extensional strain energy is negligible; therefore, A was not identified as an important parameter. A only affects the axial stiffness term $\frac{EA}{L}$. What has been neglected thus far in determining important parameters is a kinetic energy distribution analysis. From a kinetic energy standpoint, the quantity ρA appears in every entry of a beam element's mass matrix (see Eq. 4.90) except for the torsion-related terms. Since the sensitivities with respect to ρ and A are nearly identical, a possible explanation is that the total mass of the siderostat booms is important. The siderostat booms not only deform in torsion in the 16.95 Hz mode, but they also translate in the xy plane due to rotation of the structure about the z axis.

Positive sensitivities with respect to G and J and negative sensitivities with respect to ρ and A appear to indicate that a performance improvement can be achieved with a decrease in the frequency of the dominant mode. This agrees with the frequency sensitivity in Figure 4.15(d), which indicates that increasing the frequency of the 16.95 Hz mode should increase the performance RMS. On the other hand, the physical parameter sensitivities for the third siderostat bay imply that the mount frequency should be increased. This contradicts the fact that all the modal frequency sensitivities are positive. This contradiction

could point out a limitation in the modal parameter sensitivity analysis. The underlying assumption is that a single parameter is being varied (either modal mass, frequency, or damping) while everything else remains constant. This cannot happen in reality since the mode shapes, frequencies, and modal masses are all interdependent. The physical parameter sensitivity technique that has been developed takes this interdependence into account, and therefore should be a more physically-based analysis. Further work should be conducted in order to explore this issue further. It should be mentioned that similar results occurred during experimental validation, and this issue will be discussed in Chapter 6 as well.

4.7   MATLAB Implementation

The modal parameter sensitivity analysis framework developed in this chapter has been implemented in MATLAB within a function called `sens_analysis.m`. The function can compute the sensitivities analytically using the equations derived earlier in Section 4.3. It assumes that the parameters are either modal damping ratios, natural frequencies, or modal masses of open-loop structural modes. It also requires the state-space A_{zd} matrix to be of the form indicated in Eq. 4.41. The disturbance states should be placed first, followed by the open-loop modal states and the compensator states (if the system is closed-loop). The augmented disturbance/plant system should be stable, and this requires that the system have no right-half plane or $j\omega$-axis poles. These states should be eliminated from the system prior to calling the function. There is also an option to check the analytical sensitivity results by performing finite-difference approximations. Some of the inputs to the function are analogous to the inputs to the disturbance analysis function `dist_analysis.m`.

The physical parameter sensitivity analysis framework has been implemented in a function called `sens_analysis_phys.m`. As before, the state-space system should be strictly stable. This function requires the most detailed information about the state-space system being considered. The disturbance analysis technique only requires a state-space representation and does not place any restrictions on the form of the individual state-space matrices. The modal parameter sensitivity technique requires the plant model to be in a particular modal form, but additional details regarding sensors, actuators, disturbances, and performances are not needed. The function `sens_analysis_phys.m`, on the other hand, does require knowledge of this type of information, particularly in the form of the matrices β_u,

β_w, C_{zx}, and C_{yx}. It also must be given the mode shapes corresponding to the modal frequencies in the plant A_{zw} matrix.

Rather than computing the mode shape, frequency, and modal mass derivatives with respect to physical parameters, `sens_analysis_phys.m` accepts these as inputs. It assumes that they have been calculated previously using eigenvalue/eigenvector derivative functions such as `nelson.m` [48] and `nelson_mod.m`.

4.8   Summary

A method for calculating the exact sensitivities of performance RMS values with respect to open-loop modal parameters has been presented. The approach was done in a state-space framework, and the sensitivities were shown to require the solution of one Lyapunov equation to obtain the state covariance matrix and one Lyapunov equation for every performance metric. Derivatives of the state-space matrices with respect to a desired parameter are simplified when the parameter is a modal parameter and the structural open-loop state-space A matrix is in a standard modal form. Disturbances on the system are required to be modeled as a linear filter driven by unit-intensity white noise. A MATLAB function called `sens_analysis.m` has been written to implement the methodology, and results were shown when the code was used on a simple one DOF system, a multi-DOF system, and a realistic SIM Classic model. Finite-difference approximations to the sensitivities helped to validate the code for the first two systems; however, numerical conditioning problems with the finite-difference methodology precluded the validation for the SIM Classic case.

A method has also been presented which determines the exact sensitivity values of RMS outputs of a state-space model with respect to physical parameters of a structural finite-element model. Since the state-space model assumes that the structural equations of motion have been cast in modal form, the derivatives of the FEM mode shapes and natural frequencies with respect to the parameters were required. Standard eigenvalue and eigenvector derivative techniques were described, and an existing IMOS-compatible MATLAB function was implemented to calculate these derivatives with respect to beam element parameters. The capability to compute sensitivities with respect to scalar factors that multiply generic CELAS and CONM element matrices was also added. The code was also modified to account for rigid-body elements that relate certain DOF's to other DOF's.

A cantilever beam problem served to validate the analytical sensitivity equations. The predictions agreed well with the approximate sensitivities from a finite-difference approach. In addition, the use of only a subset of the total number of modes when calculating the sensitivities still produced accurate results. This suggested that only important modes need to be retained in the computations, and significant time savings are possible for large-order models. The simple beam example was also used to demonstrate a process to select the physical parameters for the sensitivity analysis. A disturbance analysis and a modal parameter sensitivity analysis were first conducted to identify critical modes. Calculating the strain energy distribution in these modes then helped to select the physical parameters based on the type of deformation that the elements undergo in each mode.

Repeating this process on the more complicated SIM model revealed that a bandlimited reaction wheel type disturbance caused several modes to be dominant in the OPD performance metric that was chosen. This was confirmed in both a cumulative RMS plot of the performance as well as the sensitivities with respect to modal parameters. Plots of the strain energy contribution and the mode shape indicated that one mode was characterized by siderostat boom torsion while two others were dominated by local siderostat bay motion. Even though this suggested certain parameters for the sensitivity analysis, all parameters were used in order to confirm the intuitive choices. A few additional sensitive parameters were identified and suggested that kinetic energy distributions should be computed as well. Furthermore, apparent contradictions between physical parameter and modal parameter sensitivity results suggested that identifying redesign options for complex systems should be based on the physical parameter sensitivity results. The modal parameter sensitivity technique is more of an artificial rather than a physical analysis.

A next step is to "close the loop" on an overall system improvement algorithm. Thus far, the modal parameter and physical parameter sensitivity analyses have been used to provide a design engineer with a sense of which modes are most important and which structural parameters should be the focus of potential redesigns. What would be beneficial is an algorithm that takes the results and then interfaces with the uncertainty analysis methodology in Chapter 5 to suggest the combination of design changes that satisfies performance requirements subject to specified uncertainties and constraints. Chapter 7 takes a first step toward achieving this goal.

Chapter 5

Uncertainty Analysis Framework

Disturbance analyses during early design stages of aerospace systems are typically conducted on simplified models of nominal point designs. The models attempt to capture the behavior of interest, and although they are generally suitable for judging relative merits between competing designs in a trade study, the validity of their use in making absolute performance predictions is not as clear. A way to account for uncertainties when assessing performance would therefore be beneficial.

What is desired is a method to propagate uncertainties through a system model and place bounds on the nominal performance predictions. A disturbance analysis is first conducted to determine the nominal values, and an uncertainty analysis is then used to place the equivalent of "error bars" around the nominal performance values. If it is found that performance requirements are met even under worst-case model uncertainties, then confidence in design margins can be increased.

A number of cases can be envisioned for the results of the disturbance and uncertainty analyses, and they are depicted in Figure 5.1. The horizontal axis represents several different designs, and the vertical axis represents a particular performance metric. In design 1, the nominal performance does not meet the specified requirement. Also, the upper bound due to the worst-case uncertainties falls above the requirement line. Since the design fails to meet requirements, the system is redesigned, and design 2 is the result. In this case, the nominal performance does satisfy the requirement; however, the upper bound does not. It is this situation that highlights the need for an uncertainty analysis. Performing only the nominal disturbance analysis would lead to the misconception that the design is satisfactory,
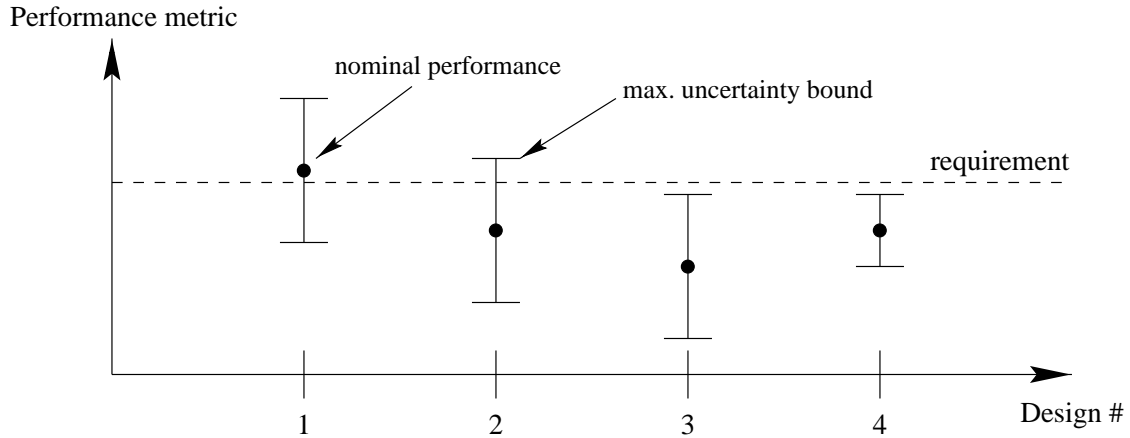
Figure 5.1: Example uncertainty bounds for different designs.

when in fact it might not satisfy the requirement. Now consider another redesign (design 3) in which both the nominal performance and its upper bound lie below the requirement. This design poses less of a risk than design 2 because it has a more comfortable design margin. It might not be possible to obtain a redesign whose worst-case performance meets the requirement as in the case of design 3. The only alternative might be to reduce the level of uncertainty so that for the same design, the uncertainty bounds are tighter. This is indicated by design 4, which has the same nominal performance as design 2, but now the upper bound is lower. Reduced uncertainty levels can be achieved by a testing program that targets the parameters of interest. Another approach to obtain design 4 is to redesign the system such that the sensitivity to uncertainty is less [77].

The following section describes the types of uncertainties that can arise. Section 5.2 then discusses four potential approaches for estimating the worst-case bound on a system's performance when parametric uncertainties exist. Two of the methods are applied to a simple spring-mass model, to a cantilevered beam model with nearly repeated modes, to a more complicated multiple spring-mass model, and finally to a closed-loop model of SIM. Techniques are developed that enable the method to be applied to large order systems such as SIM.

5.1 Types of model uncertainties

Section 2.1 provided an overview of the different pieces of the integrated modeling process for controlled opto-mechanical systems. The main challenge faced by modeling efforts during

conceptual design phases is the lack of detailed information about the design. When a model is created of the design, there will undoubtedly be errors between the model and the actual physical system if it was to be manufactured based on the nominal design. Since the actual system is not available to provide data, the model cannot be updated to better reflect the physical system.

In the most general sense, a model uncertainty represents an unknown error in a model of a physical system. We broadly divide model uncertainty into parametric and non-parametric uncertainties. A parametric uncertainty is an uncertainty in a parameter of the model. The parameter can appear either explicitly in the state-space matrices or the matrices can be implicit functions of the parameter. For example, if the system in Eq. 4.6 has an A_{zd} matrix of the form shown by Eq. 4.41, then an uncertainty in the frequency of a mode will manifest itself as an uncertainty in two parameters of the A_{zd} matrix. A physical parameter such as a stiffness does not appear explicitly in the modal state-space matrices; however, uncertainty in this parameter does have an affect on the mode shapes and frequencies, which do appear in the matrices.

Non-parametric uncertainties cannot be captured by an uncertainty in one or more parameters. For example, uncertainty in the model order implies that the number of states might be incorrect (*i.e.*, q is not the right length). This type of uncertainty can capture modeling errors such as modal truncation, lack of fidelity, and incorrect finite-element types. However, it is difficult to specify a form for this uncertainty. The error in representing a nonlinear system with a linear model is another example of a non-parametric uncertainty.

The preliminary work presented in this thesis focuses on uncertainties in the open-loop modal parameters of a structure. A goal is to enable the uncertainty analysis framework to be compatible with the disturbance and sensitivity analysis methods described in the previous chapters. The parameters are modal mass m, modal damping ζ, and natural frequency ω. The next section discusses methods to find the worst case RMS performance metrics σ_{z_i} when m, ζ, and ω are not known exactly.

5.2 Parametric Uncertainty Analysis Methods

A few potential approaches have been identified that can determine the worst-case performance due to parametric uncertainties. They include
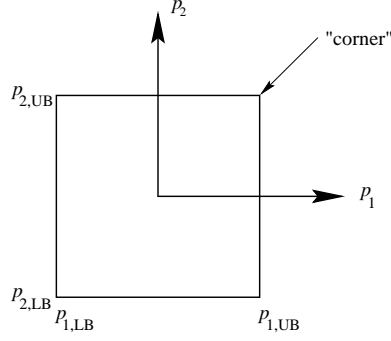
Figure 5.2: Parameter space for the case of two uncertain parameters.

- Exhaustive search of all "corners" of the uncertain parameter space

- First-order Taylor series approximation

- Constrained optimization problem

- Robust control tools for bounds on $\mathcal{H}_2$ performance

5.2.1 Evaluation of "bad corners"

To understand the motivation behind this approach, consider the case of two uncertain parameters each of which has a lower and an upper bound as indicated in Figure 5.2. The actual values of the parameters can lie anywhere within the space of the box. What is assumed is that the worst-case performance will occur when the parameters are at one of the corners of this box. For example, this is the technique used by Bryson and Mills in Reference [9] when designing robust LQG controllers via a minimax method. The LQG cost was evaluated at all of the corners to determine the maximum cost due to the uncertainties.

This approach is very straightforward to implement; however, it can be inefficient for large order systems with many uncertain parameters. If there are N parameters, then the total number of corners at which the performance must be evaluated is 2^N. Evaluating the performance at each corner implies that a separate disturbance analysis has to be conducted 2^N times. The computation time can be reduced; however, if appropriate model reduction techniques are implemented, as discussed in a subsequent section.

Another issue is the fact that the worst-case is assumed to occur at one of these corners. Reference [19] proves this for the simple case of SISO systems with no damping, but this will not be true in general. A simple counter-example consisting of a cantilevered beam

160

with nearly repeated modes is presented in Section 5.4.2. The next approach, which utilizes sensitivity information, can help to identify the potential "bad corner" *a priori*, thereby eliminating the need to perform 2^N disturbance analyses.

5.2.2 First-order approach

The first-order approach expresses the performance RMS values as a Taylor series approximation about the nominal values.

$$\sigma_z = \sigma_{z,\text{nom}} + \frac{\partial \sigma_z}{\partial p}(p - p_{\text{nom}}) + \text{H.O.T.} \tag{5.1}$$

where σ_z is a vector containing the RMS values for each performance metric. The vector p contains all of the uncertain parameters, and $\frac{\partial \sigma_z}{\partial p}$ is referred to as the sensitivity matrix. A technique for computing the sensitivities with respect to modal and physical parameters was presented in Chapter 4. Neglecting the higher order terms and making the substitutions $\Delta\sigma_z = \sigma_z - \sigma_{z,\text{nom}}$ and $\Delta p = p - p_{\text{nom}}$ results in

$$\Delta\sigma_z \approx \frac{\partial \sigma_z}{\partial p}\Delta p \tag{5.2}$$

The parameter uncertainty is captured by Δp, and in all approaches it is assumed that Δp is specified. For example, if all parameters are uncertain to within $\pm 1\%$ of the nominal values, then for the ith parameter, $\Delta p_i \in [-0.01 \;\; +0.01]p_{i,\text{nom}}$. We seek to determine the worst-case $\Delta\sigma_z$ for Δp within the specified bounds. One way to define the worst-case $\Delta\sigma_z$ is as the maximum magnitude of $\Delta\sigma_z$ over all allowable Δp. However, a problem with this definition is that a negative $\Delta\sigma_{z_i}$ has the same effect as a positive $\Delta\sigma_{z_i}$. The magnitude of a vector is only dependent on the squared values of the individual elements. We are actually interested in not only the maximum magnitude, but also in having as many of the individual elements as possible be positive. One option is to define the worst-case $\Delta\sigma_z$ to be the vector that has the largest sum. To enable performance metrics with different units to be summed, first define a normalization vector r. For instance, r could contain the performance RMS requirements as follows

$$r^T = \begin{bmatrix} \dfrac{1}{\sigma_{z1,\text{req}}} & \cdots & \dfrac{1}{\sigma_{nz,\text{req}}} \end{bmatrix} \tag{5.3}$$

where nz is the number of performance metrics. Then a scalar "cost" J can be defined as

$$J = r^T\Delta\sigma_z = \frac{\Delta\sigma_{z1}}{\sigma_{z1,\text{req}}} + \cdots + \frac{\Delta\sigma_{znz}}{\sigma_{znz,\text{req}}} \tag{5.4}$$

Expanding Eq. 5.2,

$$
\begin{aligned}
\Delta\sigma_{z_1} &= \frac{\partial\sigma_{z_1}}{\partial p_1}\Delta p_1 \;+\; \frac{\partial\sigma_{z_1}}{\partial p_2}\Delta p_2 \;+\; \cdots \;+\; \frac{\partial\sigma_{z_1}}{\partial p_{np}}\Delta p_{np} \\[2pt]
&\;\;\vdots \qquad\qquad \vdots \qquad\qquad \vdots \qquad\qquad\qquad \vdots \\[2pt]
\Delta\sigma_{z_{nz}} &= \frac{\partial\sigma_{z_{nz}}}{\partial p_1}\Delta p_1 \;+\; \frac{\partial\sigma_{z_{nz}}}{\partial p_2}\Delta p_2 \;+\; \cdots \;+\; \frac{\partial\sigma_{z_{nz}}}{\partial p_{np}}\Delta p_{np}
\end{aligned}
\tag{5.5}
$$

where np denotes the total number of uncertain parameters. Computing the cost J results in the following expression.

$$
J = \underbrace{\left(\frac{1}{\sigma_{z_1,\mathrm{req}}}\frac{\partial\sigma_{z_1}}{\partial p_1} + \cdots + \frac{1}{\sigma_{z_{nz},\mathrm{req}}}\frac{\partial\sigma_{z_{nz}}}{\partial p_1} \right)}_{\equiv a_1}\Delta p_1 + \cdots
\tag{5.6}
$$

$$
+ \underbrace{\left(\frac{1}{\sigma_{z_1,\mathrm{req}}}\frac{\partial\sigma_{z_1}}{\partial p_{np}} + \cdots + \frac{1}{\sigma_{z_{nz},\mathrm{req}}}\frac{\partial\sigma_{z_{nz}}}{\partial p_{np}} \right)}_{\equiv a_{np}}\Delta p_{np}
\tag{5.7}
$$

$$
= a_1\Delta p_1 + \cdots + a_{np}\Delta p_{np}
\tag{5.8}
$$

To maximize J, it is sufficient to maximize each of the $a_i\Delta p_i$ terms. This assumes that the Δp_i's occur independently; however, in reality, this might not be the case. For instance, if some of the uncertain parameters are modal frequencies, then specifying independent frequencies might not be physically realizable. This inconsistency will be allowed for the present purpose of finding the worst-case performance.

The Δp vector that maximizes J is therefore given by

$$
\Delta p_i = \begin{cases} \Delta p_{i,\mathrm{LB}} & , \text{ if } sgn(a_i) = -1 \\ \Delta p_{i,\mathrm{UB}} & , \text{ if } sgn(a_i) = +1 \\ \text{undefined} & , \text{ if } a_i = 0 \end{cases}
\tag{5.9}
$$

Substituting the worst-case Δp into Eq. 5.2 produces an estimate of the increase in RMS values due to the uncertainties. Thus, since the worst-case Δp is simply some combination of the bounds of the uncertain parameters, this approach identifies the "bad corner."

To summarize, the first-order approach approximates the change in performance RMS values as the product of a sensitivity matrix with a vector of parameter changes. The worst-case performance is defined as the maximum weighted sum of performance RMS values for parameter values within a specified uncertainty range. This leads to a simplistic linear programming problem whose solution places the worst-case uncertainties at either their lower or upper bounds. Instead of evaluating Eq. 5.8 at these bounds, a more accurate

value can be obtained simply by redoing a disturbance analysis with the system parameters set to the values at the "bad corner."

An advantage of this approach is that it is simple to implement once the sensitivities are computed. Also, it provides a worst-case estimate for each of the performance metrics. As will be shown, this is not possible for the robust control approach, which places a bound on the sum of the performance variances. The main disadvantage is the accuracy that can be obtained. Section 5.4 will compare the results obtained from this approach with the results from the constrained optimization approach. As the uncertainty ranges become larger, the first-order approach fails to accurately predict the worst-case performance.

5.2.3 Constrained optimization approach

This approach attempts to find a solution to the following optimization problem:

$$\max_{p} \quad J = \text{trace}(\Sigma_{\bar{z}}) \qquad (5.10)$$
$$\text{subject to } p_{\text{LB}} \leq p \leq p_{\text{UB}}$$

where as before p is a vector of uncertain parameters, and p_{LB} and p_{UB} are the lower and upper bounds, respectively, of the parameters. The covariance matrix $\Sigma_{\bar{z}}$ is based on the transformation $\bar{z} = Rz$, where R is a diagonal matrix used, for example, to normalize the performance metrics so as to include weightings or to remove units. One choice for R could be to place the elements of the r vector (described previously) along the diagonal of R. Then $\Sigma_{\bar{z}} = R\Sigma_z R^T = RC_{zd}\Sigma_q C_{zd}^T R^T$. The system is assumed to be of the form described by Eq. 4.6.

Eq. 5.10 expresses our desire to determine the set of allowable parameters that maximizes the sum of normalized performance variances. A technique that can be used to solve Eq. 5.10 is based on the Sequential Quadratic Programming (SQP) method, and the MATLAB function `constr.m` is an implementation of the method (see Reference [26]).

If the SQP method converges to a solution, it is not necessarily the global maximum. Local maxima may exist, and the SQP routine may converge to these depending on the initial guess that is provided to the routine. The only recourse is to begin with random initial guesses that are within the feasible space and then to check the consistency of the solutions that are obtained.

SQP is iterative in nature, and at each step the cost J and its gradient are computed. The major computation expense arises from solving the Lyapunov equation (Eq. 4.7) for the state covariance matrix. For large order systems, the solution time can be quite long. Also, if the routine is not provided with gradient information, it must be computed numerically. As will be shown, this reduces the efficiency of the routine. Whenever possible, gradients (*i.e.*, sensitivities) should be computed analytically; however, the sensitivity calculations also require the solution of Lyapunov equations. The next section will suggest possible model reduction strategies and approximations that can reduce the computational burden for the case of systems with a large number of states.

As in the first-order case, a benefit of the constrained optimization method is that it provides an estimate of the worst-case parameters, p. In addition, the individual performance RMS values for the worst-case p can be obtained by creating the system in Eq. 4.6 with the new parameters p instead of the nominal values. Then the solution to the Lyapunov equation, Eq. 4.7, is determined. The worst-case performance covariances follow directly from Eq. 4.8.

5.2.4   Robust control approach

Reference [87] describes a method for computing a bound on the $\mathcal{H}_2$ performance of a system with real parametric uncertainties. It builds upon the work in Reference [37]. A summary of the theory is presented in this section.

Begin by considering the system described by Eq. 4.6, but with real parametric uncertainties in the nominal A_{zd} matrix. The new system is of the form

$$
\begin{aligned}
\dot{q} &= (A_{zd} + \Delta A_{zd})\, q + B_{zd}\, d \\
z &= C_{zd}\, q
\end{aligned}
\tag{5.11}
$$

ΔA_{zd} is a real matrix which is assumed to be expressed in the form

$$
\Delta A_{zd} = B_\Delta \Delta C_\Delta
\tag{5.12}
$$

The Δ matrix can be thought of as a feedback block around the nominal system, as shown in Figure 5.3. Do not confuse the Δ matrix with the notation used to describe the change in a matrix (*e.g.*, $\Delta A_{zd} \equiv A_{zd,\text{actual}} - A_{zd,\text{nominal}}$). It should be evident from the context

which case is being used. In state-space form, the uncertain system is represented as

$$\dot{q} = A_{zd}\, q + B_\Delta\, u_\Delta + B_{zd}\, d$$

$$y_\Delta = C_\Delta\, q$$

$$z = C_{zd}\, q$$

$$u_\Delta = \Delta y_\Delta \tag{5.13}$$
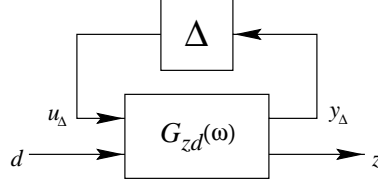
Figure 5.3: Uncertain system modeled by Δ block in feedback with nominal system.

Given np uncertain parameters that make up the vector p, we assume that they fall within a specified range given by an upper and lower bound.

$$p_{i,\mathrm{LB}} \le \delta_i \le p_{i,\mathrm{UB}} \qquad i = 1, \ldots, np \tag{5.14}$$

Define the static, diagonal matrices $M_1 = \mathrm{diag}(p_{i,\mathrm{LB}})$, $M_2 = \mathrm{diag}(p_{i,\mathrm{UB}})$, and $\Delta = \mathrm{diag}(\delta_i)$. Also, define

$$M_d = (M_2 - M_1)^{-1} \tag{5.15}$$

The worst-case performance metric function is the scalar cost that satisfies

$$J = \sup_{\Delta A} \left[\mathrm{trace}\left(B_{zd}^T P_{\Delta A} B_{zd} \right) \right] \tag{5.16}$$

for all allowable ΔA which lead to a stable $A_{zd} + \Delta A_{zd}$. $P_{\Delta A}$ is the solution to the Lyapunov equation

$$(A_{zd} + \Delta A_{zd})^T P_{\Delta A_{zd}} + P_{\Delta A_{zd}}(A_{zd} + \Delta A_{zd}) + C_{zd}^T C_{zd} = 0 \tag{5.17}$$

Note that the Lyapunov equation and the expression within the trace operator in Eq. 5.16 represent the dual formulation of the Lyapunov equation and performance covariance matrix presented in Eq. 4.7 and Eq. 4.8. Therefore, J represents the sum of the performance covariances. If desired, a normalizing matrix R can be used to define a new performance, $\bar{z} = Rz = RC_{zd}q$. This is analogous to what was presented in the constrained optimization case.

Reference [37] uses Popov analysis and dissipation theory to derive the following robust stability criterion. Given the system described by Eq. 5.11 with uncertainties specified by Eq. 5.14, then if there exist diagonal matrices $H > 0$ and $N \geq 0$, and if the following matrix is positive definite

$$R_o = HM_d + M_dH - B_\Delta^T C_\Delta^T N - NC_\Delta B_\Delta \tag{5.18}$$

then the system is robustly stable for all allowable Δ provided that there is a matrix $P \geq 0$ that solves the Riccati equation

$$(\hat{A}^T + \bar{C}_\Delta^T R_o^{-1} B_\Delta^T)P + P(\hat{A} + B_\Delta R_o^{-1} \bar{C}_\Delta) + PB_\Delta R_o^{-1} B_\Delta^T P + C_{zd}^T C_{zd} + \bar{C}_\Delta^T R_o^{-1} \bar{C}_\Delta = 0 \tag{5.19}$$

where

$$\hat{A} = A_{zd} + B_\Delta M_1 C_\Delta$$
$$\bar{C}_\Delta = HC_\Delta + NC_\Delta \hat{A}$$

In addition, a bound on the performance metric function J from Eq. 5.16 is given by

$$J \leq \mathcal{J} = \text{trace}\left[B_{zd}^T(P + C_\Delta^T(M_2 - M_1)NC_\Delta)B_{zd}\right] \tag{5.20}$$

The matrices H and N are known as stability multipliers.

Reference [87] finds the minimum $\mathcal{J}$ by specifying an optimization problem which minimizes $\mathcal{J}$ with respect to the diagonal elements of H and N subject to the constraints $H > 0$ and $N \geq 0$. The SQP method is used to find a solution, and the gradient of $\mathcal{J}$ is computed at each step. The Riccati equation constraint (Eq. 5.19) is implicitly accounted for by computing the gradient of $\mathcal{J}$ only in directions that place the trial points within the space defined by the Riccati equation. The positive definite constraint on the matrix R_o is not included because it is felt that the Riccati equation will have no solution when this constraint is not satisfied [87]. The optimization problem is shown to be convex, which implies that a converged solution should theoretically represent the overall minimum.

Although this approach appears attractive because of the rigorous mathematical theory that is used to derive the bound on J, it does suffer from a few disadvantages. One is that only a bound is provided by the method. There is no indication of exactly how tight the bound is. It also does not provide an estimate of the values δ_i of the Δ block that produce the bound. As a result, there is no way to estimate the individual worst-case performance variances. Recall that J represents the sum of the performance variances. The previous two

methods yield both the separate variances and the worst-case uncertainties. This allows the individual performance metrics to be compared against the requirements. Knowing the worst-case parameter values enables the worst case to be checked by substituting the values into the system and computing the performance.

When the system is written in structural modal form, the A_{zd} matrix is of the form shown in Eq. 4.41. For uncertainties in the open-loop damping ratios, the B_Δ and C_Δ matrices can be created as follows. First consider the case of a single mode with the corresponding A matrix

$$A = \begin{bmatrix} 0 & 1 \\ -\omega^2 & -2\zeta\omega \end{bmatrix} \tag{5.21}$$

Assume the damping uncertainty is written as

$$\zeta = \zeta_o(1 + \delta) \tag{5.22}$$

This leads to

$$A = \begin{bmatrix} 0 & 1 \\ -\omega^2 & -2\zeta_o\omega \end{bmatrix} + \begin{bmatrix} 0 & 0 \\ 0 & -2\zeta_o\omega\delta \end{bmatrix} = \underbrace{\begin{bmatrix} 0 & 1 \\ -\omega^2 & -2\zeta_o\omega \end{bmatrix}}_{A_o} + \underbrace{\begin{bmatrix} 0 \\ -2\zeta_o \end{bmatrix}}_{B_\Delta} \underbrace{\delta}_{\Delta} \underbrace{\begin{bmatrix} 0 & \omega \end{bmatrix}}_{C_\Delta}$$

$$\tag{5.23}$$

Note that this is not a unique representation for B_Δ and C_Δ since $-2\zeta_o\omega$ can be broken into two factors in several different ways.

For uncertainties in the open-loop natural frequencies, the procedure is not as direct. The main difficulty can be seen by examining the single mode A matrix. The frequency ω appears twice in the matrix. This would require Δ to contain two diagonal elements; however, there is no way to specify that the elements must be identical. This is due to the fact that the stability multipliers H and N are restricted to be diagonal. Block diagonal H and N would permit repeated elements in Δ. What is typically done in practice is to assume uncertainty in the squared natural frequency (as is done in Reference [37]).

$$\omega^2 = \omega_o^2(1 + \delta) \tag{5.24}$$

The uncertainty on ω is roughly $\delta/2$. ΔA can be expressed as

$$B_\Delta\Delta C_\Delta = \begin{bmatrix} 0 \\ -\omega_o \end{bmatrix} \delta \begin{bmatrix} \omega & 0 \end{bmatrix} \tag{5.25}$$

167

In general, if there is more than one uncertain frequency, then B_Δ and C_Δ can be constructed as follows. Let ω_i be the ith uncertain frequency, and assume that the ω_i^2 term appears at index (m, n) in the A_{zd} matrix. Then the ith column of B_Δ is

$$\begin{bmatrix} 0 \\ \vdots \\ 0 \\ -\omega_i \\ 0 \\ \vdots \\ 0 \end{bmatrix} \quad \leftarrow m\text{th row} \tag{5.26}$$

and the ith row of C_Δ is

$$\begin{bmatrix} 0 & \cdots & 0 & \omega_i & 0 & \cdots & 0 \end{bmatrix} \tag{5.27}$$
$$\uparrow n\text{th column}$$

In summary, this approach is appropriate to guarantee that the performance does not exceed a bound. This bound is computed by solving a constrained optimization problem with a Ricatti equation constraint and constraints on the stability multiplier matrices. Unfortunately, it does not provide a sense of how close the bound is to the worst case, nor does it indicate the values of the uncertain parameters that produce the bound.

5.3 Approximate Performance and Sensitivity Calculations

This section presents a model reduction technique that can be applied to large order state-space models. The motivation is to reduce the computational expense in solving Lyapunov equations. Performance assessment on a nominal state-space system involves determining the state covariance matrix from Eq. 4.7. Section 4.2 showed that computing sensitivities of performance covariances with respect to modal parameters involves solving a Lyapunov equation for every performance metric. The solution represents the Lagrange multiplier matrix that is required to compute the sensitivity. The order of a Lyapunov equation equals the order of the state-space system. The goal is to reduce the size of the system while maintaining the important dynamics. The approach is to determine a balanced realization for the system, and then to reduce states which have small Hankel singular values.

5.3.1 Balanced model reduction

5.3.1.1 Balanced realization

The first step is to create a balanced realization of the state-space system. The technique is described in Reference [65]. The criterion for a "balanced" system is that both the observability and controllability gramians are diagonal and equal. Consider again the disturbance-to-performance system, which is repeated here.

$$
\begin{aligned}
\dot{q} &= A_{zd}\, q + B_{zd}\, d \\
z &= C_{zd}\, q
\end{aligned}
\tag{5.28}
$$

The observability gramian, W_o, is the solution to the Lyapunov equation

$$
A_{zd}^T W_o + W_o A_{zd} + C_{zd}^T C_{zd} = 0
\tag{5.29}
$$

while the controllability gramian, W_c, is the solution to the dual Lyapunov equation

$$
A_{zd} W_c + W_c A_{zd}^T + B_{zd} B_{zd}^T = 0
\tag{5.30}
$$

Note that W_c appears in an identical fashion as Σ_q in Eq. 4.7; hence, W_c is the state covariance matrix in this case. In reality, W_c should be referred to as a disturbability gramian since d is a disturbance and not a control input. However this distinction does not affect the following steps.

We seek a similarity transformation matrix T such that when the states are transformed via $q = T\tilde{q}$ to produce the system

$$
\begin{aligned}
\dot{\tilde{q}} &= \underbrace{T^{-1}A_{zd}T}_{\tilde{A}_{zd}}\, \tilde{q} + \underbrace{T^{-1}B_{zd}}_{\tilde{B}_{zd}}\, d \\
z &= \underbrace{C_{zd}T}_{\tilde{C}_{zd}}\, \tilde{q}
\end{aligned}
\tag{5.31}
$$

then the gramians of the transformed system satisfy

$$
\tilde{W}_c = \tilde{W}_o = \mathrm{diag}\{\sigma_1, \cdots, \sigma_n\} \equiv \Sigma
\tag{5.32}
$$

The diagonal elements of Σ^2 will be referred to as the gramian values, and their square roots are known as the Hankel singular values [88]. It can be shown that

$$
\begin{aligned}
\tilde{W}_c &= T^{-1} W_c T \\
\tilde{W}_o &= T^T W_o T^{-1}
\end{aligned}
\tag{5.33}
$$

The transformation matrix T and the Hankel singular values are obtained from the eigenvalue decomposition of the matrix $W_c W_o$.

$$W_c W_o = T \Sigma^2 T^{-1} \tag{5.34}$$

The transformed states can be ordered such that the corresponding Hankel singular values are in decreasing order. The relative sizes of the singular values provide an indication of which states should be kept and which states might be eliminated. The intuition provided by Hankel singular values is that since the observability and controllability gramians are equal, large σ_i^2 correspond to states that are highly observable and controllable (*i.e.*, disturbable). These states are typically quite visible in the various disturbance-to-performance transfer functions. Because the system inputs are modeled with unit-intensity white-noise disturbance processes, the performance metric variances can be thought of as the area under the square of the transfer function magnitudes. Accurate performance prediction requires these states be retained in the model.

5.3.1.2   Model truncation

The model reduction step begins by partitioning the states into those that will be kept, $\tilde{q}_k$, and those that will be removed, $\tilde{q}_r$.

$$
\begin{aligned}
\left\{ \begin{array}{c} \dot{\tilde{q}}_k \\ \dot{\tilde{q}}_r \end{array} \right\} &= \left[\begin{array}{cc} (\tilde{A}_{zd})_{kk} & (\tilde{A}_{zd})_{kr} \\ (\tilde{A}_{zd})_{rk} & (\tilde{A}_{zd})_{rr} \end{array} \right] \left\{ \begin{array}{c} \tilde{q}_k \\ \tilde{q}_r \end{array} \right\} + \left[\begin{array}{c} (\tilde{B}_{zd})_k \\ (\tilde{B}_{zd})_r \end{array} \right] d \\
z &= \left[\begin{array}{cc} (\tilde{C}_{zd})_k & (\tilde{C}_{zd})_r \end{array} \right] \left\{ \begin{array}{c} \tilde{q}_k \\ \tilde{q}_r \end{array} \right\}
\end{aligned} \tag{5.35}
$$

At this point, there are two popular options for removing the unwanted states $\tilde{q}_r$. The simplest involves truncating the state-space system as shown below.

$$
\begin{aligned}
\dot{\tilde{q}}_k &= (\tilde{A}_{zd})_{kk}\, \tilde{q}_k + (\tilde{B}_{zd})_k\, d \\
z &= (\tilde{C}_{zd})_k\, \tilde{q}_k
\end{aligned} \tag{5.36}
$$

However, this does not preserve the static gain of the transfer functions. If desired, a static condensation procedure can be implemented as follows. First assume that the eliminated states are infinitely fast, such that $\dot{q}_r = 0$. Eliminating q_r from Eq. 5.35 results in the

following reduced system.

$$
\begin{aligned}
\dot{\tilde{q}}_k &= \underbrace{\left[(\tilde{A}_{zd})_{kk} - (\tilde{A}_{zd})_{kr}(\tilde{A}_{zd})_{rr}^{-1}(\tilde{A}_{zd})_{rk}\right]}_{\hat{A}_{zd}} \tilde{q}_k + \underbrace{\left[(\tilde{B}_{zd})_k - (\tilde{A}_{zd})_{kr}(\tilde{A}_{zd})_{rr}^{-1}(\tilde{B}_{zd})_r\right]}_{\hat{B}_{zd}} d \\
z &= \underbrace{\left[(\tilde{C}_{zd})_k - (\tilde{C}_{zd})_r(\tilde{A}_{zd})_{rr}^{-1}(\tilde{A}_{zd})_{rk}\right]}_{\hat{C}_{zd}} \tilde{q}_k + \underbrace{\left[(\tilde{C}_{zd})_r(\tilde{A}_{zd})_{rr}^{-1}(\tilde{B}_{zd})_r\right]}_{\hat{D}_{zd}} d
\end{aligned}
\tag{5.37}
$$

This can be written in the standard form

$$
\begin{aligned}
\dot{\hat{q}} &= \hat{A}_{zd}\,\hat{q} + \hat{B}_{zd}\,d \\
z &= \hat{C}_{zd}\,\hat{q} + \hat{D}_{zd}\,d
\end{aligned}
\tag{5.38}
$$

Notice that the static condensation method produces a D term which represents the static gain of the reduced states. This feedthrough term causes the performance variables in z to have infinite variance since the disturbance d is white noise. While $\hat{D}_{zd}$ helps the reduced model at low frequencies, it does not permit the $G_{zd}(\omega)$ transfer function matrix to roll-off at high frequencies. Thus, a way to remove $\hat{D}_{zd}$ while still preserving the low-frequency behavior is desired.

5.3.1.3   Removal of D term

A common solution to this problem is to append high-frequency poles whose low-frequency properties mimic that of the feedthrough term $\hat{D}_{zd}$. At frequencies above the poles, there will exist a natural roll-off at a rate related to the order of the pole. Various approaches append the poles in different ways. For instance, the equivalent of a low-pass filter can be placed between the actual white noise disturbance process d and a new disturbance $\bar{d}$ which drives the system. Or the low-pass filter can be appended at the output such that z represents the filtered response of the system. A faster roll-off in the filter comes at the cost of more filter states, which increase the size of the system. Recall that the goal of the current section is to examine ways to reduce the order of the state-space matrices. A first-order roll-off in $G_{zd}(\omega)$ is sufficient to ensure a bounded performance covariance matrix Σ_z.

To illustrate an approach for augmenting dynamics to remove $\hat{D}_{zd}$, append Eq. 5.38

with a new system that represents the high frequency poles.

$$
\left\{ \begin{array}{c} \dot{\hat{q}} \\ \dot{q}_a \end{array} \right\} = \underbrace{\left[\begin{array}{cc} \hat{A}_{zd} & 0 \\ 0 & A_a \end{array} \right]}_{\bar{A}_{zd}} \underbrace{\left\{ \begin{array}{c} \hat{q} \\ q_a \end{array} \right\}}_{\bar{q}} + \underbrace{\left[\begin{array}{c} \hat{B}_{zd} \\ B_a \end{array} \right]}_{\bar{B}_{zd}} d
$$
$$
\underbrace{\phantom{\left\{ \begin{array}{c} \dot{\hat{q}} \\ \dot{q}_a \end{array} \right\}}}_{\dot{\bar{q}}}
$$

$$
z = \underbrace{\left[\begin{array}{cc} \hat{C}_{zd} & C_a \end{array} \right]}_{\bar{C}_{zd}} \left\{ \begin{array}{c} \hat{q} \\ q_a \end{array} \right\} \tag{5.39}
$$

Notice that the D term has purposely been set to zero in this appended system. The transfer function matrix from d to z is given by

$$
\hat{G}_{zd}(s) = \hat{C}_{zd}(sI - \hat{A}_{zd})^{-1}\hat{B}_{zd} + C_a(sI - A_a)^{-1}B_a \tag{5.40}
$$

But the original transfer function matrix for the system described by Eq. 5.38 is of the form

$$
\hat{G}_{zd}(s) = \hat{C}_{zd}(sI - \hat{A}_{zd})^{-1}\hat{B}_{zd} + \hat{D}_{zd} \tag{5.41}
$$

Comparing Eq. 5.40 with Eq. 5.41 we see that the term $C_a(sI - A_a)^{-1}B_a$ appears in a similar fashion as the term $\hat{D}_{zd}$. Enforcing the constraint that the static gains for the two systems be identical leads to the following relationship that must be satisfied

$$
\hat{D}_{zd} = C_a(-A_a^{-1})B_a \tag{5.42}
$$

Let the dimension of $\hat{D}_{zd}$ be $m \times n$. Performing a singular value decomposition on $\hat{D}_{zd}$ leads to

$$
\hat{D}_{zd} = USV^H \tag{5.43}
$$

Suppose that the rank of $\hat{D}_{zd}$ is r. Define the new matrices

$$
\begin{aligned}
\bar{U} &= \text{ first } r \text{ columns of } U \\
\bar{S} &= \text{ upper left } r \times r \text{ submatrix of } S \\
\bar{V} &= \text{ first } r \text{ columns of } V
\end{aligned}
$$

It is straightforward to show that

$$
\hat{D}_{zd} = \bar{U}\bar{S}\bar{V}^H \tag{5.44}
$$

where now $\bar{S}$ is an $r \times r$ positive-definite diagonal matrix. If $-A_a^{-1}$ is also an $r \times r$ positive-definite diagonal matrix, then Eq. 5.44 can be manipulated into the form

$$
\hat{D}_{zd} = \underbrace{\bar{U}\sqrt{\bar{S}}\sqrt{-A_a^{-1}}}_{C_a}(-A_a^{-1})\underbrace{\sqrt{-A_a^{-1}}\sqrt{\bar{S}}\bar{V}^H}_{B_a} \tag{5.45}
$$

The required matrices B_a and C_a can be identified by comparing Eq. 5.45 with Eq. 5.42. What has not been discussed yet is how to specify A_a. The formulation above assumes that A_a is a diagonal, negative-definite matrix. This can be achieved by augmenting the system with r poles at a frequency of ω_{hi}. Then A_a will be

$$A_a = \begin{bmatrix} \ddots & & \\ & -\omega_{\text{hi}} & \\ & & \ddots \end{bmatrix} \tag{5.46}$$

The poles are typically placed at frequencies a decade above the highest frequency that is retained in the model.

5.3.1.4 Practical issues

A practical consideration when performing balanced model reduction is that if the various input/output channels have different units, then the balanced realization will favor states that are important in the transfer functions with larger magnitude. For example, suppose that the system of interest is an interferometer, and one performance metric is optical path difference (OPD) while another metric is wavefront tilt (WFT). If the OPD transfer function is orders of magnitude larger than the WFT transfer function, then states that are important to the WFT transfer function might have low Hankel singular values and be reduced out. It is important to scale the system so that transfer functions of interest have approximately the same magnitude level. (Recall that a numerical example of this issue was provided in Section 3.3).

It is also known that the balanced reduction method is not optimal with respect to the norm of the model error. The error is defined as the difference between the original transfer function and the reduced transfer function (*i.e.*, $G_{zd}(\omega) - \hat{G}_{zd}(\omega)$). Nevertheless, the method does provide a systematic approach to model reduction that can be easily implemented.

5.3.2 Analysis approximations during optimization iterations

When performing the uncertainty analysis via the constrained optimization approach described previously, it is necessary to compute the cost J and its gradient $\frac{\partial J}{\partial p}$ at each iteration step. For systems with a very large number of states, each of these computations can require a significant amount of computation time. Ideally, a reduced model would be created

initially and then used for all subsequent computations. However, the parameters of interest in the uncertainty analysis are open-loop modal parameters which appear explicitly in the system A_{zd} matrix (recall Eq. 4.41). The reduced $\bar{A}_{zd}$ matrix, while smaller in size as desired, has lost all explicit dependence on the modal parameters. Both the uncertainty analysis and the sensitivity analysis (which is used to compute $\frac{\partial J}{\partial p}$) require access to these parameters. Figure 5.4 summarizes three possible options for model reduction during the constrained optimization uncertainty analysis.

The initial solution to this problem is to perform a balanced model reduction at each iteration step, as shown in the middle path in Figure 5.4(b). A new admissible set of uncertain parameters is placed in A_{zd}, and the reduction process described in the previous section is applied to create $\bar{A}_{zd}$. The performance RMS values can then be obtained after solving Eq. 4.7 and applying Eq. 4.8 for the reduced system. The drawback to this approach is that determining the balancing transformation matrix T is the most time-consuming part of the reduction process. For example, it required approximately 6.5 minutes on a Sun Ultra 1 to compute T for a model which has on the order of 300 states. The time saved by using a reduced-order system in the Lyapunov equation, Eq. 4.7, is lost during the balancing step.

Performing balanced model reduction at each iteration, however, will not work when computing the sensitivity $\frac{\partial J}{\partial p}$. As shown in Section 4.2, the expression for the sensitivity of the cost J with respect to a parameter p is

$$\frac{\partial J}{\partial p} = \text{trace}\left[L\left(\frac{\partial A_{zd}}{\partial p}\Sigma_q + \Sigma_q\frac{\partial A_{zd}^T}{\partial p}\right)\right] \qquad (5.47)$$

where L is the Lagrange multiplier matrix and Σ_q is the state covariance matrix. It is assumed that neither B_{zd} nor C_{zd} is a function of p. The problem arises when computing $\frac{\partial A_{zd}}{\partial p}$ and $\frac{\partial A_{zd}^T}{\partial p}$. If the reduced matrix $\bar{A}_{zd}$ is used, then these derivatives cannot be readily computed.

A series of approximations is required to enable reduced-order models to be used during the optimization routine. The first one addresses the issue of recomputing the balancing transformation matrix T at each step. Let T_o be the transformation matrix that exactly balances the original, unperturbed system. The assumption that is made is that for small perturbations in the system, T_o will approximately balance the perturbed system. Considering only perturbations in the system A_{zd} matrix leads to the following approximately

original, unreduced system

$$\begin{bmatrix} A_{zd} & B_{zd} \\ C_{zd} & 0 \end{bmatrix}$$

balancing transformation: T
states to reduce: *elim_states*

perturbed, unreduced system

$$\begin{bmatrix} A_{zd}^* & B_{zd} \\ C_{zd} & 0 \end{bmatrix}$$

cost and sensitivity evaluation

J dJ/dp

SQP

$p(k+1) = p(k) + \alpha(k)\, d(k)$

converged?   N

Y

worst-case p

(a)

perturbed, unreduced system

$$\begin{bmatrix} A_{zd}^* & B_{zd} \\ C_{zd} & 0 \end{bmatrix}$$

compute T, select *elim_states*
perform balanced model reduction

approximate cost and sensitivity evaluation

J dJ/dp

SQP

$p(k+1) = p(k) + \alpha(k)\, d(k)$

converged?   N

Y

worst-case p

(b)

perturbed, unreduced system

$$\begin{bmatrix} A_{zd}^* & B_{zd} \\ C_{zd} & 0 \end{bmatrix}$$

use original T , *elim_states*
perform balanced model reduction

approximate cost and sensitivity evaluation

J dJ/dp

SQP

$p(k+1) = p(k) + \alpha(k)\, d(k)$

converged?   N

Y

worst-case p

(c)

Figure 5.4: Model reduction options during constrained optimization uncertainty analysis. (a) No model reduction. (b) Exact balanced reduction at each iteration. (c) Approximate balanced reduction at each iteration step. Both (b) and (c) rely on approximate cost and sensitivity evaluations.

balanced state-space matrices:

$$\tilde{A}^*_{zd} = T_o^{-1} A^*_{zd} T_o$$
$$\tilde{B}_{zd} = T_o^{-1} B_{zd}$$
$$\tilde{C}_{zd} = C_{zd} T_o$$

where A^*_{zd} is the perturbed A_{zd} matrix. Another assumption that can be made is that the states $\tilde{q}_r$ that are to be reduced are the same as the states removed from the original system (labeled *elim_states* in Figure 5.4). Therefore, $\tilde{A}^*_{zd}$, $\tilde{B}_{zd}$, and $\tilde{C}_{zd}$ can be partitioned as in Eq. 5.35, and the model truncation and D term removal steps can be followed as before. This will result in a reduced, perturbed system of the form

$$\dot{\bar{q}}^* = \bar{A}^*_{zd} \bar{q}^* + \bar{B}^*_{zd} d$$
$$z = \bar{C}^*_{zd} \bar{q}^* \tag{5.48}$$

which is analogous to Eq. 5.39. The estimate of the performance cost is obtained by first solving the Lyapunov equation

$$\bar{A}^*_{zd} \Sigma_{\bar{q}^*} + \Sigma_{\bar{q}^*} \bar{A}^{*T}_{zd} + \bar{B}^*_{zd} \bar{B}^{*T}_{zd} = 0 \tag{5.49}$$

and then computing

$$J = \text{trace}\left(\bar{C}^*_{zd} \Sigma_{\bar{q}^*} \bar{C}^{*T}_{zd} \right) \tag{5.50}$$

The next approximation deals with the sensitivity computation. The sensitivity formula in Eq. 5.47 can be approximated using the reduced system shown in Eq. 5.48.

$$\frac{\partial J}{\partial p} \approx \text{trace}\left[L^* \left(\frac{\partial \bar{A}^*_{zd}}{\partial p} \Sigma_{\bar{q}^*} + \Sigma_{\bar{q}^*} \frac{\partial \bar{A}^{*T}_{zd}}{\partial p} \right) \right] \tag{5.51}$$

where the Lagrange multiplier matrix is obtained from the Lyapunov equation

$$L^* \bar{A}^*_{zd} + \bar{A}^{*T}_{zd} L^* + \bar{C}^*_{zd} \bar{C}^{*T}_{zd} \tag{5.52}$$

The derivative $\frac{\partial \bar{A}^*_{zd}}{\partial p}$ is not as direct to compute. The first assumption is that the approximate, reduced $\bar{A}^*_{zd}$ is given by

$$\bar{A}^*_{zd} \approx P T_o^{-1} A^*_{zd} T_o P^T \tag{5.53}$$

The state elimination is approximated by a simple truncation performed by the matrix P, which is of the form

$$P = [I_{n_k \times n_k} \quad 0_{n_k \times n_r}] \tag{5.54}$$

where n_k is the number of states to keep and n_r is the number to remove. The second assumption is that T_o is not a function of the parameter p. This permits the derivative of $\bar{A}_{zd}^*$ to be expressed approximately as

$$\frac{\partial \bar{A}_{zd}^*}{\partial p} \approx P T_o^{-1} \frac{\partial A_{zd}^*}{\partial p} T_o P^T \tag{5.55}$$

The desired sensitivity is then computed by substituting $\frac{\partial \bar{A}_{zd}^*}{\partial p}$, L^*, and $\Sigma_{\bar{q}^*}$ into Eq. 5.51. The validity of this approximation will be analyzed in the following section. The sequence of steps that has just been outlined is shown in Figure 5.4(c).

5.4   Demonstration of Uncertainty Analysis

Having described a number of uncertainty analysis techniques and various approximations that can be made, the next step is to apply the methodology to systems of increasing order. The cases to be investigated are

- simple one degree-of-freedom (DOF) spring-mass system

- cantilevered beam with nearly square cross-section

- multiple DOF spring-mass system

- closed-loop model of the Space Interferometry Mission

The cantilevered beam example is used to motivate the need for a sophisticated uncertainty analysis method for systems with high modal density.

5.4.1   Single DOF system

A classic spring-mass system with assumed modal damping will serve to demonstrate the parametric uncertainty analysis. Figure 5.5(a) shows that the disturbance w is an inertial force acting on the mass, and the performance metric z is the position of the mass. The natural frequency is nominally $1\,\mathrm{Hz}$. The disturbance is modeled as colored noise, which means that it is the output of a linear shaping filter driven by unit-intensity, Gaussian white noise. A sensitivity analysis on the nominal system yields the normalized sensitivities in Figure 5.5(b). The power spectral density of w is plotted in Figure 5.5(c). In this example, the shaping filter is a first-order low pass filter with corner frequency at $1\,\mathrm{Hz}$.

Table 5.1: Uncertain parameters for single DOF case.

Parameter	Nominal value	Uncertainty	Worst-case	
$\omega_n/2\pi$	1 Hz	$\pm 5\%$	0.95 Hz	(-5%)
ζ	0.01	$\pm 10\%$	0.009	(-10%)
m	1	$\pm 2\%$	0.98	(-2%)

A frequency-domain disturbance analysis produces the performance PSD in Figure 5.5(d). The performance cumulative RMS plot indicates that the nominal performance RMS value is 3.59 mm. A hypothetical performance requirement line at 1 mm is also shown in Figure 5.5(d).

The three parameters that were considered uncertain are the modal frequency ω_n, the modal damping ζ, and the modal mass m. Table 5.1 lists the nominal values, the percent uncertainties that were assumed, and the worst-case parameters identified during the uncertainty analysis. Implementing the uncertainty analysis via the constrained optimization approach produces the results in Figure 5.6. Ten separate runs were conducted, each with a random initial guess for the uncertain parameters. Run 0 just shows the nominal parameter values (placed proportionally between the dotted lines representing the upper and lower bounds). Each run converged to the lower uncertainty bound for each parameter. This agrees with the intuition provided by the normalized sensitivities in Figure 5.5(b). All the sensitivities are negative, which implies that decreasing the parameters will increase the RMS. Lower damping results in a larger response magnitude. A lower natural frequency keeps the mode away from the roll-off region of the disturbance filter, thereby exacerbating the response. A lower modal mass allows the disturbance to excite the mode to a greater extent. (Recall that $\ddot{q} + 2\zeta\omega_n\dot{q} + w_n^2 = w/m$. As m decreases, the modal force increases.)

In this case, placing each parameter at the lower bound produces the largest RMS increase. This is the same logic employed by the first-order approach. In fact, the first-order approximation predicts a worst-case RMS of 4.20 mm (indicated by the dash-dot line in Figure 5.6), which is in error by only -1.76% from the actual worst-case value of 4.27 mm.

Because of the system's small number of states, the approximation techniques described previously did not have to be applied. The exact cost and gradient information could be provided to the Sequential Quadratic Programming method. Figure 5.7(a) shows that the

(a)

(b)

(c)

(d)
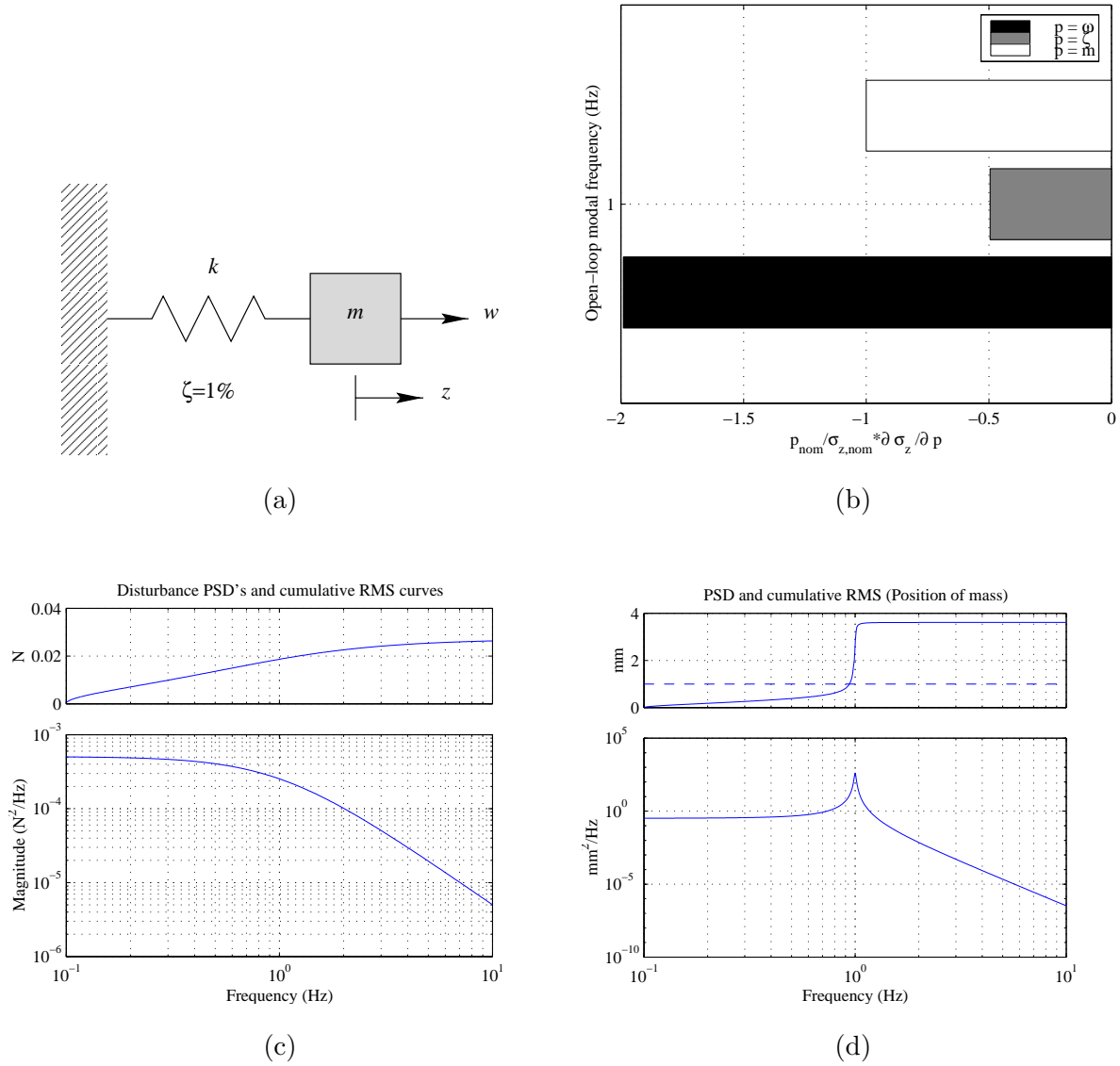
Figure 5.5: (a) Single DOF system. (b) Normalized sensitivities. (c) Disturbance PSD (bottom) and cumulative RMS (top). (d) Performance PSD (bottom) and cumulative RMS (top).
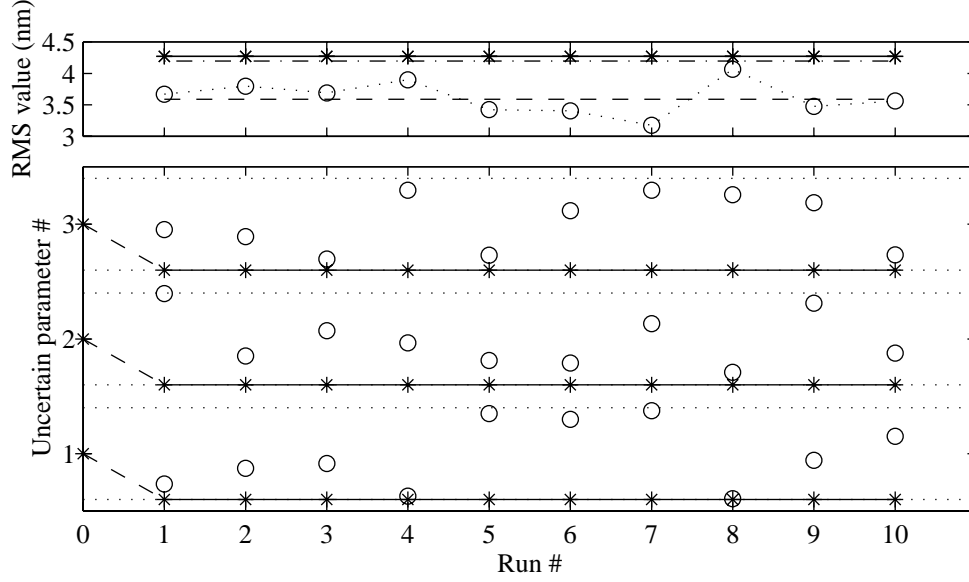
Figure 5.6: Results of uncertainty analysis on single DOF case. **Bottom plot**, parameter values: Constrained optimization initial guess, ○, and converged solution, ∗. Parameter #1 = ω_n, #2 = ζ, #3 = m. ⋯: upper or lower bound. **Top plot**, RMS values: − − − nominal; ○⋯○ initial guess; ∗ − ∗ worst case; − · − first-order approximation.

average time for the uncertainty analysis was on the order of 0.30 sec. Each of the ten runs required only three iterations to converge to the worst-case parameters.

To examine the accuracy of the first-order approach, various levels of uncertainty were assigned to the three modal parameters. The percent difference between the first-order approach and the constrained optimization approach is plotted in Figure 5.7(b) as a function of the uncertainty size. As expected, the first-order approximation produces negligible errors only when the uncertainties are small. The approximation is no longer valid for large uncertainty ranges.

In summary, it has been shown that for the case of a single mode driven by a low-pass disturbance, the largest increase in performance RMS is accomplished by placing the uncertain modal parameters at their lower bounds. The uncertainty analysis reveals that the actual performance RMS can be as much as 19.0% larger than the nominal performance for the uncertainty ranges considered.
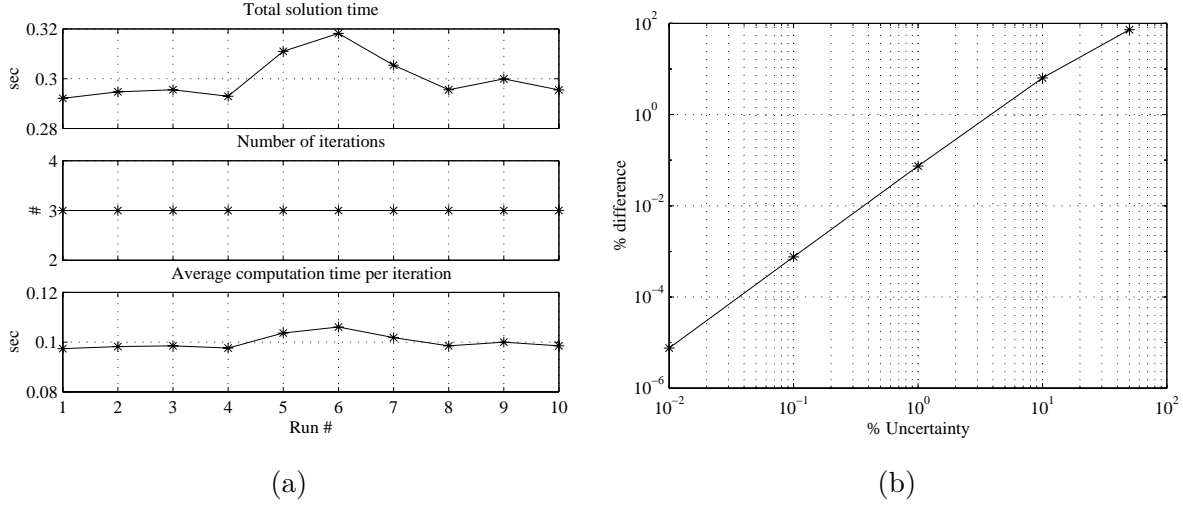
Figure 5.7: (a) Time statistics for constrained optimization uncertainty analysis. (b) Percent differences between first-order approach and constrained optimization as a function of uncertainty size.

5.4.2 Cantilever beam

It is anticipated, however, that in general the worst-case parameters will not necessarily be at the bound in the direction indicated by the sensitivity analysis. It can be envisioned that for complex systems with high modal density, the results will not be as straightforward. The coupling between parameters will not be negligible. An example of a cantilevered beam with nearly repeated frequencies is used to demonstrate this fact.

Consider the beam depicted in Figure 5.8. The material is aluminum with density $2700\,\mathrm{kg/m^3}$, Young's modulus $70\,\mathrm{GPa}$, length $0.50\,\mathrm{m}$ and width $1\,\mathrm{cm}$. Modal damping is set to 0.5%. To cause the first two bending frequencies to almost coincide, let the height of the beam be $1.05\,\mathrm{cm}$. The disturbance is a tip force oriented at a $45°$ angle in the plane of the cross-section. It is white noise with intensity $10^{-4}\,\mathrm{N^2}$. The performance metric is the tip displacement (in millimeters) along the same direction. The beam is modeled with a single Bernoulli-Euler beam element with six DOF's at the tip node. Furthermore, a consistent mass matrix formulation is used. The first two frequencies are assumed to have an uncertainty range of $\pm 5\%$.

Figure 5.9(a) shows the tip displacement PSD for the nominal beam, as well as the PSD's for several combinations of uncertainties. Notice that the largest RMS value of the cases shown corresponds to the case when the two frequencies happen to coincide at a frequency equal to the geometric mean of the two nominal frequencies. This can be seen more clearly
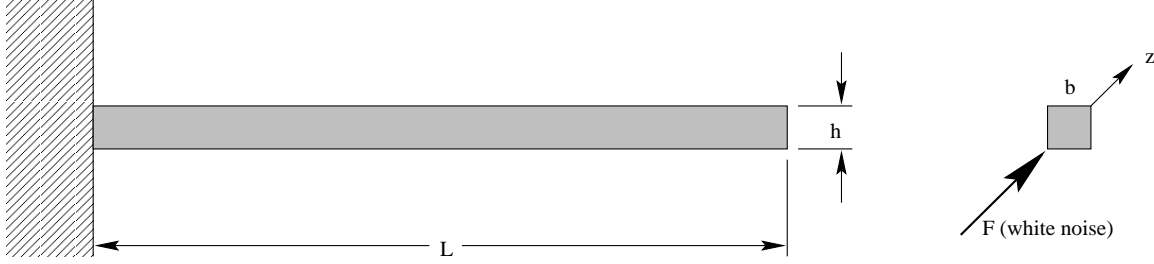
Figure 5.8: Cantilevered beam with nearly square cross-section.

in Figure 5.9(b), which zooms in on the region of interest.

The normalized sensitivities with respect to the nominal modal parameters of the first four modes are presented in Figure 5.10(a). The largest sensitivities correspond to the modal parameters of the first two modes. The signs indicate that to increase the RMS, these parameters should be decreased. If the frequency parameters are placed at the uncertainty bounds indicated by these sensitivities (*i.e.*, at -5% and -5%, respectively), the resulting RMS is not maximized. Thus a naïve guess which places the parameters at these bounds does not capture the overall worst-case parameter variations.

Figure 5.11(a) shows the sensitivities with respect to the first two frequencies as the first mode sweeps from -5% to $+5\%$ and the second mode sweeps from $+5.3\%$ to -4.8%. An arbitrary constraint that was imposed is that $\frac{\omega_1}{\omega_{1,\text{nom}}} \frac{\omega_2}{\omega_{2,\text{nom}}} = 1$, *i.e.*, the geometric mean of ω_1 and ω_2 is constant and equal to the nominal geometric mean of these two frequencies. Because the uncertainty ranges of the two frequencies overlap, the sensitivity and performance plots do not exhibit monotonic behavior in general. The frequency sensitivity curves indicate that the slopes change sign twice during the frequency sweep. The performance curves peak when the frequency ratio causes the two modes to coincide. This non-monotonic phenomenon explains why relying solely on the nominal sensitivity information does not work.

Placing the two frequencies at the geometric mean of the nominal frequencies has so far been used only as a counter-example. It demonstrates that for the case of closely-spaced modes, the worst-case performance does not necessarily occur when the uncertain modal parameters are placed at one of their bounds. To find the true worst-case performance, the uncertainty analysis optimization was applied to this beam example. Figure 5.12(a) shows the results when the first two frequencies have a $\pm 5\%$ uncertainty. The second frequency

182

Figure 5.9: Tip displacement PSD's and cumulative RMS curves for systems with various combinations of first and second mode frequencies. (a) Full frequency range. (b) Zoom around first two modes.
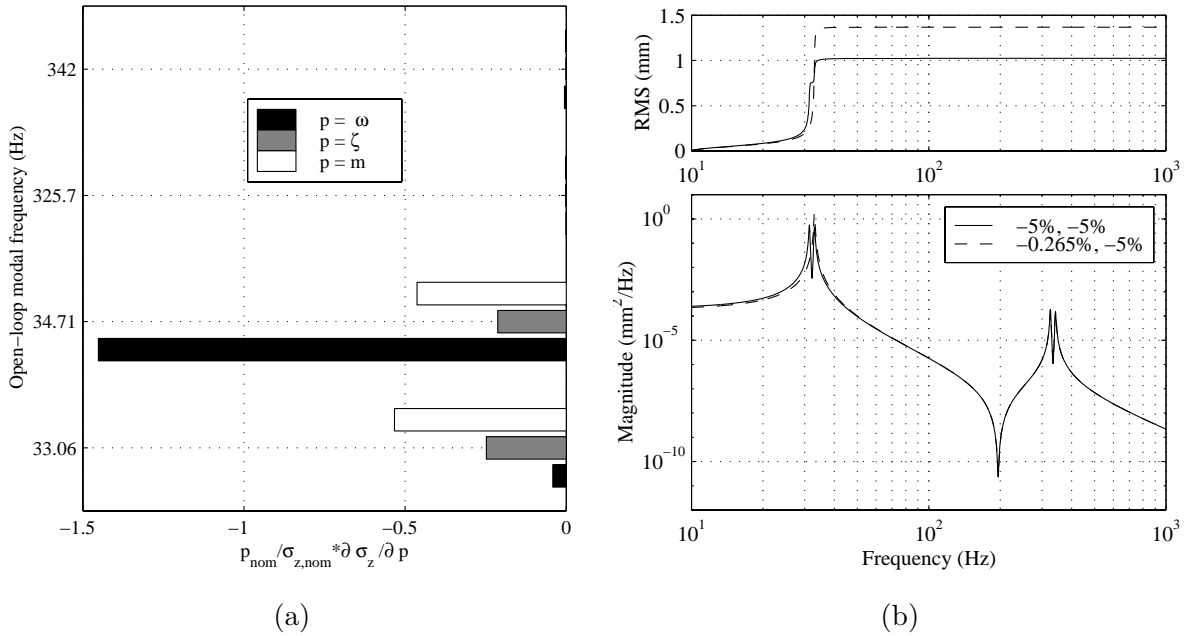
Figure 5.10: (a) Normalized sensitivities for the first four modes. (b) Tip displacement PSD's and cumulative RMS curves for system with frequencies placed at lower bounds (−) and for system with frequencies specified by uncertainty analysis results (−−).
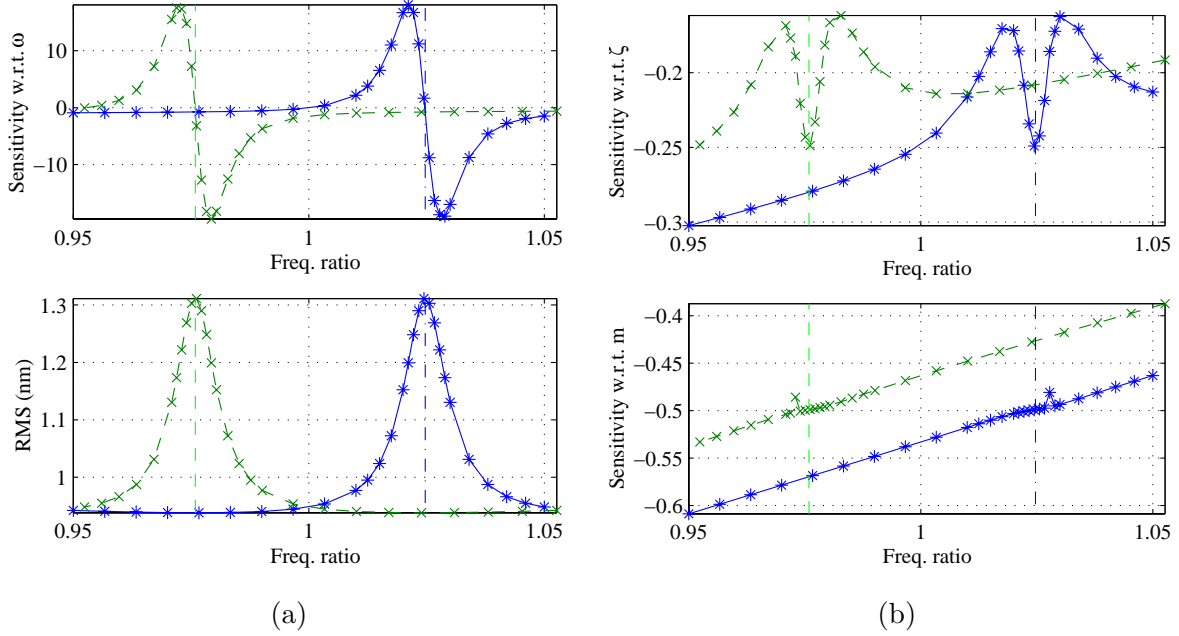
Figure 5.11: Various plots obtained when ω_1 ($*-*$) is swept up while ω_2 ($\times--\times$) is swept down. (a) Top: normalized sensitivity w.r.t. ω; bottom: performance RMS. (b) Top: normalized sensitivity w.r.t. ζ; bottom: normalized sensitivity w.r.t. m.

converges to the lower bound after each of the ten runs; however, the first frequency is not as consistent. Runs 8 and 10 place the first frequency at its lower bound, but the RMS in these runs clearly is not the worst-case value. Note also that the first-order approximation (dashed-dot line) does poorly because it assumes the worst-case occurs at the uncertainty bounds indicated by the sensitivities. It does approximate well the value obtained by the two runs (8 and 10) that converged (incorrectly) to the lower bounds.

To provide a physical explanation for these results, consider the PSD and cumulative RMS curves presented in Figure 5.10(b). The solid line corresponds to when the two frequencies are placed at their lower bounds. We saw that this produced an RMS value larger than any of the other cases which placed the frequencies at various combinations of the bounds. The dashed line corresponds to placing the frequencies at the worst-case values produced by the uncertainty optimization. The second frequency is located at its lower bound (-5%), and the first frequency is placed at this *same* frequency. The cumulative RMS curve indicates that this yields a slightly larger total RMS value.

Figure 5.12(b) shows the results when the damping ratios (uncertain parameters 3,4)

184

Figure 5.12: Results of uncertainty analysis optimization after ten runs for beam with closely-space modes. (a) Uncertainties only in frequencies of first two modes. (b) Uncertainties in frequency, damping, and modal mass of first two modes.

and modal masses (uncertain parameters 5,6) of the first two modes are also treated as uncertain. These parameters also converge to their lower bounds, which is consistent with the negative sensitivities shown in Figure 5.10(a). The sensitivity plots in Figure 5.11(b) do not exhibit monotonic behavior; however, they do not have rapid sign changes as was the case for the sensitivity curve with respect to frequency. Since the sensitivities are always negative, this could explain why the worst-case modal damping and mass parameters are at the lower bounds.

Now we turn our attention to the case when the bending mode frequencies of the cantilevered beam are well separated. This is achieved by setting the height, h, of the beam to 1.8 cm. Figure 5.13(a) contains the tip displacement PSD's and cumulative RMS curves for the nominal system as well as for systems with the first two frequencies placed at various uncertainty bounds. Because of the frequency separation, the uncertainty ranges do not overlap. The largest RMS value corresponds to the case when the two frequencies are at the lower bound of -5%. The sensitivities shown in Figure 5.13(b) confirm that the correct direction to move the frequencies is toward the left (*i.e.*, toward lower frequencies).
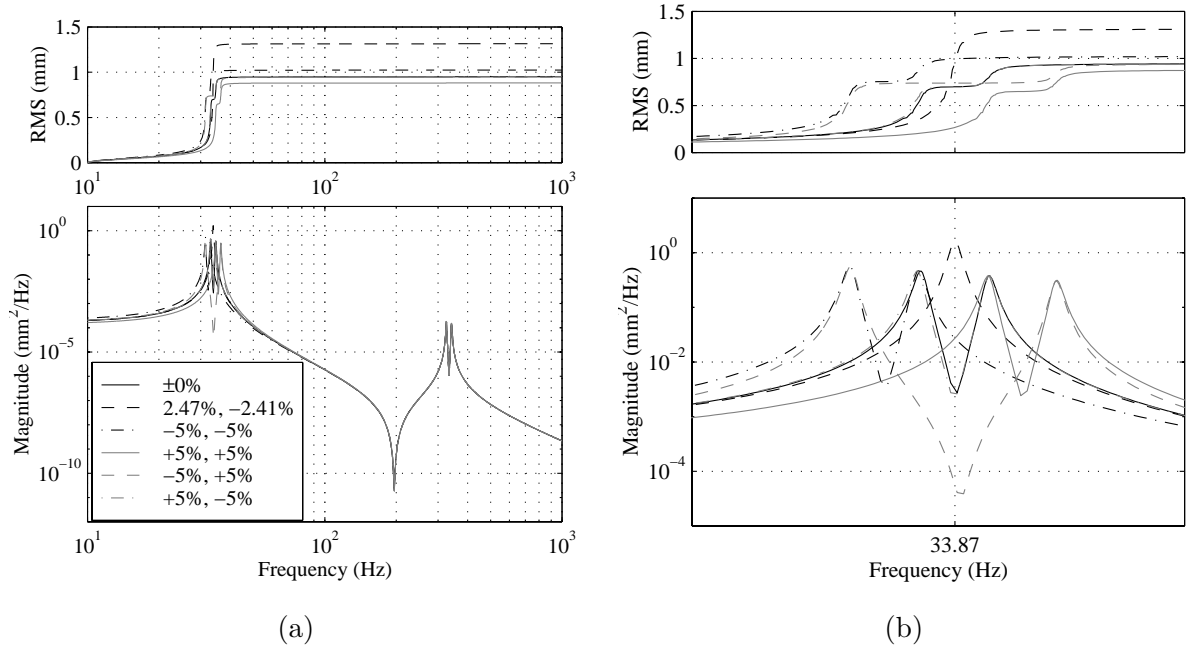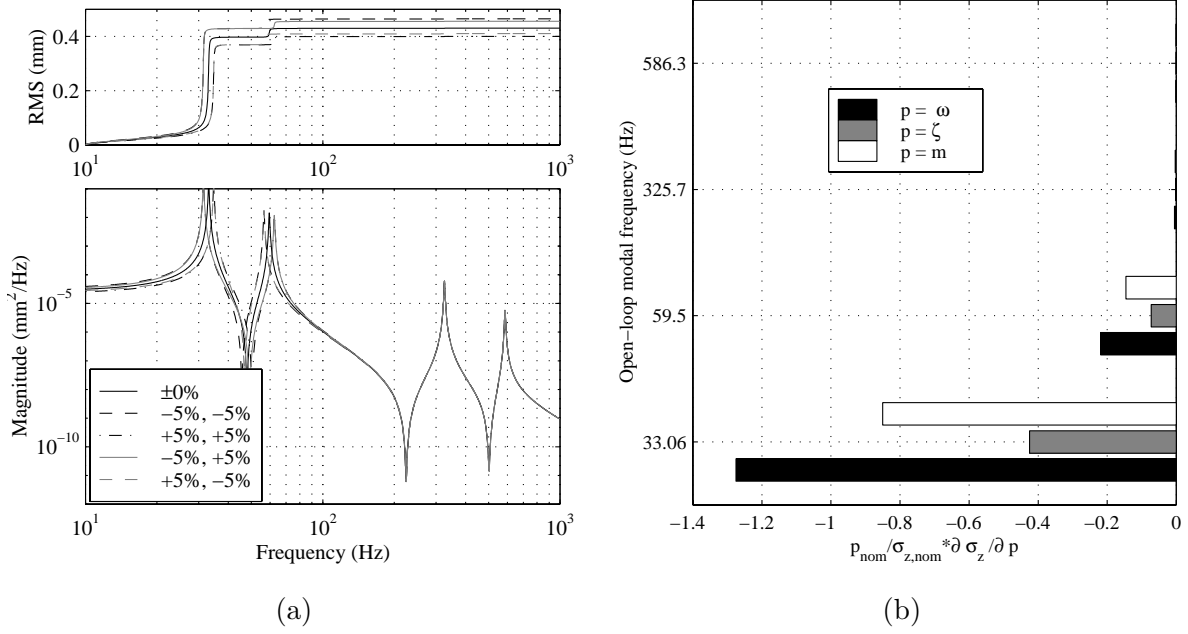
Figure 5.13: (a) Tip displacement PSD's and cumulative RMS curves for systems with various combinations of first and second mode frequencies. (b) Normalized sensitivities for the first four modes.

If we sweep the frequencies of the first and second modes in a similar fashion as was done for the previous case, we obtain the sensitivity and performance curves shown in Figure 5.14. All the curves are either monotonically increasing or decreasing. There are no drastic sign changes as was seen before. This suggests that the worst-case parameter changes should be at the bounds indicated by the signs of the sensitivities. To confirm this, the uncertainty analysis optimization method was applied, and sample results are presented in Figure 5.15. In most instances, all parameters converge to the lower bounds as expected. The cases in which the optimization routine converged to a different solution have a lower RMS value, and hence do not represent worst-case solutions.

Further work is needed to identify if in general for systems with adequate modal separation, the worst-case modal parameters will always lie at the appropriate uncertainty bound. This would greatly simplify the uncertainty analysis since the computationally-intensive optimization could be bypassed. Furthermore, this sample case showed that even for closely-spaced modes, the sensitivities with respect to damping and modal mass did not change sign over the uncertainty range. This suggests that the only parameters that might be needed for the optimization method are the frequencies of the modes. Deriving general

186
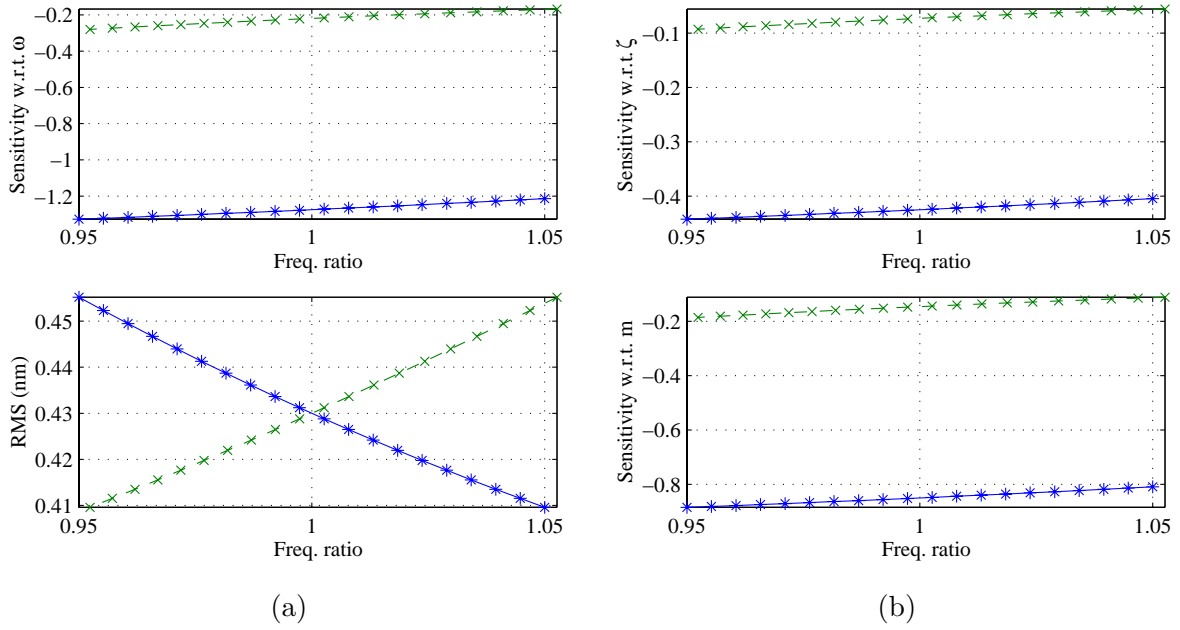
Figure 5.14: Various plots obtained when ω_1 ($*--*$) is swept up while ω_2 ($\times-\times$) is swept down. (a) Top: normalized sensitivity w.r.t. ω; bottom: performance RMS. (b) Top: normalized sensitivity w.r.t. ζ; bottom: normalized sensitivity w.r.t. m
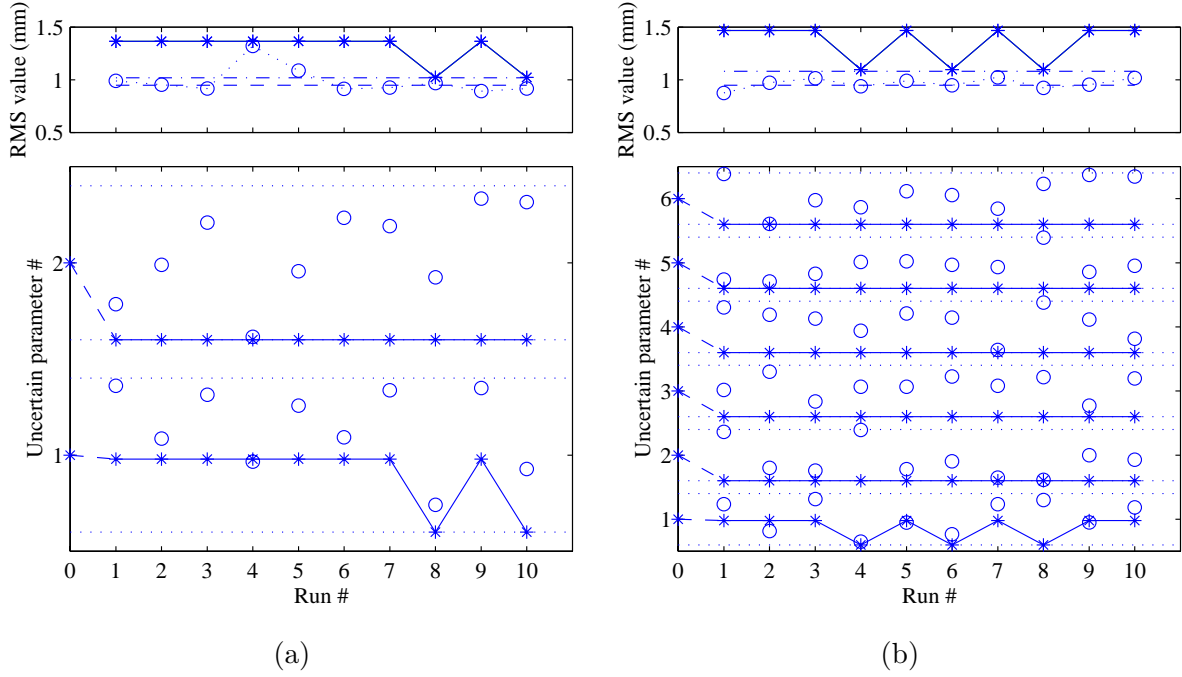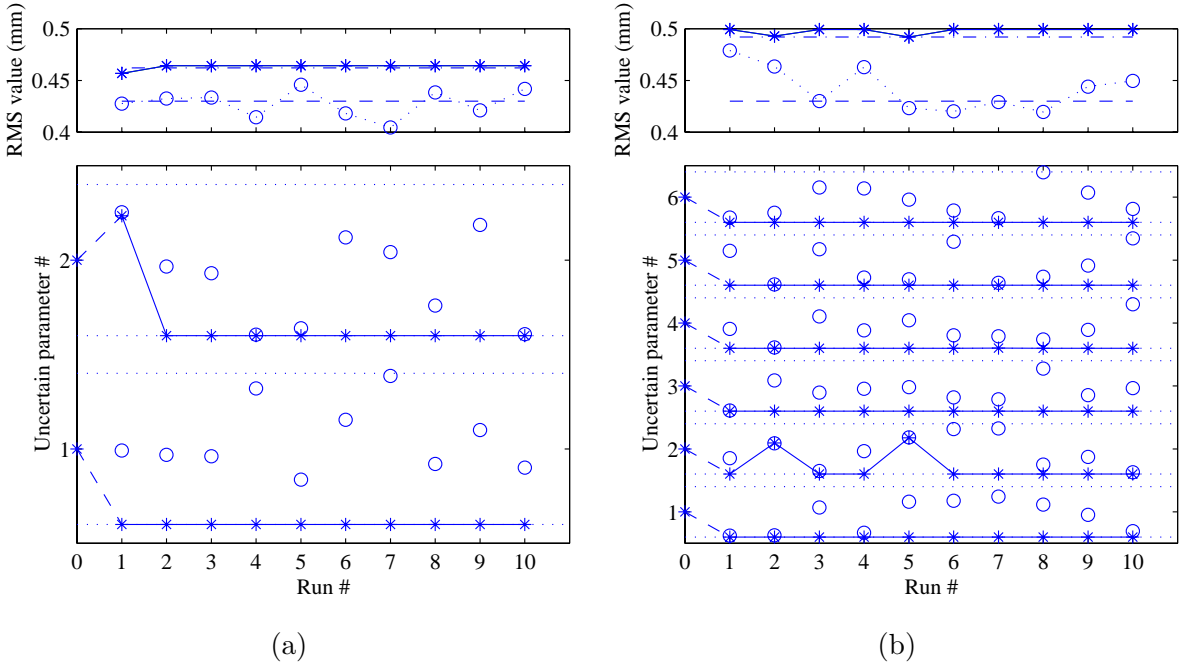

Figure 5.15: Results of uncertainty analysis optimization after ten runs for beam with well-separated modes. (a) Uncertainties only in frequencies of first two modes. (b) Uncertainties in frequency, damping, and modal mass of first two modes.

results such as this would be highly beneficial, and efforts in this area should be pursued.

5.4.3 Multi-DOF system

Now consider the system in Figure 5.16(a) consisting of 20 masses and 19 springs. Each mass and spring constant was randomly selected from a specified interval. Modal damping was uniformly assigned a value of 0.1%. There are a total of six disturbance input locations at DOF's 7 through 12. The performance metric is the differential motion of the two end masses (*i.e.*, $z = x_{20} - x_1$). The PSD's of the disturbances are shown in Figure 5.16(b), where the larger magnitude PSD corresponds to the first three disturbances and the lower magnitude PSD corresponds to the last three disturbances. Propagating these PSD's through the system disturbance-to-performance transfer function yields the performance PSD in Figure 5.16(c). Three modes contribute most to the RMS value, as indicated by the cumulative RMS curve. The normalized sensitivities with respect to the modal parameters of these modes are indicated in Figure 5.16(d).

At this point, it is useful to comment on the importance of the information provided by the sensitivity analysis and the frequency-domain disturbance analysis. Both can be used to identify the dominant system modes. When performing an uncertainty analysis, only uncertainties in parameters associated with these modes need to be considered. The uncertainties in the other modes have to be extremely large to affect the performance in a comparable manner as the uncertainties in the critical modes. Therefore, these two analyses can reduce the total number of uncertain parameters that are carried through to the uncertainty analysis. Although all modes might initially be considered uncertain to some degree, only a subset will be important. In this case, the modal parameters of the first three modes are treated as uncertain. This yields a total of nine uncertain parameters. The nominal uncertainties are shown in Table 5.2.

The multi-DOF model is useful in showing the benefits of using reduced models and of supplying the optimization routine with gradient information. The model is of a size which permits some of these issues to be explored. First, consider the efficiency of the SQP routine when it has knowledge of the gradients of the cost function. Figure 5.17(a) displays the results of ten runs of the uncertainty analysis when analytical gradients are not provided. Only one run (#9) comes closest to converging to the proper bounds. One reason for this could be that when gradients are not supplied, the MATLAB function `constr.m`
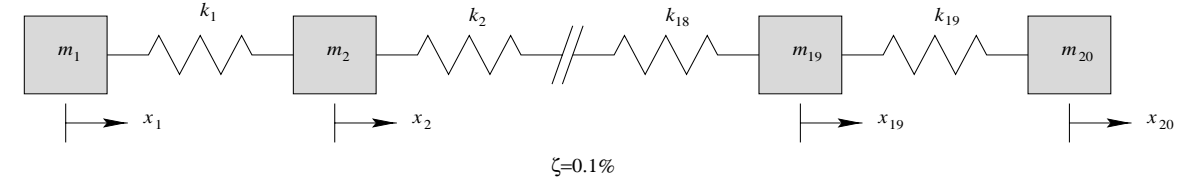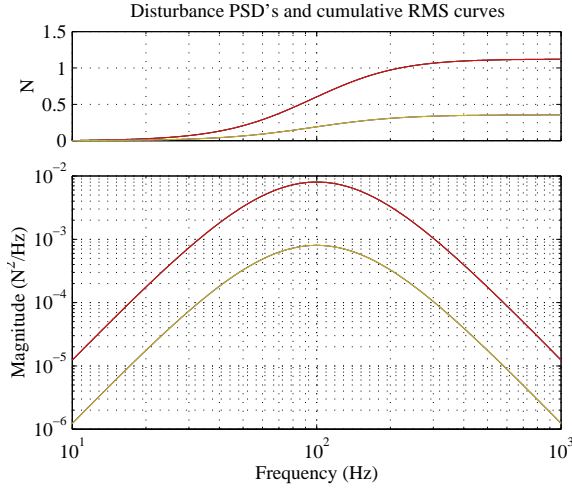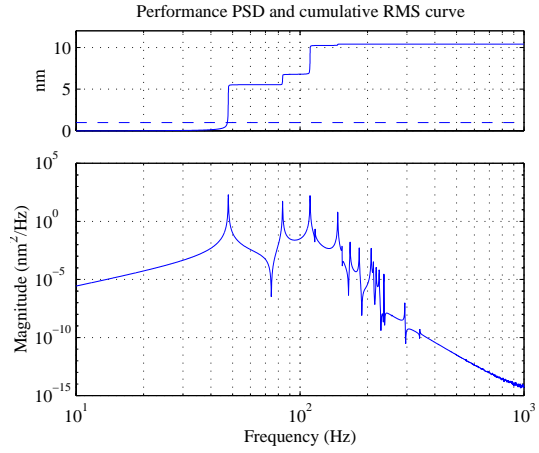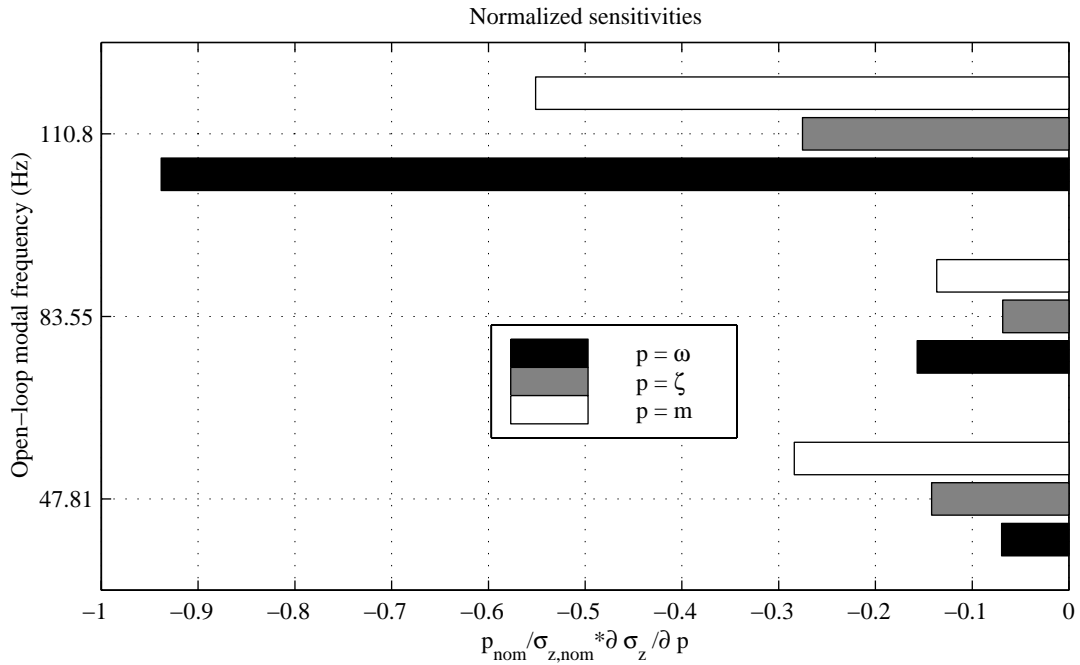
Figure 5.16: (a) 20 DOF spring/mass system. (b) Disturbance PSD's (bottom) and cumulative RMS (top). (c) Performance PSD (bottom) and cumulative RMS (top). (d) Normalized sensitivities of critical modes.

Table 5.2: Uncertain parameters for multi-DOF case.

#	Parameter	Nominal value	Uncertainty
1	$\omega_1/2\pi$	47.8 Hz	$\pm 5\%$
2	$\omega_2/2\pi$	83.5 Hz	$\pm 5\%$
3	$\omega_3/2\pi$	110.8 Hz	$\pm 5\%$
4	ζ_1	0.01	$\pm 10\%$
5	ζ_2	0.01	$\pm 10\%$
6	ζ_3	0.01	$\pm 10\%$
7	m_1	1	$\pm 2\%$
8	m_2	1	$\pm 2\%$
9	m_3	1	$\pm 2\%$

uses a finite-difference approximation. Section 4.4.2 showed that for this model, the finite-difference approximation can contain significant errors as the perturbation size is made extremely small. Figure 5.17(b) shows the results when the same initial guesses are used in the ten runs, but this time the analytical gradients are computed. All runs consistently converge to the lower bounds of the parameters. In addition, Figure 5.18(a) indicates that the computation time is improved by factors of 5–10.

The first-order approximation is expected to do best when the uncertainty ranges are small, and this is confirmed in Figure 5.18(b). The uncertainty size is assumed to be the same for all nine parameters, and this size takes on the values $\pm 10\%$, $\pm 1\%$, and $\pm 0.1\%$. As Figure 5.18(b) shows, the percent difference between the worst case predicted by the first-order approach and the worst case predicted by the optimization becomes smaller as the uncertainty size is reduced.

The advantages of using reduced-order models can be demonstrated by considering a series of reduced models with the number of states equal to 36, 28, 22, and 18, respectively. The balanced model reduction method described in the previous section was used, and the performance PSD plot for these different size models can be found in Figure 5.19(a). Also shown is the cumulative RMS plot, which indicates that all models predict essentially the same overall RMS value. Although significant differences can be seen in the PSD's, particularly at low and high frequencies, all the various size models accurately capture the

Figure 5.17: Results of uncertainty analysis optimization after ten runs. (a) Full-order model without gradient calculations. (b) Full-order model with gradient calculations.

behavior in the frequency range of the dominant modes. When performing model reduction, it is important to confirm that the reduced model still contains the necessary dynamics for accurate performance prediction.

Figure 5.19(b) plots the gramian values of the balanced, full-order system, and they are normalized such that the largest has a value of 1. They are sorted in decreasing size, and there are a total of 42 since the system has 42 states. Immediately, one notices that the last four states can be reduced out because their gramian values are several orders of magnitude smaller than the ones preceding them. Reducing out more states is then a trade-off between smaller-order models and performance prediction capability.

The main advantage of smaller-order models is that the time to solve Lyapunov equations is reduced. When performing the uncertainty analysis optimization, time savings at each iteration manifests itself as overall time savings in the solution process. This is evident in Figure 5.20(a), which shows the total solution time, the total number of iterations, and the computation time per iteration for each run of the optimization. Gradient (*i.e.*, sensitivity) information is computed at each iteration, which implies that the solution of an
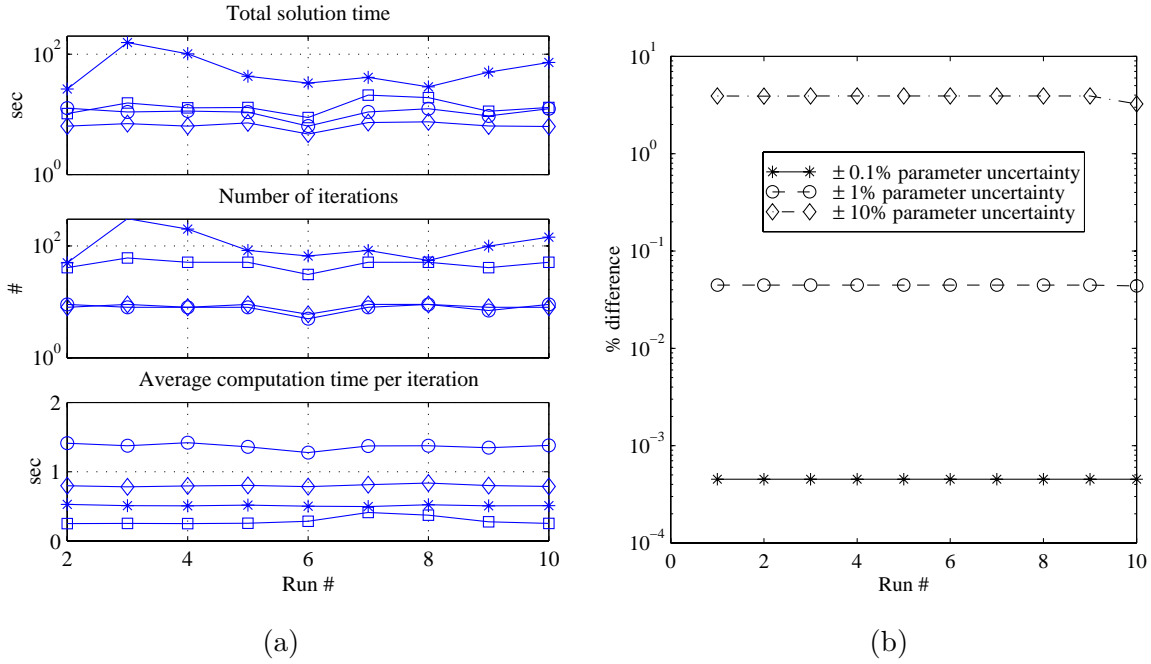
Figure 5.18: (a) Time statistics for different order models when gradients are or are not supplied. *: 42 states, no gradient info., ○: 42 states, w/ gradient info., ◇: 28 states, w/ gradient info., □: 28 states, no gradient info. (b) Effects of uncertainty size on accuracy of first-order uncertainty analysis.
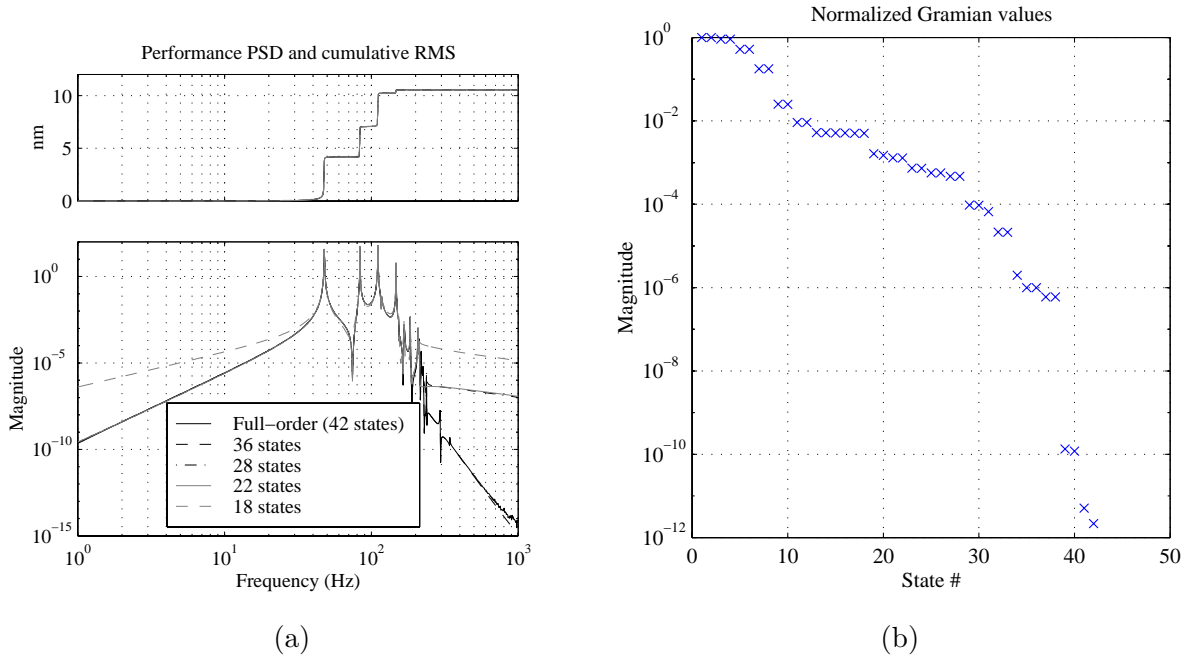
Figure 5.19: (a) Performance PSD's of different order models (bottom) and cumulative RMS (top). (b) Gramian values of balanced full-order system.
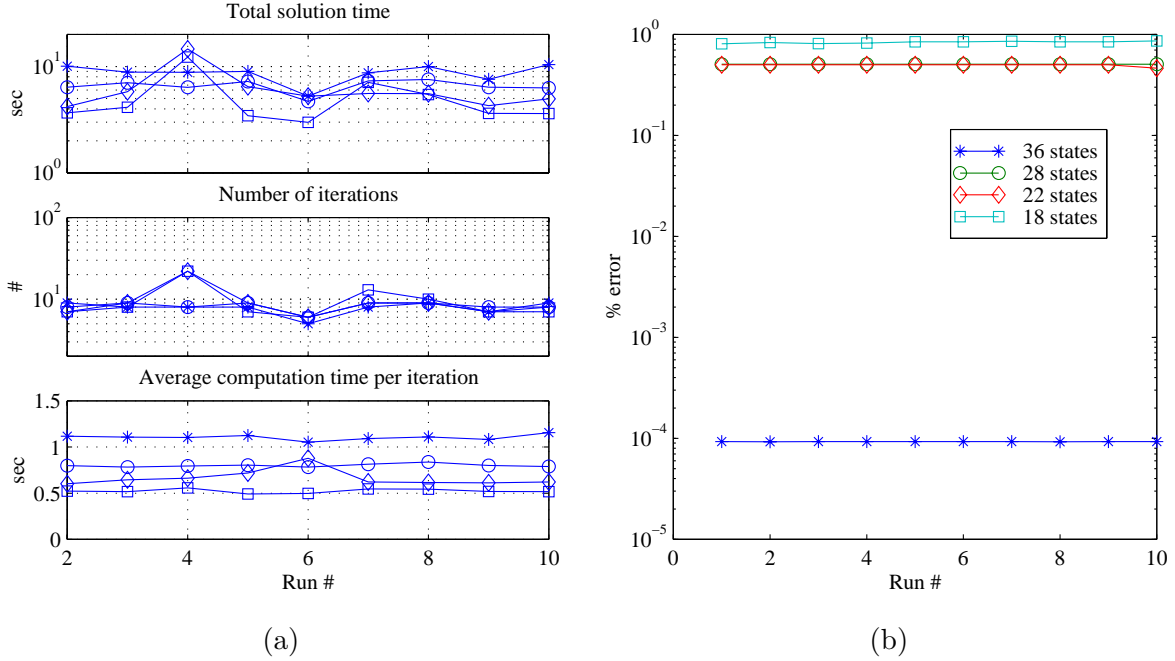
Figure 5.20: (a) Time statistics for different order models (gradients are supplied in each case). (b) Percent errors between worst-case RMS predicted by reduced-order models and worst-case RMS predicted by full-order model.

additional Lyapunov equation is required. The first run is not shown because the balancing transformation matrix for the original system occurs during this initial run and causes the solution time to increase significantly. With the exception of run 4, the general trend is that smaller models run much faster. The only reason run 4 required more time for the 22 state and 18 state models was that they required more iterations to converge to a solution. The time spent at each iteration still favors the smaller models.

Figure 5.20(b) shows how accurately the worst-case performance is predicted by the method that uses approximate balanced model reduction at each iteration. The parameter values to which the optimization converged were placed into the full-order model, and the RMS value was compared to the value obtained at the end of the run. What is plotted in Figure 5.20(b) is the percent error between the exact RMS using the full-order model and the approximate RMS using the reduced-order models at the end of each run. The error ranges from $10^{-4}\%$ for the 36 state model to almost 1% for the 18 state model. This confirms why it seems as if all the cumulative RMS curves in Figure 5.19 appear to be the same. A 1% difference is not distinguishable on the scale of the plot.
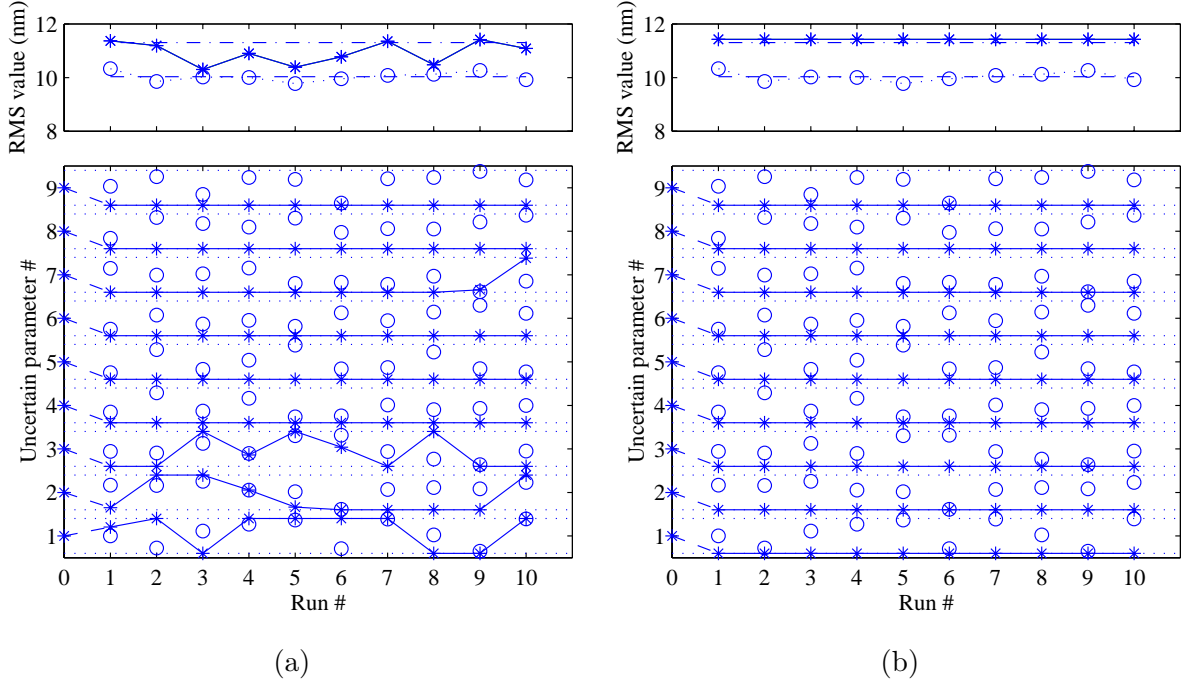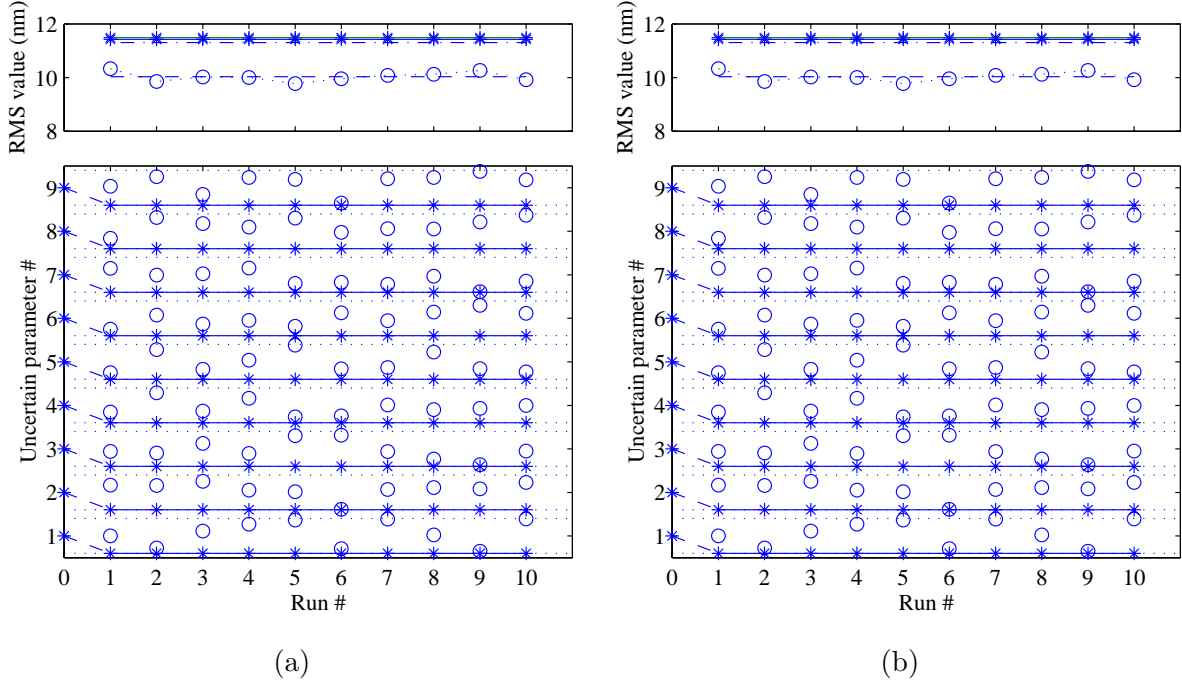
Figure 5.21: Results of uncertainty analysis optimization after ten runs. (a) Reduced-order model (28 states) without gradient calculations. (b) Reduced-order model (28 states) with gradient calculations.

Figure 5.21 shows the uncertainty analysis plots obtained after running the optimization routine ten times for the 28 state reduced model. Subplot (a) is for the case when gradients are not computed analytically at each iteration, while subplot (b) is for the case when the gradients are computed. The same initial guesses were provided to the corresponding runs of both cases. As can be seen, both cases converged to the lower bound of all the uncertain modal parameters. The time statistics for each of the runs can be found in Figure 5.18(a), and the benefits of knowing the gradients at each iteration are evident. Although the computation time per iteration becomes larger when gradients are computed, the savings are achieved because gradient information helps convergence to occur in a fewer number of iterations.

At this point, we can examine the validity of the approximation methods that were applied. Recall that one approximation is that the balancing transformation matrix of the original, unreduced system will also approximately balance the perturbed system. Figure 5.22(a) compares the exact gramian values of the balanced, perturbed system with the diagonal entries of the controllability gramian for the perturbed system after it has been

194
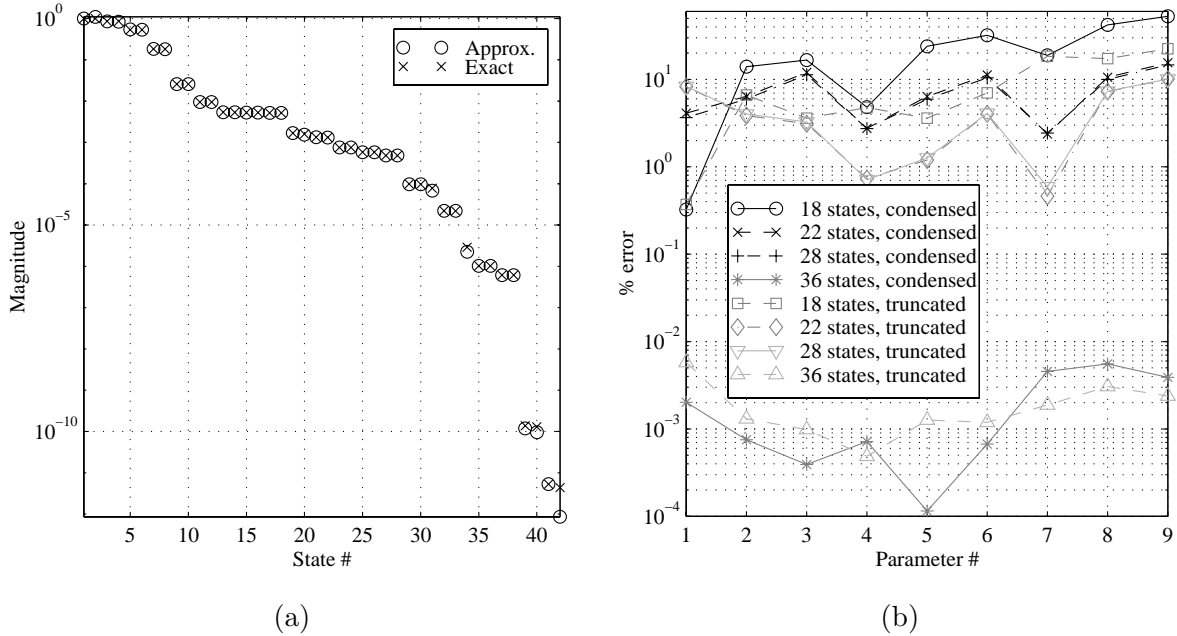
Figure 5.22: (a) Gramian values of exactly balanced system and approximately balanced system. Values shown are for one specific iteration during uncertainty optimization run. (b) Average error in approximate sensitivity computation during uncertainty optimization run.

transformed. In other words, let T_o be the original transformation matrix. The controllability gramian for the perturbed system after it has been transformed using T_o will not necessarily be diagonal. Figure 5.22(a) plots the diagonal entries of this controllability gramian matrix along with the exact gramian values. There are only minor differences in the magnitude of the two different sets of values. It is anticipated that the differences would be more apparent if the system was perturbed in a much larger fashion than it was for this demonstration case.

Figure 5.22(b) provides an indication of the error in the approximate sensitivity computations for the different size models. It shows for each of the nine uncertain modal parameters the average percent error in the sensitivities with respect to those parameters. In general, the sensitivities are more accurate when the model is not reduced drastically. Also, it appears as if the sensitivities are more accurate when the model is reduced by a strict truncation instead of by a static condensation. The only exception is for some of the parameters of the model with 36 states.

To summarize, the multiple mass-spring model has served to identify some of the impor-

tant issues regarding model reduction in the uncertainty analysis optimization technique. The lesson learned is that care must be taken in reducing the state-space system to the appropriate size to gain the benefits of faster computation time while still preserving the accuracy of the approximate cost and sensitivity estimates. In addition, the use of the original balancing transformation matrix during all of the iterations appears to be valid in this case.

5.4.4   SIM Classic

The integrated model of SIM Classic will now be used to demonstrate the uncertainty analysis technique on a system with an even larger number of states. Figure 5.23(a) shows the finite-element model and a ray trace of stellar light passing through two arms of guide interferometer #1. The model is identical to the one used in the frequency-domain disturbance analysis described in Section 3.3. The disturbance PSD's are obtained from a low-order shaping filter that approximates the PSD's of a four-wheel configuration of Hubble-class reaction wheels whose speeds are treated as uniform random variables over the range 0–3000 RPM. (A description of the shaping filter was provided in Section 4.4.3.)

The performance metric for this example is the total stellar optical path difference (OPD) of the guide interferometer visible in Figure 5.23(a). The PSD and cumulative RMS curve of the OPD when the disturbances are propagated through the SIM model are shown in Figure 5.23(c). The dominant modes are in the 10–20 Hz range as is indicated by the sharp vertical steps in the cumulative RMS curve across these frequencies. The normalized sensitivities of this RMS value with respect to the modal parameters of three of the most dominant modes are presented in Figure 5.23(d). The frequencies have positive sensitivities, and this implies that the worst-case RMS should be obtained when the modal frequencies are increased.

The disturbance and sensitivity analysis results in Figure 5.23 were used to select three critical modes for the uncertainty analysis. Initially, only the frequencies of these modes were considered to be uncertain. The frequencies and uncertainty values are listed in Table 5.3. The results of ten runs of the uncertainty analysis using the constrained optimization approach are shown in the usual form in Figure 5.24. The left subplot truncates the model to 150 states at each iteration in order to perform the approximate sensitivity performance evaluations. The right subplot truncates the model to 120 states. With the exception of
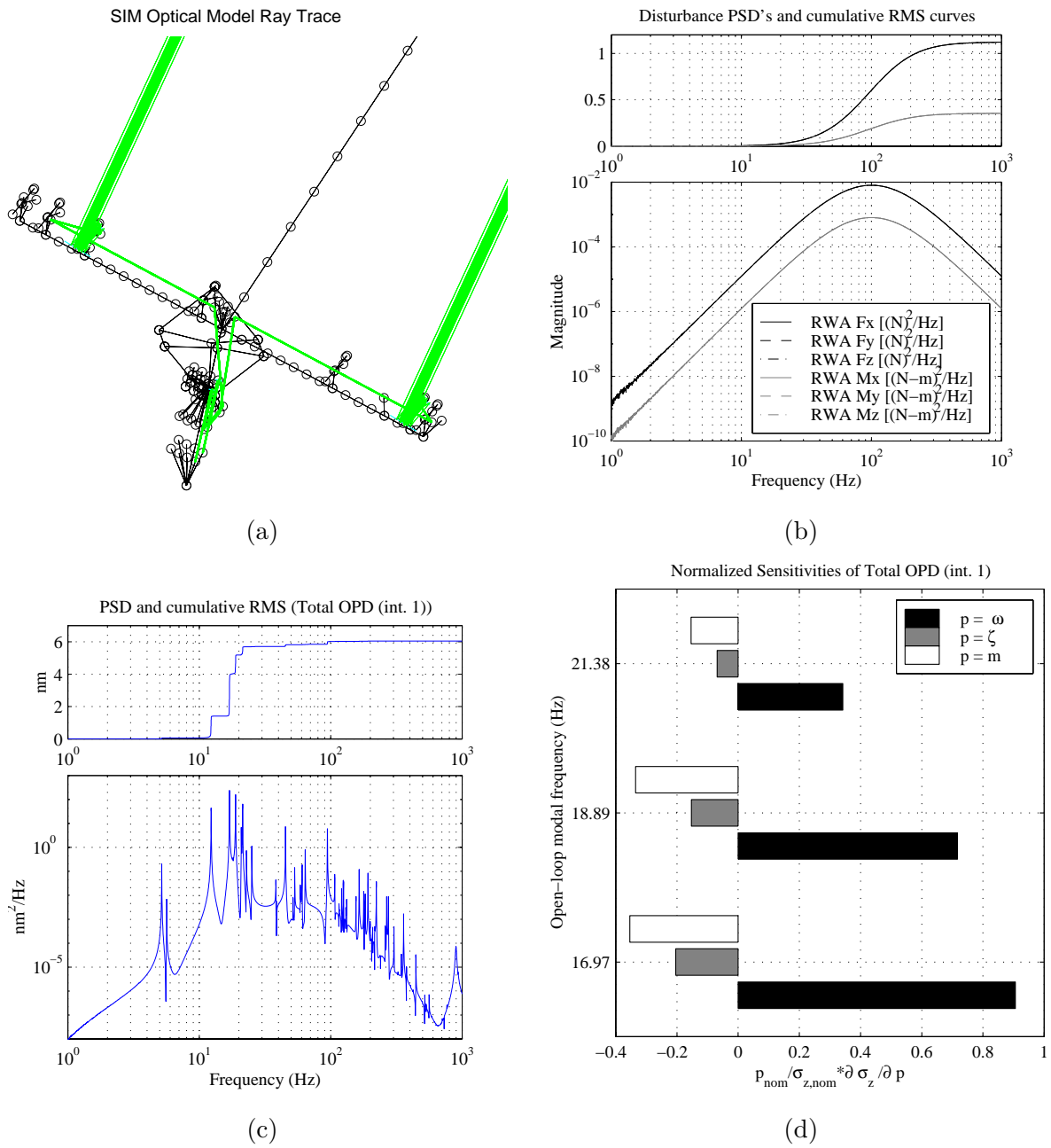
Figure 5.23: (a) Stellar ray trace through guide interferometer #1 of SIM. (b) Approximate PSD's (bottom) and cumulative RMS (top) of reaction wheel disturbances. (c) Performance PSD (bottom) and cumulative RMS (top). (d) Normalized sensitivities of performance RMS with respect to modal parameters of critical modes.

the first run, the 150 state case consistently converges to the upper bound of the modal frequencies. The reduced-order models only slightly underpredict the worst-case performance achieved when the upper bounds are placed into the full-order model and the exact RMS is computed. The first-order sensitivity approach does a good job, although it also underpredicts. The average time required to complete an iteration of the optimization was 46.6 sec, and the average number of iterations before a run would converge was 6. Thus, a typical run would only require less than five minutes to arrive at a prediction of the worst-case performance. The final result of this case indicates that with $\pm 5\%$ uncertainty in the frequencies of three critical modes, the predicted RMS value can increase from its nominal value of 5.57 nm to a worst-case value of 6.37 nm, which represents a 14.4% increase.

For the 120 state case, the reduced-order model has a larger error in its ability to predict the actual performance; consequently, the optimization routine has more difficulty in converging to the correct parameter bounds. This reveals the importance of choosing the correct size for the reduced-order model. A plot of the gramian values in Figure 5.25 indicates that the value of the 150th gramian is a factor of 10 lower than the value of the 120th gramian. Since it is not readily apparent based on this plot that the 150 state model should do significantly better than a 120 state model, several model reduction iterations are needed to ensure that the reduced model has retained a sufficient number of states for performance prediction.

Now consider the situation when we treat as uncertain all the modal parameters associated with the three dominant modes. The pertinent values are listed in Table 5.3. Figure 5.26 shows the outcome of ten runs of the optimization routine. Most runs consistently place the frequencies at the upper bounds and the damping at the lower bounds. The seven runs that produce the largest RMS (as predicted by the reduced model) place the second and third modal masses at the lower bounds and the first modal mass at the upper bound. This first modal mass is the only parameter that converges to a bound different from that indicated by the sign of the sensitivity. Upon closer examination, run 3 does place the first modal mass at the lower bound. This particular case shows that the RMS predicted by the full-order model (indicated by a $\square$) is slightly larger than the RMS predicted by the corresponding reduced-order model. These results lead to a possible conclusion that the model reduction is not accurately capturing the true RMS level. This highlights the need for proper model reduction, and the example is meant to demonstrate the results from

Table 5.3: Uncertain parameters for SIM case.

#	Parameter	Nominal value	Uncertainty
1	$\omega_{13}/2\pi$	16.97 Hz	±5%
2	$\omega_{15}/2\pi$	18.89 Hz	±5%
3	$\omega_{17}/2\pi$	21.38 Hz	±5%
4	ζ_1	0.001	±10%
5	ζ_2	0.001	±10%
6	ζ_3	0.001	±10%
7	m_1	1	±2%
8	m_2	1	±2%
9	m_3	1	±2%

(a)   (b)
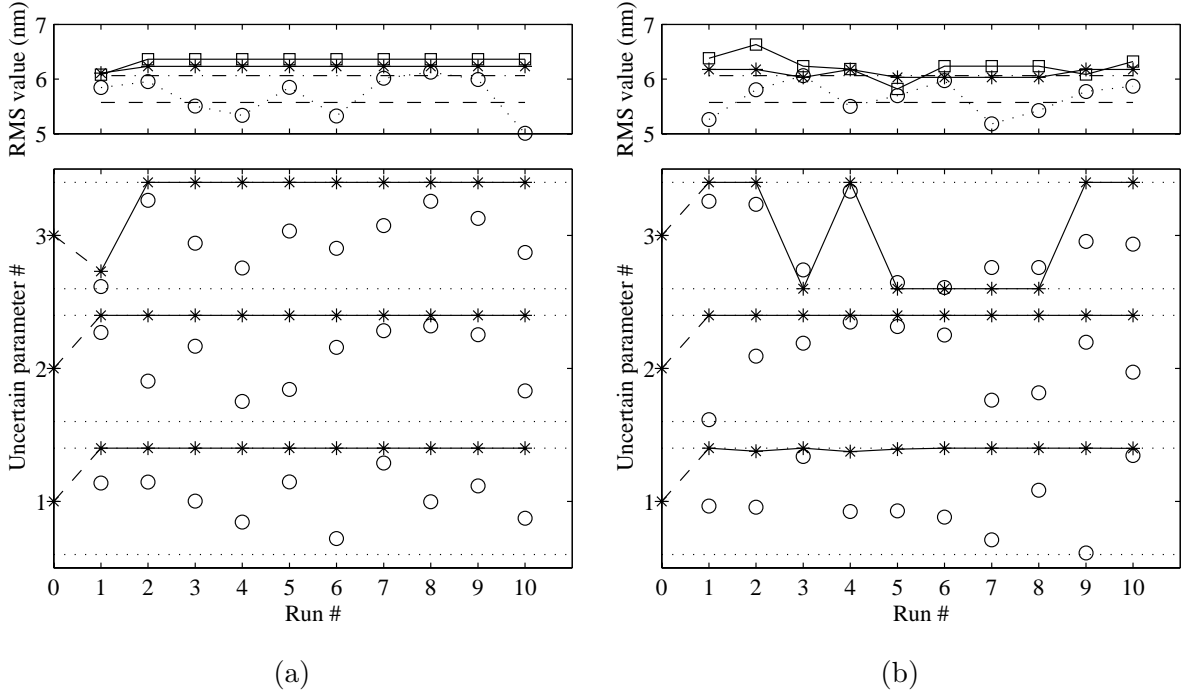
Figure 5.24: (a) Uncertainty analysis runs when SIM model is reduced to 150 states at each iteration. (b) Uncertainty analysis runs when SIM model is reduced to 120 states at each iteration. Both plots: ∘, initial guess; ∗, converged solution; ⋯, upper or lower bound; −−−, nominal; □, exact; − · −, first-order approximation.
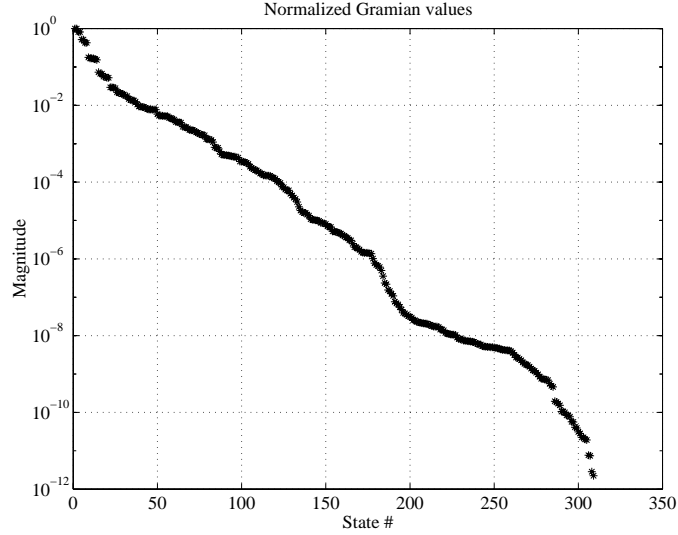
Figure 5.25: Gramian values of SIM model.

a "poor" uncertainty analysis. If a situation such as this was found to be the case, then another series of runs would have to be done.

5.5 Summary

A methodology has been developed that predicts the worst-case RMS values of a system's performance metrics. The worst-case RMS arises due to parametric uncertainties in a state-space model of the system. Initial work has considered the special case when the uncertainties are in the open-loop modal parameters, and the uncertainties are specified as bounds on these parameters. The methodology solves a constrained optimization problem, and it does not assume that the worst-case parameters occur at their bounds. As a result, it can accommodate cases in which the sensitivities change sign across the uncertainty range. This can arise, for example, when the modal separation is smaller than the uncertainty in the frequencies. Since the disturbances are modeled by filters that shape white noise, it is possible to compute exact sensitivities (*i.e.*, gradients) at each iteration of the optimization. Gradient information helps the optimization converge more efficiently. When the system has a significant number of states, an approximate balanced model reduction is performed. Instead of computing the exact balancing transformation matrix at each iteration, which is a time-consuming process, the original balancing transformation matrix is used. Approximate RMS and sensitivity values can then be computed. The methodology has
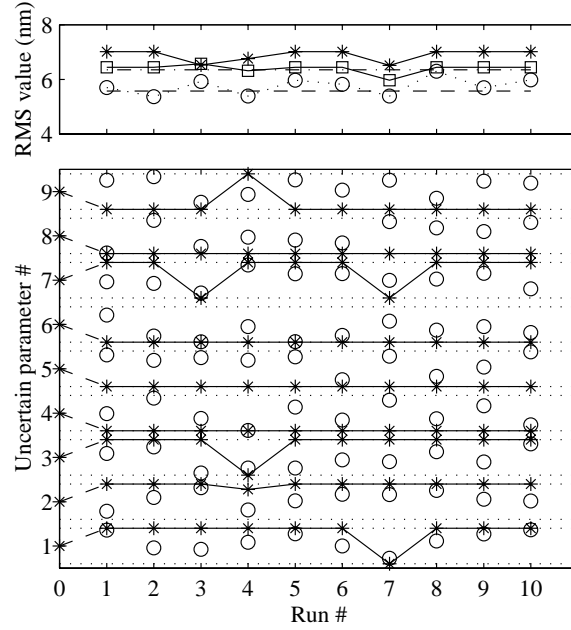
Figure 5.26: Uncertainty analysis runs when SIM model is reduced to 150 states at each iteration. (nine uncertain parameters)

been demonstrated on systems of various size, and a number of issues have been explored. When model reduction is performed, for instance, care must be taken to ensure that the reduced system still accurately predicts the RMS values. Furthermore, multiple runs of the optimization are required to gain a sense if a global maximum has been achieved.

The framework is in place to allow any element in the state-space A_{zd}, B_{zd}, and C_{zd} matrices to be treated as uncertain. This can be accomplished by modifying the uncertainty analysis code (`unc_analysis.m`) to account for this general case. The code would need to know in which matrix the parameter appears and in what form it appears (*e.g.*, linearly, quadratically, *etc.*). This enables sensitivities to be determined.

In addition to accounting for any uncertain parameters that appear explicitly in the state-space matrices, the code can also be revised to account for potential nonparametric uncertainties. Further work is necessary to determine the proper form of these uncertainties and how to incorporate them into the uncertainty analysis method.

The series of example systems that have been used in this chapter seem to indicate that for problems in which the parameter sensitivities are "well-behaved" (*e.g.*, no sign changes), the optimization routine does converge to the bounds of the uncertain parameters. This suggests that the optimization routine can be abandoned in these situations, and

only a single disturbance analysis has to be conducted on the system after placing the parameters at the bounds that lie in the directions indicated by the sensitivities. If such a generalization can be proved mathematically rather than assumed from heuristic arguments, then this would constitute a significant contribution. Efforts in this area are recommended. Furthermore, there are additional indications that even for poorly-behaved sensitivities with respect to frequencies, the sensitivities with respect to modal mass and damping never experience sign changes. This was seen in the cantilevered beam example. If this can be shown in general, then the only parameters that would have to be considered in the optimization routine are the uncertain frequencies. Once the worst-case frequencies are determined, then the uncertain damping and modal mass values can be placed at the appropriate bounds (which are usually the lower ones).

Chapter 6

Experimental Validation

The theory behind a series of analysis tools has been described in the preceding chapters. In particular, the framework for determining the sensitivity of performance RMS values with respect to physical parameters appears to be a promising design aid. It has been demonstrated on systems ranging from a cantilever beam to a closed-loop integrated model of SIM Classic; however, the key to using it with confidence is to successfully validate it in practice. Further demonstration of the code on other purely analytical systems would still not address the issue of its applicability in a real-world setting. As a result, a laboratory testbed was designed and constructed to help identify potential limitations that were not a factor during analytical simulations.

This chapter begins by describing the requirements that were placed on the testbed before the design process began. The task of meeting the requirements subject to material and time constraints led to a point design which consists of a cantilevered truss with a flexible appendage. The details of this design are provided, and this is followed by an overview of the initial finite-element model that was created in IMOS. After this, a technique to update FEM parameters based on measured transfer functions is implemented. The results of a series of experimental tests are then shown and compared to the analytical predictions made using the updated model. An example design problem concludes the chapter by illustrating in both theory and practice how the physical parameter sensitivities can identify redesigns that improve the performance.

6.1 Description of Testbed

One of the top-level requirements placed on the testbed was that it must be able to address two research topics. Its primary role is to serve as a sensitivity analysis validation platform. Its other role is to serve as a testbed for research in reaction wheel disturbance modeling. The implications of these criteria are evident in the desired testbed characteristics listed in Table 6.1. Due to constraints on time and cost, the testbed had to be constructed from as much available hardware as possible and with a minimal amount of newly machined parts. Several dozen aluminum struts and node balls were obtained from a previous experiment and used as the basic components of the testbed. A cantilevered, truss-like configuration was chosen since it was of medium complexity. A view of the overall testbed is provided in Figure 6.1(a). A more complicated structure would have required more time for construction. In addition, modeling a complex structure would possibly have introduced large errors that would have masked the issues of interest. On the other extreme, a less complex structure would not have been as traceable, even if successful experimental results were obtained.

The hole pattern in the node balls allows truss configurations with either triangular or square cross sections, and the triangular arrangement was selected since it minimizes the number of nodes and struts for a structure of a given length. Each bay of the truss consists of an inverted, square-based pyramid whose apex is connected to the apexes of neighboring bays by two struts. A plate can be easily added to the square top of any bay, and a disturbance source such as a reaction wheel can be attached to the plate. The truss was placed horizontally on an optics table to permit easy access to any bay. This is essential since sensitivity validation requires repeated modifications to the structure. The base of the truss consists of a pattern of nodes and struts that allows the truss to be attached to the optics table at four node locations.

During the course of the SIM physical parameter sensitivity analysis in Section 4.6.2, it was discovered that the critical modes consisted of a global mode and two local siderostat bay modes. To introduce a local mode to the testbed that was close in frequency to the truss primary bending modes, a flexible appendage was added at the end of the truss, and it can be seen clearly in Figure 6.1(b). Ideally, it was desired that the testbed have an optical performance metric; however, hardware constraints did not permit a laser metrology

system to be placed on the structure. Instead, the performance was chosen to be the tip displacement of the flexible appendage (obtained by post processing data from a tip accelerometer). This measurement is analogous to estimating external path difference in an interferometer based on accelerometers placed on the siderostats.

The number of truss bays and the length of the flexible appendage were selected such that the first three testbed modes (one appendage bending mode and two truss bending modes) were below 50 Hz. This ensured that a reaction wheel disturbance source would be able to excite the modes when spinning up to a maximum rate of 3000 RPM (= 50 Hz). This assumes the dominant reaction wheel disturbance harmonic is at the wheel spin frequency. Modes at low frequencies were undesirable due to limited frequency resolution of the data acquisition system, larger accelerometer noise, and increased data acquisition time. The target frequency for the first testbed mode was 30 Hz. For very light damping, the half-power bandwidth of modes near this frequency would be on the order of the available frequency resolution; therefore, it was considered advantageous if the truss incorporated some amount of augmented damping. Three struts with a constrained viscoelastic layer were placed near the root location to help increase the damping level, and they are visible in Figure 6.2(a).

Since both the global truss mode and the local appendage mode are major contributors to the performance metric, the testbed was designed such that stiffness and mass properties that affect these modes could be modified easily. Changes in mass distribution are accomplished by adding or removing small masses at various locations on the structure. Several washers can be seen at the node locations in Figure 6.2(a). The stiffness of the truss is altered by adding small springs in parallel with an existing stiff spring that connects the truss tip to ground, as shown in Figure 6.2(b). This was considered just as effective as replacing the nominal struts with modified struts. The flexible appendage consists of two parallel beams that are kept a fixed distance apart by a series of eight spacer blocks. The bending stiffness is increased by adding thin shims to the spacers. The shims and spacer blocks are visible in Figure 6.1(c), which shows the flexible appendage after it has been taken apart. More detailed information about the testbed is summarized in Table 6.2, and the supporting data acquisition hardware is listed in Table 6.3.

Table 6.1: Desired characteristics of testbed.

Characteristic	Purpose	Implementation
• constructed from available hardware	• minimize construction time and cost	• use existing strut and node hardware
• medium complexity	• minimize construction time; make results traceable; minimize modeling error issues	• cantilevered, truss-like structure with triangular cross section
• easily accessible	• facilitate structural modifications	• place horizontally on optics table
• support different disturbance sources and locations	• allow shaker or reaction wheel to exert different levels of authority on various modes	• attach shaker at any node; place reaction wheel on plate at any bay location
• representative performance metric	• make results traceable	• measure or infer structural displacement
• global and local modes contribute to performance	• mimic types of critical modes identified during SIM analysis	• add flexible appendage to truss and measure appendage tip displacement
• augmented damping	• minimize frequency resolution issues around lightly-damped modes in data	• use struts with constrained viscoelastic damping (J-struts)
• fundamental mode below 50 Hz	• places mode within frequency range of reaction wheel fundamental harmonic (for max. wheel speed of 3000 RPM)	• set testbed fundamental frequency by selecting proper number of bays and length of flexible appendage
• mass and stiffness properties of global and local modes can be easily changed	• validate as many physical parameter sensitivities as possible; allow rapid testbed reconfiguration for maximum data throughput	• add or remove lumped masses (*e.g.*, nuts, washers) at node and appendage locations; add spring at truss tip to affect truss modes; use sandwich appendage with different spacer thicknesses to adjust appendage stiffness
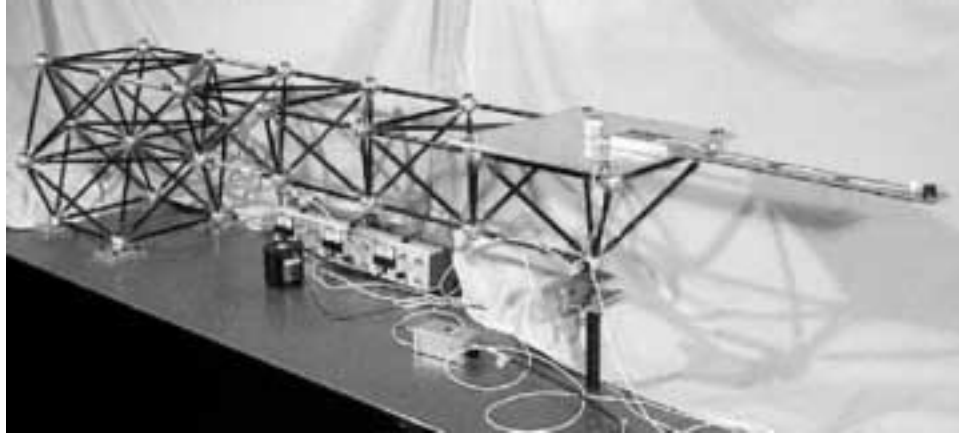
(a)

(b)

(c)

Figure 6.1: (a) View of entire testbed. (b) Close-up of flexible appendage. (c) Components of flexible appendage.

(a)

(b)
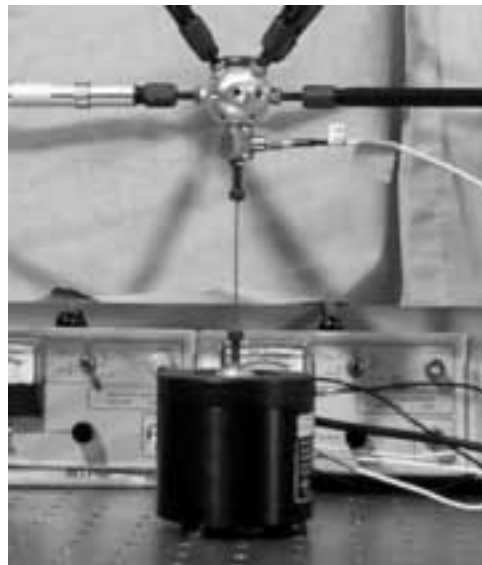
(c)

Figure 6.2: (a) Close-up of J-struts. (b) Close-up of stiff spring with added soft springs. (c) Close-up of shaker.

Table 6.2: Testbed components.

Item	Description
short strut	anodized aluminum; 3/8″ outer diameter; 58 mil wall thickness; 25 cm node center-to-center distance
long strut	anodized aluminum; 3/8″ outer diameter; 58 mil wall thickness; 35.36 cm node center-to-center distance
node ball	aluminum; 1.19″ diameter; 34.7 g
flex. appendage	aluminum; two 1/16″ × 2″ × 20.16″ beams ($\approx$ 15″ exposed) with eight 1/16″ spacers; combinations of 2 mil, 3 mil, and 5 mil shims
springs	stiff = 31.9 N/mm ; soft = 0.63 N/mm
plate	aluminum; 1/4″ thick

Table 6.3: Supporting experimental hardware.

Item	Description
Data acquisition	Tektronix 2630 Fourier Analyzer with 4 input channels and 1 output channel
Actuator	Brüel & Kjær Mini Shaker Type 4810
Sensors	1 PCB 208B load cell (530 mV/lb)
	3 Kistler 8630B5 Piezobeam accelerometers ($\approx$ 1V/g)
Signal conditioning	Kistler Piezotron Coupler 5120 (for load cell)
	Kistler Piezotron Coupler 5128A (for accels.)
Power amplifier	Crown DC-200 Series II

Top View   Isometric View

Normal View   Side View
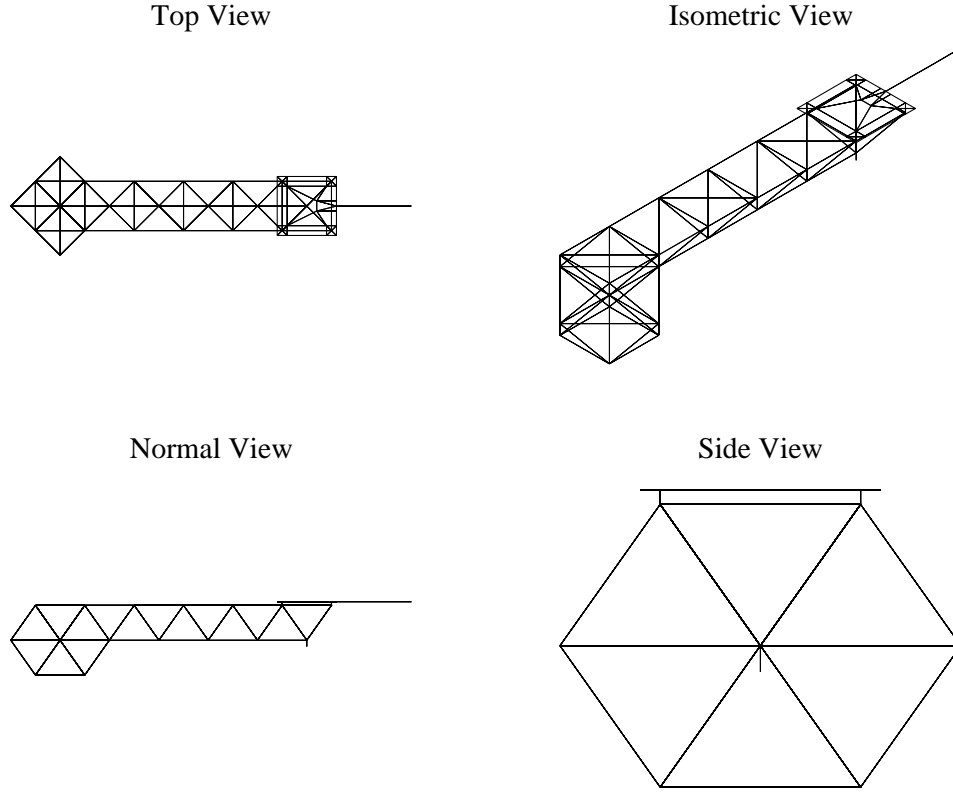
Figure 6.3: Four views of the testbed finite-element model.

6.2   Testbed Model

The finite-element model of the testbed was created using IMOS, and different views are
shown in Figure 6.3. A major modeling simplification is that each strut assembly (consisting
of a ball node, screws, nuts, and hollow aluminum tube) is represented by a single Bernoulli-
Euler beam element. This keeps the total number of DOF's in the model from becoming
excessive without sacrificing too much of the low-frequency accuracy of the model. It was
anticipated that only the first bending modes of the structure would contribute significantly
to the tip displacement performance metric, and strain energy calculations revealed that the
strut elements are primarily undergoing extension/compression in these modes. Thus, using
a single beam element with an equivalent axial stiffness (EA/L) was considered justified. If
the performance metric had been chosen such that higher frequency modes were important,
then more detailed modeling would probably have been required, such as adding more nodes
to each strut.

Component tests on single strut assemblies for a prior testbed [7] provided estimates of

the strut equivalent stiffnesses for both the long and short struts. The general modeling approach for determining the individual element properties was as follows. First, the strut assembly mass was determined by averaging mass measurements for several struts. The cross-sectional area was based on the inner and outer diameters of the strut hollow tube portion. The material density was chosen such that the total element mass $\rho A L$ equaled the average measured mass. (L is the node center-to-center distance.) Then, a value for the Young's modulus E was calculated to achieve the equivalent stiffness EA/L obtained for the previous testbed. This approach provided the initial parameter estimates for the strut elements in the finite-element model.

The mass and inertia of the spherical node balls were lumped at the corresponding nodes in the model using IMOS's `conm` function. The plate to which the flexible appendage is attached was modeled with a combination of triangular and quadrilateral plate elements. Four of the plate nodes were connected to the neighboring truss ball nodes with rigid-body elements. This allowed the midplane of the plate to be at the correct height above the top plane of the truss. The spring attached at the truss tip was modeled with an elastic spring element available through IMOS's `celas` function. A cross-axis stiffness was also included since the transverse spring stiffness was non-negligible.

The flexible appendage was modeled as a single, homogeneous, Bernoulli-Euler beam even though the actual appendage is in a sandwich configuration. A node was added at each spacer location, and the cross-sectional area and moments of inertia were computed based on having two parallel, rectangular cross-section beams at an equal distance above and below the sandwich beam midplane. The spacers were only accounted for by lumped masses at the node locations. A more detailed model was created of the sandwich beam with a cantilevered boundary condition, and the frequencies of this model were compared to the frequencies of the single beam model. The Young's modulus of the single beam model was adjusted such that the first bending mode frequency coincided with the frequency predicted by the two-beam model. The density was set to the value which produced the same mass as was measured on a scale.

6.3 Automated Finite-Element Model Updating

After having created the initial model, the next step was to update parameters in the model based on transfer function measurements. This allows the experimentally-derived physical parameter sensitivities in Section 6.5 to be compared to the predictions made by both the un-updated and updated models. The results will provide an indication of the effects of model error on the ability to identify performance-enhancing redesigns.

The topic of structural dynamic model updating has received and continues to receive much research attention. The different approaches can be categorized according to choices made for the following.

- parameters to update

- form of the data (*e.g.*, time-domain, frequency-domain, modal)

- form of the model (*e.g.*, time-domain, frequency-domain, modal)

- cost function

- optimization strategy

Choosing which model parameters to update is often one of the most difficult aspects of the model improvement process. It is usually more desirable to update physical parameters at the element level rather than parameters at the global level such as entries in the overall mass and stiffness matrices. This makes it easier to predict the results of different configurations of the system. Since the sensitivity validation tests involved making modifications to the structure, it was considered more appropriate to update at the element level. A decision still remained regarding which particular parameters should be updated. Geometric properties such as element lengths and cross-sectional dimensions were not allowed to be updated since they were assumed to contain minimal error. Also, material densities were not included in the update process because of the care taken to ensure a correct model mass. This left material stiffness properties as the potential update parameters. In particular, the Young's moduli E for the struts and flexible appendage were identified as the parameters in most need of updating. The shear modulus G also falls into this category; however, the modes of interest are dominated by extension in the struts and bending in the flexible appendage. The corresponding stiffness terms EA/L and EI/L^3 suggest that E is the relevant parameter

212

(since A, I, and L are treated as constant). It is important that the parameters chosen for updating have a large influence on the modes of interest, and it is for this reason that G was not included in the update process.

The remaining parameters that were allowed to be updated were the spring cross-axis stiffness and the modal damping ratios of the important modes. The cross-axis stiffness was not measured experimentally, and it was considered to be a parameter with a potential for significant error. The modal damping ratios are measures of the global damping rather than element damping, and these are the only parameters in the update process that characterize the structure in a modal sense instead of at the local physical-component level.

The type of experimental data that was considered appropriate for model updating was frequency response functions (*i.e.*, transfer functions). This type of data can be gathered quite easily using available data acquisition hardware. Frequency-domain data can be averaged to reduce the effects of sensor noise, and it can be used to estimate the performance metric if a PSD is computed. Other possible types include time-domain impulse response functions or modal data such as measured frequencies and mode shapes extracted from frequency response data. Since the data was in the form of transfer functions, it was necessary to compute transfer functions from the finite-element model. This was done by first creating a state-space model in structural modal form (as described in Section 4.3.1), and then using Eq. 3.2 to compute the transfer function matrix at each frequency.

In the frequency domain, a common method for computing a cost function is to subtract the model transfer function from the measured transfer function at each frequency point, then square the magnitude, and finally sum over all frequency points in all the transfer functions. The smaller the value of the cost function, the closer the model is to representing the data. The cost function used in the update of the testbed model is a slightly modified version of this, and it is based on taking the logarithm of the transfer functions prior to subtracting one from another [41]. In mathematical form, this cost function is represented as

$$J = \sum_{i=1}^{n_y} \sum_{j=1}^{n_u} \sum_{k=1}^{N} \left| \log G_{y_i u_j}(\omega_k) - \log \hat{G}_{y_i u_j}(\omega_k) \right|^2 \tag{6.1}$$

where $G_{y_i u_j}(\omega_k)$ is the measured transfer function from the jth input to the ith output at the kth frequency point. $\hat{G}_{y_i u_j}(\omega_k)$ is the corresponding FEM-based transfer function. Incorporating the logarithm into the cost function definition allows differences in the transfer

functions to accumulate not only near lightly-damped modes, but in other frequency ranges as well.

The final decision that was made regarding the model update process was the optimization strategy to use. In other words, given initial values of the parameters to be updated and a way to compute the cost J based on those parameters, what technique should be employed to find the values that minimize J? The method selected is the same as that described in Section 5.2.3 and used in the constrained optimization approach for the uncertainty analysis. Specifically, the Sequential Quadratic Programming (SQP) method was utilized since it is readily available via MATLAB's `constr` function. Constraints can be imposed on parameter variations to prevent unrealistic parameter values from occurring.

The main drawback to the model update process as described up until now is the time required to compute J once a new set of parameter values is determined. The primary steps are as follows.

1. Place the new parameter values into a vector p.

2. Create the FEM based on the new values.

3. Solve the generalized eigenvalue problem (EVP) for the modal matrix Φ and natural frequency matrix Ω.

4. Create a state-space model and compute the transfer functions at the frequency points in the data.

5. Evaluate Eq. 6.1 to obtain J.

As the size of the FEM increases, the total time to complete all of these steps is dominated by Step 2 and Step 3. To alleviate this problem, the following automated model update process is proposed which makes use of mode shape, modal frequency, and modal mass derivatives to estimate a new state-space model without having to regenerate the FEM or solve the eigenvalue problem.

1. Place the nominal parameter values into a vector p_o.

2. Create the FEM based on these values.

3. Solve the generalized EVP for Φ_o and Ω_o.

4. Compute the derivatives $\frac{\partial \Phi_o}{\partial p}$, $\frac{\partial \Omega_o}{\partial p}$ and $\frac{\partial \mathcal{M}_o}{\partial p}$. (See Section 4.5.2.)

5. Start the SQP method. Set $n_{\text{iter}} = 1$, $p_{\text{new}} = p_o$. Specify n_{max}, J_{desired}, p_{LB}, and p_{UB}.

    (a) Make the approximations

$$\Phi \approx \Phi_o + \sum_{i=1}^{n_p} \frac{\partial \Phi_o}{\partial p_i} (p_{\text{new}} - p_o)_i \tag{6.2}$$

$$\Omega \approx \Omega_o + \sum_{i=1}^{n_p} \frac{\partial \Omega_o}{\partial p_i} (p_{\text{new}} - p_o)_i \tag{6.3}$$

$$\mathcal{M} \approx \mathcal{M}_o + \sum_{i=1}^{n_p} \frac{\partial \mathcal{M}_o}{\partial p_i} (p_{\text{new}} - p_o)_i \tag{6.4}$$

$$\tag{6.5}$$

    where n_p is the total number of physical parameters being updated and p_i is the ith parameter.

    (b) Create a state-space model and compute $\hat{G}_{yu}(\omega)$.

    (c) Evaluate Eq. 6.1 to obtain J.

    (d) Obtain a new parameter estimate p_{new}.

    (e) If $n_{\text{iter}} < n_{\text{max}}$ and $J < J_{\text{desired}}$, go to Step 6. If $n_{\text{iter}} > n_{\text{max}}$, set $p_o = p_{\text{new}}$ and go to Step 2. Else, proceed.

    (f) $n_{\text{iter}} = n_{\text{iter}} + 1$

    (g) Go to Step 5a.

6. Model update process has converged.

7. Repeat Steps 2, 3, and 5b to ensure that the updated parameter values do produce a model whose transfer functions are close to the measured transfer functions.

As can be seen, this model update procedure has two primary loops. The inner loop occurs during the SQP routine and makes use of first-order sensitivity information to estimate new mode shapes, natural frequencies, and modal masses based on the change in the parameters. This inner loop continues until convergence criteria are satisfied or the maximum number of iterations has been exceeded. If the latter occurs, then the FEM is created again with the current parameter values, and new eigenderivatives are calculated. This outer loop addresses the fact that the estimates in Step 5a are only approximate and become worse

for large parameter changes. The true model is created after every $n_{\max}$ iterations of the inner loop, and this number is problem dependent. It should be made smaller if parameter variations become too large before $n_{\max}$ is reached. After the convergence criteria are met, it is important to check visually that the transfer functions based on the updated FEM do match the measured transfer functions. If the results are unsatisfactory, then possible options include tightening the convergence tolerance, easing the constraints on the parameter bounds, or adding more parameters. Care must be taken, however, to verify that the parameters being updated are chosen correctly and that the parameter bounds are realistic.

The model update of the testbed FEM occurred in two stages. First, tests were done on a bare truss assembly without the plate or flexible appendage, but with the tip spring. The parameters updated in the bare truss FEM were the E values of the short struts, long struts, the bottom J-strut, the top two J-struts, and the cross-spring stiffness (for a total of 5 E parameters). The parameters were allowed to vary by as much as a factor of 1/2 smaller or a factor of 1.5 larger. Also included in the parameter list were the modal damping ratios of the first two truss bending modes. This resulted in a total of 7 parameters for the update process. It is usually more desirable to have less update parameters than the total number of quantities to which the model is being "matched." If the number of update parameters is larger, there might be instances where there exists a non-unique solution. For the case of the bare truss tests, two transfer functions were used (1 collocated and 1 noncollocated). The frequency range of interest contained two truss modes, and the shapes of the transfer functions are determined approximately by the values of the following quantities: 1 modal frequency for each mode, 1 modal damping for each mode, and 1 residue value for each mode for each transfer function. This leads to a total of 8 quantities that govern the transfer functions. One can also argue that away from the resonant peaks, the transfer functions should also be affected by modes outside the bandwidth, and this effect can be approximately represented with a static correction term. So for the two transfer functions, there will be two static correction terms. Thus, the total number of quantities that the model update process is trying to match can be as high as 10. Therefore, the use of 7 update parameters was justified.

After the bare truss model was updated, tests were conducted on the entire assembly, and the E of the flexible appendage and the modal damping ratio of the appendage mode

Table 6.4: Parameter values for un-updated and updated models.

Parameter	Un-updated 1	Un-updated 2	Updated
E, short struts	72 GPa	77.6 GPa	68.1 GPa
E, long struts	72 GPa	83.0 GPa	41.0 GPa
E, flexible appendage	72 GPa	64.1 GPa	52.3 GPa
E, bottom J-strut	72 GPa	72 GPa	102 GPa
E, top J-struts	72 GPa	72 GPa	80.9 GPa
k, spring cross-stiffness	16.0 N/mm	16.0 N/mm	7.7 N/mm
ζ_1	0.2%	0.2%	0.4%
ζ_2	0.2%	0.2%	0.9%
ζ_3	0.2%	0.2%	0.5%

were added to the parameter update list. The E's of the truss were allowed to vary by a smaller amount, while the E of the flexible appendage was given more freedom. The reason for performing a two-stage model update process was to identify errors in the bare truss model prior to adding the complexity of the plate and appendage. This strategy is recommended for structures that evolve over time as more components are added [59]. In addition, the modal damping ratios of the three first modes were included in the update process. Table 6.4 lists the un-updated parameter values along with the final updated values. The values under the "Un-updated 1" heading are "poor" initial estimates because they set all of the E values to a handbook value of 72 GPa (aluminum). For the "Un-updated 2" case, the E values for the short and long struts produce the same equivalent axial stiffness as was measured in the prior testbed. Also, the E for the flexible appendage is based on a comparison made with a more detailed beam model, as was mentioned previously. Thus, the "Un-updated 2" values represent a better "guess" since they use more of the available information prior to the collection of data on the actual testbed.

Figure 6.4 shows the plots of two transfer functions from the data along with the corresponding predictions from the different FEM's. The lower frequency mode corresponds to the first appendage mode, and the next mode corresponds to the first bending mode of the truss. The top subplot represents the transfer function from the shaker load cell to the vertical displacement of the tip of the flexible appendage. The bottom subplot represents
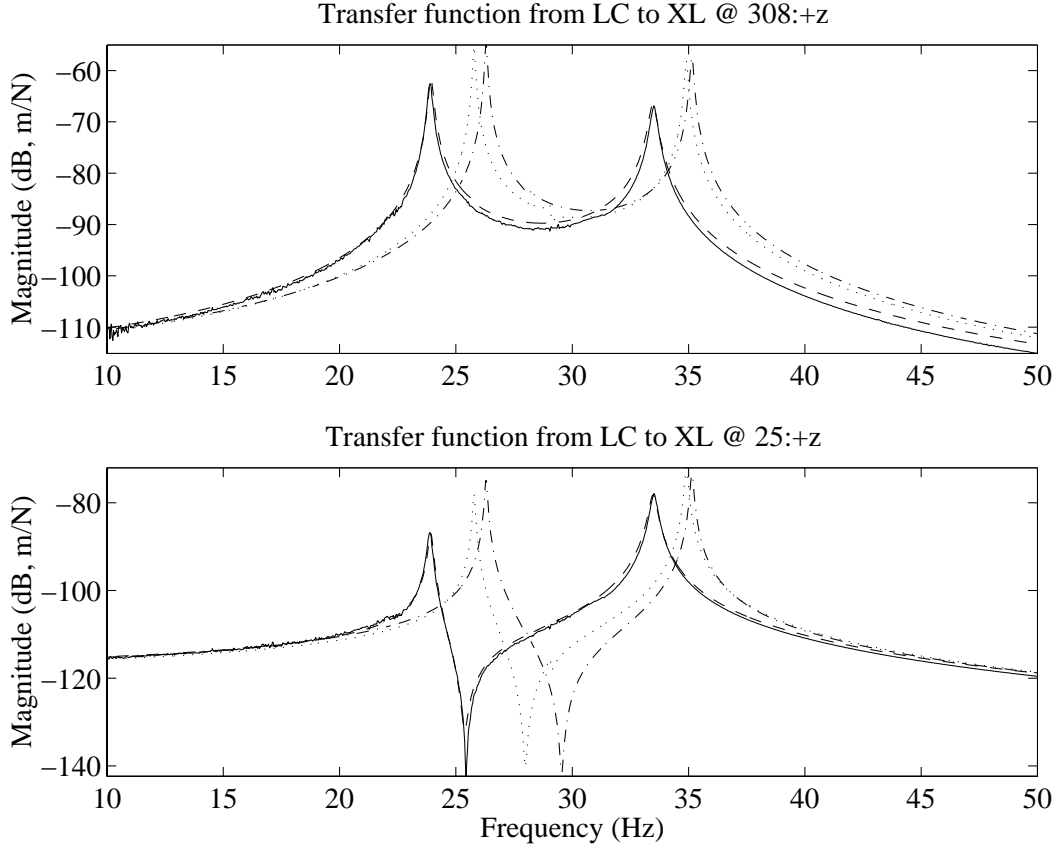
Figure 6.4: Comparison of transfer functions from data (—), updated FEM (−−), and two types of un-updated FEM (− · −, · · ·).

the transfer function from the shaker load cell to the vertical displacement of the bottom node at the end of the truss. The un-updated models have significant error, while the updated model follows the data extremely well. This suggests that the model update process was successful.

6.4   Disturbance Analysis Results

Another measure of the quality of the updated FEM is its performance prediction capability. To examine this, a sample disturbance analysis was conducted, and the results were compared to the measured performance. The Tektronix analyzer was used to output white noise to the shaker amplifier across a 0–50 Hz bandwidth of interest. This bandwidth was chosen to maximize the frequency resolution (based on a maximum number of 4096 FFT points available) while still capturing the important modes. A larger frequency range was

not considered necessary since the dominant modes for a white noise disturbance were anticipated to be modes 1 and 3. This assumption is based on the modal parameter sensitivity values in Figure 6.5(a). The PCB load cell measured the force applied to the testbed, and the PSD of this force (based on 20 averages) is shown in Figure 6.5(b). The spectral content appears to be uniformly distributed, as is expected for a white-noise disturbance. The effect of a truss mode near 34.5 Hz is somewhat visible, however.

This measured PSD served as the disturbance input for the testbed FEM, and the analysis code `dist_analysis.m` was used to implement a frequency-domain disturbance analysis. The resulting predicted tip displacement PSD is shown as a solid line in Figure 6.5(c). The measured PSD (the dashed curve) is difficult to see since it lies beneath the model-based PSD. The measured displacement PSD was derived from the measured acceleration PSD by using the following relationship [86].

$$S_X(\omega) = \frac{1}{\omega^4} S_{\ddot{X}}(\omega) \tag{6.6}$$

The slight differences between the measured and model PSD's can be seen in the cumulative RMS curves. The model slightly overpredicts the total RMS value, and most of the error appears to be attributed to the first mode. The overall error is on the order of 10%, which is a good achievement for an RMS performance prediction by a model that was updated only through changes to physical parameters and modal damping.

6.5   Sensitivity Analysis Results

The measured performance PSD plot in Figure 6.5(c) appears noisy, and this is one disadvantage of working with measured PSD's. Unlike transfer function measurements, which typically have a cleaner look after a moderate number of averages, measured PSD's do not benefit as much from the averaging process. The sensitivity estimates presented in this section are based on making slight modifications to the testbed, and as will become evident shortly, the shape of the PSD in the vicinity of a mode is extremely important. It was feared that working directly with measured PSD's might corrupt the results if the small variations in the PSD's were hidden by the "noise."

The solution to this problem was to infer the performance PSD based on the measured transfer function from the disturbance input (measured by the shaker load cell) to the tip displacement (measured by the accelerometer). If the disturbance is assumed to be a
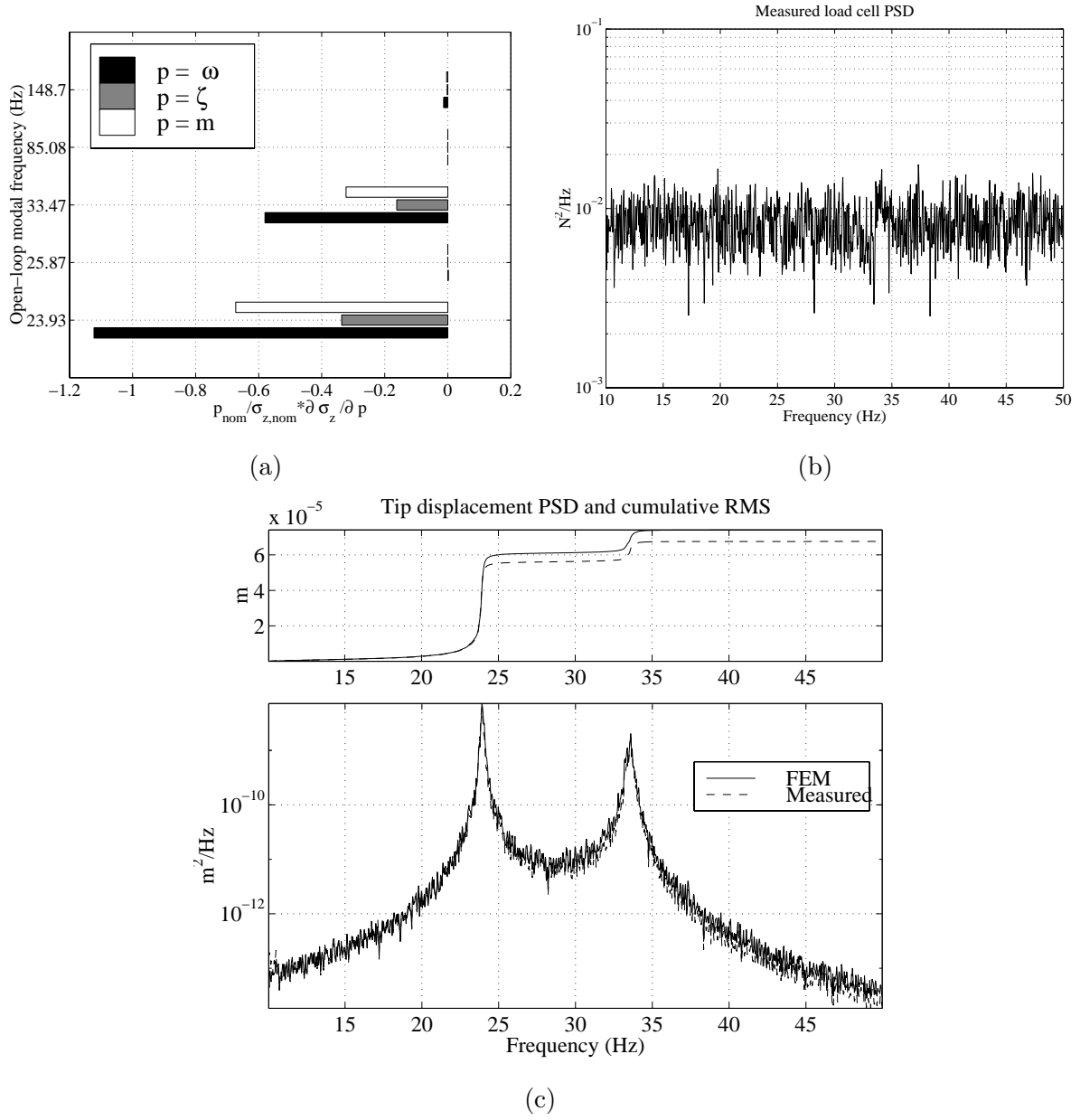
Figure 6.5: (a) Modal parameter sensitivities. (b) Measured load cell PSD. (c) Measured (—) and predicted (−−) tip displacement PSD's and cumulative RMS curves.

unit-intensity, white-noise process, then the performance PSD is simply the square of the transfer function magnitude.

$$S_{zz}(\omega) = |G_{zw}(\omega)|^2 \tag{6.7}$$

If the performance and disturbance signals have a good signal-to-noise ratio, then $G_{zw}(\omega)$ will be a relatively clean transfer function, and $S_{zz}(\omega)$ will not have the "chatter" issue associated with a measured PSD.

A total of six parameters were chosen for the physical parameter sensitivity analysis. They are: I_{33} (minimum bending moment of inertia for the flexible appendage), m_{spac} (mass of the spacers in the flexible appendage), m_{tip} (mass of the spacer at the tip of the flexible appendage), k_{spr} (spring constant of the stiff spring), m_{end} (lumped nut mass on the end of the truss at the center of the plate), and m_{ball} (mass of the node balls). The parameters m_{spac} and m_{ball} are unique in that they represent the mass at multiple locations. A 1% increase in m_{spac} implies that a mass equal to 1% of a spacer mass is added to *each* of the eight spacer nodes. Likewise, a 1% increase in m_{ball} implies that a mass equal to 1% of a ball node mass is added to *all* of the ball node locations. In a way, changes in these parameters act in a similar fashion as a change in material density would. Using the distributed lumped mass approach was considered easier than actually changing the material of either the struts or the flexible appendage. The test matrix in Table 6.5 identifies the different testbed configurations that were created to experimentally estimate the sensitivity of the tip displacement RMS value with respect to these parameters. The nominal configuration consists of a 4 mil shim thickness in the flexible appendage, 1 stiff spring (no additional soft springs), 2 washers (2.20 g each) at every truss node, no added spacer or tip mass, and 2 large hex nuts (51.14 g each) at the center of the plate.

The physical parameter sensitivity analysis framework described in Chapter 4 was applied to the updated model of the testbed, and the resulting analytical sensitivities with respect to the six parameters are plotted in bar chart form in Figure 6.6. The black bars correspond to the analytical predictions based on using 20 modes in the matrix derivative calculations. (Recall Eq. 4.67 and Eq. 4.68.) Since the code `sens_analysis_phys.m` requires a state-space model of the disturbance, a third-order low pass filter with a 100 Hz corner frequency and a unity DC gain was created to represent the 50 Hz bandwidth white-noise disturbance. This yielded a disturbance PSD that is flat from 0–50 Hz and has a magnitude of $1\,\mathrm{N^2/Hz}$. This does not match the approximately $10^{-2}\,\mathrm{N^2/Hz}$ level seen in the measured

Table 6.5: Sensitivity validation test matrix.

Parameter (% change) [# of datasets]	shim thick. (mil)	# of soft springs	# of washers at nodes	added spacer mass (g)	added tip mass (g)	added plate mass (g)
NOMINAL [5]	4	0	2	0	0	102.3
I_{33} (+14.9%)[1]	14	0	2	0	0	102.3
I_{33} (+4.36%)[1]	7	0	2	0	0	102.3
I_{33} (−2.85%)[2]*	2	0	2	0	0	102.3
I_{33} (−5.66%)[2]	0	0	2	0	0	102.3
m_{spac} (+5.60%)[2]*	4	0	2	0.176	0	102.3
m_{spac} (+11.2%)[2]	4	0	2	0.351	0	102.3
m_{spac} (+25.8%)[2]	4	0	2	0.811	0	102.3
m_{spac} (+63.4%)[1]	4	0	2	1.994	0	102.3
m_{tip} (+11.2%)[1]	4	0	2	0	0.351	102.3
m_{tip} (+91.9%)[1]	4	0	2	0	2.888	102.3
k_{spr} (+3.95%)[1]	4	2	2	0	0	102.3
k_{spr} (+7.90%)[1]	4	4	2	0	0	102.3
m_{end} (−50.0%)[2]	4	0	2	0	0	51.14
m_{end} (+104%)[1]	4	0	2	0	0	208.2
m_{end} (−100%)[2]	4	0	2	0	0	0
m_{ball} (−2.85%)[1]	4	0	1	0	0	102.3
m_{ball} (−5.66%)[1]	4	0	0	0	0	102.3
Redesign 1	0	4	2	0	2.888	0
Redesign 2	0	4	2	0	4.226	102.3

PSD in Figure 6.5(b); however, it can be easily shown that a normalized sensitivity (percent change in RMS for a percent change in a parameter) will remain unchanged even if the disturbance is scaled in magnitude.

The sensitivities in Figure 6.6(a) suggest some interesting performance enhancing options. An increase in the mass of the truss, either in the form of a lumped mass at the plate (m_{end}) or distributed lumped masses at all the nodes (m_{ball}), will lead to a larger tip RMS. Furthermore, an increase in the spring stiffness will lead to a lower RMS. These sensitivities suggest that *increasing* the frequency of the truss mode at 33.5 Hz through a stiffness increase or a mass decrease will result in a better performance. On the other hand, the sensitivities with respect to the flexible appendage parameters have the opposite trend. An increase in the mass of the appendage, either in the form of a lumped mass at the tip (m_{tip}) or distributed lumped masses at the spacer nodes (m_{spac}) will improve the RMS. Increasing the appendage stiffness via I_{33} will lead to a larger RMS. These sensitivities suggest that *decreasing* the frequency of the flexible appendage mode at 23.9 Hz through a stiffness decrease or a mass increase will result in better performance. This result appears to contradict the sensitivity with respect to natural frequency shown in Figure 6.5(a). The sensitivity is negative, which implies that an increase in the frequency of the appendage mode should improve the performance. This is an example of a case in which making redesign decisions based solely on the modal parameter sensitivities will lead to results that are the opposite of that which is desired. The modal parameter sensitivities are appropriate to identify critical modes and the relative importance of the damping in each of the modes; however, they should not be used to suggest modifications to the mass or stiffness properties of the structure. The physical parameter sensitivities are better suited for this purpose. Recall that this is a similar contradiction as was encountered during the SIM physical parameter sensitivity analysis in Section 4.6.2.

The experimental procedure for determining the physical parameter sensitivities involved measuring the disturbance-to-performance transfer function for the nominal configuration and then repeating the measurement after each modification was made to the testbed. The test matrix in Table 6.5 shows that only one parameter was varied at a time. The exceptions are the two redesign cases, and these will be discussed in the following section.

The performance metric RMS is defined as the square root of twice the area under the

223
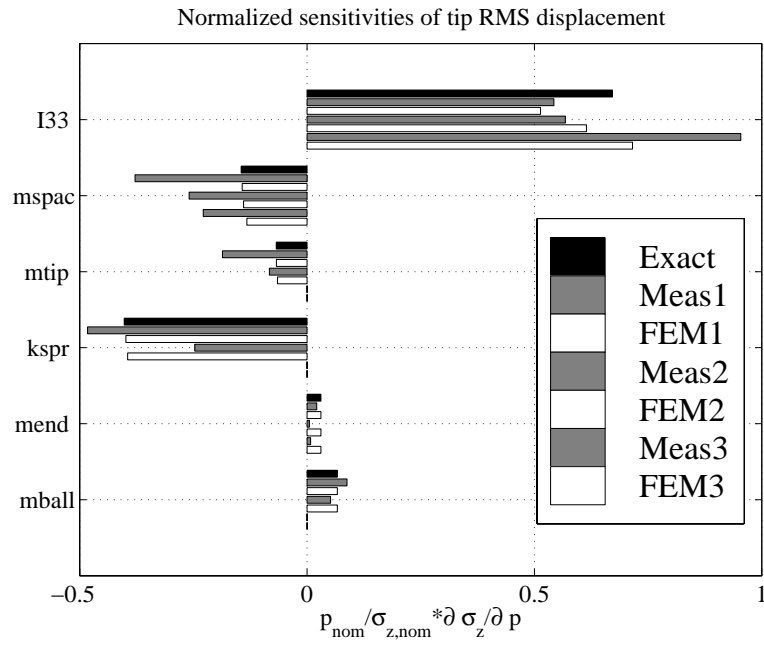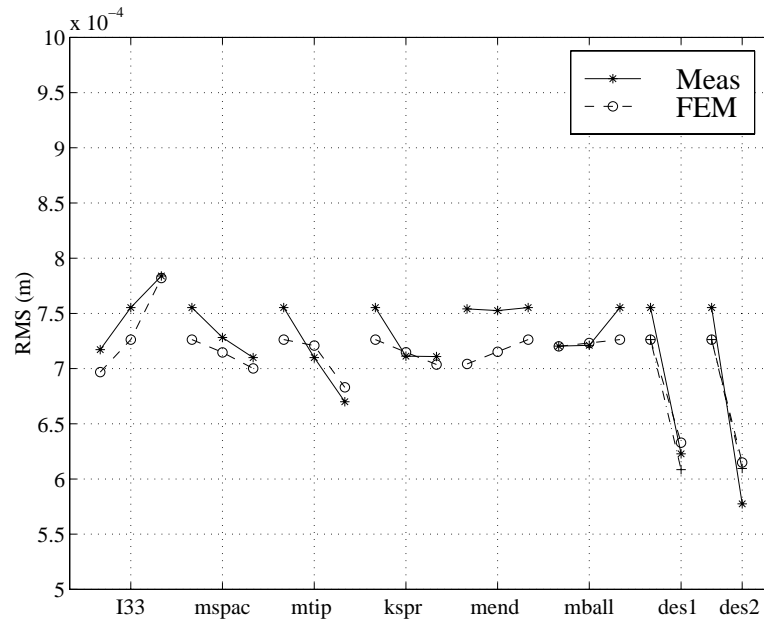
Figure 6.6: (a) Predicted and measured physical parameter sensitivities. (b) Predicted and measured RMS values.

squared transfer function across the frequency range 10 to 50 Hz.

$$\sigma_z = \left[\int_{10\,\text{Hz}}^{50\,\text{Hz}} 2\, |G_{zw}(f)|^2 \, df \right]^{\frac{1}{2}}$$ (6.8)

The constraint on the lower frequency limit was due to accelerometer noise. Since the load cell-to-accelerometer transfer function was integrated twice to obtain G_{zw}, the low frequency noise was amplified, and integrating under this portion of the PSD overestimated the true displacement RMS. Since analysis showed that the contribution to the RMS by frequencies below 10 Hz was not appreciable, this lower limit was not considered a problem. The upper limit was set by the maximum frequency available in the measured transfer function, and it, too, was considered adequate. The RMS measurements for several of the testbed configurations are presented in Figure 6.6(b). For configurations with multiple data sets, the RMS values represent an averaged quantity.

Normalized sensitivities from experimental data were determined by using the following finite-difference approximation.

$$\frac{p_{\text{nom}}}{(\sigma_z)_{\text{nom}}} \frac{\partial \sigma_z}{\partial p} \approx \frac{\frac{\sigma_z - (\sigma_z)_{\text{nom}}}{(\sigma_z)_{\text{nom}}}}{\frac{p - p_{\text{nom}}}{p_{\text{nom}}}}$$ (6.9)

The gray bars in Figure 6.6(a) represent the values of this approximation corresponding to each of the modified configurations, except for the two marked with an asterisk, in Table 6.5. The two configurations not included produced inconsistent results. This is not surprising since they are associated with the smallest parameter variations in their respective groups. If the parameter variations are too small, then the anticipated change in the frequency of the modes can be on the same order as the test-to-test variation in the frequency. In other words, repeatability issues tend to become more important as the size of the perturbation becomes smaller. Another point that should be made is that it is not the absolute percent parameter change that is important, but rather it is the effect that the parameter change has on the resonant frequencies in the transfer function. Since the performance is related to the area beneath the squared transfer function, it is critical that the change in the modal frequencies be captured accurately. If a 10% change in parameter A results in a 1% change in a dominant frequency, while a 10% change in parameter B results in only a 0.1% change, then the calculated sensitivity based on A should be a better estimate than the sensitivity based on B. The parameter variations should be large enough to cause a frequency shift that is as great as either the frequency resolution or the scatter in repeated tests.

225

This highlights the general difficulty in validating the analytical sensitivities. The parameter variations need to result in a good signal-to-noise ratio, where the "signal" is the measured RMS change and the "noise" is the variation in RMS due to non-ideal repeatability. On the other extreme, the parameter variations should be small enough such that the finite-difference approximation for the sensitivity is still valid. A step that was taken to minimize the repeatability issue was that multiple nominal transfer functions were taken, especially when tests were conducted on different days. The RMS value from a test on the modified system was compared to the nominal RMS value $(\sigma_z)_{\text{nom}}$ computed from the most recent nominal transfer function measurement. These two RMS values were then used in Eq. 6.9. For cases when several data sets existed for a given parameter change, the individual sensitivities were determined, and then an average was taken. Thus, some of the gray bars in Figure 6.6(a) are based on this averaging technique.

The white bars in Figure 6.6(a) represent the sensitivities obtained by making the corresponding parameter change in the updated FEM, computing the new RMS after performing a Lyapunov disturbance analysis, and then using the finite-difference approximation in Eq. 6.9. The RMS predictions for several of the testbed configurations are presented in Figure 6.6(b), and most come close to the measured RMS values. Each white bar in Figure 6.6(a) is associated with the gray bar above it. This FEM-based finite-difference approach served two purposes. First, it helped to validate the analytical sensitivities, and second, it was used to examine the range of parameter variations for which the linear sensitivity approximation was valid. The only parameter for which this approximation was not valid is I_{33}. The difference between the exact sensitivity and the FEM approximation is apparent for all of the shim thickness changes that were tried. The results for all of the other cases reveal that the sensitivity is rather constant for the magnitude of parameter modifications that were implemented.

A glance at Figure 6.6(a) indicates that the experimental results capture the same trends as predicted by the physical parameter sensitivity technique. Although the measured sensitivities do not exactly match the analytical sensitivities, they have the correct sign, and they do indicate the order of importance of the parameters (in terms of magnitude of the sensitivity). Achieving more accurate results in an absolute sense is difficult due to some of the experimental issues that have already been discussed. One recommendation is to perform more repeated tests in order to obtain many data sets for each parameter variation.

It is anticipated that averaging the results from more trials will reduce the discrepancies that exist; however, the results from Figure 6.6(a) are quite promising, and it would be a fair statement to say that the analytical sensitivities have been validated.

The plots in Figures 6.7 and 6.8 are sample PSD and cumulative RMS curves for two types of parameter variations. Figure 6.7 compares the measured and the predicted curves for variations in I_{33}, while Figure 6.8 compares the measured and the predicted curves for variations in k_{spr}. These plots are meant to demonstrate how dependent the overall RMS value is on the location and height of the resonant peaks. For instance, the fact that the height of the first peak of the dash-dot measured PSD in Figure 6.7 is slightly lower than in the predicted dash-dot PSD causes the overall RMS value to be slightly lower than expected. This results in an overprediction of the sensitivity magnitude. A difference between the measured and predicted first peak in Figure 6.8 also contributes to errors in the sensitivity computations. They cause the 4-spring case to underpredict and the 2-spring case to overpredict the sensitivity magnitude. Although the trends in the PSD curves are captured well in the data, it is the effect of small differences such as these that make it challenging to match the measurement-based sensitivities with the analytical sensitivities.

Another issue of practical importance is whether un-updated models can be used to make redesign decisions based on a physical parameter sensitivity analysis. As a first step toward answering this, the physical parameter sensitivity code was applied to both types of un-updated models. The resulting sensitivities are compared to those based on the updated model, and they are shown in Figure 6.9. With the exception of un-updated model #1's estimate of the I_{33} sensitivity, the un-updated models do a good job of predicting the correct sign and the relative order of importance of the parameters. It is not surprising that there are errors in the magnitude of the sensitivities, but the general trend is a good indication. A conclusion that can be drawn from this one case study is that models that do not have the benefit of test data, yet do capture the important modes, can still be used to identify critical structural parameters in the system. Since un-updated model #1 did not predict even the correct sign of the I_{33} sensitivity, this points to the need for creating a good first-generation FEM that uses all available information and past experience.
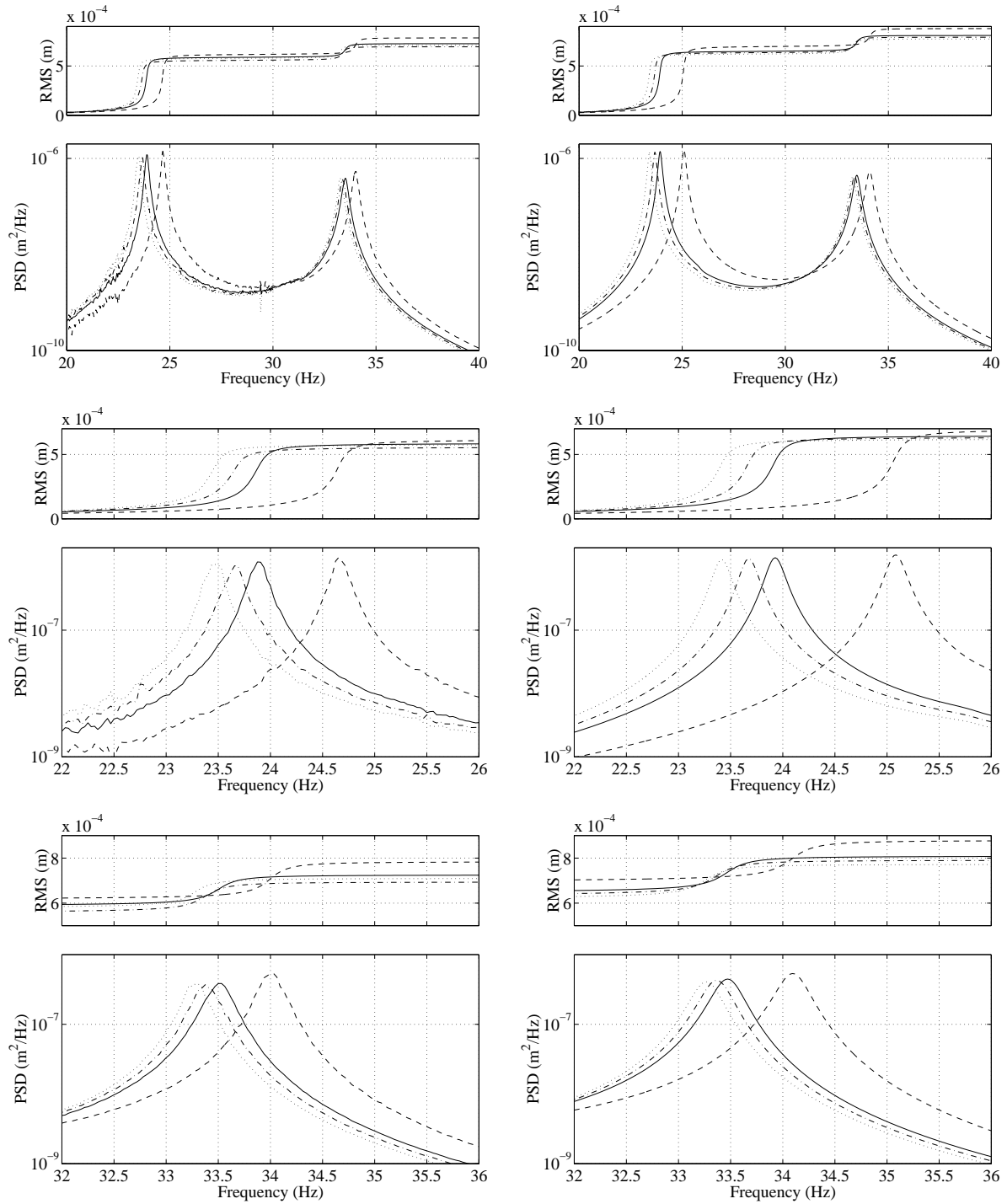
Figure 6.7: Comparison of measured (left column) and FEM (right column) PSD's and cumulative RMS curves. — Nominal (4 mil shim), − − 14 mil shim, − · − 2 mil shim, · · · no shim.
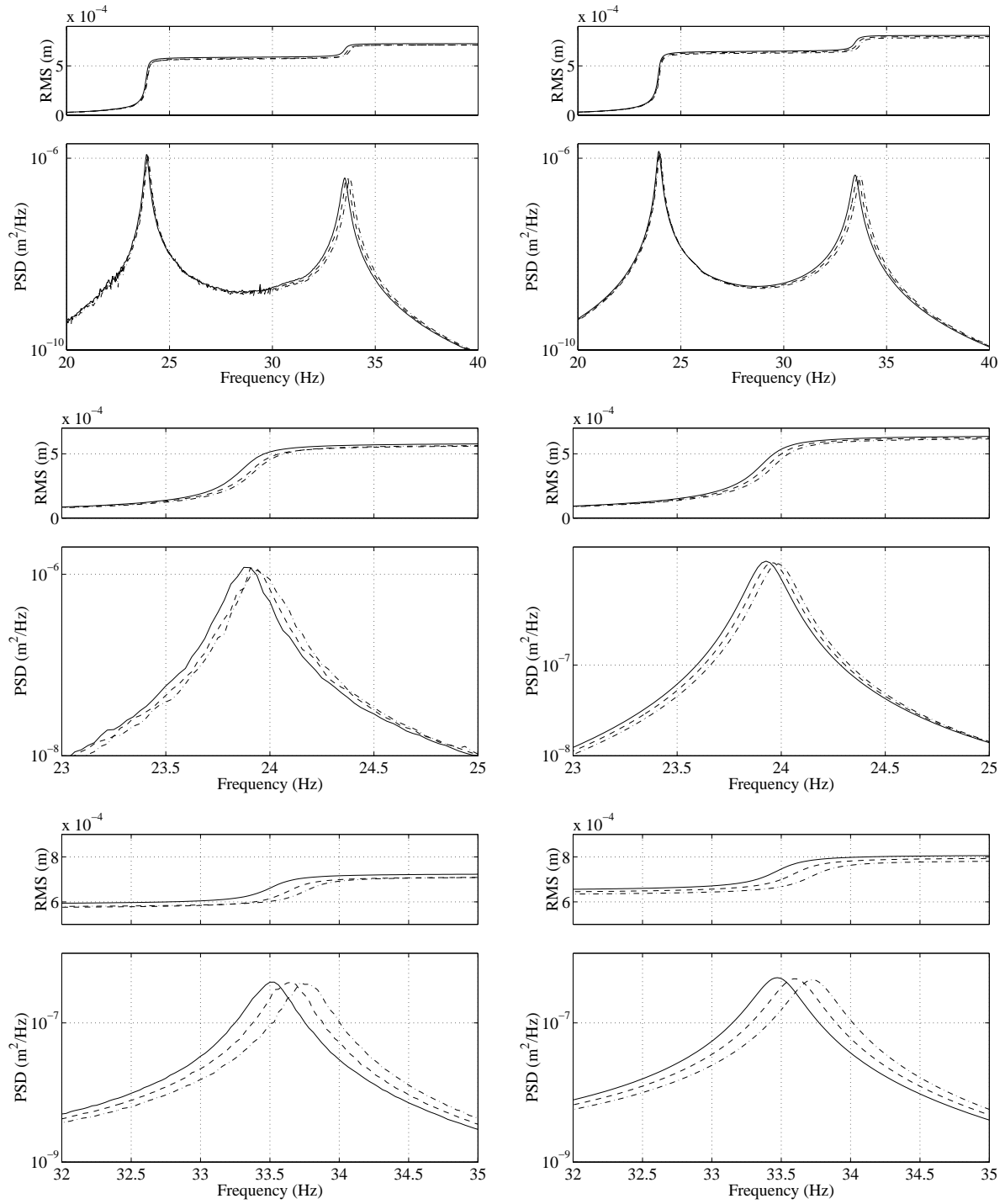
Figure 6.8: Comparison of measured (left column) and FEM (right column) PSD's and cumulative RMS curves. — Nominal (0 soft springs), −− 2 soft springs, − · − 4 soft springs.
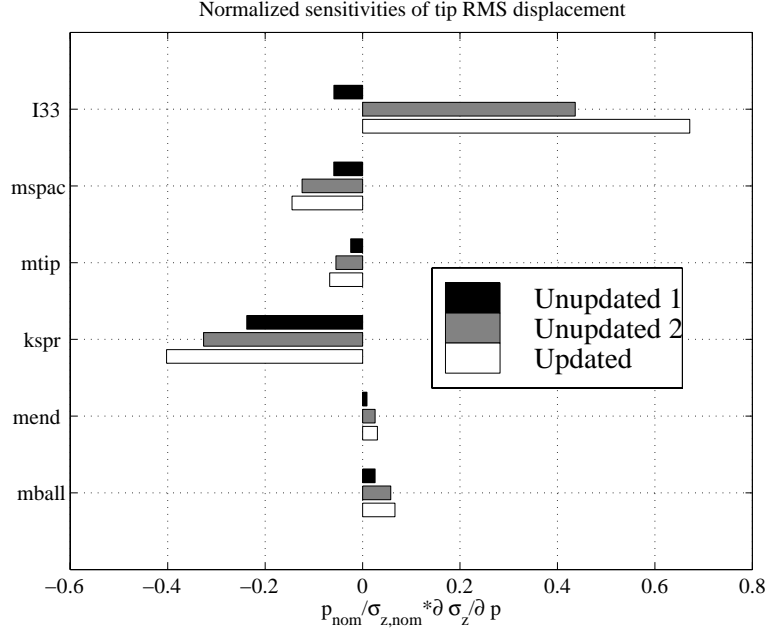
Figure 6.9: Predicted physical parameter sensitivities based on different finite-element models.

6.6 Performance Enhancement Exercise

Once the experimental validation of the physical parameter sensitivities had been completed, the next step was to use the results to suggest redesigns of the testbed that would lead to a lower RMS tip displacement. Prior to doing this, weighting factors were applied to the analytical sensitivities so that a fair comparison could be made. Recall that two of the mass parameters (m_{spac} and m_{ball}) govern the mass added at several node locations, while the two other mass parameters (m_{tip} and m_{end}) affect the mass added at only a single node location. Dividing the normalized sensitivity by the nominal parameter value and multiplying by the anticipated largest allowable parameter change results in a quantity that represents the maximum anticipated percent change in the performance RMS due to the change in the parameter. This can be seen as follows.

$$\frac{\Delta p_{\text{max}}}{p_{\text{nom}}} \frac{p_{\text{nom}}}{(\sigma_z)_{\text{nom}}} \frac{\partial \sigma_z}{\partial p} \times 100\% \approx \text{maximum \% change in } \sigma_z \text{ due to change in } p \qquad (6.10)$$

As mentioned previously, the physical parameter sensitivity values suggest that the desired modifications are those that either increase the frequency of the truss or decrease the frequency of the flexible appendage. The former can be thought of as making the truss harder to disturb by having the disturbance force push against a stiffer structure. The

latter can be thought of as isolating the motion of the appendage tip from the motion of the end of the truss. The nominal structure was designed based on *a priori* knowledge of these redesign options. The nominal shim thickness was nonzero to allow the thickness to be decreased, thereby lowering the frequency of the appendage. Washers were placed at all the node locations and hex nuts were placed on the plate to allow mass to be easily removed from the truss. Soft springs could be added in parallel with the existing stiff spring to increase the truss mode frequency.

With these options available, the following hypothetical design problem related to the nominal testbed was posed. What mass and stiffness modifications should be made to decrease the tip displacement RMS subject to the following constraints?

1. A maximum of four soft springs can be added to the structure.

2. The maximum change in the truss mass is 102 g. (This approximately equals the mass of the two large hex nuts on the plate. It also represents the total mass of the washers at all the node locations.)

3. The maximum change in the flexible appendage mass is 2.9 g. (This approximately equals the mass of two small nuts at each of the 8 spacer locations.)

4. The maximum change in the flexible appendage thickness is 4 mil.

According to Eq. 6.10, a decrease in the performance RMS (*i.e.*, a negative % change) can be achieved by increasing (decreasing) the value of the parameter if the sensitivity is negative (positive). Choosing the correct parameter changes and substituting the design constraints into Eq. 6.10 produced the weighted sensitivities shown in Figure 6.10. The sensitivity information has been converted into a form that can be directly used to suggest the design improvements.

The purpose of constraints 2 and 3 was to allow a choice to be made between either changing the distributed mass or a lumped mass at a key location. For example, constraint 2 leads to the following question. If 102 g can be removed from the truss, is it better to remove it equally from all portions of the truss or to remove it all from near the tip of the truss? Constraints 1 and 4 reflect the desire to minimize the stiffness modifications. Examining Figure 6.10 leads to the conclusion that changing the lumped mass at the tip of the appendage will lead to the largest performance improvement. Changing the appendage
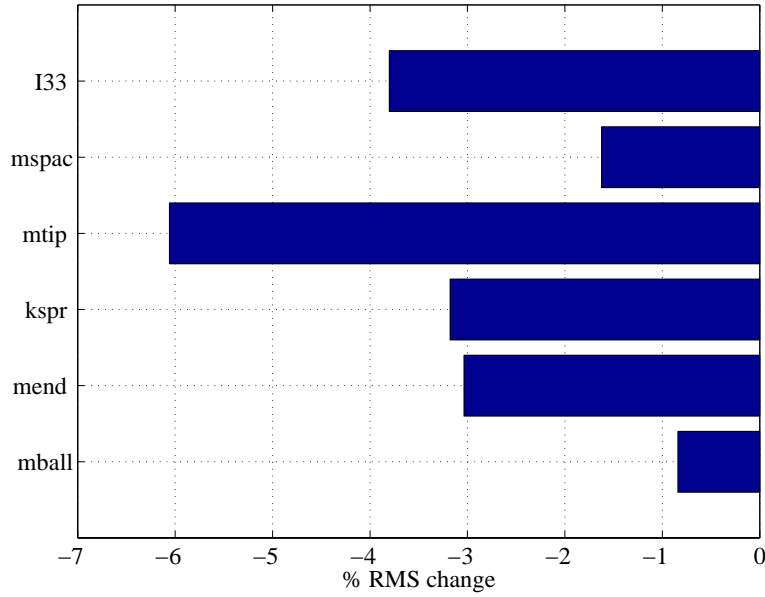
Figure 6.10: Weighted sensitivities.

stiffness and the truss spring stiffness are the next most important modifications, followed by changes in the lumped mass at the plate location and the distributed mass on the appendage and the truss.

Based on these results, the suggested testbed modifications are:

- Add 2.9 g to the tip of the flexible appendage.

- Reduce the flexible appendage shim thickness from 4 mil to 0 mil.

- Add four soft springs.

- Remove the two large nuts from the plate.

This is exactly the case represented by Redesign 1 in Table 6.5. The resulting RMS dropped from the nominal measured value of 0.755 mm to a value of 0.623 mm (refer to Figure 6.6(b)). This represents a 17.5% improvement in the tip displacement RMS. The predicted performance improvement based on adding the values in Figure 6.10 corresponding to m_{tip}, I_{33}, k_{spr}, and m_{end} is 16.1%. Thus, the weighted sensitivities proved to be an accurate and useful design aid.

Redesign 2 in Table 6.5 was used to explore the possibility of obtaining the same or greater reduction in the tip displacement RMS with less change in the overall mass. Constraint 3 was ignored, and 4.2 g was added at the appendage tip without changing the truss
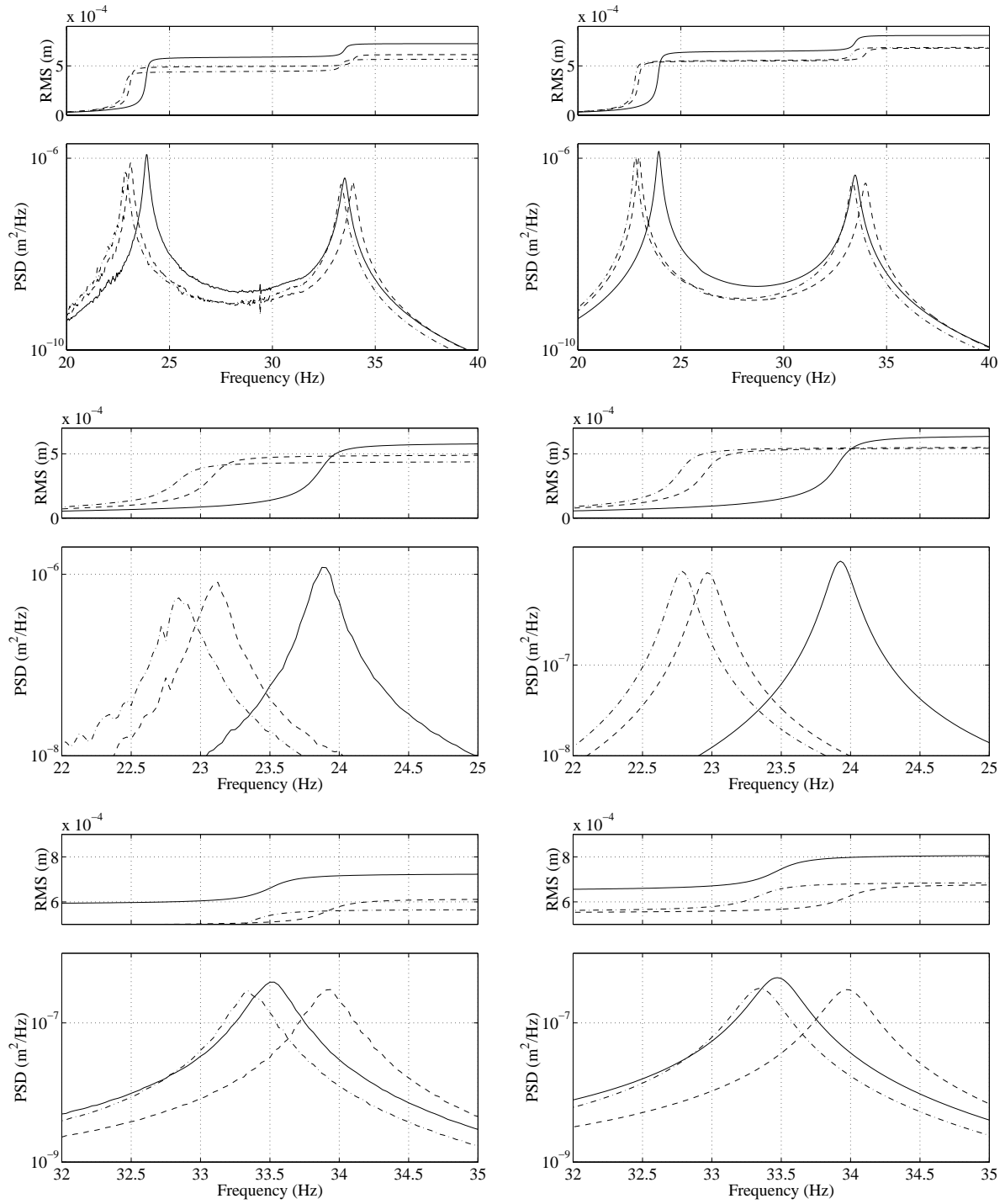
Figure 6.11: Comparison of measured (left column) and FEM (right column) PSD's and cumulative RMS curves. — Nominal , −− Redesign 1, − · − Redesign 2.

233

mass. The measured RMS was reduced to 0.578 mm, which represents a 23% decrease. This was larger than expected, and an inspection of the predicted and measured PSD's in Figure 6.11 reveals that the peak of the first mode in the data is smaller than in the FEM-based PSD.

6.7 Summary

A laboratory testbed was designed and constructed with the purpose of validating the physical parameter sensitivity technique. The testbed consisted of a truss structure with an attached flexible appendage. The performance metric was chosen to be the displacement of the tip of the appendage, and this permitted both a global truss mode and a local appendage mode to contribute to the performance. The disturbance was applied by a shaker near the root of the truss. An automated finite-element model update routine was developed that incorporates a constrained optimization algorithm with mode shape and natural frequency derivatives. The routine converges to physical parameter values that minimize the error between measured and predicted transfer functions. Mass and stiffness modifications were made to both the truss and the appendage, and sensitivities derived from experimental results were compared to the predicted sensitivities from the updated finite-element model. Although the model-based and measurement-based sensitivities did not match exactly, the overall trends in both the sign and magnitude level were comparable. Experimental issues that made the measurement of sensitivities challenging were discussed. The use of un-updated models was also examined, and results indicated that a poor, initial FEM can actually predict the wrong sign for the sensitivities. A better initial FEM does capture the overall trends in the sensitivities and can lead to proper redesign choices. An example design exercise confirmed that a combination of a truss mode frequency increase and a appendage mode frequency decrease does lead to a smaller tip displacement RMS. It also showed that changes in tip end mass are more effective than an equivalent change in distributed mass. Furthermore, the design problem highlighted the fact that design decisions based solely on modal parameter sensitivity results can lead to unexpected performance changes. Now that more confidence has been gained related to the use of physical parameter sensitivities, a performance enhancement technique that utilizes this analysis can be described and implemented on a model of SIM Classic.

Chapter 7

Performance Enhancement Framework

The disturbance and uncertainty analysis tools can be classified as methods that are used during the performance assessment of a system. The last major tool that would complete the overall conceptual design analysis framework pictured in Figure 1.1 is a performance enhancement (a.k.a. system improvement) tool. This chapter will describe an initial attempt at a performance enhancement methodology that utilizes information provided by the previous analyses. The goal of the initial effort toward this end is not to define a complicated optimization problem which must be solved, but rather to use all the results to help "point" in the direction of an improved design and to estimate how "far" to move in that direction. Trade studies are used first to identify a design that is in the vicinity of the performance requirements, then minor structural changes are identified that further improve the performance. This is where a sensitivity analysis with respect to physical parameters can provide an important link between the assessment and enhancement portions of the approach. After the preliminary enhancement methodology is introduced, it will then be implemented on the model of SIM Classic to demonstrate its use on a complicated, closed-loop system.

7.1 Methodology

As mentioned previously in Chapter 1, much research has been conducted in the area of simultaneous control-structure optimization. The objective is to choose controller and structural topologies and/or controller and structural parameters that improve certain per-

formance metrics (*e.g.*, mass, control effort, motion errors, *etc.*) subject to specified system constraints. Prior to this, work primarily concentrated on optimizing a controller for a given structural configuration or optimizing the structure for a given controller configuration. Due to the inherent difficulty in simultaneous optimization, the proposed methodology will focus on structural redesign options for a given controller.

A fundamental assumption is that a nominal point design exists. This design is based on a combination of system-level constraints (*e.g.*, total mass, location of optical elements, packaging restrictions, deployment issues, launch load requirements, *etc.*) and previous experience with similar systems (*e.g.*, control design heritage, use of similar structural components). For high performance systems which rely on closed-loop control to achieve the requirements, nominal control designs are also assumed to exist.

Figure 7.1 shows the different technologies typically found in controlled structural systems [15]. They represent a variety of options for modifying the disturbance-to-performance transmission path. Input isolation attenuates the transmission of disturbance-induced vibrations that enter the structure, while output isolation attenuates the transmission of structural-based vibrations that affect the performance metrics. Passive damping treatments serve to reduce the magnitude of response of system modes that contribute to the performance. Active structural control loops that use a suite of sensors and actuators further modify the system characteristics. Another option, which is implicit in Figure 7.1, is the relocation/modification of disturbances and/or performances. Examples of this include restricting reaction wheel speed ranges and moving a disturbance source to a point on a structure that is a node (zero displacement) of a critical mode.

The general performance enhancement methodology will be described in terms of this controlled structures technology (CST) framework. Once the performance assessment phase is completed and it is determined that performance requirements cannot be satisfied or a sufficient design margin does not exist, then disturbance and/or performance isolation is implemented first to obtain large performance improvements. Isolation is typically very effective in achieving orders of magnitude improvement. Along with this, the option for disturbance and performance relocation should be investigated. If a design is obtained whose predicted performance is close to the desired requirement, then small structural modifications (based on physical parameter sensitivities) and increased passive damping (based on modal parameter sensitivities) can be used in tandem to "fine tune" the performance. The
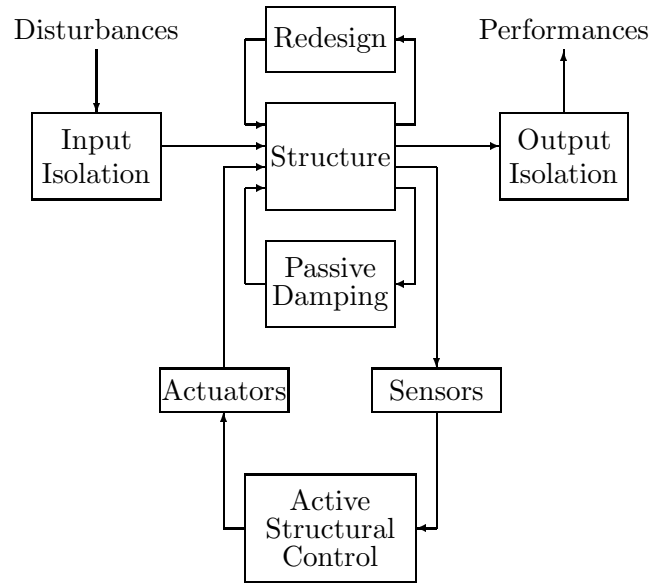
Figure 7.1: Controlled structures technology framework.

performance can be adjusted such that even worst-case predictions from an uncertainty analysis meet the requirements. If, however, a combination of isolation, damping, and minor structural redesigns does not prove to be successful, then more ambitious efforts such as active structural control and major topological redesigns should be pursued. In such a case, the benefits of combined control-structure optimization will probably be more apparent, and identifying design options that strive to optimize the control-structure interaction will be worthwhile. The steps of this methodology are summarized in Table 7.1.

7.2   Application to SIM Classic

This performance enhancement approach will now be demonstrated on the integrated model of SIM. The first step is to conduct a series of trade studies to identify the changes in performance that can be accomplished through

- changes in hexapod isolator corner frequency (disturbance isolation),
- application of various levels of optical control (performance isolation), and
- RWA speed restrictions (disturbance modification).

237

Table 7.1: Application of CST options during performance enhancement process.

CST option	When to implement
• disturbance relocation/modification	• large performance improvement needed
• performance relocation/modification	• large performance improvement needed
• disturbance isolation	• large performance improvement needed
• performance isolation	• large performance improvement needed
• small stiffness/mass modifications	• small performance improvement needed
• increased passive damping	• small performance improvement needed
• active structural control	• unsatisfactory performance with previous options
• major structural redesign	• unsatisfactory performance with previous options

The number of optical performance metrics in the model is quite large. For each of the three interferometers, the metrics include: total optical path difference (OPD), differential wavefront tilt (DWFT) in two detector axes, and differential beam shear (DBS) in two detector axes. This leads to a total of $3 \times (1 + 2 + 2) = 15$ quantities of interest. To lower this number a bit, the DWFT and DBS quantities are combined as follows to yield total values.

$$\sigma^2_{\text{DWFT}} = \sigma^2_{\text{DWFT,x}} + \sigma^2_{\text{DWFT,y}} \qquad (7.1)$$

$$\sigma^2_{\text{DBS}} = \sigma^2_{\text{DBS,x}} + \sigma^2_{\text{DBS,y}} \qquad (7.2)$$

where $\sigma^2_{\text{DWFT,x}}$ and $\sigma^2_{\text{DWFT,y}}$ are the mean-square values of DWFT in the detector x and y axes, respectively. The quantities $\sigma^2_{\text{DBS,x}}$ and $\sigma^2_{\text{DBS,y}}$ are the mean-square values of DBS in the detector x and y axes, respectively. The number of optical metrics is now $3 \times (1+1+1) = 9$.

In this performance enhancement example, SIM's astrometry mode of operation will be considered. Although it is anticipated that the nulling mode will be the most technically challenging, fringe tracking and angle tracking requirements are more readily available for the astrometry mode [52]. When the nulling requirements are more well-defined, the performance enhancement process can be repeated.

The requirement on OPD during fringe tracking is 10 nm RMS; however, error budgeting allocates approximately 4.4 nm to OPD error due to RWA disturbances. (This is based on extrapolating the error allocation for the nulling mode [52]). The remaining error is partitioned among sensor noise, actuator resolution, and quantization contributions. The requirement on angle tracking is 1.6 μrad (330 milli-arcsec) RMS, and assuming the same proportion for error budget allocation leads to a requirement on RWA disturbance-induced DWFT of 0.704 μrad. No specific requirements on DBS have been identified, but visibility reduction due to beam shear can be determined by the approximate relation [11]

$$V \approx 1 - \frac{\sigma_{\mathrm{DBS}}}{d} \tag{7.3}$$

where d is the diameter of the beam, and the approximation is valid for $\sigma_{\mathrm{DBS}}/d < 0.3$.

Figure 7.2 shows the nine performance values as a function of both isolator corner frequency and amount of optical control. The disturbance model is the same as has been used in previous chapters, namely a low-order filter approximation to disturbance PSD's of four HST wheels with random wheel speeds in the range 0–3000 RPM. The circles represent the results when no optical control is applied. As expected, no significant difference is seen between the three interferometers. The OPD requirement is not met even when a 2 Hz isolator is used; however, the DWFT requirement is satisfied with a 5 Hz isolator. Isolators with corner frequencies below 2 Hz are not shown since this frequency is approximately the limit that can be achieved with current passive isolator technology [16]. No requirement line is shown for the DBS subplots, but for reference, a value of 1 μm results in a visibility reduction of 3.33×10^{-4}, and a value of 10 μm results in a visibility reduction of 3.33×10^{-3}.

Closing the delay line and fringe tracker loops produces the series of curves in Figure 7.2 denoted with ×'s. The control designs are equivalent to those presented in Section 2.2.4. Recall that the guide interferometers have a control bandwidth of 100 Hz to represent an observation of a bright star, while the science interferometer has a 1 Hz bandwidth to represent an observation of a dim science target. As a result, the guide interferometers are able to achieve lower OPD values than the science interferometer due to their greater disturbance rejection abilities. For the DWFT and DBS metrics, the open optics (○) and closed pathlength control (×) curves overlap. This is not surprising since both DWFT and DBS are related to the pointing errors in the light beams. Only pathlength control is active, so OPD should be improved while DWFT and DBS remain virtually unchanged. The guide
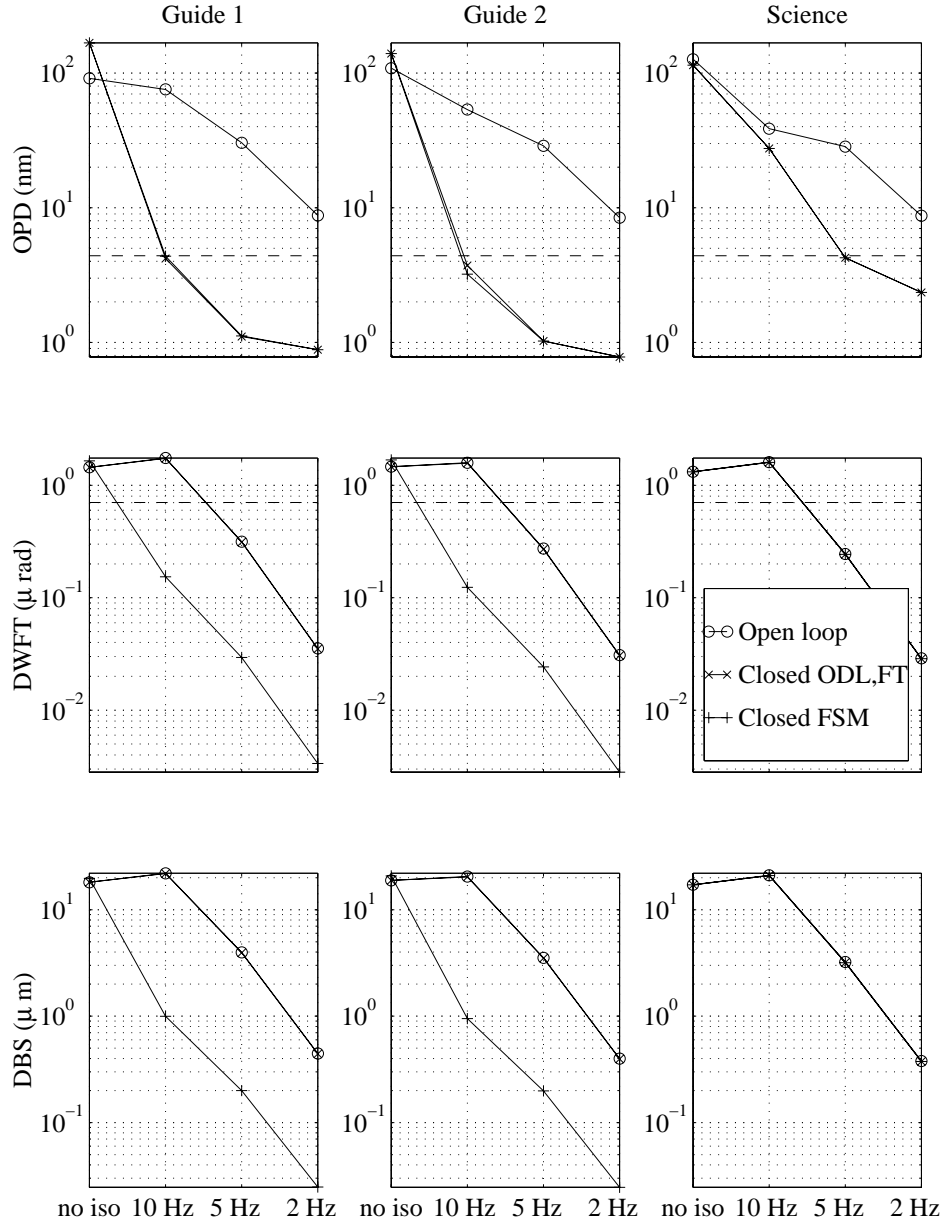
Figure 7.2: SIM optical performance metrics as a function of isolator corner frequency and levels of optical control. Structural damping = 0.1%. (Based on HST RWA 0–3000 RPM disturbance model.)
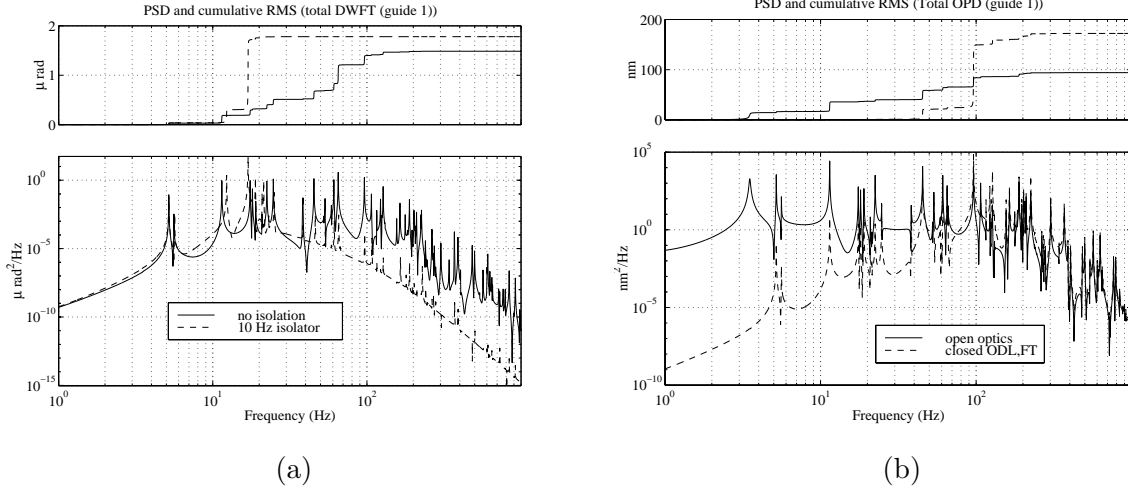
Figure 7.3: (a) Differential wavefront tilt of guide interferometer #1 with open optics loops and either no isolation or a 10 Hz isolator. (b) Total OPD of guide interferometer #1 with no isolation and either open or closed optics loops.

interferometers appear to just barely meet the OPD requirement for a 10 Hz isolator, while the science interferometer needs at least a 5 Hz isolator.

At this point, a few interesting features can be identified and discussed. The first is that a 10 Hz isolator appears to make the performance slightly *worse* compared to the no isolation case for the DWFT and DBS metrics. Plots of the PSD's and cumulative RMS curves for the DWFT of guide 1 are presented in Figure 7.3(a). It appears that one of the modes between 10 Hz and 20 Hz is greatly amplified when the design includes a 10 Hz isolator. Although the dereverberant backbone of the PSD is lowered at high frequencies due to the isolation, the amplified mode causes the overall RMS to be slightly larger than the RMS of the model without isolation.

Another surprising result is that the OPD values of guide 1 and guide 2 become *larger* for the no isolation case when the ODL and fringe tracker loops are closed. Figure 7.3(b) plots the PSD's and cumulative RMS curves for the total OPD of guide 1. Although the optics loops reduce the low frequency error, a mode near 100 Hz is amplified enough to cause the RMS to be larger than when the optics loops are open.

To better assess the DWFT and DBS metrics, fast-steering mirror (FSM) loops can be closed in the model using a 5th order SISO compensator for each of the 12 FSM input-to-WFT output loops (3 interferometers $\times$ 2 arms/interferometer $\times$ 1 FSM/arm $\times$ 2 axes/FSM). The FSM axes and detector axes are defined such that a FSM local x (or

y) command causes motion primarily in the local x (or y) axis of the detector in the corresponding interferometer arm. The cross-coupling effects are small, which enables the uncoupled SISO design approach. Since the FSM-to-WFT transfer functions are essentially flat below $1000\,\mathrm{Hz}$, the control design consists of

- a 2nd order lag filter with a break frequency two decades below the desired loop crossover frequency,

- a zero at a frequency a factor of three below the crossover frequency (to increase the slope to near -1),

- three real poles at a frequency a factor of five above the crossover frequency (to gain stabilize high frequency modes), and

- a gain to provide $0\,\mathrm{dB}$ magnitude of the loop transfer function at the desired crossover frequency.

This control design is similar to one implemented on an interferometer testbed [70], and the design incorporates realistic bandwidth and gain limitations. An example loop transfer function for one of the guide interferometer FSM loops is shown in Figure 7.4. The crossover frequency is $100\,\mathrm{Hz}$, and the corresponding gain and phase margins of this loop are approximately $10\,\mathrm{dB}$ and $40°$, respectively. The science inteferometer FSM loops are designed with a $1\,\mathrm{Hz}$ crossover to simulate integration time limitations due to dim objects.

The curves in Figure 7.2 denoted by $+$ symbols show the effects of the closed FSM loops. As anticipated, there is little improvement in OPD for the three interferometers. The FSM's are designed to tackle the pointing problem, and the greatest performance improvements occur in the DWFT and DBS metrics of the two guide interferometers. Factor of twenty improvements are evident for the isolated cases, and there appears to be little benefit of closing the FSM loops for the no isolation case. Due to the limited bandwidth available to the science interferometer FSM loops, there is no improvement seen in any of the optical performance metrics of this interferometer. This suggests that most of the RMS contribution occurs above $1\,\mathrm{Hz}$. Alternative techniques, such as angle feedforward [61], would be needed to further reduce the DWFT and DBS RMS values; however, it does appear that a $5\,\mathrm{Hz}$ isolator is sufficient to satisfy the DWFT requirement.
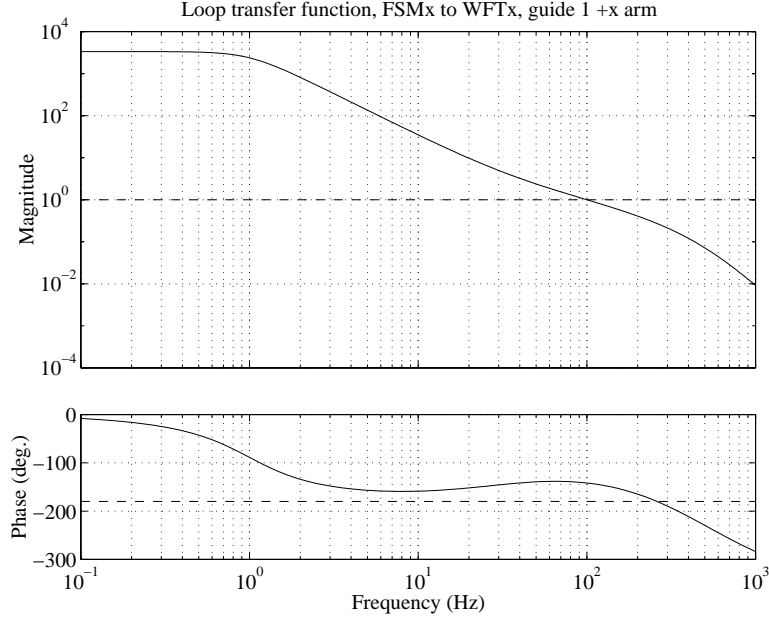
Figure 7.4: Loop transfer function for one of twelve fast-steering mirror loops.

One last surprising feature in Figure 7.2 is the "knee" in the OPD curves (closed optics cases) for both guide 1 and guide 2. There appear to be diminishing returns as the isolator corner frequency is lowered. One would expect to see further improvement as in the DWFT and DBS curves. More detailed examination of this issue revealed that the OPD PSD's exhibited a "washout" effect of the high-frequency dynamics as the corner frequency was reduced. This was due to near pole-zero cancellations that were occurring. To determine if this was a numerical conditioning issue or actually an effect of the isolator model, a sample planar, free-free beam model was created, and a sketch of it is provided in Figure 7.5. A disturbance force w acts on the lumped mass m, and the flexible structure is modeled by a uniform beam of length $10\,\text{m}$. The isolator is represented by a spring and a dashpot in parallel, and it is attached a distance of $0.5\,\text{m}$ to the left of the center of the beam. (This avoids perfect pole-zero cancellations of the symmetric modes.) The beam fundamental frequency without the isolator is $10\,\text{Hz}$, and the mass of the beam is 50 times larger than the isolated mass. The isolator damping is 20% of critical, while the beam modes have 0.5% damping. One performance metric is defined as the differential tip displacement, and the other metric is defined as the differential tip rotation.

Transfer functions from the disturbance w to the two performance metrics are shown in Figure 7.5(b) and Figure 7.5(c) for different isolator corner frequencies. Those that

correspond to the differential tip displacement do exhibit pole-zero cancellations as the corner frequency drops from 20 Hz to 2 Hz. This can be more easily seen by examining the phase plot. The 2 Hz curve has a 180° phase loss at the isolator mode, but the higher modes contribute little phase change, as is evident by the extremely small phase deviations about the −180° line. The larger frequency isolator models exhibit more phase loss due to lightly-damped beam modes that do not have neighboring lightly-damped zeros. The transfer functions for the differential tip rotation, on the other hand, do not show any signs of the washout effect. For the different isolator models, they all show large resonant behavior at the higher frequencies. These results suggest the washout phenomenon is probably not a numerical conditioning issue, especially due the fact that this example problem is not extremely complex. In fact, the results are analogous to the trends seen in the SIM trade studies. The OPD is affected by the loss of observability and/or disturbability of the higher modes, thereby causing a knee in the curves. DWFT and DBS do benefit from the additional isolation since the highly-resonant modes at higher frequencies which normally would contribute to the performance are being lowered in magnitude due to the isolation. Further work is recommended in order to confirm these findings. It should be noted, however, that the results to follow do not heavily depend on the shape of the OPD curves for lower corner frequency isolators.

Thus far, both performance and disturbance isolation have been examined. The other CST option that is listed in Table 7.1 and that can be implemented on the SIM model is disturbance modification. This is one of the options which can achieve large performance improvement on a nominal design when done properly. The original RWA disturbance model that was used to obtain the previous results is based on an assumption of wheel speeds in the 0–3000 RPM range. Now consider the case when the wheel speeds are restricted to lie within the 0–600 RPM range. It is not known how practical it would be to have a lower maximum allowable reaction wheel speed during an observation. This might not be possible during long integration times of extremely dim objects; however, this issue will be overlooked for now. Plots of the approximate disturbance PSD's for both the 0-3000 RPM case and 0–600 RPM case are visible in Figure 7.6. Reducing the maximum wheel speed serves to reduce significantly the energy at high frequencies; however, this also allows the wheels to spend more time at the lower speeds. The result is that at low frequencies, the PSD's for the 0–600 RPM case actually exceed the PSD's for the 0–3000 RPM case.

244
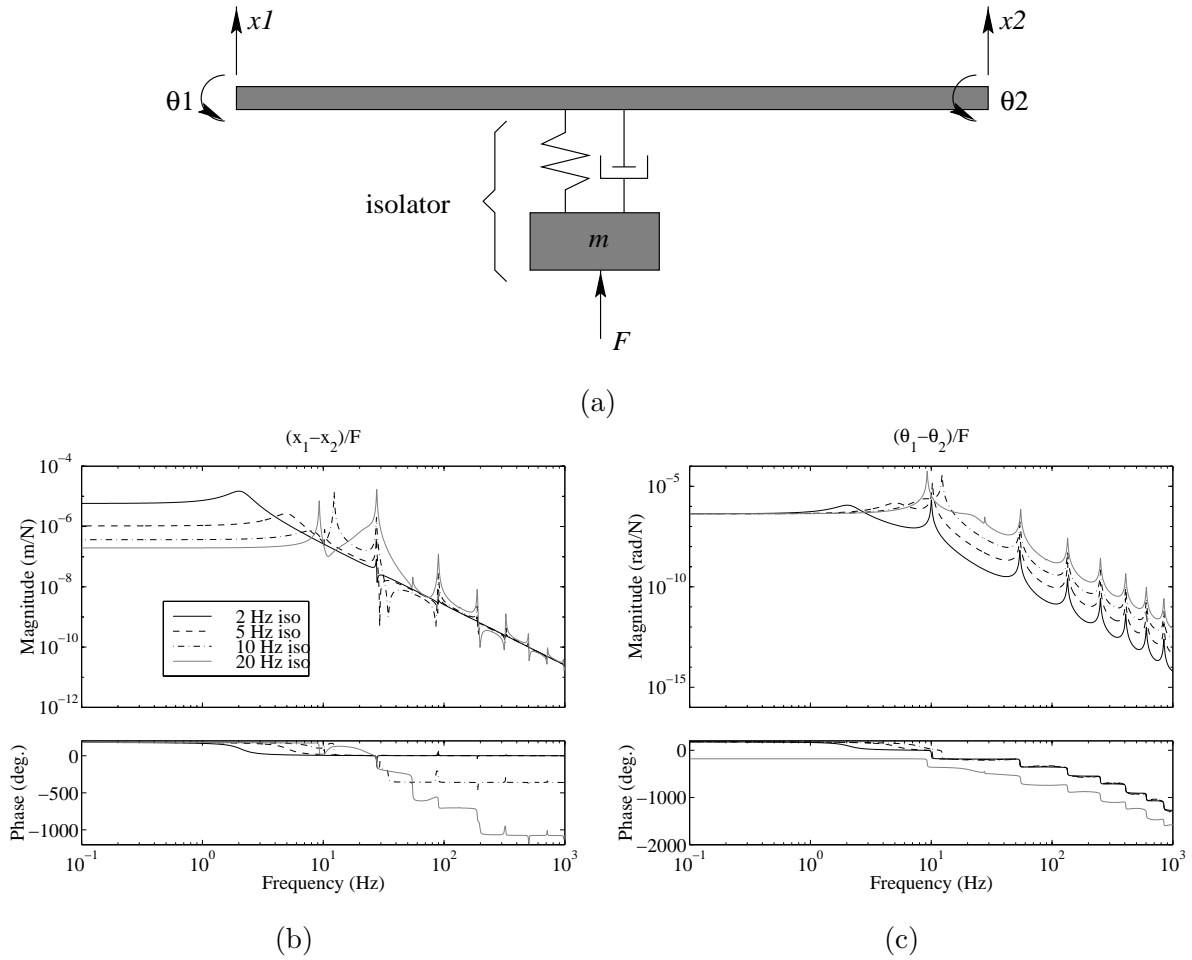
Figure 7.5: (a) Sample system to demonstrate washout effect. (b) Transfer function from disturbance to differential tip displacement for various isolators. (b) Transfer function from disturbance to differential tip rotation for various isolators.
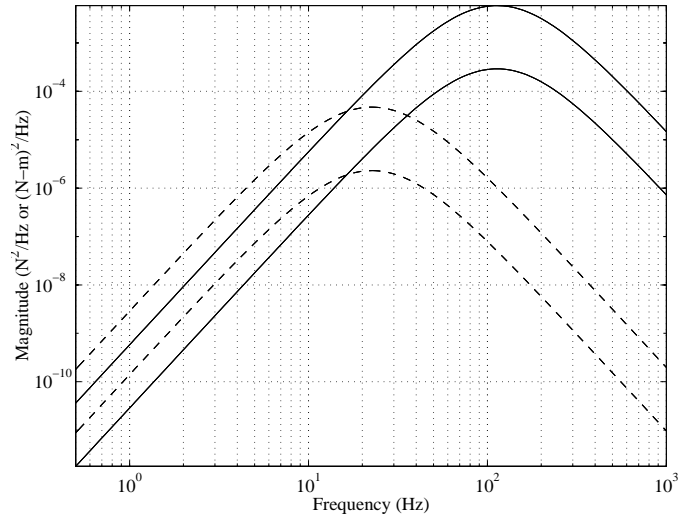
Figure 7.6: Disturbance PSD's for the 0–3000 RPM case (—) and for the 0–600 RPM case (−−).

Rerunning all of the disturbance analyses for various combinations of isolator corner frequencies and amount of optical control produces the results in Figure 7.7. When the RMS values are compared to those in Figure 7.2, some distinguishing features become apparent. First, the only consistent performance improvement in all three metrics occurs when no isolation is present. This makes sense because without isolation to attenuate the vibrations that excite the higher frequency modes, the larger energy content of the 0–3000 RPM disturbance at high frequencies ($> 20\,\text{Hz}$) passes through easily. As seen previously in Figure 7.3, modes up to and slightly beyond 100 Hz contribute a noticeable amount to the RMS values when the model does not have the benefit of isolation. When isolation is present, it is the lower frequency modes that can contribute the most to the overall RMS. If these critical modes occur below approximately 17 Hz, then the extra energy in the 0–600 RPM case at these frequencies can actually make the RMS worse. This could possibly explain the increase seen in the OPD metrics for the three interferometers when disturbance isolation is used and optics loops are open.

Another feature is that for the isolated cases of DWFT and DBS, there do not appear to be significant differences with the corresponding RMS values in the 0–3000 RPM case. Restricting the wheel speed range does not offer much benefit for these metrics. The PSD's and cumulative RMS curves in Figure 7.8(a) provide a clue as to why this is the case. This plot compares the results of the guide 1 DWFT with all optics loops closed and a

246

Figure 7.7: SIM optical performance metrics as a function of isolator corner frequency and levels of optical control. Structural damping = 0.1%. (Based on HST RWA 0–600 RPM disturbance model.)
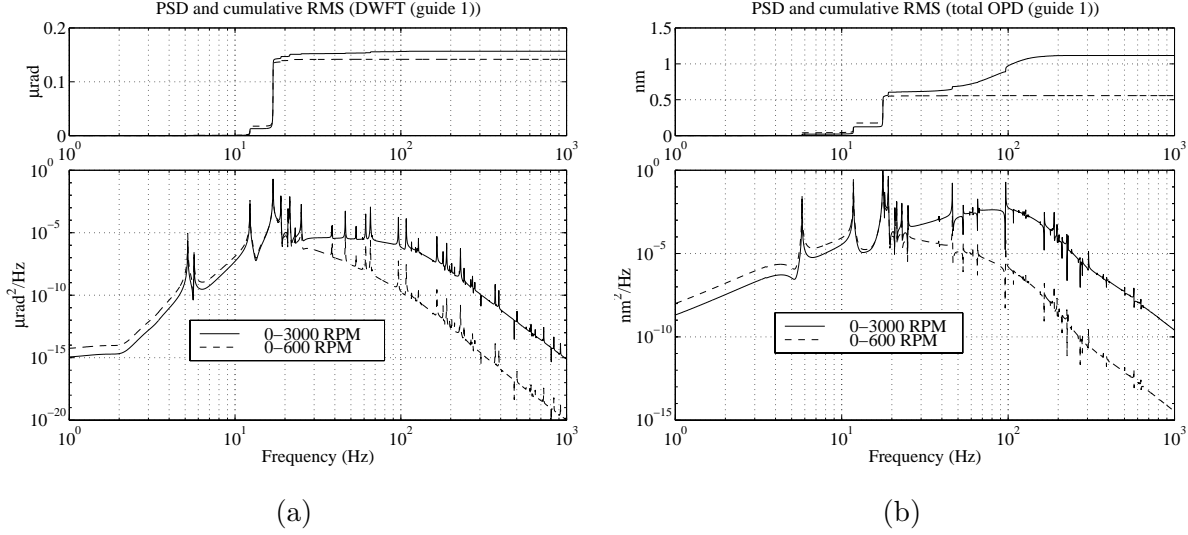
Figure 7.8: (a) Differential wavefront tilt of guide interferometer #1 with closed FSM loops and either a 0–3000 RPM RWA speed range or a 0-600 RPM speed range (10 Hz isolator). (b) Total OPD of guide interferometer #1 with closed pathlength loops and either a 0–3000 RPM RWA speed range or a 0-600 RPM speed range (5 Hz isolator).

10 Hz isolator. For both wheel speed ranges, the critical mode is near 17 Hz, which is the frequency around which the disturbance PSD's in Figure 7.6 have approximately the same magnitude. Therefore, the lower energy content at higher frequencies for the 0–600 RPM case does not matter.

The OPD values, however, are affected by the lower wheel speeds. The RMS values decrease when the optics loops are closed and increase slightly when the optics loops are open. Figure 7.8(b) compares the PSD's and cumulative RMS curves of the total OPD of guide 1 when only the pathlength control loops are closed and there is a 5 Hz isolator. For the 0–3000 RPM case, the OPD RMS value is dependent on frequencies up to around 200 Hz. When disturbance energy is lowered between 20 Hz and 200 Hz due to restricted wheel speeds, the resulting RMS is lowered as well (by a factor of about 2 in this example plot).

Based on all of the results shown so far, the recommended design consists of a 10 Hz isolator with closed pathlength (ODL, fringe tracker) and pointing (FSM) loops. The reaction wheel speeds are permitted to take on values over their entire operating regime of 0–3000 RPM. For this level of isolation and optical control, restricting the wheel speeds does not lead to a performance improvement large enough to justify placing a constraint on the

Table 7.2: Comparison of RMS values for different SIM designs.

Optical metric	Reqmt.	Design 1		Design 2	
		RMS	design margin	RMS	design margin
Total OPD (g1)	4.4 nm	4.36 nm	0.073 dB	2.71 nm	4.20 dB
Total OPD (g2)	4.4 nm	3.21 nm	2.75 dB	3.53 nm	1.91 dB
$\sqrt{J}$	1.41	1.23	1.21 dB	1.01	2.92 dB
DWFT (g1)	0.704 μrad	0.154 μrad	13.2 dB	0.124 μrad	15.1 dB
DWFT (g2)	0.704 μrad	0.124 μrad	15.1 dB	0.106 μrad	16.5 dB
DBS (g1)	N/A	0.996 μm	–	0.784 μm	–
DBS (g2)	N/A	0.949 μm	–	0.789 μm	–

time between momentum dumps of the wheels. The RMS values of this design (labeled Design 1) are compared to the requirements in Table 7.2. Values for the science interferometer are intentionally omitted since it is anticipated that other control strategies not currently in the model will be used to improve the fringe tracking and pointing peformance of this interferometer. The structural redesigns will focus on improving the performance of the guide interferometers.

The total OPD metrics have the smallest design margins (0.073 dB and 2.75 dB, respectively). Since the first margin will almost assuredly be used up when a worst-case uncertainty analysis is conducted, there is a motivation to try to increase the margins a bit. Based on the performance enhancement methodology in Table 7.1, the next options that can be implemented are increased passive damping and minor stiffness/mass modifications. Figure 7.9 shows the RMS values of the optical performance metrics for the 0-3000 RPM case when the structural damping is increased to 1%. As expected, all of the RMS values are lower than the results for the models characterized by 0.1% damping. In fact, the DWFT requirement is satisfied regardless of the presence of isolation or closed optics loops.

To better identify physical parameters that affect the total OPD values for both guide interferometers, define a weighted cost J as follows.

$$J = \frac{1}{\sigma_{\mathrm{OPD,req}}^2} \left(\sigma_{\mathrm{OPD,g1}}^2 + \sigma_{\mathrm{OPD,g2}}^2 \right) \tag{7.4}$$
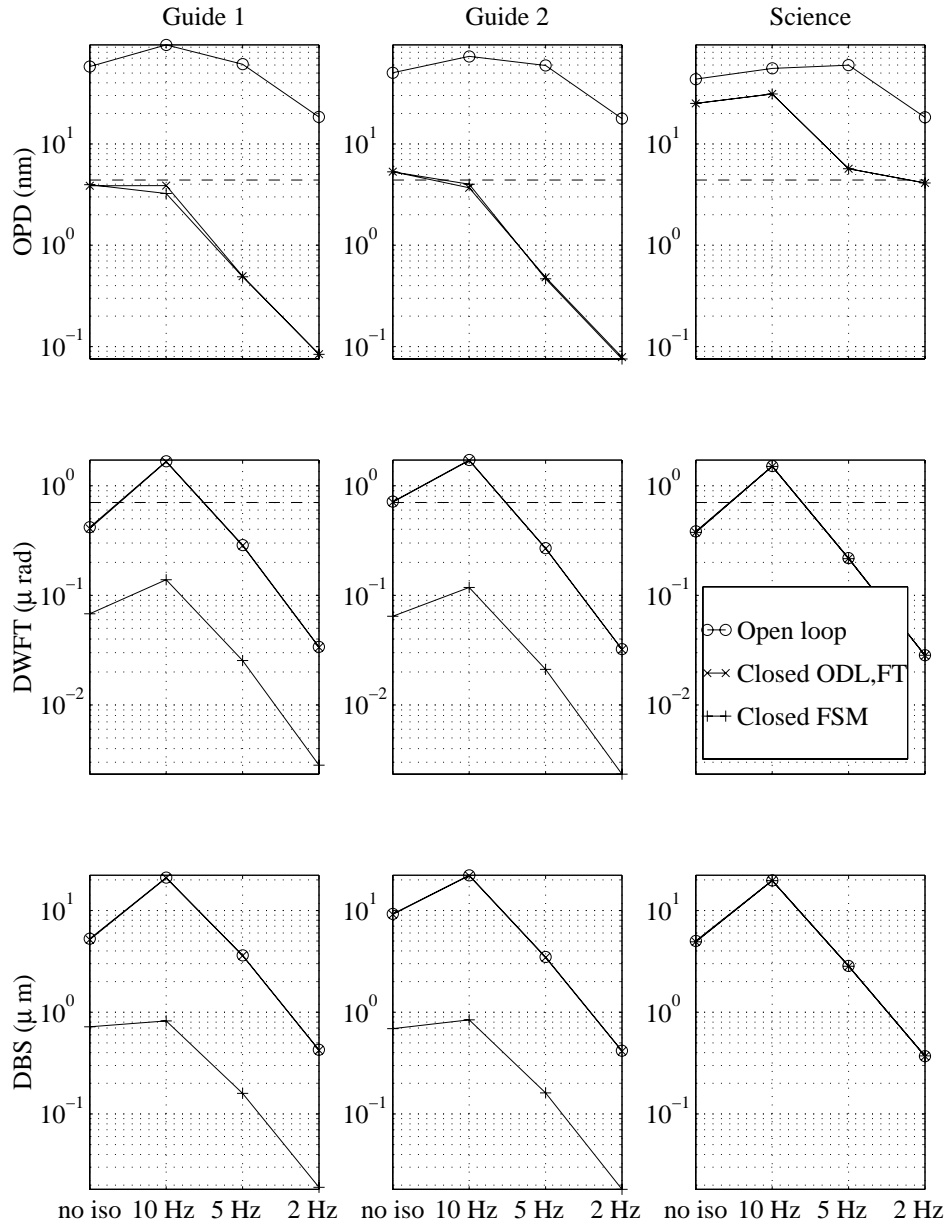
Figure 7.9: SIM optical performance metrics as a function of isolator corner frequency and levels of optical control. Structural damping = 1%. (Based on HST RWA 0–3000 RPM disturbance model.)
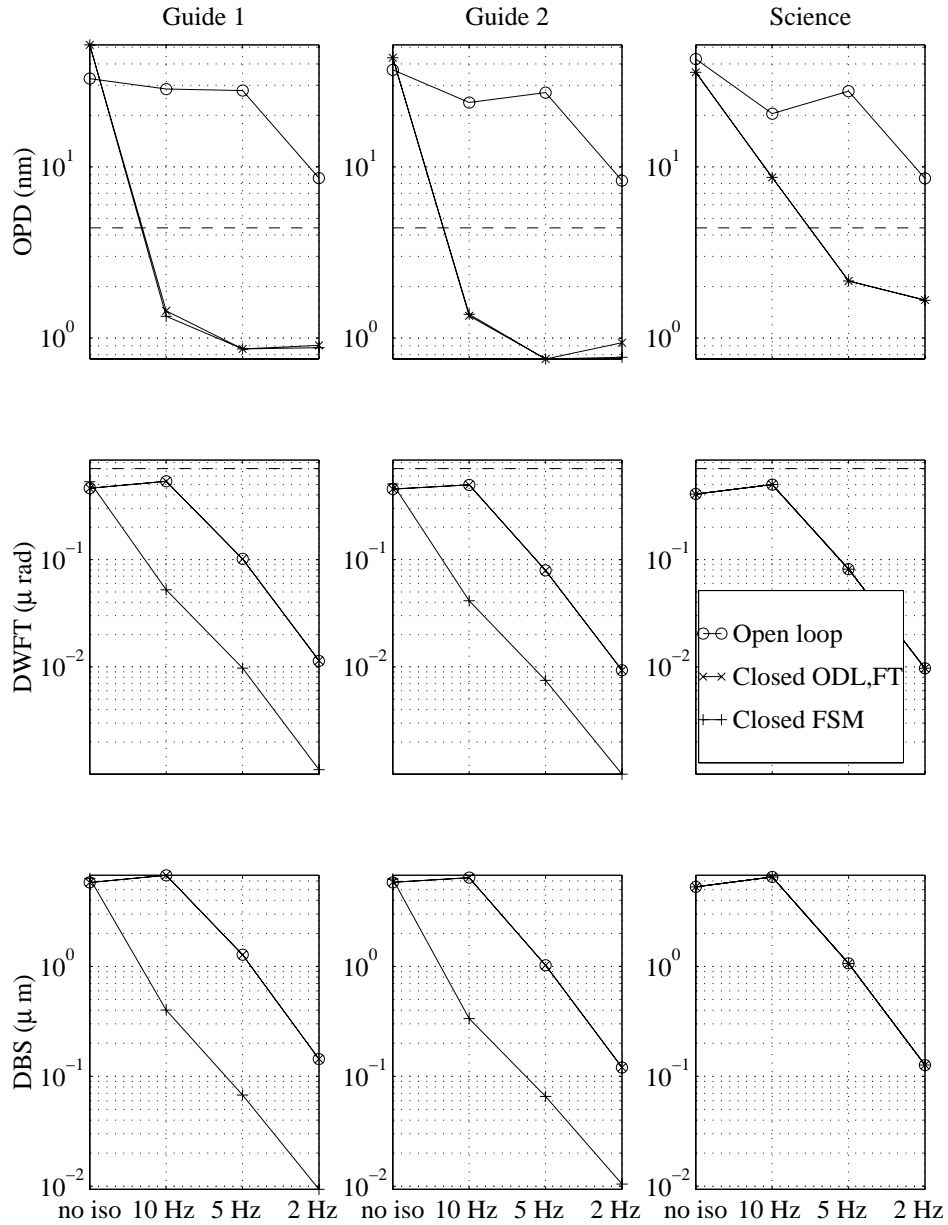
Since the OPD of guide 1 is the metric with the smallest margin, there might be a temptation to carry only this metric into a disturbance and sensitivity analysis to identify important structural parameters. However, a structural modification that improves $\sigma_{\text{OPD,g1}}$ is not guaranteed to improve $\sigma_{\text{OPD,g2}}$. The combined cost J allows identification of structural enhancements that attempt to improve both metrics. The DWFT metrics, on the other hand, have sufficient design margin and do not need to be included in the cost function. Only small structural modifications will be implemented, and they should not drastically reduce the design margins of the DWFT metrics. (The design margins will be checked, however, after the redesign is implemented.)

A frequency-domain disturbance analysis produces the cumulative RMS curve, PSD, and disturbance contribution plot in Figure 7.10(a). The bar char in Figure 7.10(b) summarizes these results, and it is apparent that the mode at 16.95 Hz contributes about 25% of the total value of J. Other critical modes are at 12.3 Hz and 18.91 Hz. Several of the modes listed are almost entirely excited by the reaction wheel M_z disturbance. The sensitivities of the square-root of J with respect to modal parameters are plotted in Figure 7.10(c), and the critical modes identified from this plot do correspond to those in Figure 7.10(b), as expected. Assuming $\pm 5\%$ uncertainty in the frequencies of the three most critical modes, a first-order uncertainty analysis predicts an approximately 7% increase in the square-root of J (14% increase in J).

Mode shape and strain energy distribution plots for the modes at 16.95 Hz, 18.91 Hz, and 21.39 Hz were shown in Section 4.6.2. Recall that the first mode is characterized by siderostat boom torsion and the latter two modes are characterized by local siderostat bay modes. The 12.3 Hz mode is one of the six hexapod modes. Three parameters were chosen for the physical parameter sensitivity analysis. They are the torsional constant J of the siderostat boom cross section (not to be confused with the cost J), a stiffness scale factor α used to adjust all of the siderostat bay stiffnesses simultaneously, and a mass scale factor β used to adjust all of the siderostat bay masses simultaneously. The sensitivities of the square-root of J with respect to these parameters are shown in Figure 7.11. Assuming that a 1% change in each of these parameters "costs" approximately the same to implement, then the torsional constant J provides the largest performance improvement potential, followed by the siderostat bay parameters α and β. All three sensitivities are positive, which indicates that performance improvement (*i.e.*, cost reduction) is achieved by decreasing the values of

(a)

(b)

(c)
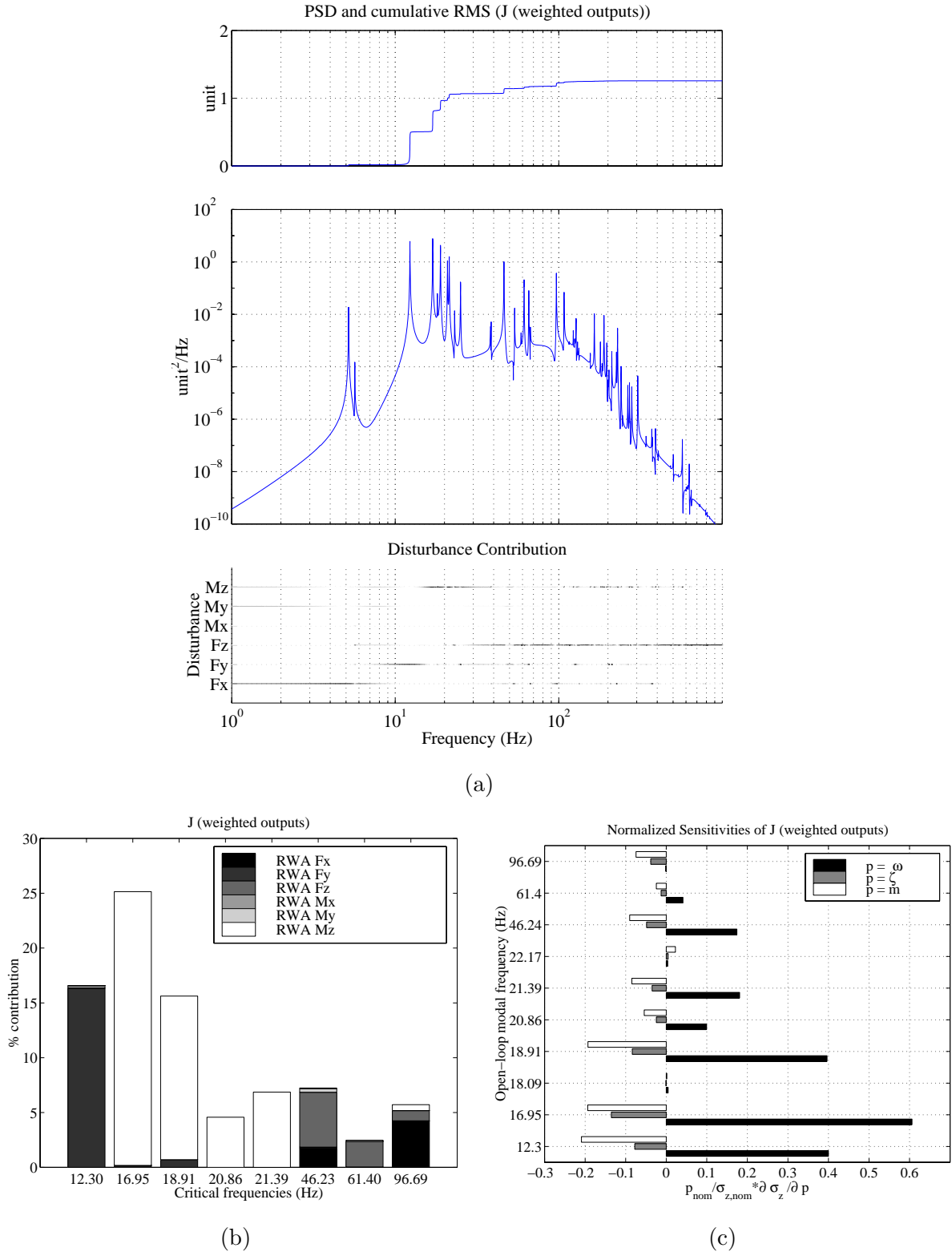
Figure 7.10: (a) PSD, cumulative RMS, and disturbance contribution plots of weighted OPD for guide 1 and guide 2. (b) Critical modes and disturbances. (b) Modal parameter sensitivities of weighted OPD.

Normalized sensitivities of J (weighted outputs) RMS value
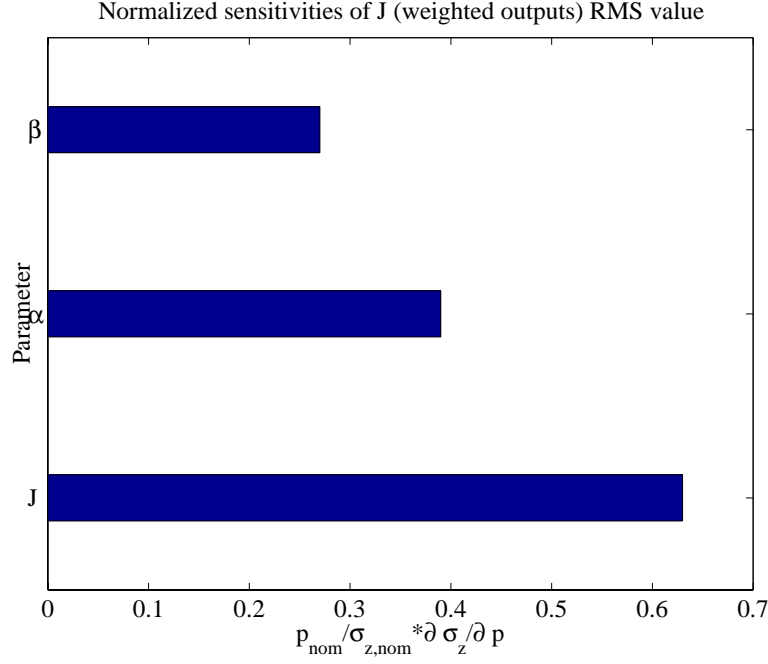
Figure 7.11: Physical parameter sensitivities.

these parameters.

Specify a hypothetical design constraint that only stiffness changes are allowed. Then based on the sensitivities in Figure 7.11, an approximately 15% decrease in both J and α should lead to about a 15% decrease in the square-root of the cost (*i.e.*, a 30% decrease in the cost). Implementing these design changes in the FEM produces the values listed under the "Design 2" column of Table 7.2. A large improvement in the $\sigma_{\text{OPD,g1}}$ margin is accomplished with only a small sacrifice in the $\sigma_{\text{OPD,g2}}$ margin. In addition, slight reductions in the DWFT and DBS RMS values are evident. A zoom into the critical frequency range of the PSD of J in Figure 7.12 reveals that the softening of the structure does lead to performance improvement over the nominal design. The square-root of the cost falls from 1.23 to 1.01, which represents an 18% decrease. This is close to the 15% decrease predicted by the physical parameter sensitivities. Thus, these sensitivities have been successfully used to identify performance enhancing structural modifications.

Although not required, passive damping can be added to the system to further improve the RMS values of the optical performance metrics. The column labeled "Design 3" in Table 7.3 shows the improvements when the nominal structural damping of Design 2 is increased from 0.1% to 1%. The results for the science interferometer are also shown, and
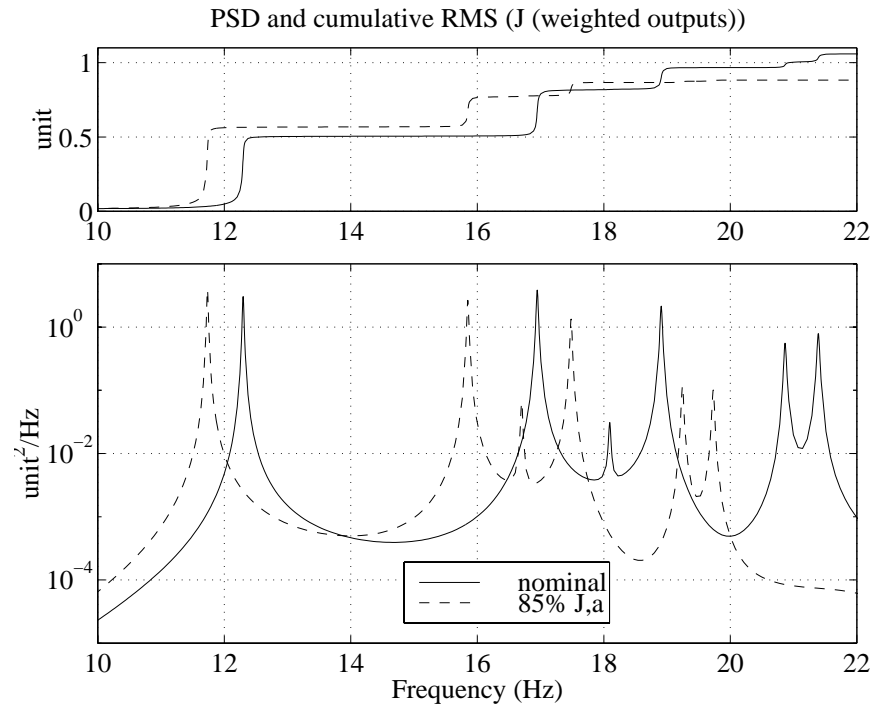
Figure 7.12: PSD's and cumulative RMS curves for the nominal design and the design with 15% decrease in torsional constant J and 15% decrease in siderostat bay stiffnesses.

Table 7.3: Comparison of RMS values for different SIM designs.

Optical metric	Reqmt.	Design 3		Design 4	
		RMS	design margin	RMS	design margin
Total OPD (g1)	4.4 nm	1.28 nm	10.7 dB	0.907 nm	13.7 dB
Total OPD (g2)	4.4 nm	1.45 nm	9.66 dB	0.939 nm	13.4 dB
Total OPD (s)	4.4 nm	7.27 nm	−4.36 dB	1.67 nm	8.4 dB
DWFT (g1)	0.704 μrad	0.044 μrad	24.1 dB	0.0115 μrad	35.8 dB
DWFT (g2)	0.704 μrad	0.0352 μrad	26.0 dB	0.0093 μrad	37.6 dB
DWFT (s)	0.704 μrad	0.446 μrad	3.97 dB	0.0097 μrad	37.2 dB
DBS (g1)	N/A	0.344 μm	–	0.144 μm	–
DBS (g2)	N/A	0.277 μm	–	0.121 μm	–
DBS (s)	N/A	5.83 μm	–	0.127 μm	–

we notice that the requirements are still not being met. The DWFT metrics of the guide interferometers, though, have no trouble meeting the requirement.

Now consider an ambitious and somewhat radical design consisting of a 2 Hz isolator, 1% structural damping, closed pathlength loops, and open FSM loops. The resulting RMS values are found under the "Design 4" column in Table 7.3. In this case, all three interferometers have positive design margins for the OPD and DWFT metrics. This design is unique in that an extremely soft isolator is used to compensate for the limited disturbance rejection properties of the science pathlength loop. It also allows most of the DWFT errors to be reduced without the use of FSM control.

Looking ahead to redoing this process for the nulling mode of operation, we can anticipate that the OPD and DWFT requirements will become more stringent by roughly a factor of 10. If this is this case, then Design 4 will not satisfy the OPD requirements, but it should still be able to satisfy the DWFT requirements. To accurately assess this mode, the integrated model will need to incorporate pathlength feedforward techniques (*e.g.*, accelerometer feedforward). In addition, the observation of even fainter science stars than have been implicitly assumed by the science pathlength and pointing control bandwidths will also require the use of these feedforward techniques.

7.3 Summary

A methodology has been described for improving the performance of a nominal system by using traditional CST options. Trade studies are conducted first to focus on the disturbance and performance aspects of the system. When a design is found that satisfies or nearly satisfies requirements, then minor structural changes such as mass and stiffness modifications or passive damping augmentation are identified that achieve desired design margins. Physical parameter and modal parameter sensitivity analyses can be conducted to help pinpoint which changes are the most beneficial. Active structural control or major topological redesigns are additional options when the other options fail to produce satisfactory results.

The overall performance assessment and enhancement framework was applied to a model of SIM Classic. Requirements for the astrometry mode of operation were identified, and trade studies investigated the performance improvements that can be achieved with RWA isolation, RWA speed restrictions, pathlength control, pointing control, and passive damping. Focus was placed on improving the performance of the guide interferometers since feedforward techniques have not yet been implemented to assess the science interferometer. Results indicate that the pathlength requirements are more difficult to meet, but can be satisifed through a combination of reaction wheel isolation and pathlength control. The wavefront tilt metrics, however, can satisfy the pointing requirement with isolation alone and do not necessarily need to rely on closed FSM loops. Restricting the maximum reaction wheel speed to be 600 RPM instead of the nominal 3000 RPM did not improve all of the optical RMS values. The only appreciable benefits were observed in the OPD metrics for the cases that used isolators with 5 Hz or lower corner frequencies.

Structural modifications based on physical parameter sensitivities were successfully implemented and achieved the predicted amount of design margin increase. The modifications consisted of decreasing by 15% the torsional rigidity of the siderostat booms and the stiffness of each siderostat bay relative to the siderostat boom. This suggests that further improvements might be achieved by "tuning" the siderostat bays individually. Additional RMS reduction was achieved by increasing the damping of the critical modes from 0.1% to 1%.

Although the goal of the design exercise was to improve the system performance during the astrometry mode, consideration was given to the eventual goal of meeting the nulling

requirements. For the 0-3000 RPM RWA case, a design consisting of a 2 Hz isolator, closed pathlength loops, and 1% structural damping failed to meet the OPD requirements; however, indications are that the DWFT requirements can be achieved. This highlights the need for pathlength feedforward techniques. The results also suggest that the DWFT error budget can be revisited such that the allocation to RWA-induced disturbances is lowered and distributed elsewhere. For instance, noisier yet less costly pointing control sensors might be permitted.

Chapter 8

Conclusions and Recommendations

This concluding chapter summarizes the performance assessment and enhancement framework that has been developed and demonstrated in the preceding chapters. The major contributions that were made during the course of the development are listed, and further work that would extend the capabilities of this framework are suggested.

8.1 Thesis Summary

The next generation of space-based scientific observatories are characterized by stringent tolerances on optical performance metrics. The success of these spacecraft depends greatly on the ability of optical control and vibration mitigation techniques to provide stabilization of collected starlight despite the excitation of flexible structural modes by disturbance sources. Early design trades and decisions rely on initial analyses that use simplified models of these high performance systems. A methodology was created that applies a systematic process to predict the effects of disturbances on the system and to estimate variations in the predictions due to model uncertainties. In addition, it suggests standard control-structure-interaction technologies and structural modifications to improve the performance when needed.

Chapter 2 described the integrated modeling process used to generate models of initial concepts. Structural dynamic modeling provides the governing equations of motion for the system and predicts the effect of control and disturbance inputs on the structural displacements. Optical modeling uses linear ray trace theory to relate the displacements of optical elements to perturbations in optical metrics such as pathlength and wavefront tilt.

Control modeling introduces a compensator that uses outputs of the model to determine the appropriate control inputs to apply to the system for purposes such as disturbance rejection or command-following. Disturbance modeling quantifies the magnitude, spectral content, and location of anticipated disturbances. Chapter 2 reviewed stochastic process theory and its potential use as a tool for characterizing disturbances. Stochastic process theory avoids a costly Monte Carlo analysis by producing "expected" disturbance levels; however, worst-case situations cannot be directly identified. The importance of disturbance modeling was emphasized, and serious efforts should be placed in this area.

The interplay between the different disciplines suggests that the modeling cannot occur independently. For instance, structural modeling must provide the locations at which optical elements exist and disturbance and control forces are applied. Everyone associated with the integrated modeling process must be aware of the requirements placed by each discipline on the others. A recommendation related to control modeling during the early conceptual design process is that the control designs implemented should be realistic, especially in terms of gain and bandwidth limitations. Performance predictions based on controllers that assume perfect sensors and actuators and utilize precise knowledge of the plant model will be misleading. For instance, large predicted performance improvement due to the control might result in fewer vibration mitigation techniques being incorporated in the design. It might be difficult to add these technologies to the system after it has been constructed and found to require them. A consideration of numerical conditioning issues revealed that compensator state-space representations that are derived from typical numerator-denominator transfer function form should be transformed into a balanced realization. Furthermore, if model reduction is to be performed, the model inputs and outputs should be scaled such that the transfer functions are of similar order of magnitude. This allows modes that are important in some input/output channels but not others to be retained in the model.

The integrated model of one concept for the Space Interferometry Mission (SIM) was also described in Chapter 2. This model was developed at the Jet Propulsion Laboratory and served as a typical spacecraft model on which to demonstrate the analysis tools that were developed. A new method for generating reaction wheel assembly (RWA) stochastic disturbance models was introduced. This method extends a current technique that models only a single wheel explicitly. This approach was used to create Hubble-based RWA disturbance models that are applied to the SIM model.

Chapter 3 reviewed three types of disturbance analyses that can be conducted when a system is represented in state-space form. A standard time simulation involves numerical integration of the equations of motion. The integration step size should be small enough to capture the highest frequencies of interest, but should be large enough such that the computational time does not become excessive. A simple spring-mass system driven by white noise showed the fundamental trade between time-simulation length and the accuracy of the predicted steady-state RMS value.

The second type of disturbance analysis is based on propagating disturbance power spectral density (PSD) functions through the system transfer functions to obtain the performance PSD's. The spring-mass system was used to demonstrate the effects of frequency resolution on the predicted RMS values. More frequency points lead to more accurate estimates, but at the cost of increased computation time. The frequency resolution around lightly-damped modes is particularly critical, and the appropriate resolution can be determined by plotting a cumulative RMS curve, which indicates the contribution to the overall RMS value as a function of frequency. Lightly-damped modes manifest themselves as sharp "steps" in the cumulative RMS function, and accurate RMS estimates require that a sufficient number of frequency points define each step. The cumulative RMS function can also be used to determine if the number of modes retained in the model is sufficient. A cumulative RMS curve that is still rising after the last mode has been reached is an indication that additional modes will probably add to the predicted RMS.

A frequency-domain disturbance analysis was also shown to provide information related to the disturbance contribution at each frequency based on an uncorrelated assumption for the disturbances. The results of the analysis can be conveniently displayed in bar chart form. For each mode, the length of the bar is proportional to that mode's contribution to the performance variance, and the bar is subdivided according to the relative contribution from each disturbance. Examining this type of plot quickly conveys the critical modes and disturbances that affect the performance metrics. A frequency-domain analysis was demonstrated on the SIM model, and the most critical mode for an optical path difference (OPD) metric was identified as a boom torsion mode that was excited most by RWA disturbances about the global z axis. In this example, neglecting the off-diagonal terms in the disturbance cross-spectral density matrix was shown to allow quicker computation times without significant loss in accuracy.

The third type of disturbance analysis assumes that the overall state-space system (with appended disturbance filter dynamics) is excited by pure white noise. A Lyapunov equation is solved to obtain the state covariance matrix, which can then be transformed to obtain the performance covariance matrix. This approach produces the exact, theoretical mean-square values of the various performance metrics. The computation time can be excessive for large-order models; however, model reduction strategies can produce a smaller system that retains accurate performance prediction capability.

Using a Lagrange multiplier approach, Chapter 4 derived the exact expression for the sensitivity (*i.e.*, derivative) of performance RMS values with respect to a generic parameter. The sensitivities require the solution of one Lyapunov equation for the state covariance matrix plus one Lyapunov equation for the Lagrange multiplier matrix for every performance metric. Also required are the derivatives of the state-space matrices with respect to the parameter. A review was provided of the steps to place a structural model in modal, state-space form. After closing control loops (if present) and placing a disturbance shaping filter in series with the system, the sensitivity equation can be simplified when the parameter of interest is a modal frequency, modal mass, or damping ratio of the open-loop structural system. A normalized sensitivity value can be computed that provides an indication of the percent change in the RMS values for a percent change in each parameter individually. The modes with the largest normalized modal parameter sensitivities were shown to correspond to the critical modes identified from a frequency-domain analysis. The exact sensitivity approach is more computationally efficient than a finite-difference approach when the number of parameters of interest exceeds the number of performance variables. Results on the SIM model indicated that the sensitivities from a finite-difference approach were not numerically stable as the parameter perturbation size was decreased.

Chapter 4 also described a method for computing sensitivities of performance RMS values with respect to physical parameters of the structural finite-element model. These sensitivities provide more intuition from a structural redesign perspective. The method requires that the derivatives of mode shapes, natural frequencies, and modal masses be computed with respect to the parameters of interest. An existing code was modified to include the modal mass derivatives and to accommodate desired parameters such as elastic spring element constants and lumped mass/inertia values. Necessary modifications were also made to the equations when the finite-element model consists of independent and

dependent degrees of freedom. The physical properties of elements with strong influence on the critical modes are chosen for the sensitivity analysis, and strain energy distribution plots help to make this selection. The sensitivity calculations can be computationally intensive for large models; however, simplifications were identified to reduce the computational effort with minimal impact on the results. For instance, the method only requires knowledge of mode shapes at DOF's associated with inputs and outputs. Also, only those modes that significantly contribute to the performance need to be retained in the computations. This was demonstrated on a simple, cantilever beam example problem. Application to the closed-loop SIM model revealed that the sensitivities of an OPD metric are large with respect to the torsional rigidity constants G and J of the siderostat booms and the generalized stiffness and mass properties of a siderostat bay. This appears to be the first attempt in the literature of computing accurately the performance sensitivities of a large-order (307 states), closed-loop model with respect to physical parameters.

The effect of model uncertainties on performance RMS predictions was the topic of Chapter 5. A technique was developed that searches for allowable values of modal frequency, modal mass, and modal damping ratios of specified modes that maximize the predicted cost. The cost is a weighted combination of performance mean-square values; therefore, the technique identifies the worst-case performances. The modes with the largest modal parameter sensitivities are selected for the uncertainty analysis. A constrained optimization approach is used to identify the worst-case parameters, and multiple runs with different initial guesses are required to improve confidence that the solution is converging to the global maximum. In addition, analytical gradient information based on modal parameter sensitivities is supplied to the optimization routine to help the solution process. The result of applying the technique to a low-order, open-loop system suggests that the worst-case modal parameters can be identified *a priori* by placing the parameters at the bounds indicated by the directional information of the modal parameter sensitivities. A counter-example was also analyzed that showed the worst-case parameters do not necessarily occur at these bounds for systems with frequency uncertainty larger than the frequency separation. To accommodate large-order models, an approximate balanced model reduction technique was developed that uses the original balancing transformation matrix at each iteration of the optimization routine. Approximate gradient information is also computed, and these gradients were shown to decrease the number of iterations required to converge to a solution.

The uncertainty analysis method was demonstrated on the SIM model and showed that $\pm 5\%$ uncertainty in three critical modes can lead to a 14% increase in the predicted RMS value of an OPD metric.

The physical parameter sensitivity approach was experimentally validated on a laboratory testbed, and the results were presented in Chapter 6. The design of the cantilever truss structure with a flexible appendage was motivated by the types of critical modes identified during the physical parameter sensitivity analysis on the SIM model. The testbed was also designed to accommodate stiffness and mass changes that could primarily affect either the global truss modes or the local appendage modes. An automated finite-element model updating routine was developed and used to suggest Young's modulus values E and modal damping ratios that minimized the error between measured transfer functions and FEM-based transfer functions. The routine relies on mode shape, frequency, and modal mass derivatives with respect to the physical parameters chosen to be updated. This allows first-order effects of parameter perturbations to be estimated without regenerating the FEM at each iteration. As a truth check, however, the FEM can be created after a specified number of iterations to correct for accumulated errors due to the first-order approximations. Physical parameter sensitivities were computed using the updated model and were compared to sensitivities obtained experimentally. The experimental estimates were calculated from a finite-difference approximation after a mass or stiffness modification was made to the nominal testbed. Performance RMS estimates were obtained by integrating under the PSD of the appendage tip displacement. The model-based sensitivities and RMS estimates were found to agree favorably with the measured quantities. Modifications to the testbed based on the sensitivity information did produce the anticipated decrease in tip displacement. This demonstrated the usefulness of the physical parameter sensitivities as a redesign tool.

Chapter 7 applied the overall performance assessment and enhancement framework to the SIM integrated model. Trade studies identified the relative benefits of RWA isolation, RWA speed restrictions, layered optical control, and passive damping on optical path difference (OPD), differential wavefront tilt (DWFT), and differential beam shear (DBS) metrics of the three interferometers. Lower isolator corner frequencies did lower the RMS values of all the metrics; however, the OPD metrics experienced diminishing returns due to a "washout" effect. This effect was observed in a sample beam problem that was created

to examine this issue further. As anticipated, closing pathlength loops improved the OPD metrics, while closing fast-steering mirror loops (FSM) improved the DWFT and DBS metrics. The DWFT metrics were able to meet astrometry requirements with higher-frequency isolators than the OPD metrics. This suggests that the OPD requirements are the most stringent. Reducing the maximum allowable wheel speed from 3000 RPM to 600 RPM was beneficial mainly for the OPD metrics and not the DWFT and DBS metrics. This was attributed to the frequencies of the critical modes for the metrics. Higher frequencies (20–100 Hz) contributed a large fraction to the OPD RMS values when optics loops were closed, while lower frequencies (< 20 Hz) contributed most to the DWFT and DBS metrics when optics loops were closed. The disturbance PSD's of the 3000 RPM case are actually about the same magnitude as the disturbance PSD's of the 600 RPM case at low frequencies (< 20 Hz); therefore, restricting the wheel speeds does not offer much benefit for the DWFT and DBS metrics.

An example performance enhancement exercise was shown that utilized physical parameter sensitivity information. The sensitivities with respect to the siderostat boom torsional rigidity and siderostat bay generalized stiffness were computed and suggested that both should be decreased to improve a weighted combination of OPD mean-square values for the guide interferometers. Design margins were successfully increased by modifying the FEM and computing the new performance. The increased design margin was large enough to enable worst-case performance predictions to still meet the requirements. The DWFT metrics had extremely large design margins, and this suggests that another iteration of the error budgeting process can relax the allocation to RWA-induced DWFT error. This might permit a larger error allocation to sensor noise or resolution, thereby allowing less costly sensors.

All of the original thesis objectives were achieved, and they are repeated here.

- Develop a consistent and general methodology for assessing the performance of systems in which the structural dynamic and control aspects must be considered.

- Implement the methodology as a series of compatible analysis tools that are applied to a nominal system model driven by disturbance models. The tools should consist of

  - a disturbance analysis tool for predicting performance outputs,

- a sensitivity analysis tool for predicting changes in performance outputs due to changes in model parameters, and

- an uncertainty analysis tool for estimating variations in the predicted performance outputs due to uncertainties in model parameters.

- Identify computation and time-saving measures that permit the analysis tools to be applied to large-order systems.

- Suggest an approach for performance enhancement that utilizes the analysis results to identify design options with improved performance.

- Validate the analysis tools on various mathematical systems and on an experimental testbed.

- Apply the overall methodology to an existing integrated model of the Space Interferometry Mission.

8.2   Contributions

The following specific and unique contributions were made during the course of meeting the thesis objectives.

- A method was developed for generating a frequency-domain stochastic disturbance model of a reaction wheel assembly. The technique assumes that the disturbances from a single wheel are wheel-speed dependent. A rigorous mathematical approach was used to generate the spectral-density matrix of net disturbance forces and moments arising from multiple reaction wheels in arbitrary orientations. Although wheel speeds are treated as independent random variables, the theory is in place to allow other assumptions (such as equal wheel speeds) to be made.

- A disturbance analysis framework was developed and implemented in MATLAB code, which was written to be general enough to be applied to any state-space system. Time-domain, frequency-domain and Lyapunov disturbance analyses can be conducted to obtain performance RMS values, and in particular, a frequency-domain disturbance analysis was shown to provide further insight. Plots of cumulative RMS curves as well as bar charts of modal and disturbance contributions are used to quickly identify

266

important modes and disturbances that affect the performance metrics. A recommendation was made to always show a cumulative RMS curve whenever a PSD is plotted. Cumulative RMS curves can also be used to determine if the frequency resolution is sufficient and if enough modes are retained in the finite-element model for accurate RMS estimates.

- A sensitivity analysis framework with respect to modal and physical parameters was developed which uses a Lagrange multiplier approach. It was implemented in MAT-LAB code so that it can be applied to general, integrated models. Normalized sensitivities are used since they provide an indication of the percent change in the performance RMS for a one percent change in the parameter. Modal parameter sensitivities can be used to identify which modes are the most important and to confirm the results of the disturbance analysis. If the critical modes occur at high frequencies, then the fidelity and accuracy of the model can be examined at those frequencies to determine if improvements to the integrated model are needed. The application of the physical parameter sensitivity framework to the SIM model is perhaps the first attempt in the literature to predict how physical parameters affect the performance RMS values of a large-order, closed-loop model and to do this without rebuilding the finite-element model. The technique utilizes structural eigen-derivatives, and an existing eigenvalue/vector code was modified to compute modal mass derivatives with respect to physical parameters. An option was also added to compute eigenvalue, eigenvector, and modal mass derivatives with respect to spring element and concentrated mass parameters and to accommodate models with dependent and independent DOF's.

- An uncertainty analysis framework was developed that predicts the worst-case RMS performance when uncertainties exist in open-loop modal parameters. The method uses a constrained optimization approach to determine the parameter values that maximize the performance cost. Although typically not provided by other methods, worst-case parameter values can be placed into the model to estimate individual RMS values that comprise the cost. This is important when it is desired to check the individual values against the requirements. An approximate balanced model reduction and gradient computation technique was added to handle large-order models with high modal density. The uncertainty analysis makes use of the sensitivity analysis

tool to provide the gradient information that improves the convergence properties of the constrained optimization routine. It was shown that some systems can avoid the constrained optimization approach by using modal parameter sensitivities to identify the worst-case parameters *a priori.*

- A performance enhancement approach was suggested which applies the well-developed controlled structures technology framework. What is unique about the approach is that it makes use of the results from the physical parameter sensitivity analysis to identify structural redesign options. Although developed for use during conceptual design, the physical parameter sensitivities can also be used to suggest slight modifications to an existing structure to improve its performance.

- The analytical physical parameter sensitivities were validated on a testbed that was designed to accommodate mass and stiffness modifications. The amount of performance improvement achieved during an example redesign exercise was predicted by the sensitivities. This validation served to increase confidence in the use of the physical parameter sensitivities to make redesign decisions.

- An automated finite-element model updating routine was developed which uses mode shape, natural frequency, and modal mass derivatives to identify FEM parameter values that minimize the error between measured and predicted transfer functions. At each iteration of the routine, the derivatives allow first-order approximations to be made that enable the state-space system to be created without regenerating the FEM and performing an eigenanalysis. To correct for errors due to this approximation, however, the FEM is created and the derivatives are recomputed periodically. The update routine was successfully applied to the testbed FEM.

8.3   Recommendations for Future Work

A number of areas have been identified in which useful extensions to the work in this thesis can be made.

- Additional disturbance analysis techniques should be investigated. In particular, wavelet theory might be better suited for capturing transient effects [69].

- The ability to determine sensitivities with respect to other parameters that appear explicitly in the state-space matrices should be added. In particular, disturbance filter corner frequencies or compensator corner frequencies might be entries in the corresponding state-space representations, and this would allow the equations derived in this thesis to be applied in these cases.

- The numerical conditioning problem discovered during the finite-difference computations in the SIM Classic example needs to be resolved. Balancing and model reduction techniques might alleviate this problem; however, the sensitivity framework currently does not support alternative system realizations. Efforts to accommodate other state-space realizations should be made.

- Alternative RWA disturbance modeling approaches should be investigated. For instance, the harmonic disturbances arising from a reaction wheel running at a constant speed can be modeled by discrete-frequency PSD's. These PSD's can be approximately represented by 2nd-order filters so that a state-space model can be created. (Recall that a state-space representation is required by the sensitivity analysis framework.) This would allow sensitivities to be computed as a function of wheel speed.

- The ability to compute curvature information (*i.e.*, the 2nd derivative of performance RMS values with respect to modal or physical parameters) would allow an estimate to be made of the range of parameter variations over which the first-order sensitivities are valid. The curvature equations are derived in Appendix C; however, it appears as if the required computational effort increases dramatically.

- Another type of sensitivity that would be beneficial is one that determines the effect of changes in disturbance location and optics locations on the performance metrics. For instance, is there a way to capture this with a parameter that acts as a weighting "knob" (*i.e.*, use interpolation function)? (For example, when the parameter $= 1$, a disturbance force enters entirely at node A. When the parameter $= 0$, the disturbance force enters entirely at neighboring node B. When parameter $= 0.5$, the disturbance force acts evenly at nodes A and B.)

- The sensitivity analysis framework should be investigated on systems that use optimal control techniques (such as LQG) rather than classical loop-shaped control de-

269

signs. Small changes in modal or physical parameters might actually cause instability sooner than the classically designed compensators. The framework can also be easily extended to compute the sensitivities of control effort RMS values with respect to various parameters. This can then be used in a simultaneous controls-structure optimization routine.

- The modal parameter sensitivity analysis should be expanded to include mode shape values at disturbance, performance, actuator, and sensor locations.

- The physical parameter sensitivity method should be validated on a closed-loop, laboratory testbed.

- The uncertainty analysis framework should be expanded to account for nonparametric uncertainties as well. A very preliminary analysis revealed that nonparametric uncertainties can contribute more than parametric uncertainties [32].

- The uncertainty analysis can also be expanded to account for uncertain physical parameters. This is anticipated to be very difficult using the current constrained optimization technique.

- The performance assessment and enhancement process should be repeated on the new SIM concept shown in Figure 8.1 once models become available. Also, applying the overall methodology to similar systems should help determine how useful and practical it is in general.
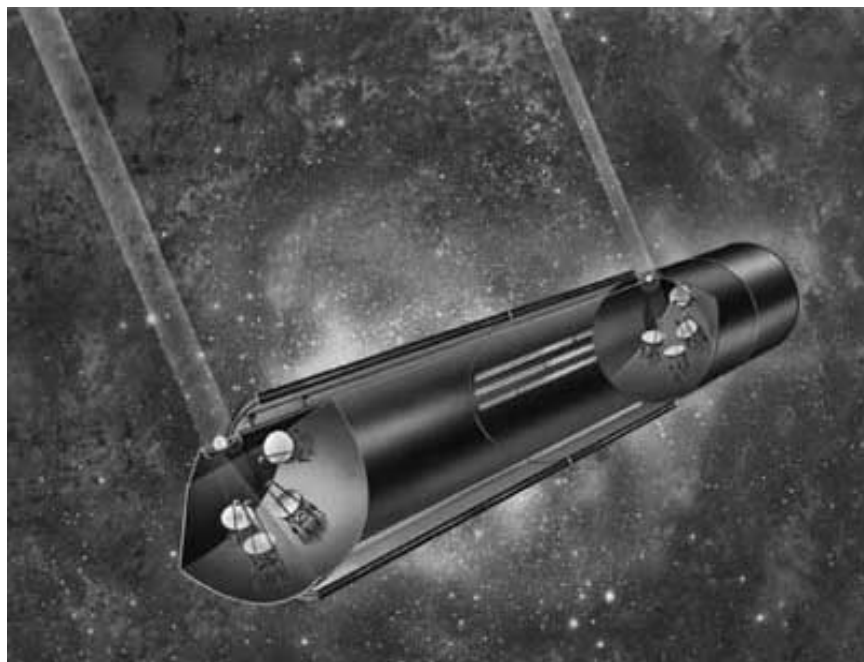
Figure 8.1: New SIM Concept.

Appendix A

Performance Assessment and Enhancement of NGST

(Note: This section shows the performance assessment and enhancement process of an early concept of the Next Generation Space Telescope (NGST). The results were obtained during a summer pre-Phase A study in 1996 conducted with Lockheed Martin Missiles & Space Corporation. The material that is presented provides insight into how the process was conducted prior to the development of the analysis tools described in this thesis. It hopefully serves to motivate the development of these tools and the corresponding methodology.)

The first step is to perform an initial assessment of the system under consideration. In this case, an initial finite-element model of NGST is created, along with models of the potential disturbance environment. In addition, performance variables are identified. The resulting performance of the system after the finite-element model has been subjected to the disturbances is then compared to requirements that have been levied. If the requirements are not satisfied, then a trouble-shooting phase is entered. Further studies are performed to compare the various controlled structures technology (CST) options and to explore the different trades involved with each option.

Although the structural configuration of a system is evolving in the early conceptual design stage, simple coarse models of the system can provide useful insights. These insights can help lead the design evolution in the right direction, thereby avoiding potential problems that might only be identified by a complicated, high-fidelity model of a mature design. At

such a stage, remedying the problem can be costly.

In keeping with the desire to maintain simplicity in the model, the NGST finite-element model (FEM) was constrained to be two-dimensional (2D). This implied that the only active degrees of freedom were those associated with translation and rotation in the plane of the model. The FEM was constructed entirely out of beam elements and concentrated masses, and attempts were made to capture in the 2D model the essential structural dynamics of the 3D structure.

Since modeling is being performed at such an early stage, not all of the required information is readily available. As a result, approximations must be made that supplement whatever information is at hand. Then estimates can be made of the component dimensions, mass properties, and stiffness properties.

An NGST concept that was modeled is one which has the following eight major components:

- spacecraft bus

- communications antenna

- primary mirror facesheet

- mirror actuators

- support truss

- primary mirror backsheet

- sun shade

- secondary mirror and support tower

Solar panels are not explicitly included since one option calls for them to be placed on the sun shades.

Figure A.1 shows the connectivity of the NGST finite-element model that was created for the purpose of this analysis. For clarity, actual grid points are not included. Due to the 2D nature of the problem, only motion in the plane of the figure is allowed. The model can be imagined as being a "slice" through the actual 3D structure. The eight different components are readily apparent. At the bottom is the communications antenna, which is

modeled as a beam cantilevered off of the spacecraft bus. The mass of the antenna is lumped at the tip of the beam. The spacecraft bus is assumed to be a rigid, solid cylinder. The line segments forming the rectangle of the spacecraft are not beam elements, but instead are included for visualization purposes. Rigid-body constraint equations are used to relate the degrees of freedom of points on the bus to motion of the center of mass of the bus. Connecting the spacecraft to the mirror assembly is a series of bars arranged in a truss-like pattern. The truss connects to the backsheet, which is simply a beam whose length equals the mirror diameter and whose bending stiffness is specified. The vertical, short line segments between the facesheet and backsheet are rods that model the mirror actuators used for figure control. The primary mirror facesheet is also modeled as a uniform beam of specified mass and stiffness. The sun shade is assumed to be a cylinder in 3D, but in 2D it is represented by two beams clamped to opposite ends of the backsheet. The tops of the beams are connected by a spring in order to try and simulate the inherent stiffness of the cylinder. The secondary mirror tower is simply a cantilevered beam whose bending stiffness is set to produce a desired fundamental bending frequency. The secondary mirror is modeled as a rigid body, and its mass is lumped at the tip of the tower beam. The mirror diameter is 8 m, and the overall length of the model is about 10 m. The total mass of this model is 2342 kg. Four mode shapes are presented in Figure A.2.

Figure A.3 shows the power spectral density functions of the disturbances used in the analysis. The solid line represents the PSD of the torque exerted at the center of mass of the spacecraft bus due to thruster firings. Most of the energy is located in the lower frequency region. The dashed curve is the PSD of the force due to reaction wheel noise, while the dashed-dotted curve is the torque PSD. The two have similar shapes, with most of the energy being concentrated at higher frequencies. These PSD's are based on a JPL-developed model. An MIT model that uses some of the JPL-derived information produces slightly different PSD's. (They are not shown, but they have similar shapes and are slightly lower in magnitude.) The overall effect is that performance values cited later in this example will be lower by a factor of 10. The PSD of the moment applied at the base of one side of the sun shade due to thermal creak is shown by the dotted line. Its energy is mainly at low frequencies.

Two performance metrics were identified as being important in describing the optical performance of the telescope. The first is referred to as differential pathlength (DPL).
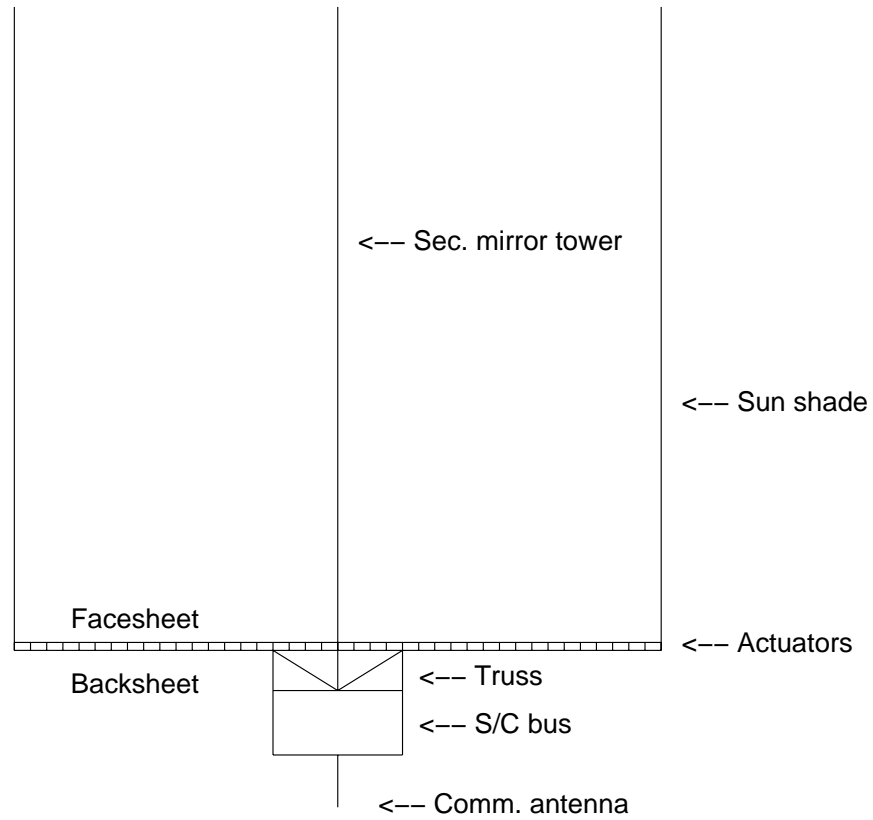
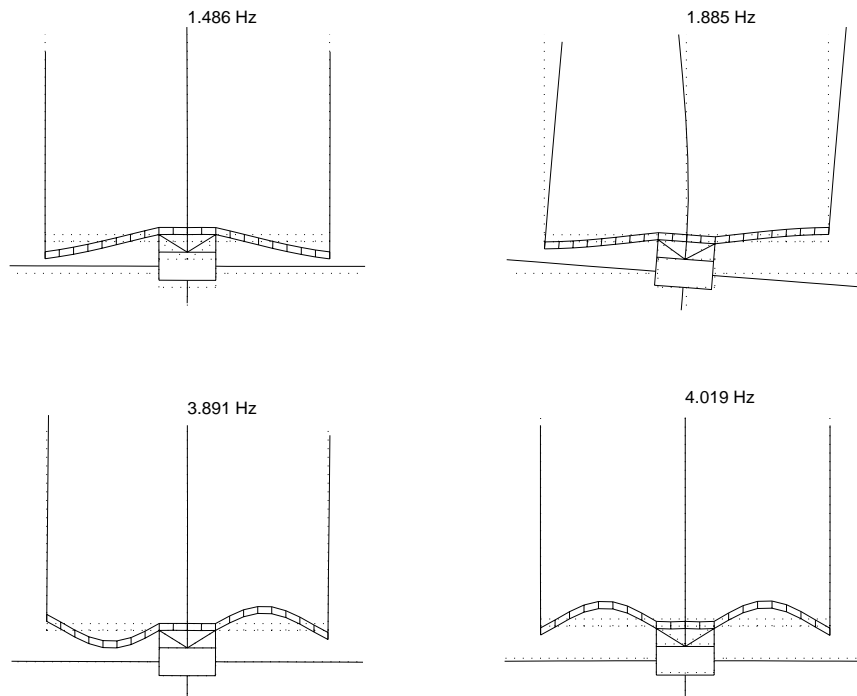**Figure A.1:** Finite-element model of an early NGST concept.

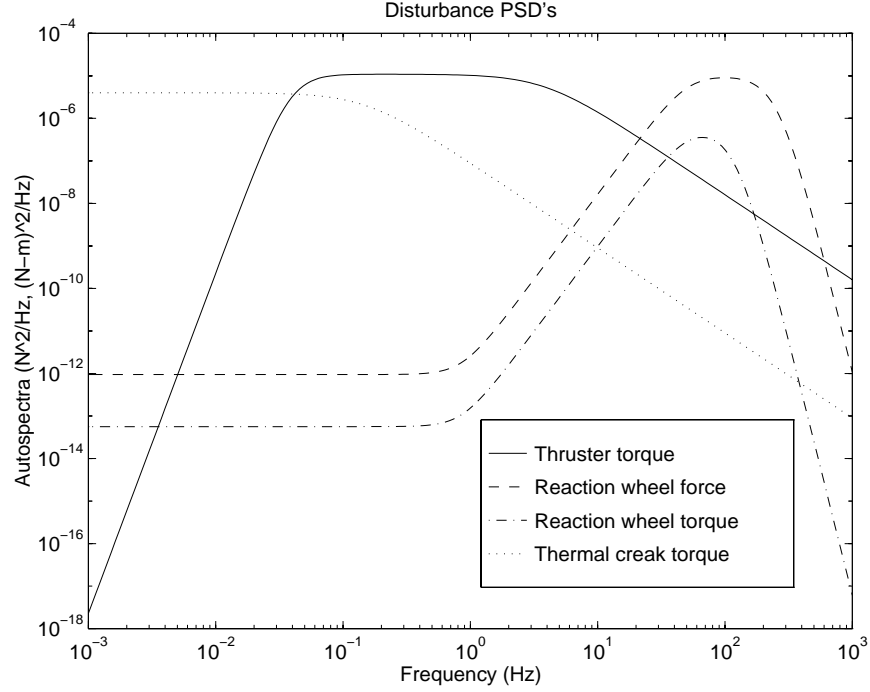**Figure A.2:** Four modes of the finite-element model.

Figure A.3: Disturbance PSD's.

When the telescope is in its nominal configuration, light that strikes the primary mirror will travel a certain distance along its path to the science instruments near the base of the secondary mirror tower. As the telescope undergoes deformation due to disturbances, this pathlength will change. This change in the phase of the wavefronts that reach the detectors should affect image quality. Consequently, DPL can be considered a phasing problem. The second performance metric is referred to as wavefront tilt (WFT). As the secondary mirror or individual elements of the primary mirror rotate, the wavefront of the science light will rotate as well. This can also degrade optical performance. WFT can be thought of as a pointing problem.

Figure A.4 shows how DPL and WFT are obtained for a single light ray that is incident upon a node of the primary mirror. The dashed line represents the nominal path of the light as it travels from distant source A to primary mirror node B, then to secondary mirror node C, and finally to node D at the base of the tower. When the telescope is disturbed, nodes B and C will be located at positions B' and C', respectively, after having displaced and rotated. DPL is the change in total pathlength, while WFT can be expressed in terms of the angle between line segments CD and C'D'. The computation of the exact values of
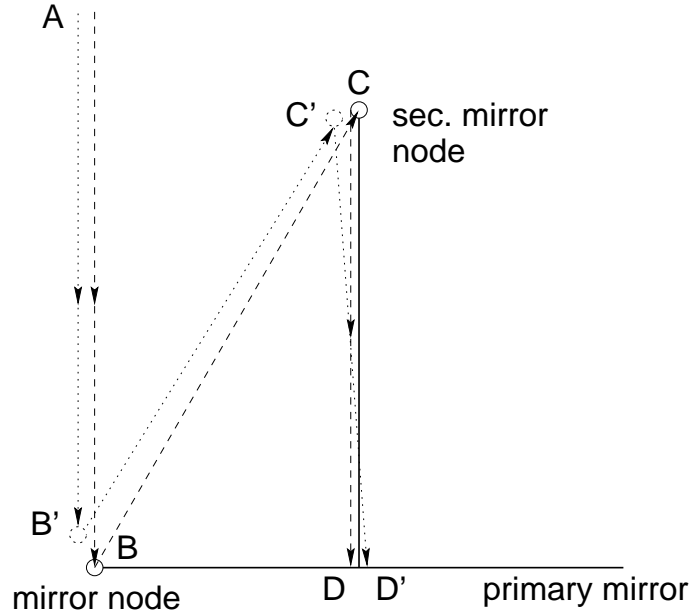
Figure A.4: Ray trace used to define DPL and WFT.

DPL and WFT involves nonlinear operations, which cannot be incorporated in the analysis method to be described. However, small angle and small displacement approximations permit DPL and WFT to be estimated as linear combinations of the degrees of freedom of the mirror nodes and the secondary mirror node.

A couple of additional points should be made. Only the contributions to DPL and WFT due to the flexible modes of the structure are considered. The effect of rigid-body motion is neglected and assumed to be treated by the attitude control system. Also, even though the primary mirror is modeled as a flat surface, it is assumed that the undeformed mirror will redirect the incident light toward the secondary mirror.

Since a stochastic analysis is performed, mean-square values of DPL and WFT are obtained for each light ray. The number of rays is equal to the number of mirror nodes, and by averaging DPL and WFT across the mirror, a sense can be gained of the average RMS errors.

The equations of motion of the FEM can be transformed to modal coordinates by using a truncated set of modes from the eigensolution. These matrix equations can then be recast in state-space form and used in a dynamic analysis. The disturbance w acts to drive the states of the system, and the performance variable z (a vector) is a linear combination of these states. When doing a stochastic analysis, the disturbance w can be thought of as

278

the output of a filter whose input is unit intensity, Gaussian white noise. The frequency response of this filter is related to the PSD of w. When the states of this filter are appended to the states of the model, a Lyapunov equation can then be solved in order to yield the covariance matrix of z. The ith diagonal element of this matrix is the mean-square value of the ith element of the performance variable. Since these variables represent the DPL and WFT errors across the mirror, trade studies can be performed to see how various CST options reduce these errors.

The analysis process described previously was implemented on a baseline NGST model. The baseline model incorporates a secondary mirror tower whose fundamental bending mode occurs at 2 Hz. Since light damping is assumed, all the global modes are assigned modal damping ratios of 0.1%. This value is at the low end of inherent structural damping, which implies that the analysis is conservative. It should be mentioned that a method was developed using the Component Mode Synthesis technique to specify damping at the component level instead. The damping of the global modes is then analytically predicted using the component-level information [31]. This permits the various substructures to possess different amounts of damping. For instance, the damping of the sun shade can be set at 0.7% while the damping of the tower is set at 0.2%. The baseline model also does not include any form of vibration isolation. These characteristics of the model were varied in order to examine the sensitivity of performance to them.

The three disturbances were applied separately, and their effects on performance were quantified. The DPL mean-squares were averaged, and then a square root was taken in order to get units of length. The same computation was done on the WFT mean-squares. The resulting quantity will be referred to as RMMS (root mean mean-square). The RMMS values obtained from the analysis are then multiplied by 3 to produce three-sigma values. For the DPL case, an extra factor of 2 is applied so as to approximate in-plane motion due to out-of-plane disturbances. It is these values that will be cited from now on.

The RMMS values of both DPL and WFT for the baseline model subjected to the three different disturbances are summarized in Table A.1. As expected, the thruster disturbance case results in the largest DPL error (1500 nm), followed by the reaction wheel disturbance case (269 nm), and the thermal creak disturbance case (57.5 nm). The largest WFT error is due to the reaction wheel disturbance (0.362 arcsec), followed by the error due to thruster firings (0.197 arcsec) and the error due to thermal creak (0.008 arcsec). A the bottom of the

Table A.1: Results of disturbance analysis on nominal NGST model.

Disturbance	DPL (nm)	WFT (arcsec)
Thruster	1500	0.197
Reaction wheel	263	0.362
Thermal creak	57.5	0.008
Typical requirement	20	0.005

table are typical requirements. The value of 20 nm represents a $\lambda/50$ specification, where λ = 1 micron. As is evident, the baseline structure cannot meet the requirements under any of the disturbance scenarios. Consequently, the CST methodology needs to be employed.

(Note: The thermal creak disturbance case was not carried into subsequent analyses because of time constraints. Only the thruster and reaction wheel disturbances will be used to illustrate the remaining steps of this troubleshooting process.)

Figure A.5 represents the average differential pathlength PSD across the mirror. The high modal density of the model is quite evident. The top curve (which has been shifted up by a factor of 10^{10} to avoid overlap with the other curve) is obtained by propagating the two reaction wheel disturbance PSD's through the system. The middle curve is obtained by doing a similar process with the thruster disturbance PSD. The lowest curve (shifted down by a factor of 10) is for the thermal creak disturbance case.

Another method that can be used to obtain the RMMS value is to integrate under the performance PSD (either DPL or WT) and then take the square root. The horizontal bars that appear in the plot represent the area of the curve lying between the width of each bar. By comparing the relative height of these bars, a sense can be gained of what portions of the curve contribute most to the performance metric. For the thruster disturbance case and thermal creak disturbance case, most of the performance is due to the response of the first mode. This mode is dominated by the first bending mode of the secondary mirror tower. For the reaction wheel case, the contribution to performance is more evenly spread across the higher frequencies. The modes at these frequencies tend to be dominated by mirror motion. The slight slope at low frequencies for the lower curve is due to a rigid body mode that has been artificially placed at 0.01 Hz and assigned 70.7% damping. This is to simulate
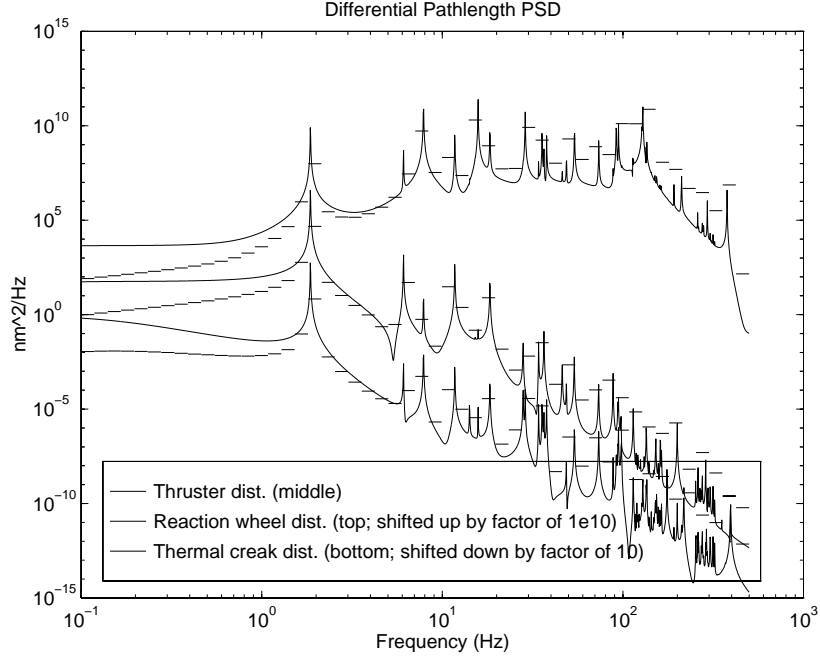
Figure A.5: DPL PSD's.

the effect of the attitude control system.

So as to avoid confusion, performance in this context is taken to mean the RMMS values of the WFT and DPL performance variables in z. Performance is improved whenever these values are *lowered*. A statement like "Added damping improved performance" implies that damping decreased the RMMS values of WFT and DPL.

The PSD's in Figure A.6 correspond to the wavefront tilt component of performance. The same trends that appeared in the DPL autospectra are evident in these plots. More modes appear at the higher frequencies because the higher order mirror modes are characterized by fairly large rotations of the mirror nodes. Consequently, wavefront tilt is affected more than is differential pathlength.

Figure A.7 indicates the RMS value of differential pathlength for each light ray that is incident upon a node of the primary mirror. The horizontal axis represents the position on the mirror that the incoming light ray strikes. The thruster disturbance and thermal creak disturbance cases have similar shapes. Both these disturbances excite the lower frequency modes. The dominant low frequency mode is the tower bending mode. As the tower bends, its horizontal motion contributes more to the DPL of the rays striking the outer mirror edge than to the DPL of rays striking near the center (ignoring any blockage effects). The
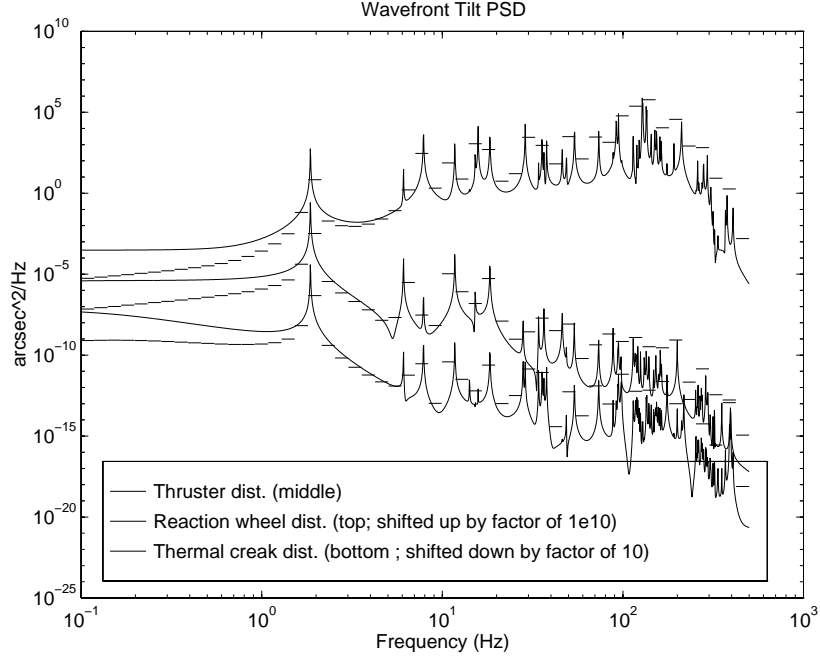
Figure A.6: WFT PSD's.

projection of this tower motion onto the direction joining a mirror node to the secondary mirror node is largest at the outer edge. In the limit as the incoming ray strikes the center of the mirror (again ignoring blockage effects and the fact that the mirror has a hole at its center), this projection goes to zero. This is the reason for the sharp drop in the two curves. For the reaction wheel disturbance case, the DPL values are more nearly uniform. Referring back to the DPL PSD, the highest bar is in the vicinity of a peak near 130 Hz. This peak corresponds to an axial mode of the tower. The motion of the secondary mirror node is in the vertical direction instead of lateral. As a result, the DPL of all the light rays is affected in a similar manner.

Figure A.8 indicates the RMS value of wavefront tilt for each light ray that is incident upon a node of the primary mirror. As before, the thruster and thermal creak disturbance cases have similar shapes. In this instance, they are both fairly uniform. The main contribution to WFT error (as seen in the WFT PSD) is the tower bending mode near 2 Hz. The WFT error for all the light rays is dominated by the rotation of the secondary mirror node. The curve for the reaction wheel disturbance case is more complex. A high order mirror mode shape appears to dominate. Since it is probably a symmetric mode shape, the rotation of the center node should be close to zero, hence the sudden drop in the middle of
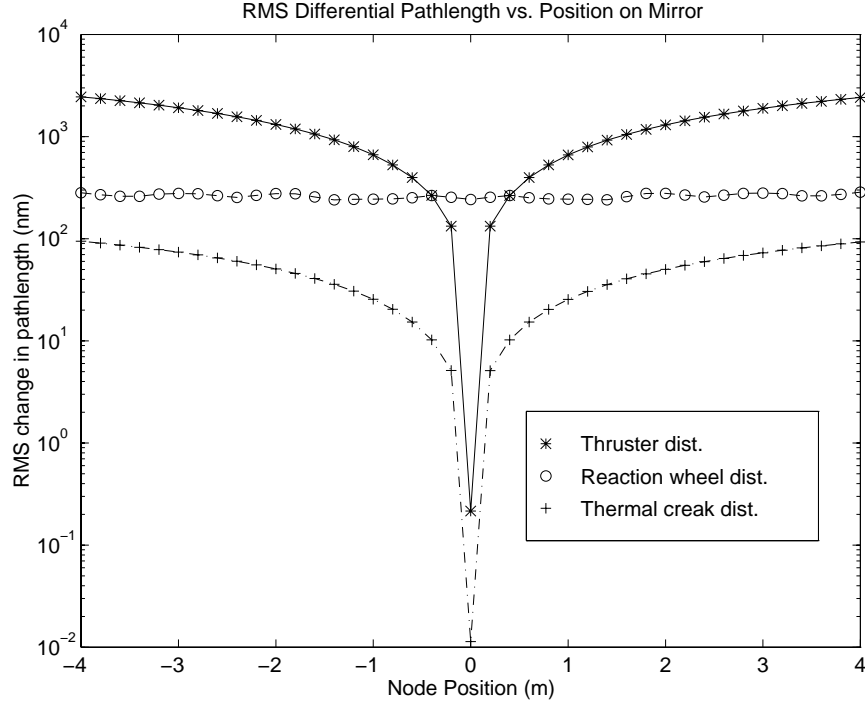
282

Figure A.7: DPL as a function of location on mirror.

the plot.

Since the baseline NGST model is unable to satisfy the performance requirements, there is a need to identify which CST options would be particularly helpful. The usual first-cut strategy would be to look at either structural redesign, passive vibration isolation, or damping augmentation as potential remedies. These will be addressed in the remainder of this demonstration in the form of sample trade studies. If no reasonable combination can be found to help the system reach the desired performance level, then the next step would be to look at active structural control. An example would be to extend the bandwidth of the primary mirror actuators and/or of the tertiary fast-steering mirrors.

As mentioned previously, one parameter in the model is the frequency of the bending mode of the tower (assuming the tower is clamped at its base). Recall from the PSD plots of DPL and WFT for the thruster disturbance case that the performance is dominated by this bending mode. Stiffening the tower would make the frequency of this mode higher, thereby moving it into a region where the thruster autospectrum is rolling off and exhibiting less influence on the modes. Physically, a stiffer tower would mean less motion of the secondary mirror. This should reduce the amount of DPL and WFT caused by tower motion. As the
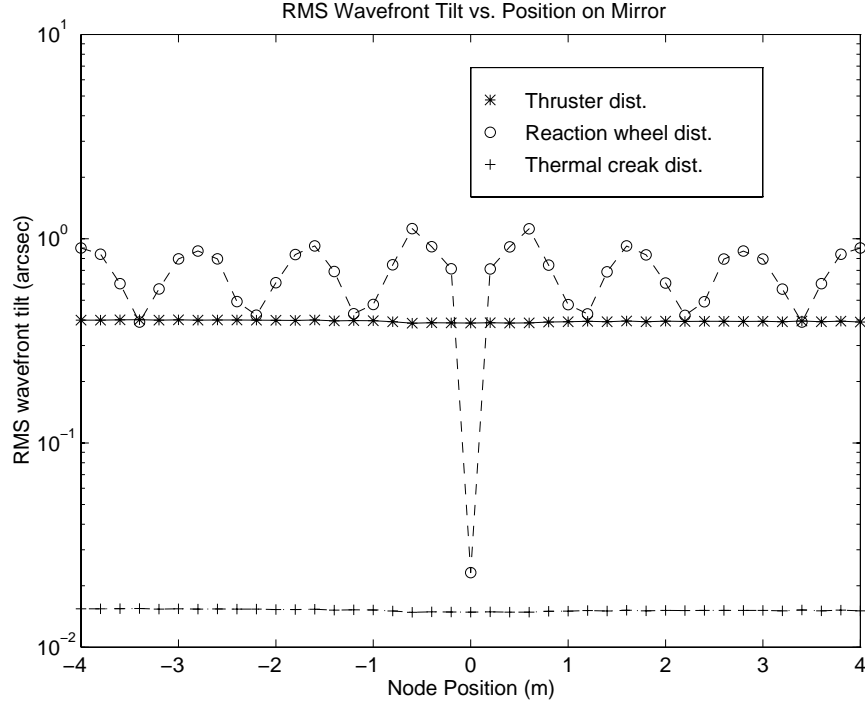
Figure A.8: WFT as a function of location on mirror.

tower becomes even more rigid in bending, the performance should become dominated by mirror motion instead. This can be seen in Figure A.9. A "knee" appears in the curves for the thruster disturbance case, and the curve levels off at higher tower frequencies. The performance is relatively insensitive for the reaction wheel case because tower bending is not dominant at the higher frequencies where the reaction wheel disturbance possesses more energy. The horizontal dotted lines represent performance specifications (10 nm is $\lambda/50$ for $\lambda/50 = 0.5$ micron). The vertical dotted lines represent the nominal model. Although it appears as if the specifications cannot be met no matter how stiff the tower is, a redesign that brings the tower frequency to 5 Hz from 2 Hz can bring about a 30 dB improvement in performance. Another CST option can then be implemented to improve the performance even further. (Reminder: The thermal creak disturbance source has not been carried through to these various trades.)

The previous trade looked at redesigning the secondary mirror support tower by adjusting its bending stiffness to produce a desired fundamental frequency. In a manner analogous to this, consider a redesign of the primary mirror backsheet that increases its bending stiffness. Specifically, assume that the cross-sectional moment of inertia is varied. This could be
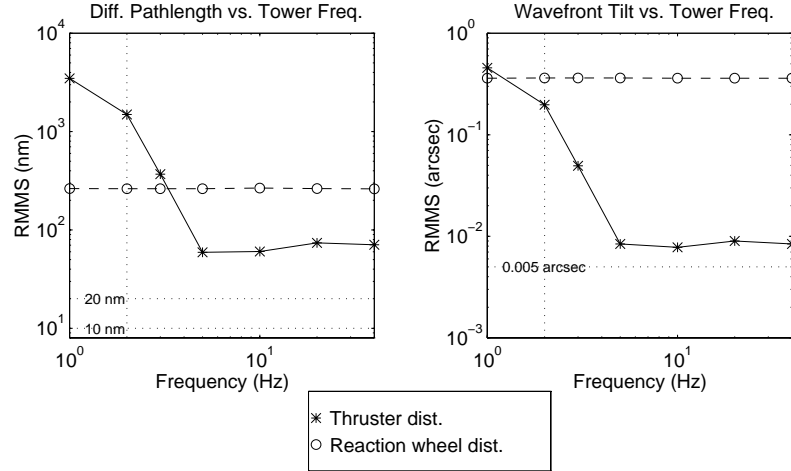
Figure A.9: Tower frequency trade study.

accomplished by varying the backsheet from a thin sheet, to a sandwich-honeycomb struc-
ture, to a truss support structure. The performance plots for this trade in Figure A.10 do
not show recognizable trends. In all instances, the required performance cannot be achieved.
For the thruster disturbance case, the lack of improvement can be explained as follows. The
mode responsible for the largest contribution to the performance metric is the fundamental
bending mode of the tower. The tower is modeled as being clamped to the backsheet. As
the stiffness of this backsheet changes, the frequency of the global mode characterized by
tower bending will change to an extent that depends on the degree of coupling. However,
the frequency shift is not substantial. Since the roll-off region of the thruster disturbance
PSD occurs in the vicinity of this mode, the contribution to performance will depend on
where the mode is relative to the roll-off. This can explain the relative insensitivity of DPL
and WFT to backsheet stiffness. Put another way, the DPL and WFT RMMS values will
still be dominated by tower motion, no matter how stiff the backsheet is. Probably the
next step that should be performed is to repeat this trade, but for the case of a 5 Hz tower.
(Remember, this trade is for the nominal design, which has a 2 Hz tower.) Mirror motion
should comprise more of the performance in that case.

For the reaction wheel disturbance case, the same kind of relative insensitivity is ap-
parent. A possible reason for this is that the low order mirror modes are being shifted up
in frequency. These modes previously were not in the frequency region of largest reaction
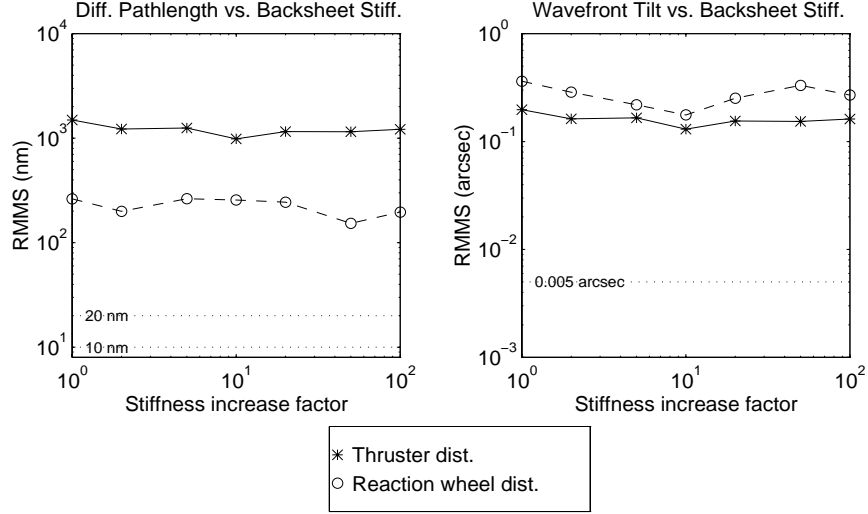
Figure A.10: Backsheet stiffness trade study.

wheel disturbance energy. As the mirror modes that used to contribute most to performance move past this region, new modes approach from below. The net result is that DPL and WFT errors remain about the same.

Another parameter in the model is the modal damping ratio assigned to all the flexible modes. More damping should result in a smaller magnitude of response of these modes. As seen in Figure A.11, higher damping leads to smaller RMMS values of DPL and WFT, as expected. Most of the trends appear linear when plotted on a logarithmic scale. The rate of performance improvement does not seem sufficient. High damping of all the modes is required before the specifications are close to being reached. However, these levels of damping are not realistic. Inherent structural damping can fall in the range from 0.1% to 0.5%. Passive damping augmentation can increase modal damping to about 3%. Beyond that, active damping enhancement is required to reach higher levels. As before, the horizontal dotted lines represent performance specifications.

Since tower motion was identified as being a major contributor to both DPL and WFT error at the lower frequencies for the thruster disturbance case, another method to reduce this motion (in addition to stiffening the tower) is to increase the level of damping present within the tower. The plots in Figure A.12 show that the rate of improvement in performance is greater when the only disturbance is due to thruster firings. This confirms our
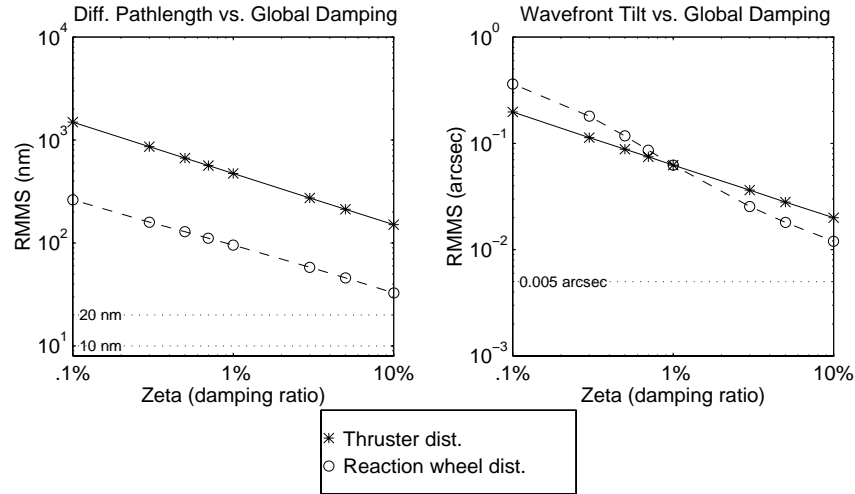
286

Figure A.11: Modal damping trade study.

intuition. The effect of damping appears linear in these logarithmic plots, and the slope is shallower for the reaction wheel disturbance case. This again matches previous statements regarding the effect of tower motion on performance when the system is excited by reaction wheel chatter. The level of performance at even high amounts of tower damping is still not near the desired specification. This suggests that adding large quantities of damping treatments, which come at the cost of extra mass and complexity (for active damping), is not worthwhile.

Since mirror motion was identified as contributing to both DPL and WFT error at the higher frequencies for the reaction wheel disturbance case, adding damping to the mirror will aid in reducing these errors. Figure A.13 confirms this statement. However, the amount of damping required to yield substantial performance improvement is in the active damping range. Mirror damping appears to affect WFT error more than DPL error. Going from 0.1% damping to 10% damping only reduces DPL RMMS by a factor of 3, while it reduces WFT RMMS by a factor of 10. The plots also confirm that mirror damping has no effect on performance when the system is being excited by thruster firings. This is because the dominant mode in this case has little mirror motion.

This trade and the previous trade indicate that:

- the tower should be damped if the predominant disturbance source is due to thrusters

287
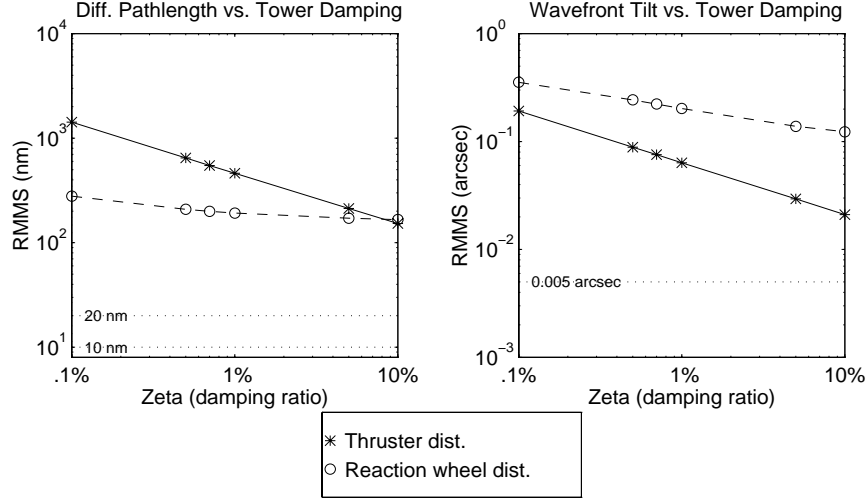
Figure A.12: Tower modal damping trade study.

- the mirror should be damped if the predominant disturbance source is due to reaction wheel noise

Isolation in the truss that serves as the interface between the spacecraft (where the disturbances enter) and the mirror assembly (where the performance is affected) is one common method used to attenuate the transmission of vibrations. One characteristic of an isolator is its so-called "corner" frequency. The plots in Figure A.14 show how the performance can be improved by decreasing this frequency. Passive isolation was added to the model by reducing both the extensional stiffness and bending stiffness of the truss members, and by setting the truss damping to an arbitrary level of 20%. The bending destiffening was required in order to avoid "blocking zeros" which arise when a cross-axis stiffness limits the performance of an isolator [38]. A soft truss leads to three additional modes that are dominated by motion of the truss. The highest frequency of these modes will be considered an indication of the corner frequency. A moderate corner frequency is required to meet the performance specifications for the reaction wheel disturbance case. An extremely low corner frequency is required for the thruster disturbance case. This is probably due to the fact that the corner frequency should be below the frequencies of the modes contributing to the performance. In this case, the problematic mode is the tower bending mode near 2 Hz.

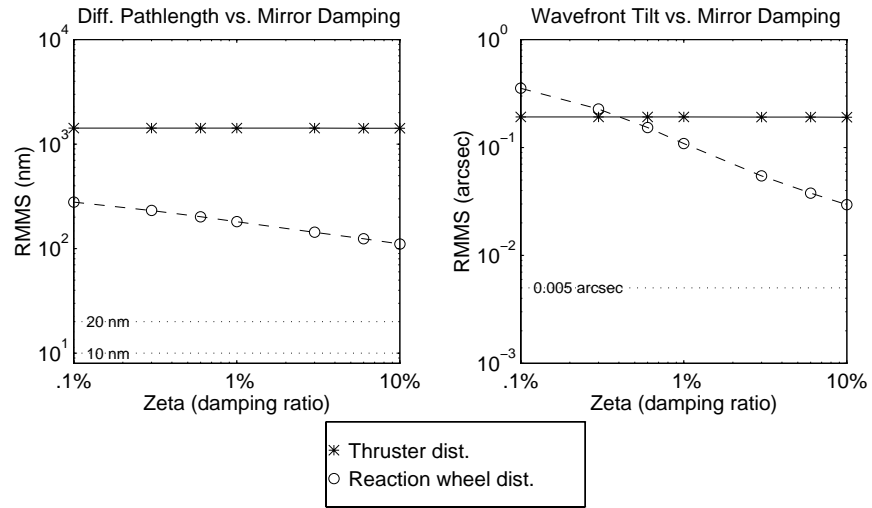**Figure A.13:** Mirror modal damping trade study.
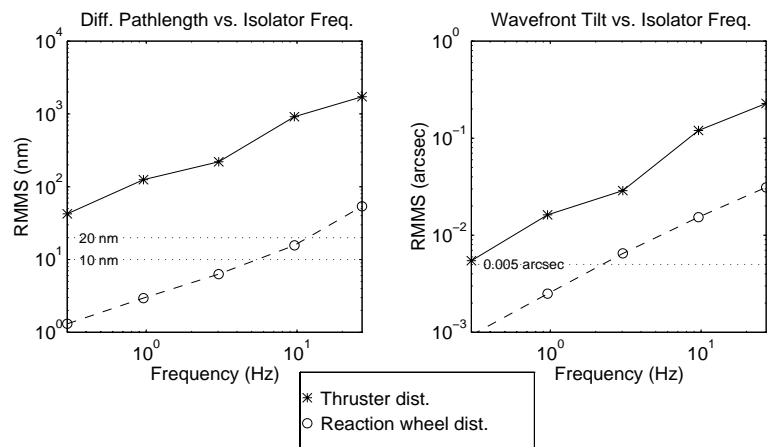
Figure A.14: Isolator corner frequency trade study.

Table A.2: Comparison of use of controlled structures technologies.

CST option	Helpful?	Amount Needed	Feasible?
Stiffer tower	Yes, for thruster disturbance case	Cannot achieve requirements	—
Increased global damping	Yes	Must be $> 50\%$	No
Increased tower damping	More so for thruster disturbance	Cannot achieve requirements	—
Isolation	Yes	**Thruster dist.:** 40 dB, 0.2 Hz, 20% damping	Not likely
		RWA dist.: 30 dB, 2 Hz, 20% damping	Yes

Based on the trends that appear in the previous plots, estimates can be made of how much of each CST option would be required to satisfy the performance requirements (assuming it is the only option implemented). Table A.2 summarizes the findings. For each option, comments are made regarding how helpful it is to performance enhancement, how much would be required to meet the requirements (if possible), and how feasible this amount would be.

The results can be summarized as follows:

- Increasing the bending stiffness of the tower does help quite a bit for the thruster disturbance case, yet it cannot alone bring the DPL and WFT values down to the desired level.

- Increasing overall damping is also helpful, but the rate of performance improvement is not fast enough to make the required amount of global damping feasible. Not even 50% modal damping for all the modes is sufficient to achieve both DPL and WFT specifications.

- Increasing tower damping is more effective in reducing errors due to thruster firings; however, no amount of damping can cause the desired performance to be met for both

disturbance cases.

- Isolation does appear to have much promise, which is not surprising. About a 2 Hz isolator with 20% damping can provide the approximately 30 dB performance improvement required for the reaction wheel case. This could be achievable with current technology. For the thruster disturbance case, a 40 dB, 0.2 Hz isolator with 20% damping appears to be required. This type of passive isolator is probably not feasible, mainly because of the low corner frequency and the large dB reduction that is required.

It is obvious that there is no single controlled structures technology that can help the telescope meet the specified performance requirements under the disturbance environments that have been modeled. As a result, a layering approach is required that combines the CST options. The layering of technologies is also necessary since the actual problem will be worse than what is being considered in this analysis. For instance, multiple disturbances will be present and will act simultaneously. Up to this point, the disturbances have been considered separately. An attempt has not been made to combine the effects of the separate disturbances. In addition, unforeseen disturbances are always a possibility, and they may further compound the problem. The levying of design margins will mean that performance requirements will be split among different subsystems. For example, the WFT performance that CST is designed to achieve might be specified to be 0.003 arcsec instead of the systems-level requirement of 0.005 arcsec. All of these factors suggest that a layering approach is essential.

Table A.3 summarizes the results of two cases of CST layering. The results of the nominal case are shown for reference. The first combination incorporates a 3 Hz passive isolator with 20% damping. The tower has been stiffened to 5 Hz and is also passively damped (2% modal damping). Two out of the four performance requirements are met. The exceptions are the DPL due to the thruster disturbance case and the WFT due to the reaction wheel disturbance case. Nevertheless, the new values are much closer to the specifications than they were before.

The second combination uses a 2 Hz passive isolator with 30% damping. The tower frequency is still at 5 Hz, while the tower damping remains at 2%. Mirror damping has also been included at a level of 1% modal damping. This time, three out of the four performance

Table A.3: Results of CST Layering.

CST Layered Design	DPL (nm)		WFT (arcsec)	
	Thruster	RWA	Thruster	RWA
Nominal design	1500	263	0.197	0.362
Isolator (3 Hz, 20% damp.) 5 Hz tower 2% tower damp.	32.6	6.24	0.0042	0.0063
Isolator (2 Hz, 30% damp.) 5 Hz tower 2% tower damp., 1% mirror damp.	25.1	5.27	0.0032	0.0026
Typical requirement	20		.005	

requirements are met. The exception is the DPL for the thruster disturbance case, but this time it is closer to meeting the 20 nm level. It is within 25% of the desired value.

It is anticipated that a few more iterations like this will lead to a reasonable design that can meet all the requirements for both disturbance cases. However, as mentioned before, the actual problem faced could be much worse due to several simultaneous disturbances. As a result, some form of active control would need to be investigated. An advantage of active control is that it can be redesigned while on-orbit (by uplinking reconfigured software) in order to account for any unforeseen or mismodeled disturbances. This adaptive ability is highly desirable, but with any active system there is the chance for instability, so care must be taken.

A number of additional studies can be done that build upon the results obtained thus far. Further trade studies can be performed to examine the effect on performance of a variety of other design parameters. The issue of the use of active structural control needs to be addressed (for the reasons discussed previously). Besides the NGST point design that has been modeled, alternative structural architectures can be studied using this analysis methodology. Finally, a traditional sensitivity analysis can be performed.

Sensitivity analysis is an attractive method for a number of reasons. What it provides is an indication of how changes made to model parameters affect a cost functional or performance metric that has been defined. Essentially, it can provide the slope of a performance

vs. parameter curve at a nominal value of the parameter. A steep slope indicates that the performance is very sensitive to the parameter; consequently, that parameter should be considered as a possible design variable. A sensitivity analysis can be more efficient than performing the process manually, as was done to create the performance vs. parameter curves shown previously. The "manual" process involves changing the parameter of interest, rerunning the dynamic analysis, and then seeing what the value of performance is. This is then repeated for another value of the parameter.

The parameter sensitivities can reveal which model parameters provide more "bang for the buck." For example, if a 1% change in component stiffness produces the same effect as a factor of 100 increase in component damping, then obviously the stiffness redesign should be implemented instead. Once a series of parameter sensitivities has been determined (and properly normalized), then an optimization routine can be employed that identifies what combination of parameters will minimize and hopefully satisfy the performance metric. This can then aid in allocating requirements to the different CST options.

The example jitter analysis that was conducted showed that the performance of the nominal NGST finite-element model exceeded typical requirements on wavefront tilt and differential pathlength by factors of 10 to 100. Since no single controlled structures technology option could realistically satisfy the performance specifications, this indicated that a layered CST approach was required. After analyzing the impact of a number of different options (structural redesign, passive damping, passive isolation) on the performance, a few sample combinations were shown to be particularly effective.

What should be taken from this demonstration is not the actual numbers that resulted from the analysis, but rather a sense of the usefulness of this approach. This analysis tool allows early insights into redesigns and technology applications that can lead to favorable results. It also permits early partitioning of subsystem requirements based on the available information rather than ad hoc allocation. As more up-to-date information is gathered, the structural, disturbance, and performance models can be updated. The analysis tool evolves along with the design of the system. The two should go hand-in-hand, with one helping to steer the direction of the other. This approach should be considered essential because as results of systems trades are arrived at during the early conceptual design stages, solutions and remedies can be incorporated in a cost-effective manner.

Appendix B

Derivation of RWA Disturbance Cross-Spectral Density Function

We consider the case when $p = q$ and $(r, s) \in [(1, 2), (2, 1), (4, 5), (5, 4)]$ and rewrite Eq. 2.33 accordingly.

$$R_{w_{m_{pr}}w_{m_{ps}}}(t_1, t_2) = E\left[\sum_{k=1}^{n_r}\sum_{l=1}^{n_s}\frac{C_{rk}C_{sl}f_p^4}{2}\left\{\cos\left(2\pi f_p(h_{rk}t_1 - h_{sl}t_2) + \phi_{prk} - \phi_{psl}\right)\right.\right. \tag{B.1}$$
$$\left.\left. - \cos\left(2\pi f_p(h_{rk}t_1 + h_{sl}t_2) + \phi_{prk} + \phi_{psl}\right)\right\}\right]$$

Using an argument similar to that expressed in Eq. 2.38, we notice that the expectation of the cosine terms with $\phi_{prk} + \phi_{psl}$ will be zero (since it is never assumed that $\phi_{prk} + \phi_{psl}$ can equal zero). In addition, the expectation of cosine terms with $\phi_{prk} - \phi_{psl}$ will vanish unless the relationship expressed by Eq. 2.22 holds. Thus, the previous expression simplifies to

$$R_{w_{m_{pr}}w_{m_{ps}}}(t_1, t_2) = E\left[\sum_{k=1}^{n_r}\frac{C_{rk}C_{sk}f_p^4}{2}\left\{\cos\left(2\pi f_p(h_{rk}t_1 - h_{sk}t_2) \pm \frac{\pi}{2}\right)\right\}\right], \quad \begin{cases} + & , \quad r > s \\ - & , \quad r < s \end{cases}$$
$$\tag{B.2}$$

Another assumption is that for the (r, s) pairs being considered in this case, $h_{rk} = h_{sk}$ and $C_{rk} = C_{sk}$. This leads to

$$R_{w_{m_{pr}}w_{m_{ps}}}(t_1, t_2) = E\left[\sum_{k=1}^{n_r}\frac{C_{rk}^2 f_p^4}{2}\cos\left(2\pi f_p h_{rk}(t_1 - t_2) \pm \frac{\pi}{2}\right)\right], \quad \begin{cases} + & , \quad r > s \\ - & , \quad r < s \end{cases} \tag{B.3}$$

But because of the identity $\cos(A \pm \frac{\pi}{2}) = \mp\sin A$, this can be rewritten as

$$R_{w_{m_{pr}}w_{m_{ps}}}(t_1, t_2) = \mp E\left[\sum_{k=1}^{n_r}\frac{C_{rk}^2 f_p^4}{2}\sin\left(2\pi f_p h_{rk}(t_1 - t_2)\right)\right], \quad \begin{cases} - & , \quad r > s \\ + & , \quad r < s \end{cases} \tag{B.4}$$

Bringing the expectation operator within the summation and letting $\tau = t_1 - t_2$,

$$R_{w_{m_{pr}} w_{m_{ps}}}(\tau) = \mp \sum_{k=1}^{n_r} \frac{C_{rk}^2}{2} E\left[f_p^4 \sin\left(2\pi f_p h_{rk}\tau\right)\right], \quad \begin{cases} - & , \quad r > s \\ + & , \quad r < s \end{cases} \tag{B.5}$$

Now invoking the definition of the expectation operator,

$$R_{w_{m_{pr}} w_{m_{ps}}}(\tau) = \mp \sum_{k=1}^{n_r} \frac{C_{rk}^2}{2} \int_{-\infty}^{+\infty} f_{F_P}(f_p) f_p^4 \sin\left(2\pi f_p h_{rk}\tau\right) df_p, \quad \begin{cases} - & , \quad r > s \\ + & , \quad r < s \end{cases} \tag{B.6}$$

Taking the Fourier transform of Eq. B.6 and noting that the Fourier transform of a sine is a pair of impulses at the frequency of the sine (one with amplitude $j\pi$ and the other of amplitude $-j\pi$) [8],

$$S_{w_{m_{pr}} w_{m_{ps}}}(\omega) = \mp \sum_{k=1}^{n_r} \frac{C_{rk}^2}{2} \int_{-\infty}^{+\infty} f_{F_P}(f_p) f_p^4 \int_{-\infty}^{+\infty} \sin\left(2\pi f_p h_{rk}\tau\right) e^{-j\omega\tau} d\tau df_p \tag{B.7}$$

$$= \mp \sum_{k=1}^{n_r} \frac{C_{rk}^2}{2} \int_{-\infty}^{+\infty} f_{F_P}(f_p) f_p^4 j\pi \left[\delta(\omega + 2\pi f_p h_{rk}) - \delta(\omega - 2\pi f_p h_{rk})\right] df_p$$

Now make the substitutions

$$u_1 = \omega + 2\pi f_p h_{rk} \Rightarrow du_1 = 2\pi h_{rk} df_p$$

$$u_2 = \omega - 2\pi f_p h_{rk} \Rightarrow du_2 = -2\pi h_{rk} df_p$$

to obtain

$$S_{w_{m_{pr}} w_{m_{ps}}}(\omega) = \mp \sum_{k=1}^{n_r} \frac{j\pi C_{rk}^2}{2} \left[\int_{-\infty}^{+\infty} f_{F_P}\left(\frac{u_1 - \omega}{2\pi h_{rk}}\right) \left(\frac{u_1 - \omega}{2\pi h_{rk}}\right)^4 \delta(u_1) \left(\frac{1}{2\pi h_{rk}}\right) du_1 \right. \tag{B.8}$$

$$\left. + \int_{-\infty}^{+\infty} f_{F_P}\left(\frac{-u_2 + \omega}{2\pi h_{rk}}\right) \left(\frac{-u_2 + \omega}{2\pi h_{rk}}\right)^4 \delta(u_2) \left(\frac{-1}{2\pi h_{rk}}\right) du_2\right]$$

The integral of the product of a function and a delta function with respect to the argument of the delta function is simply the value of the function evaluated at zero.

$$S_{w_{m_{pr}} w_{m_{ps}}}(\omega) = \mp \sum_{k=1}^{n_r} \frac{j\pi C_{rk}^2}{2} \left[f_{F_P}\left(\frac{-\omega}{2\pi h_{rk}}\right) \left(\frac{-\omega}{2\pi h_{rk}}\right)^4 \left(\frac{1}{2\pi h_{rk}}\right) \right. \tag{B.9}$$

$$\left. + f_{F_P}\left(\frac{\omega}{2\pi h_{rk}}\right) \left(\frac{\omega}{2\pi h_{rk}}\right)^4 \left(\frac{-1}{2\pi h_{rk}}\right)\right]$$

This can be further simplified to obtain

$$S_{w_{m_{pr}} w_{m_{ps}}}(\omega) = \mp \sum_{k=1}^{n_r} \frac{j\pi C_{rk}^2 \omega^4}{2(2\pi h_{rk})^5} \left[f_{F_P}\left(\frac{\omega}{2\pi h_{rk}}\right) + f_{F_P}\left(\frac{-\omega}{2\pi h_{rk}}\right)\right], \quad \begin{cases} - & , \quad r > s \\ + & , \quad r < s \end{cases}$$
$$\tag{B.10}$$

At this point, no further steps can be made until a specific probability density function is assumed for $f_{F_P}(f_p)$.

Appendix C

Derivation of Curvature Equation

Chapter 4 obtained the following expression for the derivative of the ith performance variance, $\sigma_{z_i}^2$, with respect to a generic parameter p. (See Eq. 4.22.)

$$\frac{\partial \sigma_{z_i}^2}{\partial p} = \text{trace}\left[\Sigma_q \frac{\partial(C_i^T C_i)}{\partial p}\right] + \text{trace}\left[L_i\left(\frac{\partial A_{zd}}{\partial p}\Sigma_q + \Sigma_q \frac{\partial A_{zd}^T}{\partial p} + \frac{\partial(B_{zd}B_{zd}^T)}{\partial p}\right)\right] \qquad \text{(C.1)}$$

where Σ_q is the solution to

$$A_{zd}\Sigma_q + \Sigma_q A_{zd}^T + B_{zd}B_{zd}^T = 0 \qquad \text{(C.2)}$$

and L_i is the solution to

$$L_i A_{zd} + A_{zd}^T L_i + C_i^T C_i = 0 \qquad \text{(C.3)}$$

We seek now to determine the curvature of $\sigma_{z_i}^2$ with respect to p. In other words, we wish to compute the second derivative $\frac{\partial^2 \sigma_{z_i}^2}{\partial p^2}$. We can follow the same procedure as that used in Section 4.2 to obtain the sensitivity equation. First, create the Lagrangian of $\frac{\partial \sigma_{z_i}^2}{\partial p}$ by augmenting the constraint equations given by Eq. C.2 and Eq. C.3 with Lagrange multiplier matrices $M_{i,p}$ and $N_{i,p}$. These are dependent not only on the performance metric of interest, but also the parameter of interest.

$$\begin{aligned}\left(\frac{\partial \sigma_{z_i}^2}{\partial p}\right)^* &= \frac{\partial \sigma_{z_i}^2}{\partial p} + \text{trace}\left[M_{i,p}\left(L_i A_{zd} + A_{zd}^T L_i + C_i^T C_i\right)\right] \\ &\quad + \text{trace}\left[N_{i,p}\left(A_{zd}\Sigma_q + \Sigma_q A_{zd}^T + B_{zd}B_{zd}^T\right)\right]\end{aligned} \qquad \text{(C.4)}$$

The derivative of $\frac{\partial \sigma_{z_i}^2}{\partial p}$ with respect to p is equal to the derivative of the Lagrangian function if and only if the derivatives with respect to Σ_q, L_i, $M_{i,p}$, and $N_{i,p}$ are equal to zero.

$$\frac{\partial^2 \sigma_{z_i}^2}{\partial p^2} = \left.\frac{\partial^2 \left(\sigma_{z_i}^2\right)^*}{\partial p^2}\right|_{\frac{\partial\left(\sigma_{z_i}^2\right)^*}{\partial \Sigma_q}=0,\,\frac{\partial\left(\sigma_{z_i}^2\right)^*}{\partial L_i}=0,\,\frac{\partial\left(\sigma_{z_i}^2\right)^*}{\partial M_{i,p}}=0,\,\frac{\partial\left(\sigma_{z_i}^2\right)^*}{\partial N_{i,p}}=0} \qquad \text{(C.5)}$$

$\frac{\partial(\sigma_{z_i}^2)^*}{\partial L_i} = 0$ and $\frac{\partial(\sigma_{z_i}^2)^*}{\partial \Sigma_q} = 0$ simply recover Eq. C.2 and Eq. C.3, respectively. The derivative of Eq. C.4 with respect to L_i produces

$$
\begin{aligned}
\frac{\partial \left(\sigma_{z_i}^2\right)^*}{\partial L_i} &= M_{i,p} A_{zd}^T + A_{zd} M_{i,p} \\
&+ \frac{\partial A_{zd}}{\partial p} \Sigma_q + \Sigma_q \frac{\partial A_{zd}^T}{\partial p} + \frac{\partial (B_{zd}^T B_{zd})}{\partial p} = 0
\end{aligned}
\tag{C.6}
$$

This is another Lyapunov equation and is used to determine $M_{i,p}$. The derivative of Eq. C.4 with respect to Σ_q produces

$$
\begin{aligned}
\frac{\partial \left(\sigma_{z_i}^2\right)^*}{\partial \Sigma_q} &= N_{i,p} A_{zd} + A_{zd}^T N_{i,p} \\
&+ \frac{\partial A_{zd}^T}{\partial p} L_i + L_i \frac{\partial A_{zd}}{\partial p} + \frac{\partial (C_i C_i^T)}{\partial p} = 0
\end{aligned}
\tag{C.7}
$$

which is a Lyapunov equation used to determine $N_{i,p}$. The final equation for the curvature of $\sigma_{z_i}^2$ with respect to p is

$$
\begin{aligned}
\frac{\partial^2 \sigma_{z_i}^2}{\partial p^2} &= \text{trace}\left[\Sigma_q \frac{\partial^2 (C_i^T C_i)}{\partial p^2}\right] \\
&+ \text{trace}\left[L_i \left(\frac{\partial^2 A_{zd}}{\partial p^2}\Sigma_q + \Sigma_q \frac{\partial^2 A_{zd}^T}{\partial p^2} + \frac{\partial^2 (B_{zd} B_{zd}^T)}{\partial p^2}\right)\right] \\
&+ \text{trace}\left[M_{i,p} \left(\frac{\partial A_{zd}^T}{\partial p}L_i + L_i \frac{\partial A_{zd}}{\partial p} + \frac{\partial (C_i^T C_i)}{\partial p}\right)\right] \\
&+ \text{trace}\left[N_{i,p} \left(\frac{\partial A_{zd}}{\partial p}\Sigma_q + \Sigma_q \frac{\partial A_{zd}^T}{\partial p} + \frac{\partial (B_{zd} B_{zd}^T)}{\partial p}\right)\right]
\end{aligned}
\tag{C.8}
$$

where Σ_q, L_i, $M_{i,p}$, and $N_{i,p}$ are obtained from Eq. C.2, Eq. C.3, Eq. C.6, and Eq. C.7, respectively.

Table C.1 indicates the number of Lyapunov equations that must be solved when computing sensitivities and curvatures. The total number of performance metrics is n_z and the total number of parameters of interest is n_p. The size of A_{zd} is $n_s \times n_s$. The computational cost greatly increases when curvature information is desired. An additional $2n_z n_p$ Lyapunov equations need to be solved, and this can be an important issue for large-order systems with several performance variables and parameters.

A "normalized" curvature of the performance RMS value with respect to p can be computed as follows. First, write the variance sensitivity in terms of the RMS sensitivity.

$$
\frac{\partial \sigma_{z_i}^2}{\partial p} = 2\sigma_{z_i}\frac{\partial \sigma_{z_i}}{\partial p}
\tag{C.9}
$$

Table C.1: Number of Lyapunov equations needed for exact sensitivity and curvature calculations.

Calculation	Comments	# of order n_s Lyap. equations
Sensitivity	• 1 order n_s Lyap. equation to obtain nominal Σ_q	
	• 1 order n_s Lyap. equation to obtain L_i for each z_i	$1 + n_z$
Curvature	• 1 order n_s Lyap. equation to obtain nominal Σ_q	
	• 1 order n_s Lyap. equation to obtain L_i for each z_i	
	• 1 order n_s Lyap. equation to obtain $M_{i,p}$ for each z_i and p	
	• 1 order n_s Lyap. equation to obtain $N_{i,p}$ for each z_i and p	$1 + n_z(1 + 2n_p)$

Now take another derivative with respect to p and use the chain rule.

$$\frac{\partial^2 \sigma_{z_i}^2}{\partial p^2} = 2\left(\frac{\partial \sigma_{z_i}}{\partial p}\right)^2 + 2\sigma_{z_i}\frac{\partial^2 \sigma_{z_i}}{\partial p^2} \tag{C.10}$$

Solving for the curvature of the RMS value leads to

$$\frac{\partial^2 \sigma_{z_i}}{\partial p^2} = \frac{1}{2\sigma_{z_i}}\left[\frac{\partial^2 \sigma_{z_i}^2}{\partial p^2} - 2\left(\frac{\partial \sigma_{z_i}}{\partial p}\right)^2\right] \tag{C.11}$$

Multiplying through by $\frac{p^2}{\sigma_{z_i}}$ to make the curvature dimensionless results in

$$\frac{p^2}{\sigma_{z_i}}\frac{\partial^2 \sigma_{z_i}}{\partial p^2} = \left[\frac{p^2}{2\sigma_{z_i}^2}\frac{\partial^2 \sigma_{z_i}^2}{\partial p^2} - \left(\frac{p}{\sigma_{z_i}}\frac{\partial \sigma_{z_i}}{\partial p}\right)^2\right] \tag{C.12}$$

Now divide through by the normalized sensitivity to obtain the normalized curvature.

$$\underbrace{\frac{1}{\left(\frac{p}{\sigma_{z_i}}\frac{\partial \sigma_{z_i}}{\partial p}\right)}\left[\frac{p^2}{\sigma_{z_i}}\frac{\partial^2 \sigma_{z_i}}{\partial p^2}\right]}_{\text{normalized curv.}} = \underbrace{\frac{1}{\left(\frac{p}{\sigma_{z_i}}\frac{\partial \sigma_{z_i}}{\partial p}\right)}}_{\text{normalized sens.}}\left[\frac{p^2}{2\sigma_{z_i}^2}\frac{\partial^2 \sigma_{z_i}^2}{\partial p^2} - \underbrace{\left(\frac{p}{\sigma_{z_i}}\frac{\partial \sigma_{z_i}}{\partial p}\right)^2}_{\text{normalized sens.}}\right] \tag{C.13}$$

The left-hand side of the equation can be approximated by

$$\frac{\Delta\left(\frac{p}{\sigma_{z_i}}\frac{\partial\sigma_{z_i}}{\partial p}\right)}{\frac{p}{\sigma_{z_i}}\frac{\partial\sigma_{z_i}}{\partial p}} = \frac{\%\text{ change in normalized sensitivity}}{\%\text{ change in parameter }p} \tag{C.14}$$

which can be thought of as a normalized curvature value.

A large value indicates that the sensitivity changes rapidly for small parameter values. A small value, on the other hand, suggests that the sensitivity is relatively constant and first-order approximations can be used to a good degree of accuracy.

References

[1] K. J. ÅSTRÖM AND B. WITTENMARK, *Computer-Controlled Systems: Theory and Design*, Prentice-Hall, Inc., 1997.

[2] M. ATHANS, *Lecture notes for Multivariable Control Systems II, MIT course 6.234J*, January 1995.

[3] BALL AEROSPACE AND TECHNOLOGIES CORPORATION, *Electro-Optical Line-of-Sight Controls*, URL <http://www.ball.com/aerospace/ptlos.html>. Accessed December 5, 1998.

[4] BALL AEROSPACE AND TECHNOLOGIES CORPORATION, *Gimbal Designs*. URL <http://www.ball.com/aerospace/gimbals.html>. Accessed December 5, 1998.

[5] K. J. BATHE, *Finite Element Procedures*, Prentice-Hall, Inc., 1996.

[6] B. BIALKE, *A compilation of reaction wheel induced spacecraft disturbances*, in Proceedings of the 20th Annual AAS Guidance and Control Conference, Breckenridge, CO, February 5–9, 1997. AAS Paper No. 97-038.

[7] G. H. BLACKWOOD, R. N. JACQUES, AND D. W. MILLER, *The MIT multipoint alignment testbed: technology development for optical interferometry*, in Proceedings of the SPIE Conference on Active and Adaptive Optical Systems, vol. 1542, San Diego, CA, July 1991, pp. 371–391.

[8] R. G. BROWN AND P. Y. C. HWANG, *Introduction to Random Signals and Applied Kalman Filtering*, John Wiley & Sons, Inc., 1997.

[9] A. E. BRYSON AND R. A. MILLS, *Linear-quadratic-gaussian controllers with specified parameter robustness*, Journal of Guidance, Control, and Dynamics, 21 (1998), pp. 11–18.

[10] M. E. CAMPBELL AND E. F. CRAWLEY, *Development of structural uncertainty models*, Journal of Guidance, Control, and Dynamics, 20 (1997), pp. 841–849.

[11] M. COLAVITA, *Visibility and phasing*, JPL Interoffice Memorandum, To SITE distribution, August 10, 1994.

[12] R. D. COOK, D. S. MALKUS, AND M. E. PLESHA, *Concepts and Applications of Finite Element Analysis*, John Wiley & Sons, Inc., 1989.

[13] R. CRAIG JR., *Structural Dynamics: An Introduction to Computer Methods*, John Wiley & Sons, Inc., 1981.

[14] S. H. CRANDALL AND W. D. MARK, *Random Vibration in Mechanical Systems*, Academic Press, 1963.

[15] E. F. CRAWLEY, B. P. MASTERS, AND T. T. HYDE, *Conceptual design methodol-*

ogy for high performance dynamic structures, in Proceedings of the 36th AIAA Structures, Structural Dynamics, and Materials Conference, New Orleans, LA, April 1995, pp. 2768–2787. AIAA Paper No. 95-2557.

[16] L. P. Davis, D. Cunningham, and J. Harrell, *Advanced 1.5 Hz passive viscous isolation system*, in Proceedings of the 35th AIAA/ASME/ASCE/AAS/ASC Structures, Structural Dynamics, and Materials Conference, Hilton Head, SC, April 18–24, 1994, pp. 2655–2665. AIAA Paper No. 94-1651.

[17] L. P. Davis, J. F. Wilson, R. E. Jewell, and J. J. Roden, *Hubble space telescope reaction wheel assembly vibration isolation system*, in Vibration Damping Workshop, Marshall Space Flight Center, March 1986.

[18] O. de Weck, D. Miller, and H. Gutierrez, *Structural dynamics and controls for NGST*, in Proceedings of the 34th Liège International Astrophysics Colloquium, Liège, Belgium, June 15–18, 1998.

[19] L. E. El Ghaoui and A. E. Bryson, *Wost parameter changes for stabilized conservative systems*, in AIAA Guidance, Navigation, and Control Conference, New Orleans, LA, 1991, pp. 1490–1495.

[20] C. E. Eyerman and J. F. Shea, *A systems engineering approach to disturbance minimization for spacecraft utilizing controlled structures technology*, MIT SERC Report #2-90, June 1990.

[21] R. L. Fox and M. P. Kapoor, *Rates of change of eigenvalues and eigenvectors*, AIAA Journal, 6 (1968), pp. 2426–2429.

[22] G. F. Franklin and J. D. Powell, *Digital Control of Dynamic Systems*, Addison-Wesley Publishing Co., Inc., 1980.

[23] B. Friedland, *Control System Design: An Introduction to State-Space Methods*, McGraw-Hill, Inc., 1986.

[24] A. Gelb, ed., *Applied Optimal Estimation*, The M.I.T. Press, 1974.

[25] R. M. Glaese, *Impedance Matching for Structural-Acoustic Conrol*, PhD thesis, Massachusetts Institute of Technology, April 1997. SERC Report #2-97.

[26] A. Grace, *Optimization Toolbox User's Guide*, The MathWorks, Inc., 1994.

[27] C. Z. Gregory, *Reduction of large flexible spacecraft models using internal balancing theory*, Journal of Guidance, Control, and Dynamics, 7 (1984), pp. 17–32.

[28] S. C. O. Grocott, *Comparision of control techniques for robust performance on uncertain structural systems*, Master's thesis, Massachusetts Institute of Technology, January 1994. SERC Report #2-94.

[29] R. L. Grogan and R. A. Laskin, *On multidisciplinary modeling of the space interferometry mission*, in Proceedings of the American Control Conference, Philadelphia, PA, June 1998.

[30] H. Gutierrez, M. Levine, and R. Grogan, *Analysis of IPEX-2 pre-flight ground integration test data*, Tech. Rep. D-14905, NASA Jet Propulsion Laboratory, October 1997.

[31] H. L. Gutierrez, *Damping formulations in substructure synthesis*, Master's thesis, Massachusetts Institute of Technology, May 1994.

[32] H. L. GUTIERREZ AND D. W. MILLER, *Disturbance analysis of integrated structural/optical models with uncertainties*, in Proceedings of the American Control Conference, Philadelphia, PA, June 1998.

[33] T. K. HASSELMAN, J. D. CHROSTOWSKI, AND T. J. ROSS, *Interval prediction in structural dynamic analysis*, in Proceedings of the 33rd AIAA/ASME/AHS/ASC Structures, Structural Dynamics, and Materials Conference, Dallas, TX, April 1992, pp. 1272–1284. AIAA Paper No. 92-2215.

[34] ——, *Propagation of modeling uncertainty through structural dynamic models*, in Proceedings of the 35th AIAA/ASME/AHS/ASC Structures, Structural Dynamics, and Materials Conference, Hilton Head, SC, April 1994.

[35] G. J. HOU AND S. P. KENNY, *Eigenvalue and eigenvector approximate analysis for repeated eigenvalue problems*, AIAA Journal, 30 (1992).

[36] G. J. HOU AND G. KOGANTI, *Sensitivity analysis of Lyapunov and Ricaati equations with application to controls-structures integrated design*, in Proceedings of the 34th AIAA/ASME/ASCE/AHS/ASC Structures, Structural Dynamics and Materials Conference, LaJolla, CA, April 1993, pp. 1906–1915. AIAA Paper No. 93-1529.

[37] J. P. HOW, *Robust Control Design with Real Parameter Uncertainty Using Absolute Stability Theory*, PhD thesis, Massachusetts Institute of Technology, February 1993. SERC Report #1-93.

[38] T. T. HYDE, *Active Vibration Isolation for Precision Space Structures*, PhD thesis, Massachusetts Institute of Technology, January 1996. SERC Report #4-96.

[39] M. INGHAM, *Microdynamics and thermal snap response of deployable space structures*, Master's thesis, Massachusetts Institute of Technology, June 1998. SERC Report #2-98.

[40] R. N. JACQUES, *An approach to the preliminary design of controlled structures*, Master's thesis, Massachusetts Institute of Technology, February 1991. SERC Report #1-91.

[41] ——, *On-line System Identification and Control Design for Flexible Structures*, PhD thesis, Massachusetts Institute of Technology, May 1995. SERC Report #3-95.

[42] L. JANDURA, *Analysis of hexapod isolator requirements necessary to meet SIM OPD requirements for astrometry and nulling*, Interoffice Memorandum SIM/ITP LJAN9705151, Jet Propulsion Laboratory, May 15, 1997.

[43] JET PROPULSION LABORATORY, *Origins Missions*, URL <http://origins.jpl.nasa.gov/missions/sbobs.html>. Accessed November 29, 1998.

[44] JET PROPULSION LABORATORY, *Space Interferometry Mission*, URL <http://huey.jpl.nasa.gov/sim/index.html>. Accessed November 11, 1998.

[45] JET PROPULSION LABORATORY, *Modeling and Analysis for Controlled Optical Systems User's Manual*, 1997.

[46] ——, *Integrated Modeling of Optical Systems User's Manual*, January 1998. JPL D-13040.

[47] A. J. KEANE AND A. P. BRIGHT, *Passive vibration control via unusual geometries: Experiments on model aerospace structures*, Journal of Sound and Vibration, 192 (1996).

[48] S. Kenny, *Eigenvalue and eigenvector derivatives for structures*, Final Report, MIT Course 2.093: Computer Methods in Dynamics, April 29,1997.

[49] Y. Kim, *Thermal Creak Induced Dynamics of Space Structures*, PhD thesis, Massachusetts Institute of Technology, February 1999. SERC Report #14-98.

[50] W. J. Larson and J. R. Wertz, eds., *Space Mission Analysis and Design*, Microcosm, Inc. and Kluwer Academic Publishers, 1991.

[51] R. A. Laskin, *Technology for space optical interferometry*, in Proceedings of the 33$^{\text{rd}}$ AIAA Aerospace Science Meeting and Exhibit, Reno, NV, January 1995. AIAA Paper No. 95-0825.

[52] R. A. Laskin, *SIM Dynamics & Control Requirements Flowdown Process*. Presentation at the SIM Project Preliminary Instrument System Requirements Review, JPL, March 17–18, 1998.

[53] R. A. Laskin and M. San Martin, *Control/structure system design of a spaceborne optical interferometer*, in Proceedings of the AAS/AIAA Astrodynamics Specialist Conference, Stowe, VT, August 1989. AAS Paper No. 89-424.

[54] M. Levine, R. Bruno, and H. Gutierrez, *Interferometry program flight experiment #1: Objectives and results*, in Proceedings of the 16$^{\text{th}}$ International Modal Analysis Conference, Santa Barbara, CA, 1998, pp. 1184–1190.

[55] M. B. Levine, *Interferometry program flight experiments: IPEX I and II*, in Proceedings of the SPIE Conference on Astronomical Interferometry, R. D. Reasenberg, ed., vol. 3350, Kona, HI, March 1998, pp. 707–718.

[56] P. Maghami, S. Gupta, K. B. Elliot, S. M. Joshi, and J. E. Walz, *Experimental validation of an integrated controls-structures design methodology for a class of flexible space structures*, in NASA Technical Paper 3462, November 1994.

[57] B. P. Masters and E. F. Crawley, *Evolutionary design of controlled structures systems*, in Proceedings of the 38$^{\text{th}}$ AIAA Structures, Structural Dynamics, and Materials Conference, Kissammee, FL, April 1997. AIAA Paper No. 97-1263.

[58] ——, *An experimental investigation of optimized precision optical controlled-structures*, in Proceedings of the SPIE Conference on Smart Structures and Materials, vol. 3041, San Diego, CA, March 1997, pp. 348–359. Paper No. 3041-28.

[59] J. Melody and M. Levine, *Model updating and evolutionary structures*, in Proceedings of the 15$^{\text{th}}$ Biennial Conference on Mechanical Engineering and Noise, Boston, MA, September 1995.

[60] J. W. Melody, *Discrete-frequency and broadband reaction wheel disturbance models*, Interoffice Memorandum 3411-95-200csi, Jet Propulsion Laboratory, June 1995.

[61] ——, *SIM wavefront tilt disturbance analysis and angle feedforward*, Interoffice Memorandum 3411-96-336 ITP, Jet Propulsion Laboratory, November 1996.

[62] J. W. Melody and H. C. Briggs, *Analysis of structural and optical interactions of the precision optical interferometer in space (POINTS)*, in Proceedings of the SPIE Conference on Spaceborne Interferometry, Orlando, FL, April 1993.

[63] J. W. Melody and G. W. Neat, *Integrated modeling methodology validation using the micro-precision interferometer testbed: Assessment of closed-loop performance prediction capability*, in Proceedings of the American Control Conference, Albuquerque,

NM, June 1997.

[64] M. MILMAN, M. SALAMA, R. SCHEID, AND J. S. GIBSON, *Combined control-structural optimization*, Computational Mechanics, (1991), pp. 1–18.

[65] B. C. MOORE, *Principal component analysis of linear systems: Controllability, observability, and model reduction*, IEEE Transactions on Automatic Control, AC-26 (1981), pp. 17–32.

[66] D. V. MURTHY AND R. T. HAFTKA, *Survey of methods for calculating sensitivity of general eigenproblems*, in Sensitivity Analysis in Engineering, Langley Research Center, September 1986, pp. 177–196. NASA CP 2457.

[67] G. W. NEAT, J. F. O'BRIEN, N. M. NERHEIM, AND R. J. CALVET, *Micro-Precision interferometer testbed: First stabilized fringes*, in Proceedings of the SPIE International Symposium on AeroSense, Conference on Spaceborne Interferometry II, vol. 2477, Orlando, FL, April 1995, pp. 104–115.

[68] R. B. NELSON, *Simplified calculations of eigenvector derivatives*, AIAA Journal, 14 (1976), pp. 1201–1205.

[69] D. E. NEWLAND, *An Introduction to Random Vibrations, Spectral and Wavelet Analysis*, John Wiley & Sons, Inc., 1993.

[70] J. F. O'BRIEN AND G. W. NEAT, *Micro-Precision interferometer: Pointing control system*, in Proceedings of the 4th Conference on Control Applications, Albany, NY, September 1995, pp. 464–469.

[71] K. OGATA, *Modern Control Engineering*, Prentice-Hall, Inc., 1990.

[72] M. O'NEAL, D. ELDRED, D. LIU, AND D. REDDING, *Experimental verification of nanometer level optical pathlength control on a flexible structure*, in Proceedings of the 14th Annual Rocky Mountain Guidance and Control Conference, Keystone, CO, February 2–6, 1991, pp. 231–249.

[73] M. C. O'NEAL AND J. T. SPANOS, *Optical pathlength control in the nanometer regime on the JPL phase B interferometer testbed*, in Proceedings of the SPIE Conference on Active and Adaptive Optical Systems, vol. 1542, San Diego, CA, July 1991, pp. 359–370.

[74] *Origins: Roadmap for the Office of Space Science Origins Theme*, National Aeronautics and Space Administration, 1997. Prepared by the Origins Subcommittee of the Space Science Advisory Committee. Available from URL <http://origins.jpl.nasa.gov/library/scienceplan/scienceidx.html> (accessed November 29, 1998).

[75] *OSI: Orbiting Stellar Interferometer*, Jet Propulsion Laboratory, March 1996. Report for NASA Science and Technical Review.

[76] A. PARKINSON, C. SORENSEN, AND N. POURHASSAN, *A general approach for robust optimal design*, Journal of Mechanical Design, 115 (1993), pp. 74–80.

[77] J. I. PRITCHARD, H. M. ADELMAN, AND J. SOBIESZCZANSKI-SOBIESKI, *Optimization for minimum sensitivity to uncertain parameters*, AIAA Journal, 34 (1996), pp. 1501–1504.

[78] D. C. REDDING AND W. G. BRECKENRIDGE, *Optical modeling for dynamics and control analysis*, Journal of Guidance, Control, and Dynamics, 14 (1991), pp. 1021–

1032.

[79] S. B. SHAKLAN, J. W. YU, AND H. C. BRIGGS, *Integrated structural and optical modeling of the orbiting stellar interferometer*, in Proceedings of the SPIE Conference on Space Astronomical Telescopes and Instruments II, P. Y. Bely and J. B. Breckinridge, eds., vol. 1945, Orlando, FL, April 1993, pp. 123–132.

[80] R. E. SKELTON, *Model error concepts in control design*, International Journal of Control, 49 (1989), pp. 1725–1753.

[81] *The Space Interferometry Mission: Taking the Measure of the Universe*, April 5, 1996. Final Report of the Space Interferometry Science Working Group. Available from URL <http://www.ess.sunysb.edu/~simswg/siswg/siswg.html> (accessed November 29, 1998).

[82] J. SPANOS, Z. RAHMAN, AND G. BLACKWOOD, *A soft 6-axis active vibration isolator*, in Proceedings of the American Control Conference, Seattle, WA, June 1995.

[83] G. STRANG, *Introduction to Applied Mathematics*, Wellesley-Cambridge Press, 1986.

[84] J. TING AND E. F. CRAWLEY, *Characterization of damping of materials and structures from nanostrain levels to one thousand microstrain*, AIAA Journal, 30 (1992), pp. 1856–1863.

[85] J. VAN DE VEGTE, *Feedback Control Systems*, Prentice-Hall, Inc., 1990.

[86] P. H. WIRSCHING, T. L. PAEZ, AND H. ORTIZ, *Random Vibrations: Theory and Practice*, John Wiley & Sons, Inc., 1995.

[87] K. Y.-L. YANG, *Efficient Design of Robust Controllers for H_2 Performance*, PhD thesis, Massachusetts Institute of Technology, October 1996. SERC Report #8-96.

[88] K. ZHOU, J. C. DOYLE, AND K. GLOVER, *Robust and Optimal Control*, Prentice-Hall, Inc., 1996.